THE UNIVERSITY OF QUEENSLAND

AUSTRALIA

Preparation and Mechanism Study of Non-precious Metal Catalysts for Electrochemical Oxygen Reduction

Ruifeng Zhou

Master of Science

A thesis submitted for the degree of Doctor of Philosophy at

The University of Queensland in 2015

Australian Institute for Bioengineering and Nanotechnology

Abstract

Fuel cell is an electrochemical device which can convert chemical energy into to electricity. Compared with steam engine and internal combustion engine, the fuel cell has higher conversion efficiency and lower pollution. The energy conversion in fuel cells is based on the oxidation of fuel and reduction of oxygen, both of which need electrocatalyts to smooth the reactions. However, the oxygen reduction reaction (ORR) is sluggish. Therefore, high-performance ORR catalyst is crucial to the overall performance of the fuel cell. State-to-art ORR catalyst are those based on Pt and its alloys. Therefore, developing new inexpensive eletrocatalysts for ORR is very demanding.

This thesis is committed to develop carbon based ORR catalysts. The research comprises synthesis of material, characterization and electrochemical test. The research specially emphasizes on facile synthesis of nitrogen and non-precious metal co-doped graphitic carbon, characterization of metal-nitrogen interaction and methodology in electrochemical analysis.

The first three parts of the thesis is about the synthesis of non-precious metal/ nitrogen-doped reduced graphene oxide (N-rGO) composite and study of their ORR catalytic activity. The first part of the thesis is focused on synthesis of N-rGO, and for the first time, a nanocomposite of CuO/N-rGO with a very high ORR performance in alkaline electrolyte was synthesized. It is confirmed that CuO, with negligible ORR reactivity by itself, introduces a synergistic effect by combining with N-rGO through the interactions with nitrogen, resulting in a significant ORR activity enhancement. The experiment revealed that rapid reduction of HOO^- intermediate by the CuO/N-rGO leads to more positive onset potential, higher current density and higher four-electron selectivity catalysed than both the CuO/rGO and N-rGO. Meanwhile, the CuO hindered restacking of N-rGO, providing the resultant nanocomposite much higher specific surface area and larger pore size to facilitate oxygen transfer, resulting in higher ORR current than that of Pt/C at low potential.

In the second part of the thesis, three types of silver/ reduced graphene oxide (Ag/rGO) nanocomposites (one doped with nitrogen and another two without) are synthesized to investigate their atomic structures and the oxygen reduction reaction (ORR) performance with them as the electrocatalysts. For the first time, the bonding interaction between Ag and N in N-rGO is confirmed by both high resolution X-ray photoelectron spectroscopy (XPS) and surface enhanced Raman spectroscopy (SERS). The Ag/N-rGO shows excellent ORR performance, including very high onset potential and current density, which outperforms those Ag/rGOs without N doping. Detailed electrochemical analysis shows that the ORR

mechanism on Ag/N-rGO is different from both Ag and N-rGO, and its excellent performance is caused by the Ag-N bonding which alters the electronic structure of N-rGO.

In the third part of the thesis, a novel Fe/N co-doped graphitic carbon bulb (Fe/N-gCB) is synthesized as a high-performance ORR catalyst. The key findings include: 1) highly graphitic and lowly defective carbon with extraordinarily high N content can be synthesized at low temperature of 550 °C. 2) High Fe content facilitates the formation of high specific surface area and graphitic structure at low temperature. 3) The low temperature process retains high level of N. 4) Fe/N-gCB shows comparable performance with Pt/C in alkaline electrolyte and adequate performance in acidic electrolyte. 5) Only the Fe coordinated to N in the shell can contribute ORR activity.

The forth part of the thesis focus on the study methodology of ORR. The forced convection methods on rotation electrode are carefully investigated in theory and verified by experiment to study the electron transfer number (n) of ORR on non-Pt catalysts in aqueous electrolyte. It is found that the widely used Koutechy-Levich (KL) plot is not suitable in determining n neither theoretically nor experimentally. The oxygen reduction reaction is neither a single-step nor irreversible so it does not meet the precondition of KL theory. By construction of a simple mathematical model, it is prove that the ORR is even not a first-order reaction in some cases, which is also essential to KL theory. Practically, the n of oxygen reduction is significantly dependent on the angular velocity of the electrode, which makes the linear fitting of KL plot meaningless. The KL plot is always not linear, even though the measurement error is excluded. Therefore, forced linear fitting results in incorrect n.

The fifth part of the thesis is the extension of the forth part. A new mathematical method is developed to determine the rate constants and the orders of reaction of the sub-reactions in ORR. The method can extract the oxygen and peroxide concentration on the electrode surface and the current destiny from different sub-reactions of ORR. So it can be used to determine order of reaction. This method is applied to various catalysts and the orders of reactions are determined not to be 1 for most cases.

Declaration by author

This thesis is composed of my original work, and contains no material previously published or written by another person except where due reference has been made in the text. I have clearly stated the contribution by others to jointly-authored works that I have included in my thesis.

I have clearly stated the contribution of others to my thesis as a whole, including statistical assistance, survey design, data analysis, significant technical procedures, professional editorial advice, and any other original research work used or reported in my thesis. The content of my thesis is the result of work I have carried out since the commencement of my research higher degree candidature and does not include a substantial part of work that has been submitted to qualify for the award of any other degree or diploma in any university or other tertiary institution. I have clearly stated which parts of my thesis, if any, have been submitted to qualify for another award.

I acknowledge that an electronic copy of my thesis must be lodged with the University Library and, subject to the policy and procedures of The University of Queensland, the thesis be made available for research and study in accordance with the Copyright Act 1968 unless a period of embargo has been approved by the Dean of the Graduate School.

I acknowledge that copyright of all material contained in my thesis resides with the copyright holder(s) of that material. Where appropriate I have obtained copyright permission from the copyright holder to reproduce material in this thesis.

Publications during candidature

1. **Zhou, R. F.**; Zheng, Y.; Hulicova-Jurcakova, D.; Qiao, S. Z., Enhanced electrochemical catalytic activity by copper oxide grown on nitrogen-doped reduced graphene oxide. *J. Mater. Chem. A* **2013**, 1, (42), 13179-13185.

2. **Zhou, R. F.**; Qiao, S. Z., Silver/Nitrogen-Doped Graphene Interaction and Its Effect on Electrocatalytic Oxygen Reduction. *Chem. Mater.* **2014**, 26, (20), 5868-5873.

3. **Zhou, R. F.**; Qiao, S. Z., Fe/N co-doped graphitic carbon bulb for high-performance oxygen reduction reaction. *Chem. Comm.* **2015**, 51, 7561

4. Liang, J.; **Zhou, R. F.**; Chen, X. M.; Tang, Y. H.; Qiao, S. Z., Fe-N Decorated Hybrids of CNTs Grown on Hierarchically Porous Carbon for High-Performance Oxygen Reduction. *Adv. Mater.* **2014**, 26, (35), 6074-6079.

5. Yang, T.; **Zhou, R.**; Wang, D.-W.; Jiang, S. P.; Yamauchi, Y.; Qiao, S. Z.; Monteiro, M. J.; Liu, J., Hierarchical mesoporous yolk-shell structured carbonaceous nanospheres for high performance electrochemical capacitive energy storage. *Chem. Comm.* **2015**. 51, (13), 2518-2521.

6. Yang, T.; Liu, J.; **Zhou, R.**; Chen, Z.; Xu, H.; Qiao, S. Z.; Monteiro, M. J., N-doped mesoporous carbon spheres as the oxygen reduction reaction catalysts. Journal of *Mater. Chem. A* **2014**, 2, (42), 18139-18146.

7. Liu, H.; Su, D.; **Zhou, R.**; Sun, B.; Wang, G.; Qiao, S. Z., Highly Ordered Mesoporous MoS_2 with Expanded Spacing of the (002) Crystal Plane for Ultrafast Lithium Ion Storage. *Adv. Energy Mater.* **2012**, 2, (8), 970-975.

8. **Zhou, R. F.**; M. Jaroniec.; Qiao, S. Z., Nitrogen Doped Carbon Electrocatalysts Decorated with Transition Metals for Oxygen Reduction Reaction. Accepted by *Chemcatchem*.

9. **Zhou, R. F.**; Zheng Y.; Zelenay P.; Qiao, S. Z., Measurement of Electron Transfer Number of Oxygen Reduction Reaction: from Theory to Experiment. Submitted to *J. Am. Chem. Soc.*

Publications included in this thesis

Zhou, R. F.; M. Jaroniec.; Qiao, S. Z., Nitrogen Doped Carbon Electrocatalysts Decorated with Transition Metals for Oxygen Reduction Reaction. Submitted to *Chemcatchem*. – incorporated as Chapter 2.

Contributor	Statement of contribution
Ruifeng Zhou (Candidate)	Wrote and edited paper (80%)
Mietek Jaroniec	Wrote and edited paper (10%)
Shizhang Qiao	Wrote and edited paper (10%)

Zhou, R. F.; Zheng, Y.; Hulicova-Jurcakova, D.; Qiao, S. Z., Enhanced electrochemical catalytic activity by copper oxide grown on nitrogen-doped reduced graphene oxide. *J. Mater. Chem. A* **2013**, 1, (42), 13179-13185– incorporated as Chapter 3.

Contributor	Statement of contribution
Ruifeng Zhou (Candidate)	Designed experiments (80%) Conducted experiments (100%) Wrote and edited paper (70%)
Yao Zheng	Wrote and edited paper (10%)
Denisa Hulicova-Jurcakova	Wrote and edited paper (10%)
Shizhang Qiao	Designed experiments (20%) Wrote and edited paper (10%)

Zhou, R. F.; Qiao, S. Z., Silver/Nitrogen-Doped Graphene Interaction and Its Effect on Electrocatalytic Oxygen Reduction. *Chem. Mater.* **2014**, 26, (20), 5868-5873– incorporated as Chapter 4.

Contributor	Statement of contribution
Ruifeng Zhou (Candidate)	Designed experiments (80%) Conducted experiments (100%)

	Wrote and edited paper (70%)
Shizhang Qiao	Designed experiments (20%) Wrote and edited paper (30%)

Zhou, R. F.; Qiao, S. Z., Fe/N co-doped graphitic carbon bulb for high-performance o xygen reduction reaction. *Chem. Comm*. **2015**, 51 7561- incorporated as Chapter 5.

Contributor	Statement of contribution
Ruifeng Zhou (Candidate)	Designed experiments (80%) Conducted experiments (100%) Wrote and edited paper (70%)
Shizhang Qiao	Designed experiments (20%) Wrote and edited paper (30%)

Zhou, R. F.; Zheng Y.; Zelenay P.; Qiao, S. Z., Measurement of Electron Transfer Number of Oxygen Reduction Reaction: from Theory to Experiment. Submitted to J. Am. Chem. Soc. – incorporated as Chapter 6.

Contributor	Statement of contribution
Ruifeng Zhou (Candidate)	Designed experiments (80%) Conducted experiments (100%) Wrote and edited paper (60%)
Yao Zheng	Wrote and edited paper (10%)
Piotr Zelenay	Wrote and edited paper (10%)
Shizhang Qiao	Designed experiments (20%) Wrote and edited paper (20%)

Contributions by others to the thesis

Contributions by Shizhang Qiao in experiment design, concept, analysis, interpretation, drafting, and writing in the advisory capacity.

Statement of parts of the thesis submitted to qualify for the award of another degree

None.

.

Acknowledgements

First and foremost, I would like to express my sincere gratitude to Prof. Shi Zhang Qiao for his valuable guidance, support and encouragement throughout my PhD study. The suggestions continuously motivate me in both scientific research and logical reasoning in my life. I also want to thank Dr. Denisa Hulicova-Jurcakova who gave me many useful advices during my research and paper writing.

Furthermore I am very grateful to Dr Jian Liu who discussed with me about multi aspects of research. I also appreciate several collaborators who provided me with opportunities to be in touch with some advanced material characterization techniques. They are Dr. Youhong Tang, Mr Pengfei Yin and Ms Xuemin Chen. My research has been greatly solidified by their effort.

I want to extend my sincere thanks to the following collaborators (in no particular order) with whom I have published a few papers: Dr. Hao Liu, Dr Yao Zheng, Dr Ji Liang and Mr Tianyu Yang. All the group members from Prof. Qiao's group in AIBN and University of Adelaide are appreciated for their technological assistance and useful discussion.

Special thanks go to University of Queensland, ARCCFN managing officers, Ms Celestien Warnaar-Notschaele, Ms Cheryl Berquist, Mr Chaoqing Lu; and University of Adelaide, School of Chemical Engineering managing officers, Ms Sue Earle and Ms Monica Dinan, and analytical services coordinator, Dr Qiuhong Hu for their administrative helps during the study.

I also would like to thank very much Prof. Joe Da Costa and Prof. John Zhu, who assess my conformation, mid-term review and thesis review and gave me very valuable suggestion on my progress

I would also like to acknowledge Endeavour IPRS and UQ Centennial Scholarship for their financial support.

Many thanks to all my friends in Australia for helping me enjoy living here. Most of all I would like to thank my mother for her long time encourage, support and unconditional love. Any step toward my dream cannot be made without her.

Keywords

Fuel Cell, Catalyst, Nanomaterial, Carbon, Non-precious Metal, Electrochemistry, Oxygen Reduction Reaction, Forced Convection Theory, Electron Transfer Number, Order of Reaction.

Australian and New Zealand Standard Research Classifications (ANZSRC)

ANZSRC code: 030302, Nanochemistry and Supramolecular Chemistry, 50%
ANZSRC code: 030604, Electrochemistry, 50%

Fields of Research (FoR) Classification

FoR code: 0303, Macromolecular and Material Chemistry, 50%
FoR code: 0306, Physical Chemistry (incl. Structural), 50%

Table of Contents

List of Figures and Tables

Chapter 1

Chapter 2

Figure 6. Schematic illustration of the formation mechanism of Mn_3O_4 nitrogen doped graphene, with permission from Royal Society of Chemistry.

Figure 7. High resolution XPS of N1s of N-rGO (a) and Ag_2O/NrGO and Ag/N-rGO (b). The four peaks are pyridinic, pyrrolitic/aminic, graphitic, and oxidized nitrogen, from low to high binding energy, respectively, with permission from American Chemical Society.

Figure 8. STXM XANES spectra of Co_3O_4/N-rGO, N-rGO, Co_3O_4 and CoO; (a) the orientation of a flat graphene sample with respect to the incident X-ray beam in STXM, the electric vector of the beam is parallel to the graphene basal plane; (b) C K-edge, (c) N K-edge, (d) O K-edge, and (e) Co L-edge XANES spectra, with permission from Royal Society of Chemistry.

Figure 9. EXAFS of 3 Fe–N-MWCNTs. Raw data (black open circles) are fitted (solid line) as referring to FeTMPP-Cl (for Fe–N_x) and Fe foil (for Fe–Fe). (d) Averaged coordination number (x) of Fe–N_x, with permission from Royal Society of Chemistry.

Figure 10. Electrochemical characterization of the CNT–G ORR catalyst. (a) CVs of commercial 20% Pt/C (black) and CNT–G (red) catalysts in O_2-saturated (solid) or Ar-saturated (dotted) 0.1M $HClO_4$. (b) RRDE polarization curves and peroxide yield of Pt/C (black) and NT–G (red) in O_2-saturated 0.1M $HClO_4$. (c) Kinetic current densities versus potential (d) RRDE polarization curves and peroxide yield of Pt/C (black) and NT–G (red) in O_2-saturated 0.1M KOH, with permission from Nature Publishing Group.

Figure 11. a, Rotation ring-disk electrode voltammograms recorded with Co_3O_4/rGO hybrid and Co_3O_4/N-rGO hybrid in O_2-saturated 0.1M KOH at 1600 rpm. b, Percentage of peroxide and the electron transfer number (n) of Co_3O_4/rmGO and Co_3O_4/N-rmGO hybrids, with permission from Nature Publishing Group.

Figure 12. a, RDE measurements of the ORR activity of carbon-supported CuDAT in O_2-saturated pH 6 phosphate buffer alone (black) and containing 10 mM poisons (left). RDE measurements of the ORR activity of carbon-supported FePc (blue lines) and pyrolyzed carbon supported FePc (red lines) in O_2-saturated 0.1 M NaOH alone (solid lines) and containing 10 mM KCN, with permission from American Chemical Society.

Table 1. TM-NC synthesized by furnace process.

Table 2. TM-NC synthesized by solvothemal process.

Chapter 3

Figure 1. (a) Low magnification TEM and selected area electron diffraction (inset) of CuO/N-rGO. (b) High resolution TEM of single CuO crystal.

Figure 2. (a) XRD patterns of N-rGO, CuO and CuO/N-rGO. (b) N_2 adsorption-desorption isotherms of N-rGO and CuO/N-rGO.

Figure 3. (a) XPS survey of N-rGO and CuO/N-rGO. High-resolution XPS of C1s (b) and N 1s (c) of N-rGO. (d) High-resolution XPS of Cu 2p of CuO.

Figure 4. CV of N-rGO (a) and CuO/N-rGO (b) under O_2 or N_2 saturation (0.1 V s^{-1}). (c) Comparison of CV of CuO/GO and CuO/N-rGO (O_2 saturation, 0.1 V s^{-1}).

Figure 5. LSV (5 mV s-1) of N-rGO (a) and CuO/N-rGO (b) at different rotation rate (0, 400, 800, 1200, 1600, 2000 and 2400 rpm).

Figure 6. (a) KL plot at -0.3 V of N-rGO, CuO/N-rGO and Pt/C. (b) Tafel plots and limiting currents (inset) of N-rGO, CuO/N-rGO and Pt/C.

Figure 7. (a) RRDE disk and ring current density (1600 rpm, 5mV s-1). (b) Peroxide percentage of the catalysts v.s. potential.

Figure 8. (a) LSV (1600 rpm, 5 mV s^{-1}) of the catalysts in0.1 M KOH + 0.01 M H_2O_2. (b) The current density –voltage and current density – power density plot of DMFC with N-rGO and CuO/N-rGO as cathode catalysts.

Figure S1. SEM image of CuO/N-rGO. Micrometer-scale pores are shown.

Figure S2. XRD pattern of GO and N-rGO. High-shifted interplanar diffraction of N-rGO is attributed to decreased interplanar displacement by elimination of functional groups during reduction.

Figure S3. TGA of CuO/N-rGO in air. N-rGO is burnt out and CuO is remained.

Figure S4. N_2 adsorption-desorption isotherms of GO and CuO/GO. Specific surface increases by CuO intercorporation.

Figure S5. FTIR of GO and N-rGO. Carboxyl groups are eliminated after reduction while hydroxyl groups remain.

Figure S6. High resolution XPS of O 1s of N-rGO. Carbonyl groups are of low amount after reduction.

Figure S7. 1st (solid) and 20th (dash) CV of GO (a), CuO/GO (b), N-rGO (c) and CuO/N-rGO (d). GO is a poor in conductivity so that it shows very low capacitance. It is reduced at low potential and achieves high conductivity after 20 cycles of CV. N-rGO already has good conductivity but can still be reduced a bit.

Figure S8. LSV of Pt/C at different rotation rate (rpm).

Figure S9. Electron transfer number of different catalysts calculated from RRDE test. The n is in accordance with that calculated from KL plot.

Figure S10. MeOH tolerance test of CuO/N-rGO and Pt/C under -0.3 V and 1600 rpm.

Chapter 4

Figure 1. Low (a) and high (b) resolution TEM of Ag/N-rGO. Inset: XRD pattern of Ag/N-rGO. (c) XPS survey of Ag/rGOs.

Figure 2. CV curves of e-rGO, c-rGO, and N-rGO (a) and Ag/e-rGO, Ag/c-rGO and Ag/N-rGO (b) in nitrogen and oxygen saturated electrolytes. The scan rate is 20 mV s-1.

Figure 3. LSV of e-rGO and Ag/e-rGO (a); c-rGO and Ag/c-rGO (b); N-rGO and Ag/N-rGO (c) on RRDE at 1600 rpm. The cathodic current (Id) is the dick current density. The anodic current (Ir) is the ring current normalized by the area of disk and magnified by 10 times for better view. (d) Peroxide production ratio of the catalysts during ORR.

Figure 4. Tafel plot of Pt/C and Ag (a); e-rGO and Ag/e-rGO (b); c-rGO and Ag/c-rGO (c); N-rGO and Ag/N-rGO (d). Data are collected at 2400 rpm.

Figure 5. High resolution XPS of N1s of N-rGO (a), and Ag2O/N-rGO and Ag/N-rGO (b). The four peaks are pyridinic, pyrrolitic/aminic, graphitic and oxidized nitrogen, from low to high binding energy respectively. (c) Raman spectra of N-rGO and Ag/rGOs.

Figure S1. XPS survey of GO (a) and N-rGO (b). High-resolution XPS of C1s of GO (c), N-rGO (d), c-rGO (e) and e-rGO (f). The peaks centred at 284.6 eV, 286.7 eV, 287.6 eV and 288.8 eV are attributed to carbon in C-C, C-OH, C=O and O-C=O structures respectively.

Figure S2. XRD of the Ag2O/GO. All peaks are attributed to Ag2O.

Figure S3. The first 8 cycles of CV of Ag2O/GO. The scan rate is 100 mv s-1.

Figure S4. TEM image of Ag/e-rGO (left) and Ag/c-rGO (right).

Figure S5. XRD patterns of Ag/e-rGO (left) and Ag/c-rGO (right).

Figure S6. LSV of Pt/C (a), Ag (b), e-rGO (c), Ag/e-rGO (d), c-rGO (e), Ag/c-rGO (f), N-rGO (g) and Ag/N-rGO (h). The scan rate is 5 mV s-1 and IR compensated (50 Ω). The legend numbers are angular velocities (rpm).

Figure S7. KL plot of Pt/C (a), Ag (b), e-rGO (c), Ag/e-rGO (d), c-rGO (e), Ag/c-rGO (f), N-rGO (g) and Ag/N-rGO (h). The legend numbers are potentials (V).

Figure S8. LSV of Ag/N-rGO and Pt/C at 1600 rpm at different catalyst loadings.

Figure S9. Stability test of Ag/N-rGO. The potential is fixed at 0.8 V.

Figure S10. Amperometric curve of Pt/C and Ag/N-rGO at 0.7 V and 1600 rpm in O2 saturated 0.1 M KOH. Methanol is injected into the electrolyte at the 60th second to reach a concentration of 3 M.

Figure S11. Raman spectra of N-rGO, e-rGO and c-rGO under identical measurement condition. The data are normalized to identical G band intensity.

Figure S12. Raman spectra of e-rGO and Ag/e-rGO under identical measurement condition. The data are plotted without any treatment.

Figure S13. Raman spectra of Ag/N-rGO. Curves 1 to 5 are measured at different locations of the same sample under 1% of full power. The bottom curve is measured under 10% intensity. The dash lines are at 1000 cm^{-1} and 1160 cm^{-1}.

Table S1. Price estimation of Ag/N-rGO.

Table S2. Tafel slopes of ORR on Ag, C and Ag/C catalysts.

Chapter 5

Figure 1. (a) and (b) TEM images of PPB. Inset: Fourier transformation of core. (c) and (d) TEM images of Fe/N-gCB. Inset: enlarged part in red frame. The arrow points at an iron dot.

Figure 2. (a) XRD of PPB and Fe/N-gCB. The black index is assigned to graphitic carbon and red indexes are assigned to metallic Fe. (b) XPS survey of Fe/N-gCB. Inset: high resolution XPS of N1s of Fe/N-gCB. (c) Raman spectrum Fe/N-gCB. (d) N2 isothermal sorption of Fe/N-gCB. Inset: corresponding pore distribution.

Figure 3. Normalized disk (Id) and ring (Ir) current at 1600 rpm in alkaline (a) and acid (b) electrolyte. Both currents are normalized by the area of disk. Corresponding peroxide ratio in alkaline (c) and acid (d) electrolyte. The potential is versus reversible hydrogen electrode (RHE).

Figure 4. Normalized disk current at 1600 rpm in alkaline (a) and acid (b) electrolyte. Corresponding Tafel plot in alkaline (c) and acid (d) electrolyte. The numbers are Tafel slopes in mV per decade.

Figure S1. TEM image of PB.

Figure S2. XRD pattern of PB.

Figure S3. TGA of Pyrolysis of PB in N2.

Figure S4. XRD of PPB at 900 °C.

Figure S5. TEM image of PPB.

Figure S6. XPS of acid leached PPB from 600 °C.

Figure S7. XPS of acid leached PPB from 700 °C.

Figure S8. XPS of acid leached PPB from 800 °C.

Figure S9. TGA of Fe/N-gCB in air.

Figure S10. Raman spectrum of N-MCN.

Figure S11. Raman spectrum of N-rGO.

Figure S12. CVs of Fe/N-gCB and PPB in O2 saturated 0.1 M KOH.

Figure S13. Normalized disk current at 1600 rpm in alkaline electrolyte.

Figure S14. LSV of acid leached PPBs in alkaline electrolyte.

Figure S15. LSV of acid leached PPBs in acid electrolyte.

Figure S16. Tafel plots in alkaline electrolyte.

Figure S17. Stability of ORR of Fe/N-gCB in alkaline and acid electrolytes.

Figure S18. LSV of Fe/N-gCB before and after 50,000 s test in alkaline electrolyte.

Figure S19. LSV of Fe/N-gCB before and after 50,000 s test in acid electrolyte.

Chapter 6

Figure 1. (a) NC of RRDE loaded with catalysts. The loadings are the 0.1 mg cm^{-2} except Au. (b-d) NC of RRDE loaded with N-rGO (b), N-MCN (c) and $Co(OH)_2$/N-rGO (d). The numbers are the loading amount of catalysts in mg cm^{-2}.

Figure 2. . CV of Pt ring (a) and Au ring (b) at 400 rpm. CV of Pt ring (c) and Au ring (d) at ω of 225 rpm, 625 rpm, 1225 rpm, 2025 rpm and 3025 rpm from bottom to top. The scann rate is 10 mV s^{-1}. (e) The amperometric i-t plots. (f) KL plot derived from (e). The electrolyte is 0.1 M KOH containing 1 mM H_2O_2 for all experiments except the lowest curves in (a) and (b).

Figure 3. KL plot of $Fe(CN)_6^{3-}$ on bare (a), N-rGO (b) or N-MCN (c) loaded RDE. The potential is 0.1 V .The numbers beside the line are ω in rpm and the numbers in legend are the loading amount of catalysts in mg cm-2. (d) B and r values of the corresponding KL plot.

Figure 4. The n of Ru (a), Au (b), Ag (c), e-rGO (d), N-rGO (e) and $Co(OH)_2$/N-rGO (f). n_{RRDE} (circles) are measured at ω of 225 rpm (Black), 625 rpm (red), 1225 rpm (green) 2025 rpm (blue) and 3025 rpm (cyan). Magenta cross: n_{KL}.

Figure 5. Correlation coefficients of KL plots of ORR.

Figure 6. 1/p vs $1/m_p$ plot of ORR on Ru (a), Au (b), Ag (c), e-rGO (d), N-rGO (e) and $Co(OH)_2$/N-rGO (f). The potential is 0.1 V (black), 0.2 V (red), 0.3 V (green), 0.4 V (blue), 0.5 V (cyan) and 0.6 V (magenta), respectively.

Figure S1. LSV of bare GC disk in 0.1 M KOH and 0.004 M K3Fe(CN)6. The ring is biased at 1.5V. The cathodic current is disk current and the anodic current is ring current. The current is normalized with disk area. The legends are angular velocity in rpm.

Figure S2. LSV of Pt ring in 0.1 M KOH and 0.004 M K3Fe(CN)6. The disk is bare GC and biased at 0.1 V. The current is normalized with disk area.

Figure S3. SEM image of the surface of N-rGO electrode.

Figure S4. SEM image of the surface of N-MCN electrode.

Figure S5. SEM image of the surface $Co(OH)_2$/N-rGO electrode.

Figure S6. LSV of the Ru disk. The angular velocities are 225 rpm (Black), 625 rpm (red), 1225 rpm (green) 2025 rpm (blue) and 3025 rpm (cyan).

Figure S7. Ring current densities of Ru.

Figure S8. LSV of the Au disk.

Figure S9. Ring current density of Au.

Figure S10. LSV of the disk of Ag.

Figure S11. Ring current density of Ag.

Figure S12. LSVof the disk of e-rGO.

Figure S13. Ring current density of e-rGO.

Figure S14. LSV of the disk of N-rGO.

Figure S15. Ring current density of N-rGO.

Figure S16. LSV of the disk of $Co(OH)_2$/N-rGO.

Figure S17. Ring current density of $Co(OH)_2$/N-rGO.

Figure S18. KL plot of Ru.

Figure S19. KL plot of Au.

Figure S20. KL plot of Ag.

Figure S21. KL plot of e-rGO.

Figure S22. KL plot of N-rGO.

Figure S23. KL plot of $Co(OH)_2$/N-rGO.

Chapter 7

Figure 1. The disk current density and normalized ring current density during ORR on Au (a), e-rGO (b), N-rGO (c) and $Co(OH)_2$/N-rGO (d). The relative O_2 flows are 6 (Black), 12 (red), 25 (green), 50 (blue) and 100 (cyan).

Figure 2. The electron transfer number of ORR on Au (a), e-rGO (b), N-rGO (c) and $Co(OH)_2$/N-rGO (d). The relative O2 flows are 6 (Black), 12 (red), 25 (green), 50 (blue) and 100 (cyan).

Figure 3. The PRR current densities of Au (a), e-rGO (b), N-rGO (c) and $Co(OH)_2$/N-rGO (d). The peroxide concentrations are 0.1 mM (Black), 0.2 mM (red), 0.5 mM (green), 1 mM (blue) and 2 mM (cyan).

Figure 4. The rate constants of reactions of j_O (black), $j_{2'}$ (red), j_2 (green) and j_4 (blue) on Au (a), e-rGO (b), N-rGO (c) and $Co(OH)_2$/N-rGO (d). The rate constants are in m s^{-1}. The Tafel slopes are in mV $decade^{-1}$.

Figure 5. The order of reactions of j_O (black), $j_{2'}$ (red), j_2 (green) and j_4 (blue) on Au (a), e-rGO (b), N-rGO (c) and $Co(OH)_2$/N-rGO (d).

Figure S1. 1/j vs 1/nFm plot at selected relative O_2 flows (in %). The number beside dash lines are the C_O^* in mole m^{-3}.

Figure S2. The C_P^0 during PRR on Au (a), e-rGO (b), N-rGO (c) and $Co(OH)_2$/N-rGO (d). The peroxide concentrations are 0.1 mM (Black), 0.2 mM (red), 0.5 mM (green), 1 mM (blue) and 2 mM (cyan).

Figure S3. The $\log(C_P^0)$ vs $\log(j_P)$ plot of Au (a), e-rGO (b), N-rGO (c) and $Co(OH)_2$/N-rGO (d). The C_P^0 is in mole m^{-3}. The j_P is in A m^{-2}. The potentials are 0.6 V (Black), 0.5 V (red), 0.4 V (green), 0.5 V (blue), 0.2 V (cyan) and 0.1 V (magenta).

Figure S4. The C_O^0 (solid) and C_P^0 (dash) during ORR on Au (a), e-rGO (b), N-rGO (c) and $Co(OH)_2$/N-rGO (d). The relative O_2 flows are 6 (Black), 12 (red), 25 (green), 50 (blue) and 100 (cyan).

Figure S5. The j_O (solid) and $j_{2'}$ (dash) during ORR on Au (a), e-rGO (b), N-rGO (c) and $Co(OH)_2$/N-rGO (d). The relative O_2 flows are 6 (Black), 12 (red), 25 (green), 50 (blue) and 100 (cyan).

Figure S6. The j_4 (solid) and j_2 (dash) during ORR on Au (a), e-rGO (b), N-rGO (c) and $Co(OH)_2$/N-rGO (d). The relative O_2 flows are 6 (Black), 12 (red), 25 (green), 50 (blue) and 100 (cyan).

Figure S7. The $\log(C_O^0)$ vs $\log(j_O)$ plot of Au (a), e-rGO (b), N-rGO (c) and $Co(OH)_2$/N-rGO (d). The C_O^0 is in mole m^{-3}. The j_O is in A m^{-2}. The potentials are 0.6 V (Black), 0.5 V (red), 0.4 V (green), 0.5 V (blue), 0.2 V (cyan) and 0.1 V (magenta).

Figure S8. The $\log(C_O^0)$ vs $\log(j_4)$ plot of Au (a), e-rGO (b), N-rGO (c) and $Co(OH)_2$/N-rGO (d). The C_O^0 is in mole m^{-3}. The j_4 is in A m^{-2}. The potentials are 0.6 V (Black), 0.5 V (red), 0.4 V (green), 0.5 V (blue), 0.2 V (cyan) and 0.1 V (magenta).

Figure S9. The $\log(C_O^0)$ vs $\log(j_2)$ plot of Au (a), e-rGO (b), N-rGO (c) and $Co(OH)_2$/N-rGO (d). The C_O^0 is in mole m^{-3}. The j_2 is in A m^{-2}. The potentials are 0.6 V (Black), 0.5 V (red), 0.4 V (green), 0.5 V (blue), 0.2 V (cyan) and 0.1 V (magenta).

List of Abbreviations Used in the Thesis

ORR:	Oxygen Reduction Reaction
HER:	Hydrogen Oxidation Reaction
SEM:	Scanning Electron Microscopy
TEM:	Transmission Electron Microscopy
SAED:	Selected Area Electron Diffraction
XRD:	X-Ray Diffraction
XPS:	X-Ray Photoelectron Spectroscopy
SERS:	Surface Enhanced Raman Spectroscopy
XAFS:	X-Ray Absorption Fine Structure
XANES:	X-Ray Absorption Near Edge Structure
EXAFS:	Extended X-Ray Absorption Fine Structure
STXM:	Scanning Transmission X-ray Microscopy
ToF-SIMS:	Flight of Time Secondary Ion Mass Spectrometry
BET:	Brunauer-Emmett-Teller
BJH:	Barrett-Joyner-Halenda
SSA:	Specific Surface Area
TGA:	Thermogravimetric Analysis
FTIR:	Fourier Transform Infrared Spectroscopy
DFT:	Density Functional Theory
DOS:	Density of States
RDE:	Rotation Disk Electrode
RRDE:	Rotation Disk-Ring Electrode
CV:	Cyclic Voltammetry
LSV:	Linear Scanning Voltammetry
RHE:	Relative Hydrogen Electrode
PEM:	Proton Exchange Membrane

DMFC:	Direct Methanol Fuel Cell
CNT:	carbon Nanotube
SWCNT:	Single-wall Carbon Nanotube
MWCNT:	Multi-wall Carbon Nanotube
OPR:	Ordered Porous Resin
OPC:	Ordered Porous Carbon
Pc:	Phthalocyanine
TM:	Transition Metal
NC:	Nitrogen Doped Carbon
GO:	Graphene Oxide
e-rGO:	Electrochemical Reduced Graphene Oxide
c-rGO:	Chemically Reduced Graphene Oxide
N-rGO:	Ammonia Reduced Graphene Oxide
N-MCN:	Nitrogen Doped Mesoporous Carbon Nanosphere
PB:	Prussian Blue
PPB:	Pyrolyzed Prussian Blue
Fe/N-gCB:	Fe/N co-doped Graphitic Carbon Bulb
GC:	Glassy carbon
KL:	Koutechy-Levich

Chapter 1: Introduction

1.1 Background

Fuel cells are electrochemical energy conversion devices that directly convert chemical energy to electric power with much higher efficiency and lower greenhouse gases emissions than other well-established technologies based on conventional fossil fuel combustion. The development and commercialization of fuel cells have been driven by increasing concerns over issues such as climate change and energy security as a result of dwindling petroleum supplies. Low temperature fuel cells, including proton-exchange-membrane fuel cells, alkaline fuel cell and direct methanol fuel cells etc., are particularly attractive due to their higher efficiency, lower operation temperature, and longer life span.

A fuel cell is composed of multiple components, including the electrolyte, the anode, the cathode, the fuel and the oxidant. The electrolyte is ion conductive, which allows ions to pass through, but electrons must go through an outer electric current. The electrolyte also keeps the fuel and oxidant apart. The anode is the electrode where oxidation takes place. In a fuel cell, the anode is electrically negative. The cathode is the electrode where reduction takes place, which is electrically positive. There are various fuels, among which H_2 is the most popular for its highest energy density. O_2 is the best oxidant because it is gathered from the atmosphere which reduces cost and carrying weight.

When running a fuel cell, for example the H_2/O_2 PEM fuel cell, H_2 fuel is introduced to the anode of the fuel cell, while air with O_2 is introduced to the cathode. At the anode, catalyst causes the H_2 to split into protons and electrons. The chemical reaction equation is shown below:

Anode: $2H_2 \rightarrow 4H^+ + 4e$

The electrolyte allows only the protons to pass through it to the cathode. At the cathode, the electrons and protons combine with O_2 to form water (oxygen reduction reaction), which flows out of the cell.

Cathode: $O_2 + 4H^+ + 4e \rightarrow 2H_2O$

Overall: $2H_2 + O_2 \rightarrow 2H_2O$

For in alkaline electrolyte, the equations are rewritten as:

Anode: $2H_2 + 4OH^- \rightarrow 2H_2O$

Cathode: $O_2 + 2H_2O + 4e \rightarrow 4OH^-$

Overall: $2H_2 + O_2 \rightarrow 2H_2O$

The structure of an alkaline fuel cell is shown in Figure 1. Membrane.

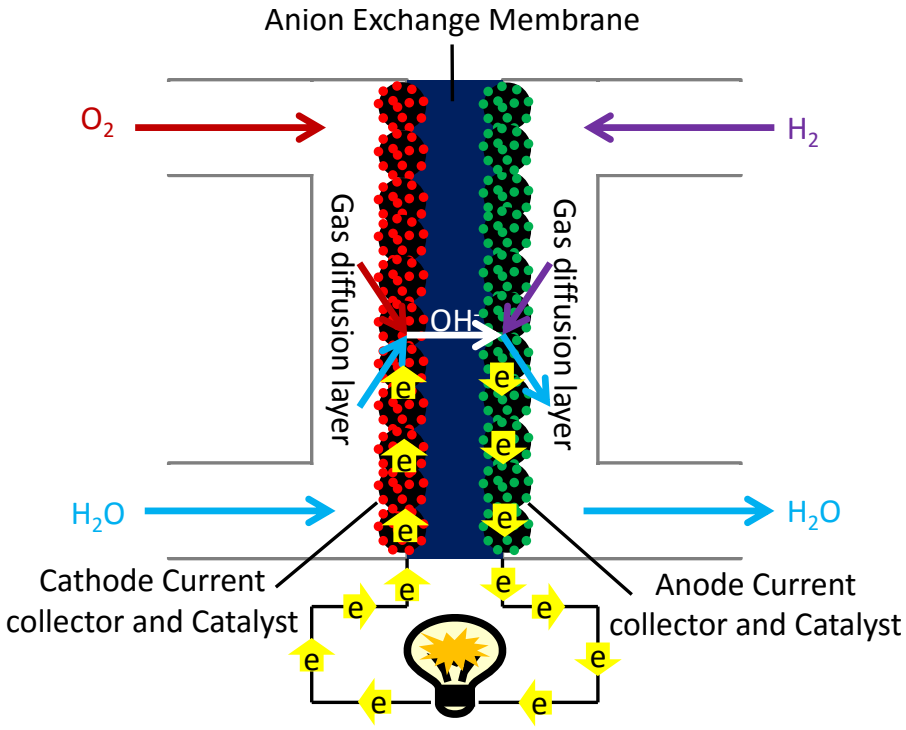

Figure 1. Structure of an alkaline fuel cell.

From the aspect of dynamics, the oxygen reduction reaction (ORR) is very slow. Therefore in current commercial fuel cells, platinum supported on carbon is used as a catalyst. Platinum is selected as the electrocatalyst because it shows the best performance i.e. highest current density at certain overpotential and highest efficiency (ratio between output electric energy and input chemical energy). However, the usage of platinum pushes up the price of the fuel cells, which is the main reason why fuels is not widely commercialized to replace internal consumption engine in vehicles and other mobile appliances. Therefore, development of non-precious metal electrocatalyst is desirable.

1.2 Aims

The key questions in non-precious ORR catalyst development include:

1. What kind of material is active in electrocatalysing ORR?

2. How is catalyst synthesized?

3. How does the catalyst perform in ORR?

To answer these questions, some more questions must be answered first:

1. What is the composition of the catalyst?

2. What is the morphology of the catalyst?

3. What is the relationship between different components in the catalyst?

Finally, there are some more profound questions to be answered:

1. How the performance of ORR is measured?

2. What quantities can be extracted from the result of measurement?

3. What information about ORR mechanism can be extracted from these data?

The aim of this thesis is to answer all of these questions. The study will cover from the synthesis of catalyst, to physical characterization; from performance measurement to mechanism discussion.

1.3 Methodology

To answer the question in the aims, various techniques are used which are summarized in this section.

Scanning electron microscopy (SEM) reveals the surface morphology of materials. The SEM images were taken with Philips XL30 FEG SEM. The resolution is about 10 nm.

Transmission electron microscopy (TEM) reveals the structure of material with a spatial resolution of higher than SEM. Selected area electron diffraction (SAED) is a technique associated with TEM to study the crystal structure of mater. The TEM images were collected with Tecnai F20.

X-ray diffraction (XRD) is a technique to study the crystal structure of mater. Each peak in a XRD pattern is attributed to an interplanar spacing. The higher the interplanar spacing, the lower the diffraction angle. The XRD spectrums were measured with Rigaku Miniflex benchtop XRD with Cu Kα line.

X-ray photoelectron spectroscopy (XPS) is a quantitative spectroscopic technique that measures the elemental composition, chemical state and electronic state of the elements that exist within a material. The XPS were taken by KRATOS Axis Ultra DLD with Al Kα line.

Raman spectroscopy is used to observe vibrational, rotational, and other modes in a system, which can be used to determine the structure of the material. Raman spectra were collected with HORIBA LabRAM HR Evolution with 532 nm laser.

N_2 adsorption/desorption isotherm is a technique to study the surface area and pore size distribution. The specific surface area is determined by multipoint BET equation and the pore size distribution is determined by BJH equation. The N_2 adsorption/desorption isotherm measurement was carried out with Micromeritics Tristar II at 77 K.

Fourier transform infrared spectroscopy (FTIR) is used to study the functional group of mater. The FTIR were collected with Nicolet 6700 FTIR.

Thermal gravimetric analysis (TGA) is a method of thermal analysis in which changes in weight of materials are measured as a function of increasing temperature, to give information about material's component. The TGA were measured with SETARAM ABSYSTM Thermogravimetric Analysis.

The electrochemical test is carried out under conventional tree-electrode configuration. Unless otherwise specified, nitrogen or oxygen saturated 0.1 M KOH is used as electrolyte. A Ag/AgCl in 4 M KCl is used as reference electrode (0.2 V vs. standard hydrogen electrode). A platinum wire is used as counter electrode. A rotation disk electrode (RDE) or rotation ring-disk electrode (RRDE) is used as working electrode. The illustration of electrochemical cell is shown in Figure 2.

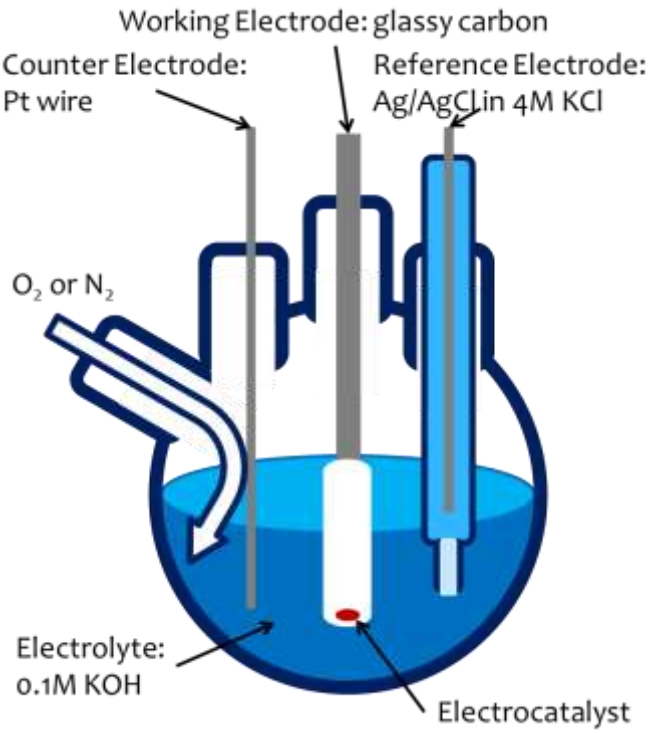

Figure 2. Configuration of electrochemical cell.

Linear sweep voltammetry (LSV) is a voltammetric method where the current at a working electrode is measured while the potential between the working electrode and a reference electrode is swept linearly in time. LSV is used to measure the electrochemical current of reactions. Cyclic voltammetry (CV) is a measurement in which the working electrode potential is ramped linearly versus time like LSV. When CV reaches a set potential, the working electrode's potential ramp is inverted. This inversion can happen multiple times during a single experiment. CV is used to determine the potential where the reaction is under equilibrium.

RDE is a working electrode that can be rotated under certain rates. By rotating the electrode, a forced convection is applied to the electrochemical cell. To compare different catalysts' activity, the LSVs on RDE at 1600 rpm are used according to academic standard. RRDE is similar to RDE, while a platinum ring is positioned around the disk. When the platinum ring is biased to about 0.5 V, some of the produced peroxide will be oxidized and the current can be measured. The mass transfers on RDE and RRDE are shown in figure 3.

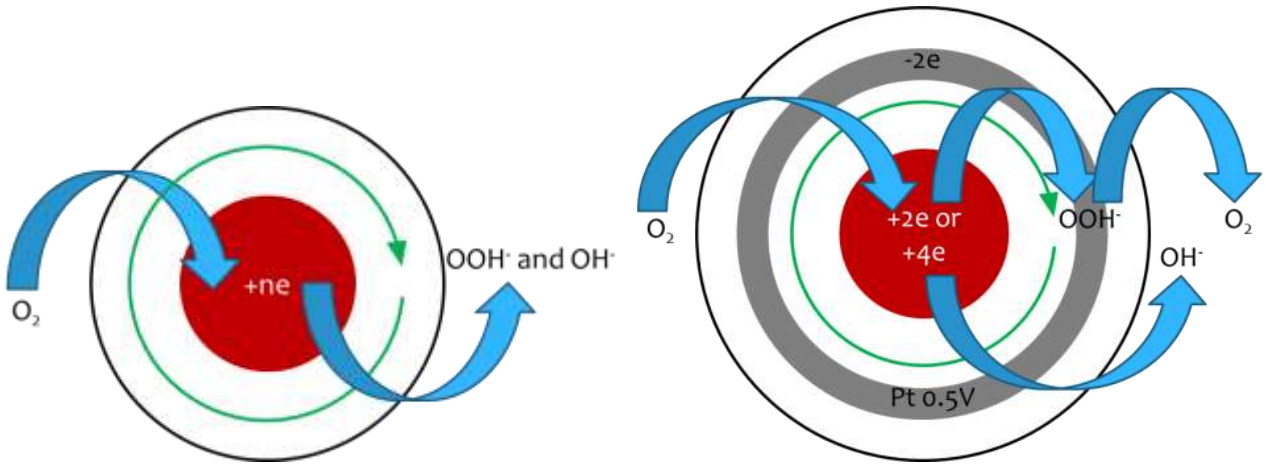

Figure 3. ORR on RDE (left) and RRDE (right) in alkaline electrolyte.

Before the electrochemical test, the catalyst is dispersed in a mixture of water and Nafion. A typical mass ratio between the catalyst, Nafion and water is 1:1:1000. The mixture is then supersonicated to achieve a uniform catalyst ink. The catalyst ink is then dropped on the RDE or RRDE. The electrode is then dried under ambient environment. The preparation of electrode from catalyst ink and glassy carbon (GC) RDE is illustrated in Figure 4.

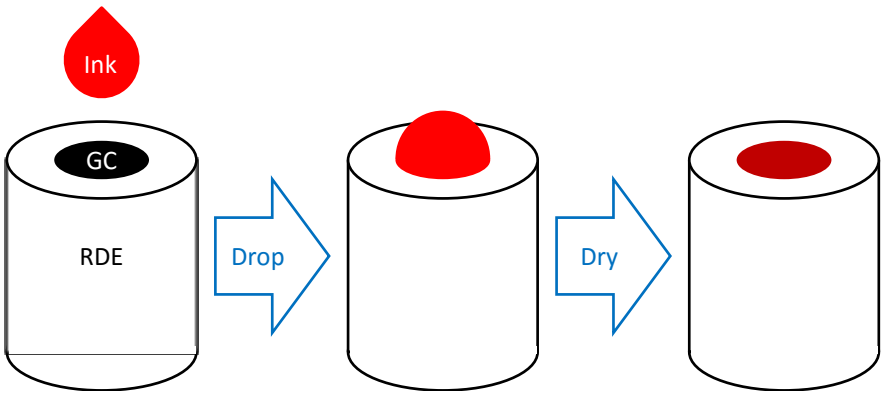

Figure 4. Preparation of electrode.

Chapter 2: Literature Review

Introduction

This chapter is the literature review of transition metal decorated carbon nanomaterials for electrochemical oxygen reduction reaction. This chapter covers the topics, including theoretical approaches to decorated carbon for ORR, decoration types and strategies, characterization of interaction between carbons and decorations, ORR performance of decorated carbon materials, ORR mechanism of decorated carbon materials and outlook and future challenges.

This chapter is accepted by *ChemcatChem*.

More focused literature review can be found in corresponding chapters.

Nitrogen Doped Carbon Electrocatalysts Decorated with Transition Metals for Oxygen Reduction Reaction

Ruifeng Zhou,[a, b] Mietek Jaroniec[c] and Shi Zhang Qiao*[a]

Abstract: The high cost of catalysts is the main disadvantage of aqueous fuel cells. In a conventional fuel cell, both the anode and cathode reactions need Pt based catalysts to catalyse respective electrochemical reactions, for example, the oxygen reduction reaction (ORR) on the cathode. Since the ORR is very sluggish, more Pt catalyst is needed to balance the anode and cathode currents. In recent years, many alternative catalysts have been explored for ORR, mostly carbon-based ones, including non-metal decorated carbons and metal decorated carbons. The transition metal and nitrogen co-doped carbons have shown the best ORR performance among all non-precious metal catalysts, which is comparable to Pt under analogous conditions. This paper reviews nitrogen doped carbon nanomaterials decorated with transition metals as ORR catalysts, their synthesis, characterization, and performance, with special emphasis on the mechanism and theoretical aspects of ORR.

1. Introduction

Fuel cell is a device that converts chemical energy to electric energy. When a fuel cell works, a reductant (fuel) is introduced to the anode and loses some electrons, which migrate through the outer circuit and are received by an oxidant on the cathode. The ions migrate through the electrolyte to reach the charge equilibrium. The fuel cells are usually classified on the basis of the electrolytes used. The solid oxide fuel cells are used at high temperatures for a high power output. At low temperatures (<100 °C), alkaline aqueous solutions, phosphoric acid and proton exchange membranes (PEMs) can be used as electrolytes, which are favorable for mobile applications such as vehicles. The most typical oxidant is O_2 because it can be gathered from air.

The cathode reactions (oxygen reduction reaction, ORR) of a fuel cell in acid and alkaline electrolytes are shown below.

Acid: $O_2 + 4H^+ + 4e \rightarrow 2H_2O$

Alkaline: $O_2 + H_2O + 4e \rightarrow 2H_2O + 4OH^-$

As compared to the hydrogen oxidation reaction (HOR) on the anode, the ORR is more complicated, which involves more electrons to be transferred and strong O=O double bond to be broken, so it is much more sluggish than HOR. A proper catalyst is essential to achieve satisfactory current. Conventional catalysts are based on Pt, which still shows the best performance among all the ORR catalysts especially in acid electrolytes, but the extremely high cost of Pt makes it unrealistic for wide applications. Two approaches have been explored toward reduction of the cost of ORR catalysts. One of them is focused on better utilization of Pt by improving the catalyst performance per Pt mass. The other approach is focused on the replacement of Pt by less expensive materials. Among the alternative catalysts, carbon has attracted the major attention due to its unique properties. First, carbon structures with high fraction of sp^2 are electron conductive, which is essential for electrochemical processes. Second, carbons can

[a] School of Chemical Engineering, the University of Adelaide, Adelaide, SA 5005, Australia
E-mail: s.qiao@adelaide.edu.au
[b] Australian Institute of Bioengineering and Nanotechnology, the University of Queensland, St Lucia, QLD 4072, Australia
[c] Department of Chemistry and Biochemistry, Kent State University, Kent, OH 44242, USA

Ruifeng Zhou received his BSc and MSc in physics from Tsinghua University. Currently, he is a PhD student at Australian Institute for Bioengineering and Nanotechnology (AIBN) of the University of Queensland and conducts a collaborative reseach at School of Chemical Engineering of the University of Adelaide with Professor Shi Zhang Qiao. His research interests are in nanomaterials for electrochemical energy conversion devices and their evaluation.

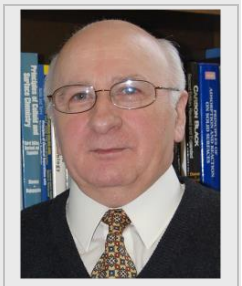

Mietek Jaroniec received his PhD from M. Curie-Sklodowska University (Poland); afterward, he was appointed as a faculty at the same University. Since 1991, he is Professor of Chemistry and Biochemistry at Kent State University, Kent, Ohio (USA). His research interests include interfacial chemistry and chemistry of materials, especially adsorption at the gas/solid and liquid/solid interfaces and nanoporous materials. At Kent State he has established a vigorous research program in the area of nanomaterials such as ordered mesoporous silicas, organosilicas, inorganic oxides, carbons, and nanostructured catalysts/photocatalysts, focusing on their synthesis, characterization and environmental and energy-related applications.

Shi-Zhang Qiao received his PhD in chemical engineering from Hong Kong University of Science and Technology in 2000. Currently, he is a chair professor at School of Chemical Engineering of the University of Adelaide, and an Honorary Professor at AIBN of the University of Queensland. His research expertise is in nanostructured and nanoporous materials for drug/gene delivery and for new energy technologies. He has coauthored more than 220 papers in refereed journals with over 11700 citations (H-index 55). In recognition of his achievements in research, he was honored with prestigious ARC Discovery Outstanding Researcher Award (2013), Emerging Researcher Award (2013, ENFL Division of the American Chemical Society), ARC ARF and APD Fellowships

be prepared with very high specific surface area. Since the carbon-based catalysts show low activity per electrochemically active area, it is essential to enlarge their surface area as high as possible. Third, carbons can be modified by various methods to achieve the desired properties for specific applications. This can be done by doping the structure of carbons with various heteroatoms and/or decorating it with different metals or nonmetals. Fourth, carbon is inexpensive and can be synthesized by using various organic and inorganic precursors ranging from biomass, organic wastes, and polymers to organic compounds and graphite.

There are already a few excellent reviews on heteroatom doped carbon and metal free materials for ORR.[1-3] Therefore, this review will be focused on nitrogen doped carbons (NC) decorated with non-precious metals because they have shown an excellent ORR performance as reported in recent literature. In this review, the non-precious metals are called transition metals (TM) because the main-group metals are not catalytically active toward ORR. Though Pt-group metals are a subcategory of TM, they are not discussed due to their high cost. This review will cover the mechanistic studies and theoretical aspects of ORR as well as the synthesis, characterization, performance of the carbon-based ORR catalysts.

2. Density functional theory studies of ORR on TM-NC

According to the theory of coordination chemistry, nitrogen with lone pair is a ligand able to coordinate TM with empty orbitals. In NC, nitrogen can be in graphitic, pyrrolic, pyridinic or oxidized state. The pyridinic nitrogen has a lone pair like in pyridine. The pyrrolic cation (with the lost proton) also has a lone pair. Thus, they theoretically have the potential to coordinate TM. The structure of nitrogen atoms is shown in figure 1.

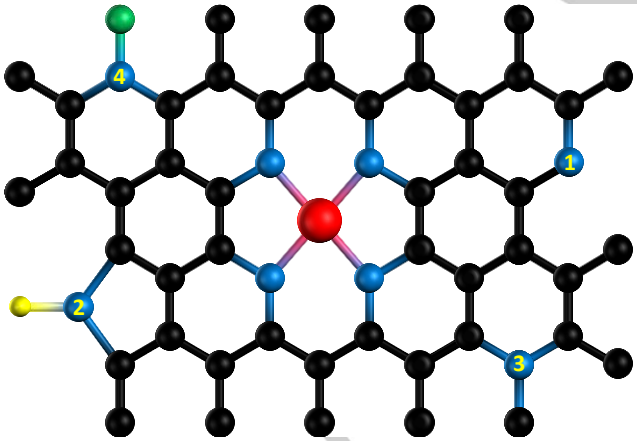

Figure 1. An schematic diagram of atomic structure of TM-NC. The atoms are carbon (black), nitrogen (blue), oxygen (green), hydrogen (yellow) and TM (red). The nitrogen atoms are pyridinic (1) and pyrrolic (2) graphitic (3) and oxidized (4). The motif in the centre is Fe-N_4.

When TM is incorporated into NC, various structures are possible. To simplify the density functional theory (DFT) modeling, the so called TM-N_4 structure (figure 1) is usually used.[4-11] This structure has the lowest formation energy among all TM-N_x motifs, so it is the most likely and stable structure in TM-NC. Other structures including TM-N_2, TM-polypyrrole and TM-macrocyclic molecule complexes are also studied.[9-14] Fe and Co are usually selected as TM because the Fe-NC and Co-NC are the most popular TM-NC ORR catalysts in practice. Mn-NC is also studied for its good ORR performance. Ni-NC is studied to better understand its low activity.

According to the widely accepted conclusion form DFT, the origin of the ORR activity is the adsorption of intermediates (O_2, HOO, H_2O_2, O and OH etc.) on the catalysts. And the adsorption energy is the determinant of reaction rate.[15] For example, the product of the first electron transfer in ORR, the HOO, has very high free energy as a free radical. So the rate of the first electron transfer is very low unless HOO has low adsorption energy on the catalyst. When ORR takes places on the TM-N_X motif, the TM is the only centre where the reaction intermediate is adsorbed. The adsorption energy depends mainly on the type of TM and modestly on the chemistry of macrocyclic ligands. For instance, Fe-N_4 usually has lower adsorption energy than Co-N_4. All intermediates have similar adsorption energy trend with the change of macrocyclic ligands (Fig 3). Only Fe-N_4 has ability to split O=O bond to reduce H_2O_2 to H_2O due to its strong interaction with H_2O_2.[12]

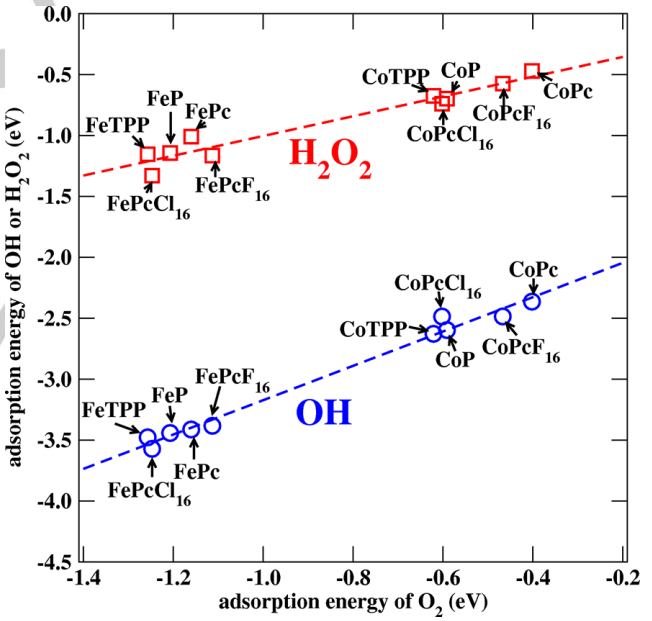

Figure 2. The calculated adsorption energy of OH (blue circles) and H_2O_2 (red squares) species as a function of the calculated adsorption energy of O_2 molecule on the Fe and Co macrocyclic complexes. P: porphyrins. TPP: tetraphenylporphyrins. Pc: phthalocyanines. $PcCl_{16}$ or PcF_{16}: fluorinated phthalocyanines, or chlorinated phthalocyanines,[12] with permission from American Chemical Society.

The ORR pathway on Fe-N_4 was studied by Wang and Zhu et al.[7] They found that O_2 molecules chemisorbed on Fe sites prefer hydrogenation into OOH species rather than direct breakage of the O=O bond. This step is the rate determining step of ORR. The formation of H_2O_2 is energetically unfavorable so the O_2 is directly reduced to H_2O.[7] Szakacs et al. found the same ORR pathway on the same Fe-N_4 motif, but they showed

that adsorption of O_2 is side-on position rather than end-on.[11] The side-on O_2 has larger O=O bond length, i.e., lower O=O bond energy, which is beneficial for bond breaking. They also considered some more complicated structures with a more pyridine molecule bonded to Fe. In this case oxygen is in end-on position. Liu et al. also considered a Fe-(CN)N_4 structure, which shows more 2 electron transfer ratio than on Fe-N_4.[5]

Kiefer et al. compared the formation energy of Co-N_4 and Co-N_2 in a perfect graphene and found that Co-N_4 is more stable within the whole ORR potential window. Co-N_4 has ability to reduce O_2 to H_2O_2, but it cannot further reduce H_2O_2 to H_2O. On the other hand, Co-N_2 is less stable but is active for H_2O_2 reduction.[9] If Co-N_4 is located between two pieces of graphene, the reduction of peroxide is then activated. The Ni-N_4 is not active for ORR.[14] But Ni-N_2 on graphene edge is energetically favorable and active.[8] Flyagina et al. found that Mn centre has even stronger intermediate binding. Mn-N_4 favors the two-electron oxygen reduction pathway and thus yields H_2O_2.[10]

There is a possibility that in ORR, the catalyst is not the adsorption site for reaction intermediates. If TM cluster is embedded in a graphene layer, the inner TM changes the work function of the outer graphene. Bao et.al used the DFT calculations to indicate that the catalytic activity could arise from a decreased local work function on the carbon surface by the electron transfer from Fe particles to the single wall carbon nanotubes (SWCNTs). N doping that increases density of states (DOS) on the Fermi level decreases also the work function.[16] In fact, some DFT studies suggest that adsorption of intermediates may not be necessary in ORR. The electron can penetrate the double layer and directly transfer to the outer Helmholtz plane.[17] In this case, the performance is purely controlled by the work function of the catalyst.[18] However, this mechanism is not widely accepted so far. If this theory is correct, the work function will be the only determinant of any electrochemical reaction. However the reality of electrochemistry is much more complicated. Furthermore, Fe-N_4 CNTs do not have lower work function than the pristine CNTs but show much better ORR performance.[19] So we think that the work function may influence the ORR performance but adsorption energy is still crucial factor.

3. TM-NC types and synthesis strategies

As discussed in the theoretical part, the active sites in TM-NC are the TM centers in TM-N_x motif. However, it is unrealistic to synthesize a material exactly the same as the theoretical model. In practice, various TM-NCs can be synthesized by using different methods.

Various TM-macrocyclic complexes can be directly and physically mixed with carbon. This type of decoration does not represent typical TM-NC since the TM-N_x motif is not covalently bond to the carbon structure. However, it is exactly the same as the ORR active center in TM-NC; thus, it is discussed here. The synthesis of this type of catalyst is relatively simple and involves co-dispersion of the TM-macrocyclic complex and carbon in a solvent. The latter is then evaporated, giving carbon particles decorated with TM-macrocyclic complexes. There is no limitation on the carbon used, but the selection of solvent depends on the solubility of the decorating complex. For example, water soluble tetrasulfophthalocyanine[20] or tetrakishydroxyphenyl porphyrin[21] can be dispersed in water. TM-phthalocyanine (Pc) is not soluble in water, so organic solvents such as chloroform,[22] dimethylformamide,[23, 24] tetrahydrofuran,[25] and ethanol[26] have to be used. The TM-macrocyclic decorator can also be synthesized directly on the carbon, which may reduce the cost of catalysts since TM-macrocyclic compounds are not cheap.[27]

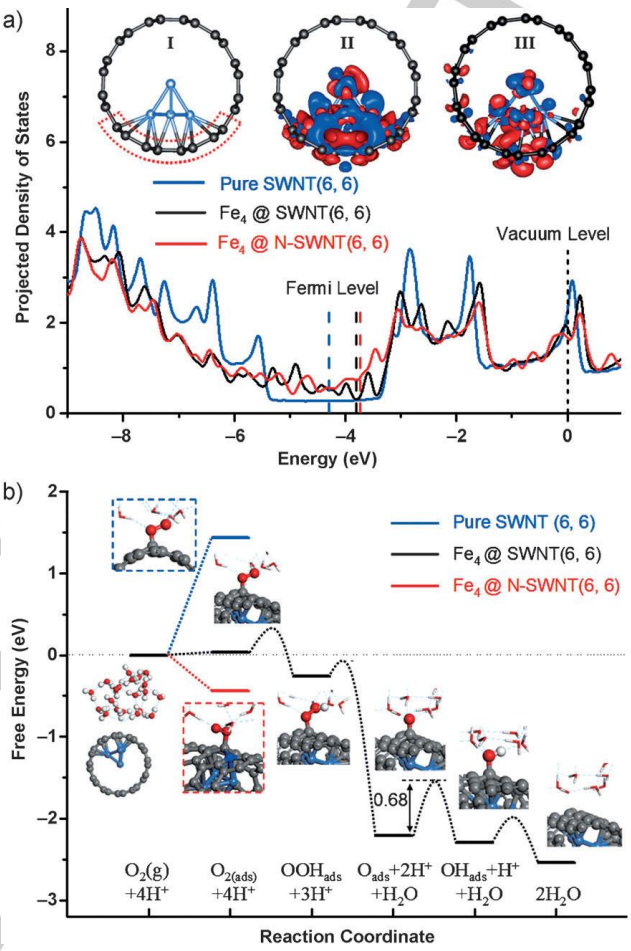

Figure 3. Results of the DFT calculations: a) projected DOS of the p orbitals of C atoms bonded to Fe_4 in Fe_4@SWCNT and Fe_4@N-SWCNT as compared to that of pure SWCNT. The vacuum level is aligned at 0 eV. The insets I and II in panel show the optimized structure of Fe_4@SWNT and its difference in the charge density, inset III in this panel refers to Fe_4@N-SWCNT. The red and blue regions in insets II and III indicate charge increase and decrease, respectively. b) Free-energy diagram of ORR on Fe_4@SWCNT in water (black line) under the following experimental conditions: onset potential = 0.6 V vs. normal hydrogen electrode, pH = 0. With permission from Wiley.[16]

NC can be synthesized by using different routes. A straightforward route is the pyrolysis of carbon precursor together with a nitrogen-containing precursor. The carbon precursors can be the same as those used for the synthesis of carbon materials, for instance, thermosetting polymers. The nitrogen-containing compounds should be nitrogen-rich molecules. When TM is required in the final material, its precursor (usually a TM-containing salt) is mixed with the carbon and nitrogen precursors, and the resulting mixture is carbonized. Fig 5 shows a synthetic procedure for obtaining a composite material composed of Fe-N co-doped carbon nanotubes and ordered porous carbon (Fe-N-CNT-OPC).[28] In this procedure, the ordered porous resin (OPR), melamine and $FeCl_x$ are the

carbon, nitrogen and TM precursors, respectively. The aforementioned carbon precursors produce the resultant porous carbon, which is beneficial for electrochemical reactions. In practice, arbitrary carbon, nitrogen and TM precursors can be combined. Also, carbon and nitrogen can be introduced by using a single precursor such as polyaniline. Fig 6 shows the schematic diagram for the synthesis of TM-NC from polyaniline, which contain both carbon and nitrogen atoms.[29] Nitrogen and TM can be also introduced by using a single precursor such as TM-Pc.[30] Though the majority of reports claim that high temperature around 900 °C is necessary for obtaining a good TM-NC ORR catalyst, we recently proved that 550 °C is sufficient temperature if Prussian blue is selected as a single carbon, nitrogen and iron precursor.[31]

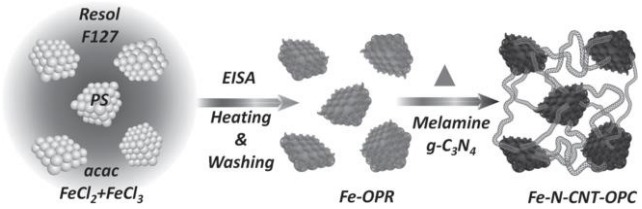

Figure 4. Synthetic rout for obtaining Fe–N–CNT–OPC materials,[28] with permission from Wiley.

Post-treatment of the existing carbon is another way to introduce nitrogen. In this case the highly graphitized carbon such as graphene and CNT can be used to achieve highly conductive material as compared to poorly conductive amorphous carbon. High-temperature treatment is an effective way to achieve nitrogenation and introduce TM at the same time. For better blending of the precursors, the carbon precursors are usually oxidized to achieve better dispersibiliy in water. For example, graphene oxide (GO) is used instead of graphene. Table 1 lists some recent papers on TM-NC by furnace process.

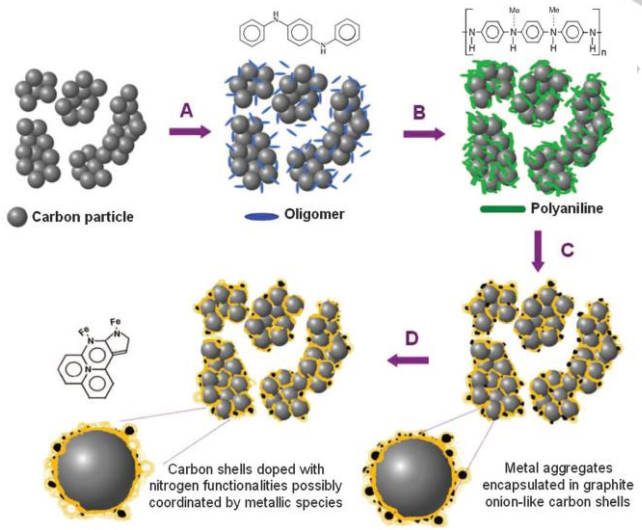

Figure 5. Scheme illustrating the synthesis of TM-NC catalysts. (A) Mixing carbon with aniline oligomers and TM (Fe and/or Co). (B) Oxidative polymerization of aniline by addition of ammonium persulfate. (C) Heat treatment in N_2 atmosphere. (D) Acid leaching,[29] with permission from American Association for The Advancement of Science.

Table 1. TM-NC synthesized by furnace process.

C precursor	N precursor	TM precursor	T[a]	Ref
HEDA[b]	HEDA	$Co(NO_3)_2$	900	[32]
PANI[c]	Melamine	$FeCl_3$	700-1000	[33]
PANI	PANI	Mn_3O_4	900	[34]
Polypyrrole	Polypyrrole	$FeCl_3$	800-1100	[35]
GO, PANI	PANI	$FeCl_2$, $Co(NO_3)_2$	850	[36]
CNF[d], PANI	PANI, EDA	$Co(NO_3)_2$	800	[37]
KetjenBlack, PANI	PANI	$FeCl_3$, $Co(NO_3)_2$	400-1000	[29, 38]
VB12[e]	VB12	VB12	600-900	[39]
AFC[f]	AFC	AFC	500-800	[40]
PB[g]	PB	PB	550	[31]
P123	Melamine	$Fe(NO_3)_3$	800	[41]
Co porphyrin	based	polymer	600-1000	[42]
PF Resin[h]	Melamine	$FeCl_2$, $FeCl_3$	750-1050	[28]
SBA-15	2,2-bipyridine	$FeCl_3$	600-1000	[43]
Mesoporous carbon	cyanimide	$Co(NO_3)_2$	900	[44]
PWAR[i]	Ammonia	$FeCl_2$	1000	[45]
Ketjenblack	Melamine	$FeCl_2$	800-1000	[46]
Ketjenblack	EDA[j]	$Co(NO_3)_2$, $FeSO_4$	900	[47]
KetjenBlack	FePc, CoPC	FePc, CoPC	600, 800	[30]
BP 2000[k]	Melamine	$FeCl_3$	900	[48]
BP 2000	Cyanamide	$Fe(OAc)_2$	950	[49]
BP 2000	TPPZ[l]	$Fe(OAc)_2$	600-900	[50]
BP 2000	DETA[m]	$CoCl_2$	600-900	[51]
Vulcan XC-72R	DCDA	Fe_2O_3	700-900	[52]
Vulcan XC-72R	Pyridine	$Co(SO_4)_2$	200-900	[53]

Vulcan XC-72R, GO	Urea	$FeCl_3$	1000	[54]
GO	C_3N_4	$FeCl_3$	800	[55]
GO	PEHA[n]	$FeCl_3$	900	[56]
GO	Ammonia	CoO	500	[57]
GO	Cyanamide	$FeCl_3$	900	[58]
GO	Polypyrrole	$Fe(OAc)_2$	600	[59]
GO, CNT	Ammonia	Fe	900	[60]
CNT	BTA[o]	$Co(NO_3)_2$	300-800	[61]
MWCNT[p]	C_3N_4	$FeCl_3$, FeTMPP-Cl[q]	800	[62]
GO	thiourea	$Co(OAc)_2$, $Ni(OAc)_2$	EG	200	[66]
GO	NH_4OH	$Co(OAc)_2$	Ethanol	150	[68]
GO	NH_4OH	$Co(OAc)_2$ $Mn(OAc)_2$	Ethanol	150	[69]
CNT	NH_4OH	$Co(OAc)_2$	Ethanol	150	[70]

[a] Annealing temperature in °C. If multistep heating is adopted, the highest temperature is shown. [b] Hexamethylenediamine. [c] Polyaniline. [d] Carbon nanofibre. [e] Vitamin B12. [f] Ammonium ferric citrate. [g] Prussian blue. [h] Phenol formaldehyde resin. [i] Polyacrylic weak-acid cation-exchange resin. [j] Ethylenediamide. [k] Black Peals 2000. [l] Tripyridyltriazine. [m] Diethylenetriamine. [n] Pentaethylenehexamine. [o] Benzotriazole. [p] Multiwall CNT. [q] 5,10,15,20-tetrakis(4-methoxyphenyl)-21H,23H-porphine iron (III) chloride.

Solvothermal (including hydrothermal) method is another effective way to synthesize NC, and avoid the expense of furnace process. In the solvothermal process, defective carbon reacts with nitrogen precursor to form NC. We developed a hydrothermal process-based synthesis of nitrogen doped reduced graphene oxide (N-rGO). The as prepared N-rGO has very high dispersibility in water, which facilitates the TM incorporation.[63, 64] Solvothermal method is also an effective way to synthesize nanosized TM oxides (TMO). Thus, TMO-NC can be synthesized in one pot. Though TMOs are not as active as TM-N_x in ORR, their presence can avoid the stacking of carbon so the surface area and mass transfer are better. Figure 7 shows a schematic illustration of the formation mechanism of Mn_3O_4 nitrogen doped graphene (MNG).[65] In this approach, ammonia plays the role of both reducing and nitrogenating agent in processing GO. Mn acetate is the precursor of Mn_3O_4. Solvothermal method can be also used for sulfide synthesis.[66] Table 2 lists some recent papers on TM-NC prepared by the solvothermal process.

Table 2. TM-NC synthesized by solvothemal process.

C precursor	N precursor	TM precursor	Solvent	T	Ref
GO	NH_4OH	$CuCl_2$	water	90	[64]
GO	NH_4OH	AgNO3	water	90	[63]
GO	NH_4OH	$Mn(OAc)_2$	EG[a]	80	[65]
GO	NH_4OH	$Mn(OAc)_2$	Butanol, pentanol	150, 200	[67]

[a] Ethyleneglycol.

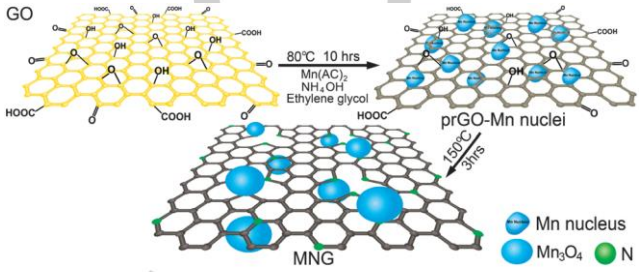

Figure 6. Schematic illustration of the formation mechanism of Mn_3O_4 nitrogen doped graphene,[65] with permission from Royal Society of Chemistry.

4. Characterization of TM-NC

The basic techniques to characterize TM-NC are similar to those used for other carbon nanomaterials. Scanning electron microscopy (SEM) and transmission electron microscopy (TEM) are adopted to reveal the morphology of the materials. N_2 adsorption/desorption is used to measure the specific surface area and pore size distribution, which are important to electrocatalysts. X-ray diffraction (XRD) is useful to identify the TM oxide and graphitic structure. Fourier transform infrared spectroscopy (FTIR) is usually used to reveal the functional groups in carbons.

However, as discussed in the theoretical part, the interaction between TM and NC is the origin of ORR activity, which is the key issue in characterization of TM-NCs. Unfortunately, the TM-N_x motif cannot be “seen” by electron microscopy. Theoretically, the atoms in different chemical environments will have slightly different characteristic energies. Such difference is possibly observable by some very precise energy spectroscopies. A popular technique is the X-ray photoelectron spectroscopy (XPS), because of its relatively low cost and wide accessibility. However, the energy resolution of XPS is not high enough to deconvolute every single chemical state. The broad peaks of different chemical environments may overlap heavily. Furthermore, the signal to noise ratio is usually too high when nitrogen and TM contents are low. Therefore, the longtime measurements and careful comparison between samples under identical measurement conditions are essential to get solid conclusions. Only very few reports met these requirements. We used the N-rGO and Ag/N-rGO to study the difference in the XPS patterns. We found that N1s of Ag/N-rGO is slightly different from that of N-rGO regardless before or after

electrochemical measurements. The peak at lower binding energy (usually assigned to pyridinic nitrogen) is higher in the case of Ag/N-rGO than that of N-rGO, which may be caused by Ag-N_x structure (Figure 7).[63] Kim also observed similar phenomenon that the concentration of pyridinic nitrogen increases with increasing Co content in Co-NC.[37]

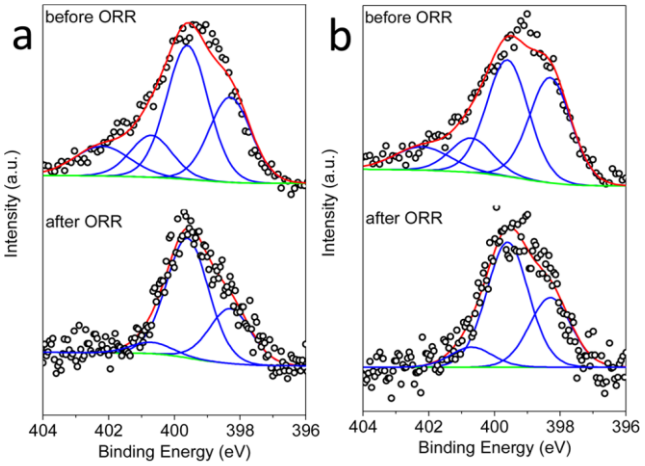

Figure 7. High resolution XPS of N1s of N-rGO (a) and Ag_2O/NrGO and Ag/N-rGO (b). The four peaks are pyridinic, pyrrolitic/aminic, graphitic, and oxidized nitrogen, from low to high binding energy, respectively,[63] with permission from American Chemical Society.

To achieve higher energy resolution, the X-ray absorption fine structure (XAFS) can be used. XAFS includes the X-ray absorption near edge structure (XANES) and the extended X-ray absorption fine structure (EXAFS). XANES is sensitive to charge transfer and orbital occupancy. EXAFS provides the information of distances between central and neighboring atoms and the number of neighboring atoms. Thus, XANES and EXAFS are powerful tools to reveal the structure and interaction of TM-NC.Dai et al. claimed that there may be strong coupling between Co_3O_4 and N-rGO because the peak attributed to functionalized carbon in XANES is more intense than that in N-rGO.[68, 70] But this phenomenon is just caused by the increase of functionalization and could not prove TM-N bonding. They later performed the same measurement on nitrogen and found that the π* peaks are greatly enhanced. They attributed it to the coordination of nitrogen to TM.[69] Wang et al. did a more detailed study using scanning transmission X-ray microscopy (STXM) as the X-ray source. They found that: 1) carbon functionalization is increased by Co_3O_4; 2) nitrogen species are important anchoring sites on N-rGO; 3) $Co^{3+}(O_h)$ in Co_3O_4/N-rGO has been partially reduced to $Co^{2+}(O_h)$, which is the anchor site on Co_3O_4. In other words, the Co_3O_4 particles interact strongly (covalent bonding) with N-rGO (Figure 8).[71] Ferrandon et al. used 16 iron standards to fit the XANES of Fe-NC and calculated the fraction of each Fe species.[72] Shao-Horn et al. used EXAFS to determine the coordination number of Fe in Fe-N-MWCNT (which is 3 or 4) and the distance between them as 1.92 - 1.99 Å. This estimation is very close to that predicted by the DFT calculations performed for Fe-N_x (Figure 9).[62]

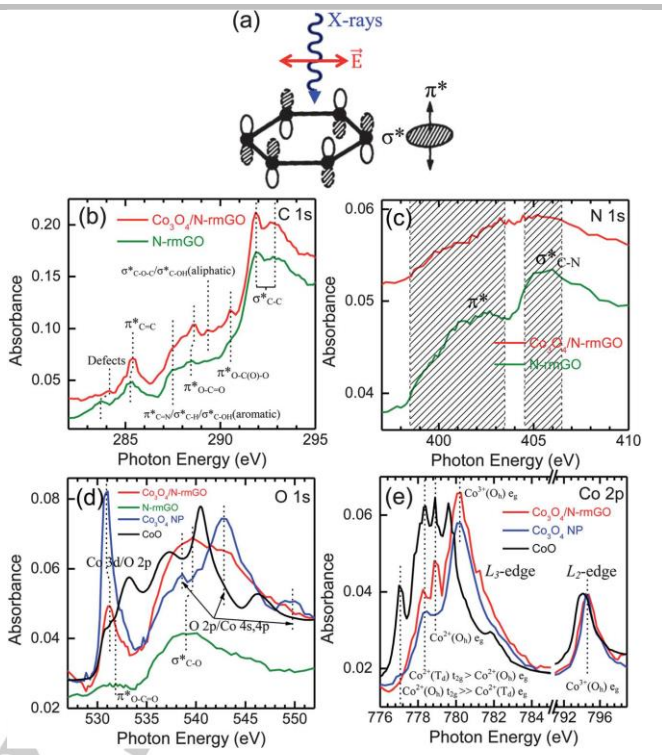

Figure 8. STXM XANES spectra of Co_3O_4/N-rGO, N-rGO, Co_3O_4 and CoO; (a) perpendicular orientation of the incident X-ray beam in STXM to a graphene sheet, and parallel orientation of the electric vector of the beam to a graphene basal plane; (b) C K-edge, (c) N K-edge, (d) O K-edge, and (e) Co L-edge XANES spectra,[71] with permission from Royal Society of Chemistry.

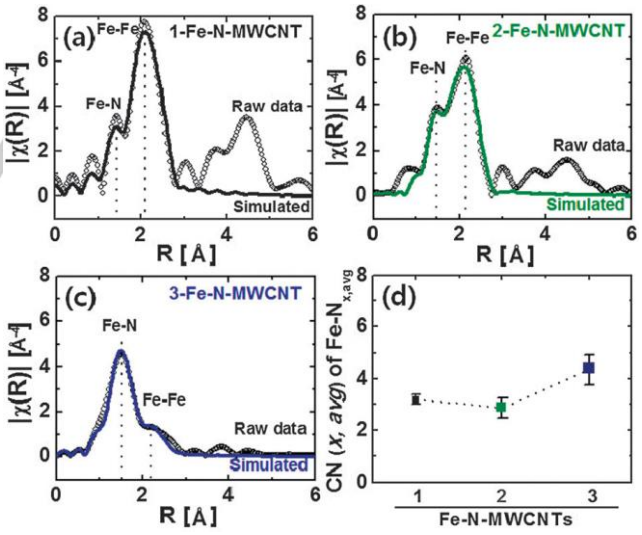

Figure 9. EXAFS of three Fe–N-MWCNTs. Raw data (black open circles) are fitted (solid line) in reference to FeTMPP-Cl (for Fe–N_x) and Fe foil (for Fe–Fe). (d) The average coordination number (x) of Fe–N_x,[62] with permission from Royal Society of Chemistry.

Mössbauer spectroscopy is another very precise technique providing information about chemical environment of TM, and useful for characterization of Fe-NC. Kramm et al. found that various Fe species exist in high-temperature ammonia treated Fe-NC, including superparamagnetic Fe, Fe nitride and Fe-N_4, (D1).[73] Later, Fe-N_{2+2} (D2, N from two pieces of graphene) and

N-Fe-N_{2+2} (D3, a more N from top) motifs were considered.[74] Recent studies showed that ammonia treatment is beneficial to the formation of D1 and D3 motifs, which are ORR active.[75] Chen et al. used the flight of time secondary ion mass spectrometry (ToF-SIMS) to detect the Fe containing species in Fe-NC. They found that the detected Fe^+, $C_3N_2^-$, and $C_3N_2O^-$ fragments originate from the same spatial location. Based on these results they inferred that there is a high possibility that the fragments are originated from the Fe-N_4 type of active sites.[76]

5. ORR performance of TM-NC

Performance of the newly developed catalysts is always a very important issue. However, we do not want to emphasize too much this topic because the recently reported TM-NC catalysts perform very well, analogously as Pt under similar conditions. Although some reports indicate that performance of these catalysts is even better than that of Pt, such conclusion was often achieved in relation to a very poor Pt reference. Analysis of the relevant literature indicates some inconsistencies in the reported performance data, which has been summarized by Lee et al.[77] Here, we just show some results that in our opinion are reliable.

3.1. Fe-NC catalysts

The Fe-NC catalysts for ORR have been studied for a long time. The major advantage of Fe-NC is not only the extremely low cost of Fe, but first of all its very good performance in both alkaline and acid electrolytes. Note that the metal-free NC shows ORR activity only in alkaline electrolytes. Figure 11 presents the ORR performance of a CNT-graphene (G) complex with Fe,[60] which shows a very good performance with high onset potential and current density.

The performance of Fe-NC varies from case to case. In general, the performance depends on the Fe and N content, graphitization degree and specific surface area. The higher these parameters are, the better catalyst's performance is. The best Fe-NCs are usually obtained by processing graphitic carbon precursor at high temperatures.[28, 33, 46, 48, 49] The latter is supposed to be energetically necessary to form Fe-N_4 structure.[78] Low temperature synthesis, such as in solvothermal method, usually leads to a material with lower performance.[59]

3.2. Co-NC catalysts

Co-NC is the second popular ORR catalyst. As compared to Fe-NC, Co-NC shows good activity only in alkaline electrolytes.[68] A good Co-NC catalyst can be synthesized by both furnace and solvothermal methods. Figure 11 shows the performance of Co_3O_4/N-rGO synthesized by a solvothermal method.[68] In alkaline electrolytes, the best performance of Co-NC is close to that of Pt.[39]

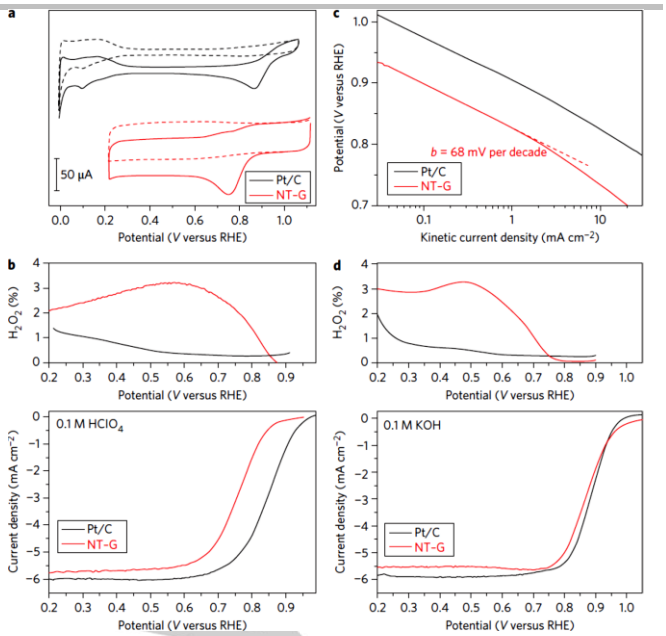

Figure 10. Electrochemical characterization of the CNT–G ORR catalyst. (a) CVs of commercial 20% Pt/C (black) and CNT–G (red) catalysts in O_2-saturated (solid) or Ar-saturated (dotted) 0.1M $HClO_4$. (b) RRDE polarization curves and peroxide yield of Pt/C (black) and NT–G (red) in O_2-saturated 0.1M $HClO_4$. (c) Kinetic current densities versus potential. (d) RRDE polarization curves and peroxide yield of Pt/C (black) and NT–G (red) in O_2-saturated 0.1M KOH,[60] with permission from Nature Publishing Group.

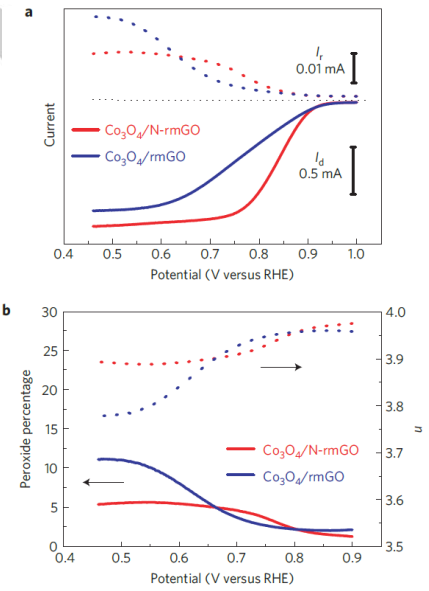

Figure 11. a, Rotation ring-disk electrode voltammograms recorded for Co_3O_4/rGO and Co_3O_4/N-rGO hybrids in O_2-saturated 0.1M KOH at 1600 rpm. b, Percentage of peroxide and the electron transfer number (n) of Co_3O_4/rmGO and Co_3O_4/N-rmGO hybrids,[68] with permission from Nature Publishing Group.

3.3. Other TM-NC catalysts

There are many reports on FeCo-NC.[29, 30, 32, 36, 47] Although some cases it was claimed that the dual-TM-NCs show higher performance than the corresponding single-TM-NCs, the dual-TM-NCs did not outperform the other best single-TM-NCs reported in literature. There is no any theoretical support of the

benefit of dual-TM systems. Besides Fe and Co, other TM-NCs have been also studied as ORR catalysts, including Mn,[34, 65] Cu[64] and Ag[63] etc. All TM-NCs show better ORR performance than the corresponding NCs in alkaline electrolytes. The Mn-TM and Ag-TM show especially good performance, which is on par with the best Fe-NC and Co-NC.

3.4. Other features of TM-NC catalysts

TM-NCs have also some special features, as compared to Pt based ORR catalysts. First, Pt particles suffer from degradation during ORR. This decreases the electrochemical active surface area, and consequently, the catalytic performance. TM-NCs do not show such degradation. Numerous studies have reported that TM-NCs show excellent stability in basic and acid electrolytes.[39, 41, 48, 49, 53, 60] A second feature of TM-NCs is their methanol tolerance. As H_2 storage is still difficult, the methanol as an alternative fuel in fuel cells is widely accepted due to its easy storage and high energy density. Such fuel cell is called as the direct methanol fuel cell (DMFC). However, methanol can penetrate the electrolyte, such as PEM, from anode to cathode. Pt on cathode oxidizes methanol so that the ORR current is offset and fuel is wasted. TM-NCs have been proven to be not active in methanol oxidation at all and the ORR current is not affected by methanol, so that it is ideal for DMFC.[21, 22, 26, 34-36, 40, 41, 44, 46, 60, 65, 66]

6. Experimental study of ORR mechanism on TM-NC

The ORR mechanism has been discussed in the theoretical part. Normally, the mechanism should be verified experimentally. However, the experimental determination of ORR is extremely difficult because of the complexity of this reaction. A larger number of steps and intermediates are involved in ORR than in other classical electrochemical reactions such as hydrogen evolution. Nonetheless, some efforts have been undertaken in this direction.

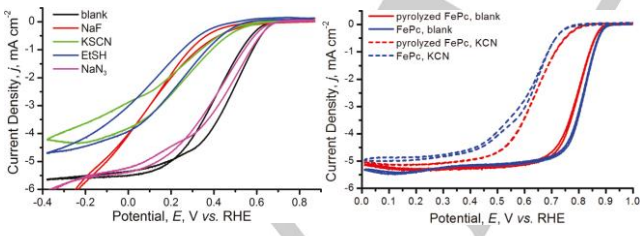

Figure 12. a, RDE measurements of the ORR activity of carbon-supported CuDAT in O_2-saturated pH 6 phosphate buffer alone (black) and containing 10 mM poisons (left). RDE measurements of the ORR activity of carbon-supported FePc (blue lines) and pyrolyzed carbon supported FePc (red lines) in O_2-saturated 0.1 M NaOH alone (solid lines) and containing 10 mM KCN,[79] with permission from American Chemical Society.

The NC active sites are carbon atoms bonded to nitrogen. These carbon atoms also exist in TM-NC, but according to the DFT calculations, active sites are TM atoms. To verify whether it is true, some ligands were used because they may have strong affiliation with TM. If TM is saturated by these ligands in the electrolyte, it cannot adsorb ORR intermediates. Therefore, if the TM-NC is not poisoned by the ligands, the active site is the TM, otherwise not. Dai et al. tried the poisoning test on Fe-NC. The ORR performance with CN^- in the electrolyte is significantly poorer than that without CN^- and close to that of N-rGO. This proves that the active site is Fe.[60] Gewirth et al. did a more comprehensive study on both Fe-NC and Cu-NC. They found the Cu-NC can be poisoned by fluoride, azide, thiocyanate, ethanethiol, and cyanide while Fe-NC can only be poisoned by cyanide (figure 12).[79] Chen used the same CN^- method the determine that the Fe in Fe-N_4 motif is the active site.[76]

As we've mentioned in the DFT part, TM embedded in graphitic structure may also contribute to ORR. Li et al reported such catalyst with Fe_3C/C core shell structure and claimed that its good performance is due to the lower work function.[80] However, they cannot exclude the contribution of intermediates adsorption on Fe-N_x. Mukerjee et al. found that the metallic Fe particles are active toward peroxide reduction in acid electrolytes, where Fe-N_4 only reduces oxygen to peroxide.[81]

As regards the reaction pathway, there is no technique to "see" the adsorbed intermediates suggested by the DFT calculations. However, there is possibility that H_2O_2 desorbs from the electrode surface. The H_2O_2 production can be detected by a rotation ring-disk electrode (RRDE). With RRDE, the ratio between 2e transfer (H_2O_2 produced) and 4e transfer (H_2O produced) can be determined. Numerous works indicate that TM-NCs show lower H_2O_2 production than the corresponding NCs.[29, 34, 44, 46, 61, 63, 64, 70] That means that the adsorption energy of H_2O_2 is lower on TM-NCs than that on NCs. So the adsorption energy of other intermediates should also be lower according to the DFT calculations. Though this finding is not a quantitative result, it explains why TM-NCs have higher ORR activity than NCs.

Another measurable quantity in ORR is the Tafel slope, which in general is reversely proportional to the electron transfer number of the rate determining step. ORR is too complicated process so an explicit rate determining step is not known, but the Tafel slope still reflects the electron transfer capability of the catalyst. It was shown that in the case of TM-NC the Tafel slope is lower than that of the corresponding NC,[62-64] and also lower than that of the corresponding TMO.[57, 68] So the reaction pathway on TM-NC should be different from that on both TMO and NC.

7. Outlook and future challenges

A great progress has been made in the last few years in the development of the TM-NC ORR catalysts. In terms of the catalytic performance, the latter is comparable to that of Pt in alkaline electrolytes. However, the most mature fuel cell device is based on PEM, which requires the electrolyte to be acid. Thus, the performance of TM-NC in acid electrolytes still needs to be improved to be competitive to that of Pt. Theoretical calculations explained the ORR mechanism on some TM-N_X motifs, but the real TM-NCs are much more complicated than the model ones. In fact, a slight difference in the model may result in completely different activity and mechanism. The aforementioned complexity also makes the characterization of catalysts very difficult. For example, the XANES spectra are essential for

determining a single chemical environment because they possess multi peaks to be assigned to different orbitals from a single chemical environment. When TM-NC has a complicated structure, all these peaks from different chemical environments and different orbitals overlap each other, making their accurate deconvolution difficult. Similarly, when the ORR mechanism is studied, its complexity makes difficult to separate different reaction pathways on different active sites. Also, the existence of intermediates and their adsorption energy have not been fully proven and measured. Thus, it is still a long way to go toward full understanding ORR on TM-NC catalysts.

First, further advances in the DFT calculations are required to provide more details on the ORR mechanism on TM-NCs. For example, the relationship between the adsorption energy of intermediates, work function of the catalyst and reaction rate should be clearly resolved. Furthermore, the current DFT studies suggest that some kind of active sites favour the four electron transfer while others favour the two electron transfer. But in reality, both four and two electron transfers occur at the same time. Thus, it is still unclear if this behaviour is caused by combination of different active sites on the same catalyst, or by a single active site allowing the occurrence of both four and two electron transfers simultaneously. Second, more active catalysts should be developed, especially suitable for acid electrolytes. Beside high areal current density, the catalysts should also exhibit very high volume and mass current densities, because in real fuel cells, the cathodes should not be too thick or heavy. Too thick catalyst may have some mass transfer problem, while too heavy catalyst is not desired in mobile appliances such as vehicles. Lastly but most importantly, more precise techniques should be adopted to reveal the real and complete structure of TM-NC. The in-situ electrochemical characterization is highly desired because the catalyst may change during ORR when the potential, current, temperature, pressure or time changes. This characterization may also confirm the existence of ORR intermediates, and provide more information such as their adsorption energy. All these issues require further studies in the future.

Acknowledgements

This work is financially supported by the Australian Research Council (ARC) through the Discovery Project programs (DP130104459 and DP140104062).

Keywords: Oxygen Reduction Reaction • Decorated Nanomaterials • Nitrogen Doped Carbon • Transition Metal

[1] D. W. Wang, D. S. Su *Energy Environ. Sci*. **2014**, 7, 576-591.
[2] Z. Yang, H. G. Nie, X. Chen, X. H. Chen, S. M. Huang *J. Power Sources*. **2013**, 236, 238-249.
[3] Y. Zheng, Y. Jiao, M. Jaroniec, Y. Jin, S. Z. Qiao *Small*. **2012**, 8, 3550-3566.
[4] F. Calle-Vallejo, J. I. Martinez, J. Rossmeisl *Phys. Chem. Chem. Phys.* **2011**, 13, 15639-15643.
[5] J. Sun, Y. H. Fang, Z. P. Liu *Phys. Chem. Chem. Phys.* **2014**, 16, 13733-13740.
[6] A. G. Saputro, H. Kasai *Phys. Chem. Chem. Phys.* **2015**, 17, 3059-3071.
[7] J. Zhang, Z. J. Wang, Z. P. Zhu *J. Power Sources*. **2014**, 255, 65-69.
[8] S. Kattel, P. Atanassov, B. Kiefer *J. Phys. Chem. C*. **2012**, 116, 17378-17383.
[9] S. Kattel, P. Atanassov, B. Kiefer *Phys. Chem. Chem. Phys.* **2013**, 15, 148-153.
[10] I. S. Flyagina, K. J. Hughes, M. Pourkashanian, D. B. Ingham *Int. J. Hydrogen Energy*. **2014**, 39, 21538-21546.
[11] C. E. Szakacs, M. Lefevre, U. I. Kramm, J. P. Dodelet, F. Vidal *Phys. Chem. Chem. Phys.* **2014**, 16, 13654-13661.
[12] H. He, Y. K. Lei, C. Xiao, D. R. Chu, R. R. Chen, G. F. Wang *J. Phys. Chem. C*. **2012**, 116, 16038-16046.
[13] Z. Shi, H. S. Liu, K. Lee, E. Dy, J. Chlistunoff, M. Blair, P. Zelenay, J. J. Zhang, Z. S. Liu *J. Phys. Chem. C*. **2011**, 115, 16672-16680.
[14] S. Kattel, G. F. Wang *J. Mater. Chem. A*. **2013**, 1, 10790-10797.
[15] J. K. Norskov, J. Rossmeisl, A. Logadottir, L. Lindqvist, J. R. Kitchin, T. Bligaard, H. Jonsson *J. Phys. Chem. B*. **2004**, 108, 17886-17892.
[16] D. H. Deng, L. Yu, X. Q. Chen, G. X. Wang, L. Jin, X. L. Pan, J. Deng, G. Q. Sun, X. H. Bao *Angew. Chem. Int. Ed.* **2013**, 52, 371-375.
[17] C. H. Choi, H.-K. Lim, M. W. Chung, J. C. Park, H. Shin, H. Kim, S. I. Woo *J. Am. Chem. Soc.* **2014**, 136, 9070-9077.
[18] J. Y. Cheon, J. H. Kim, J. H. Kim, K. C. Goddeti, J. Y. Park, S. H. Joo *J. Am. Chem. Soc.* **2014**, 136, 8875-8878.
[19] D. H. Lee, W. J. Lee, W. J. Lee, S. O. Kim, Y. H. Kim *Phys. Rev. Lett.* **2011**, 106.
[20] Y. Z. Zhang, G. Q. Mo, X. W. Li, J. S. Ye *J. Power Sources*. **2012**, 197, 93-96.
[21] H. J. Tang, H. J. Yin, J. Y. Wang, N. L. Yang, D. Wang, Z. Y. Tang *Angew. Chem. Int. Ed.* **2013**, 52, 5585-5589.
[22] G. F. Dong, M. H. Huang, L. H. Guan *Phys. Chem. Chem. Phys.* **2012**, 14, 2557-2559.
[23] Y. Y. Jiang, Y. Z. Lu, X. Y. Lv, D. X. Han, Q. X. Zhang, L. Niu, W. Chen *ACS Catal.* **2013**, 3, 1263-1271.
[24] M. Li, X. Bo, Y. Zhang, C. Han, L. Guo *J. Power Sources*. **2014**, 264, 114-122.
[25] A. Morozan, S. Campidelli, A. Filoramo, B. Jousselme, S. Palacin *Carbon*. **2011**, 49, 4839-4847.
[26] C. Z. Zhang, R. Hao, H. Yin, F. Liu, Y. L. Hou *Nanoscale*. **2012**, 4, 7326-7329.
[27] Z. W. Xu, H. J. Li, G. X. Cao, Q. L. Zhang, K. Z. Li, X. N. Zhao *Journal of Molecular Catalysis a-Chemical*. **2011**, 335, 89-96.
[28] J. Liang, R. F. Zhou, X. M. Chen, Y. H. Tang, S. Z. Qiao *Adv. Mater.* **2014**, 26, 6074-6079.
[29] G. Wu, K. L. More, C. M. Johnston, P. Zelenay *Science*. **2011**, 332, 443-447.
[30] V. Bambagioni, C. Bianchini, J. Filippi, A. Lavacchi, W. Oberhauser, A. Marchionni, S. Moneti, F. Vizza, R. Psaro, V. Dal Santo, A. Gallo, S. Recchia, L. Sordelli *J. Power Sources*. **2011**, 196, 2519-2529.
[31] R. Zhou, S. Z. Qiao *Chem. Commun.* **2015**. **DOI:** 10.1039/C5CC00995B
[32] G. Wu, M. Nelson, S. G. Ma, H. Meng, G. F. Cui, P. K. Shen *Carbon*. **2011**, 49, 3972-3982.
[33] H. L. Peng, Z. Y. Mo, S. J. Liao, H. G. Liang, L. J. Yang, F. Luo, H. Y. Song, Y. L. Zhong, B. Q. Zhang *Scientific Reports*. **2013**, 3.
[34] Y. M. Tan, C. F. Xu, G. X. Chen, X. L. Fang, N. F. Zheng, Q. J. Xie *Adv. Funct. Mater.* **2012**, 22, 4584-4591.
[35] Y. Su, H. Jiang, Y. Zhu, X. Yang, J. Shen, W. Zou, J. Chen, C. Li *J. Mater. Chem. A*. **2014**, 2, 7281-7287.
[36] X. G. Fu, Y. R. Liu, X. P. Cao, J. T. Jin, Q. Liu, J. Y. Zhang *Appl. Catal., B*. **2013**, 130, 143-151.
[37] H. S. Oh, H. Kim *J. Power Sources*. **2012**, 212, 220-225.
[38] G. Wu, C. M. Johnston, N. H. Mack, K. Artyushkova, M. Ferrandon, M. Nelson, J. S. Lezama-Pacheco, S. D. Conradson, K. L. More, D. J. Myers, P. Zelenay *J. Mater. Chem.* **2011**, 21, 11392-11405.
[39] H. W. Liang, W. Wei, Z. S. Wu, X. L. Feng, K. Mullen *J. Am. Chem. Soc.* **2013**, 135, 16002-16005.
[40] J. Wang, G. Wang, S. Miao, X. Jiang, J. Li, X. Bao *Carbon*. **2014**, 75, 381-389.
[41] W. X. Yang, X. J. Liu, X. Y. Yue, J. B. Jia, S. J. Guo *J. Am. Chem. Soc.* **2015**, 137, 1436-1439.
[42] Z.-S. Wu, L. Chen, J. Liu, K. Parvez, H. Liang, J. Shu, H. Sachdev, R. Graf, X. Feng, K. Muellen *Adv. Mater.* **2014**, 26, 1450-1455.
[43] A. Kong, X. Zhu, Z. Han, Y. Yu, Y. Zhang, B. Dong, Y. Shan *ACS Catal.* **2014**, 4, 1793-1800.
[44] M. Li, X. Bo, Y. Zhang, C. Han, A. Nsabimana, L. Guo *J. Mater. Chem. A*. **2014**, 2, 11672-11682.
[45] L. Wang, J. Yin, L. Zhao, C. G. Tian, P. Yu, J. Q. Wang, H. G. Fu *Chem. Commun.* **2013**, 49, 3022-3024.
[46] J. S. Lee, G. S. Park, S. T. Kim, M. L. Liu, J. Cho *Angew. Chem. Int. Ed.* **2013**, 52, 1026-1030.
[47] X. G. Li, B. N. Popov, T. Kawahara, H. Yanagi *J. Power Sources*. **2011**, 196, 1717-1722.
[48] J. Liu, X. J. Sun, P. Song, Y. W. Zhang, W. Xing, W. L. Xu *Adv. Mater.* **2013**, 25, 6879-6883.
[49] H. T. Chung, J. H. Won, P. Zelenay *Nature Communications*. **2013**, 4.
[50] A. Velazquez-Palenzuela, L. Zhang, L. C. Wang, P. L. Cabot, E. Brillas, K. Tsay, J. J. Zhang *J. Phys. Chem. C*. **2011**, 115, 12929-12940.
[51] H.-J. Zhang, H. Li, X. Li, H. Qiu, X. Yuan, B. Zhao, Z.-F. Ma, J. Yang *Int. J. Hydrogen Energy*. **2014**, 39, 267-276.
[52] C. H. Choi, S. Y. Lee, S. H. Park, S. I. Woo *Appl. Catal., B*. **2011**, 103, 362-368.
[53] J. L. Qiao, L. Xu, L. Ding, L. Zhang, R. Baker, X. F. Dai, J. J. Zhang *Appl. Catal., B*. **2012**, 125, 197-205.
[54] Q. Liu, H. Y. Zhang, H. W. Zhong, S. M. Zhang, S. L. Chen *Electrochim. Acta*. **2012**, 81, 313-320.
[55] H. R. Byon, J. Suntivich, Y. Shao-Horn *Chem. Mater.* **2011**, 23, 3421-3428.
[56] K. Kamiya, K. Hashimoto, S. Nakanishi *Chem. Commun.* **2012**, 48, 10213-10215.
[57] S. Mao, Z. H. Wen, T. Z. Huang, Y. Hou, J. H. Chen *Energy Environ. Sci.* **2014**, 7, 609-616.
[58] K. Parvez, S. B. Yang, Y. Hernandez, A. Winter, A. Turchanin, X. L. Feng, K. Mullen *ACS Nano*. **2012**, 6, 9541-9550.
[59] Z. S. Wu, S. B. Yang, Y. Sun, K. Parvez, X. L. Feng, K. Mullen *J. Am. Chem. Soc.* **2012**, 134, 9082-9085.
[60] Y. G. Li, W. Zhou, H. L. Wang, L. M. Xie, Y. Y. Liang, F. Wei, J. C. Idrobo, S. J. Pennycook, H. J. Dai *Nat. Nanotech.* **2012**, 7, 394-400.

[61] A. Morozan, P. Jegou, B. Jousselme, S. Palacin *Phys. Chem. Chem. Phys.* **2011**, 13, 21600-21607.
[62] H. R. Byon, J. Suntivich, E. J. Crumlin, Y. Shao-Horn *Phys. Chem. Chem. Phys.* **2011**, 13, 21437-21445.
[63] R. F. Zhou, S. Z. Qiao *Chem. Mater.* **2014**, 26, 5868-5873.
[64] R. F. Zhou, Y. Zheng, D. Hulicova-Jurcakova, S. Z. Qiao *J. Mater. Chem. A.* **2013**, 1, 13179-13185.
[65] J. J. Duan, Y. Zheng, S. Chen, Y. H. Tang, M. Jaroniec, S. Z. Qiao *Chem. Commun.* **2013**, 49, 7705-7707.
[66] Q. Liu, J. T. Jin, J. Y. Zhang *Acs Applied Materials & Interfaces*. **2013**, 5, 5002-5008.
[67] J. Duan, S. Chen, S. Dai, S. Z. Qiao *Adv. Funct. Mater.* **2014**, 24, 2072-2078.
[68] Y. Y. Liang, Y. G. Li, H. L. Wang, J. G. Zhou, J. Wang, T. Regier, H. J. Dai *Nat. Mater.* **2011**, 10, 780-786.
[69] Y. Y. Liang, H. L. Wang, J. G. Zhou, Y. G. Li, J. Wang, T. Regier, H. J. Dai *J. Am. Chem. Soc.* **2012**, 134, 3517-3523.
[70] Y. Y. Liang, H. L. Wang, P. Diao, W. Chang, G. S. Hong, Y. G. Li, M. Gong, L. M. Xie, J. G. Zhou, J. Wang, T. Z. Regier, F. Wei, H. J. Dai *J. Am. Chem. Soc.* **2012**, 134, 15849-15857.
[71] J. Wang, J. Zhou, Y. Hu, T. Regier *Energy Environ. Sci.* **2013**, 6, 926-934.
[72] M. Ferrandon, A. J. Kropf, D. J. Myers, K. Artyushkova, U. Kramm, P. Bogdanoff, G. Wu, C. M. Johnston, P. Zelenay *J. Phys. Chem. C.* **2012**, 116, 16001-16013.
[73] U. I. Kramm, I. Herrmann-Geppert, P. Bogdanoff, S. Fiechter *J. Phys. Chem. C.* **2011**, 115, 23417-23427.
[74] U. I. Kramm, J. Herranz, N. Larouche, T. M. Arruda, M. Lefevre, F. Jaouen, P. Bogdanoff, S. Fiechter, I. Abs-Wurmbach, S. Mukerjee, J.-P. Dodelet *Phys. Chem. Chem. Phys.* **2012**, 14, 11673-11688.
[75] U. I. Kramm, M. Lefevre, N. Larouche, D. Schmeisser, J. P. Dodelet *J. Am. Chem. Soc.* **2014**, 136, 978-985.
[76] W. M. Li, J. Wu, D. C. Higgins, J. Y. Choi, Z. W. Chen *ACS Catal.* **2012**, 2, 2761-2768.
[77] D. Shin, B. Jeong, M. Choun, J. D. Ocon, J. Lee *RSC Adv.* **2015**, 5, 1571-1580.
[78] N. Ramaswamy, U. Tylus, Q. Y. Jia, S. Mukerjee *J. Am. Chem. Soc.* **2013**, 135, 15443-15449.
[79] M. S. Thorum, J. M. Hankett, A. A. Gewirth *Journal of Physical Chemistry Letters*. **2011**, 2, 295-298.
[80] Y. Hu, J. O. Jensen, W. Zhang, L. N. Cleemann, W. Xing, N. J. Bjerrum, Q. Li *Angew. Chem. Int. Ed.* **2014**, 53, 3675-3679.
[81] U. Tylus, Q. Jia, K. Strickland, N. Ramaswamy, A. Serov, P. Atanassov, S. Mukerjee *J. Phys. Chem. C.* **2014**, 118, 8999-9008.

Chapter 3: Enhanced Electrochemical Catalytic Activity by Copper Oxide Grown on Nitrogen-Doped Reduced Graphene Oxide

Introduction

This chapter is the first research project of the thesis. It is the try to synthesize TM-NC and first try on ORR measurement. In this project, a method to synthesize N-rGO was developed. The simple low temperature hydrothermal method produces highly water soluble N-rGO, which is very easy to be made in to non-precious metal composites. These composites are the foundation of this thesis.

Using the first time made CuO/N-rGO as an example, the physical properties and ORR performance are studied. It is found that the Cu-N interaction is responsible of the high ORR activity.

This chapter has been published in *J. Mater. Chem. A* **2013**, 1, (42), 13179-13185.

Journal of Materials Chemistry A

RSC Publishing

PAPER

View Article Online
View Journal | View Issue

Cite this: J. Mater. Chem. A, 2013, 1, 13179

Enhanced electrochemical catalytic activity by copper oxide grown on nitrogen-doped reduced graphene oxide†

Ruifeng Zhou,[ab] Yao Zheng,[ab] Denisa Hulicova-Jurcakova[c] and Shi Zhang Qiao*[a]

A copper oxide/nitrogen-doped reduced graphene oxide (CuO/N-rGO) nanocomposite is synthesized through a low-temperature aqueous process. The resultant nanocomposite is characterized by spectroscopies which show significant interaction between copper and nitrogen. Electrochemical tests show that the nanocomposite exhibits superior oxygen reduction (ORR) activity, which is significantly higher than that of both N-rGO and CuO/GO, and is close to that of commercial Pt/C. Further mechanistic study confirms that the enhancement of ORR activity is prompted by the synergistic effect of copper and nitrogen, which largely accelerates the electrochemical reduction of the peroxide reaction intermediate on N-rGO during ORR, leading to higher onset potential, larger current density and electron transfer number. Larger porosity created by CuO intercalation also helps to lift the limiting current. The CuO/N-rGO not only serves as an alternative to the expensive Pt based ORR electrocatalyst due to its low price but is also promising for other applications such as peroxide/borohydride fuel cells and H_2O_2 detection/elimination. The study also gives an insight into the study method and mechanism of the metal–nitrogen synergistic effect on electrochemical catalysis which may inspire development of other new cost-effective electrocatalysts.

Received 20th August 2013
Accepted 29th August 2013

DOI: 10.1039/c3ta13299d

www.rsc.org/MaterialsA

1 Introduction

In recent years, there has been an increasing interest in electrochemical energy conversion and storage devices due to their potential in replacing traditional low efficiency, resource consuming and environmentally unfriendly power sources. In these areas, the electrocatalyst is always at the heart which makes the electrochemical reactions fast and efficient. There are still many issues to be addressed, for example, the mechanism of electrochemical reactions on the catalyst surface. Although the reaction pathways of Pt and its alloys' catalysis, *e.g.* the hydrogen evolution reaction (HER) and oxygen reduction reaction (ORR),[1–3] have been well established because of Pt's simple and ideal surface, the catalytic mechanisms of non-noble-metal catalysts, especially their composites, are still to be developed. Another important driving force of studying the non-noble-metal catalysts is to reduce the price of practical devices by replacing very expensive Pt.[4,5] For instance heteroatoms, especially nitrogen-doped carbons are usually considered as effective metal-free electrocatalysts for ORR,[6] and these include N-doped graphite,[7] N-doped carbon nanotubes,[8–10] N-doped graphene,[11–13] N-doped amorphous carbon,[14–16] N-doped carbon xerogel[17] as well as carbon supported carbon nitride.[18,19] Such catalysts show good catalytic activity but their performances are fundamentally limited by the 2 + 2 mechanism, where the first two-electron transfer (oxygen to peroxide) is faster than the latter (peroxide to water), leading to incomplete four-electron transfer (oxygen to water).[20–22] To address this inherent issue of metal-free materials, non-precious metals, such as manganese,[23–25] iron,[26,27] and cobalt,[28,29] have been incorporated onto carbon supports to thoroughly alter the ORR's mechanism and achieve four-electron transfer. Among those catalysts, Fe and Co oxides on N-doped carbons showed superior performance to those without N doping.[30–35] The presence of Co–N coupling interaction between Co_3O_4 and N-doped graphene has been revealed by an X-ray study,[36] and is possibly responsible for the enhanced ORR performance. The density functional theory (DFT) study also suggests the interaction between Co–N and Ni–N in similar composites, and gives reasonable explanation of their ORR mechanism.[37,38] However, there is still no experimental study on the mechanism of such catalysts, for example, the reason for higher four-electron process selectivity.

Currently, most effective non-precious metal catalysts for ORR are Mn, Co and Fe-based composites while other transition metals, *e.g.* Cu, are low in activity by themselves.[39] However,

[a]School of Chemical Engineering, The University of Adelaide, Adelaide, SA 5005, Australia. E-mail: s.qiao@adelaide.edu.au; Fax: +61 8 8303 4373; Tel: +61 8 8313 6443

[b]Australian Institute of Bioengineering and Nanotechnology, The University of Queensland, St Lucia, QLD 4072, Australia

[c]School of Chemical Engineering, The University of Queensland, St Lucia, QLD 4072, Australia

† Electronic supplementary information (ESI) available. See DOI: 10.1039/c3ta13299d

Cu^{2+} has very high complex formation constant with N based ligands, implying a possible interaction with N-doped graphene. Therefore, Cu is selected as a model of non-precious metal to study the metal–nitrogen synergistic effect. Herein, by combining CuO and N-doped reduced graphene oxide (N-rGO), we report, for the first time, a nanocomposite of CuO/N-rGO with a very high ORR performance in alkaline electrolyte. It is confirmed that CuO introduces a synergistic effect by combining with N-rGO through its interactions with N, resulting in a significant ORR activity enhancement. The experiment revealed rapid reduction of the HOO^- intermediate by the CuO/N-rGO, leading to more positive onset potential, higher reduction current and higher four-electron selectivity than both the CuO/GO and N-rGO. Meanwhile, the CuO hindered restacking of N-rGO provided the resultant nanocomposite with a much higher specific surface area to facilitate oxygen transfer and reduction, resulting in a higher ORR current than that of Pt/C at a high overpotential. Finally, the CuO/N-rGO shows excellent methanol tolerance, making it promising for applications such as direct methanol fuel cells (DMFCs). This study may give insight into the relationship between structure and catalytic activity of such non-precious metal/N-doped carbon composite materials and catalyse other applications such as metal–air batteries and biosensing *etc.*

2 Experimental

2.1 Synthesis of N-rGO suspension

GO is synthesized similar to the method reported in ref. 40, and is described in the ESI in detail.† To synthesize N-rGO, 70 ml of 0.1% GO aqueous solution was mixed with 5 ml of 25% NH_3 aqueous solution. The mixture was stirred under 90 °C for 12 hours. Thereafter, the resulting suspension was filtered, washed with water and re-dispersed in ethanol by ultrasonication to form uniform suspension of 0.5 mg ml^{-1}.

2.2 Synthesis of CuO/N-rGO

0.2 ml of 0.1 M $CuCl_2$ was added to 16 ml of N-rGO suspension and was stirred for 5 min at 25 °C. Then, 0.75 ml of 0.1 M NaOH was added to the suspension and stirred for another 1 hour. The suspension was then centrifuged, washed with water and dispersed in ethanol (1 mg ml^{-1}). Synthesis of CuO/GO and CuO can be found in the ESI.†

2.3 Electrochemical measurement

0.1 M KOH aqueous solution, a 4 M KCl Ag/AgCl electrode (0.2 V *vs.* standard hydrogen electrode) and a Pt wire were used as the electrolyte, reference electrode and counter electrode. The electrolyte is saturated with O_2 of 1 atm unless otherwise specified. The rotating disk electrode (RDE) is glassy carbon

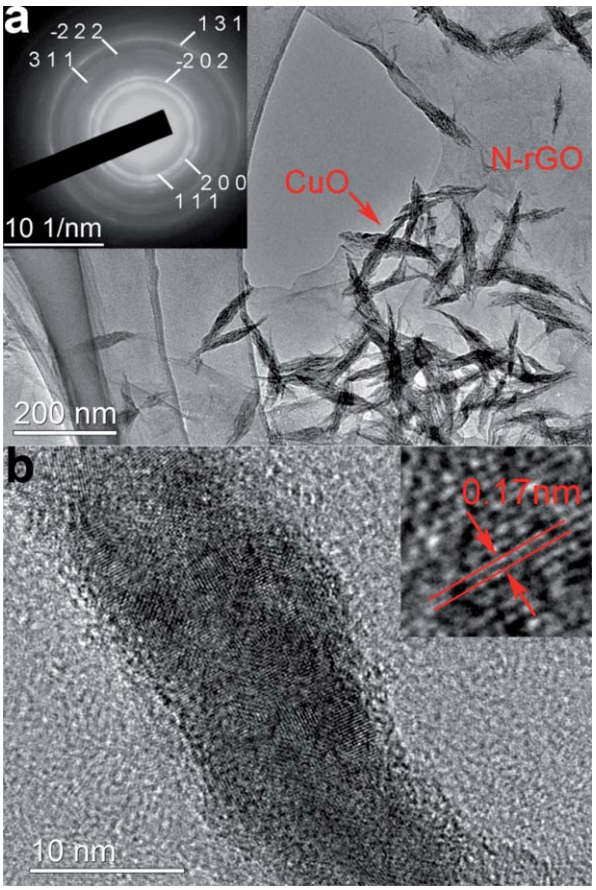

Fig. 1 (a) Low magnification TEM and selected area electron diffraction (inset) of the CuO/N-rGO. (b) High resolution TEM of a single CuO crystal.

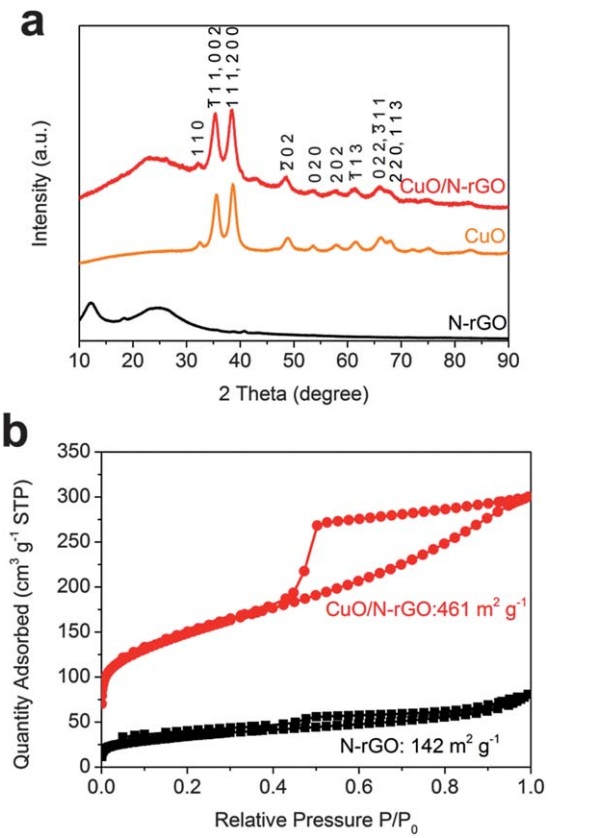

Fig. 2 (a) XRD patterns of N-rGO, CuO and CuO/N-rGO. (b) N_2 adsorption–desorption isotherms of N-rGO and CuO/N-rGO.

with a diameter of 5 mm. The rotating ring-disk electrode (RRDE) is composed of a glassy carbon disk and a Pt ring with a collection ratio of 0.37. The ring is biased at 0.5 V. The catalyst loading on the RDE and RRDE is 0.1 mg cm^{-2}, with Nafion (50% weight of the catalyst).

2.4 DMFC test

Both cathode and anode catalysts were loaded on glassy carbon electrodes. The loading amount is 0.2 mg cm^{-2}. The electrolyte was 0.1 M KOH/3 M MeOH saturated with pure O_2. The cathode (CuO/N-rGO) was rotated at 1600 rpm and the anode (Pt/C) was located 2 cm away from the cathode.

3 Results and discussion

The microstructure of the as-prepared CuO/N-rGO is shown in low (Fig. 1a) and high (Fig. 1b) magnification transmission electron microscopy (TEM) images. Leaf-like CuO is uniformly loaded on N-rGO with an average length and width of about 100 and 15 nm, respectively. The 0.17 nm interplanar spacing denoted in the Fig. 1b inset is indexed (020), suggesting crystal growth along that direction. Micrometer-scale large pores of CuO/N-rGO are confirmed by scanning electron microscopy (Fig. S1†).

X-ray diffraction (XRD) patterns of N-rGO and CuO/N-rGO are shown in Fig. 2a (as prepared CuO is also shown as a reference). Two wide peaks are found in the N-rGO pattern (12.2° and 26°). The former peak is high-shifted from that of GO (10.8°, Fig. S2†), showing reduced interplanar displacement of graphene layers. The latter peak emerges from a broad background of GO, indicating remaining of the (020) crystal index of graphite. The reason for the alteration of XRD after NH_3 reduction is further discussed by a spectroscopic study below. The XRD pattern of the CuO/N-rGO is almost the same as that of pure CuO, with a peak at 25° but without peaks at 12° from N-rGO. This is caused by the CuO growth on the N-rGO sheets at functionalized sites, which mitigates graphene's restacking during drying, leading to a too weak signal of interplanar diffraction to be observed in XRD.

Mitigated restacking of N-rGO by CuO is further confirmed by N_2 adsorption–desorption isotherms (Fig. 2b). N-rGO shows a specific surface area (SSA) of 142 $m^2 g^{-1}$, which is much lower than the theoretical value of graphene (2630 $m^2 g^{-1}$) due to the restacking. However, after CuO incorporation, the SSA increases to 461 $m^2 g^{-1}$, in spite of the presence of heavier CuO (~30 wt%, Fig. S3†). Similar mitigated restacking of GO by CuO is also proved by N_2 adsorption–desorption isotherms (Fig. S4†).

To investigate the chemical composition of the N-rGO, Fourier transform infrared (FTIR) spectroscopies of GO and

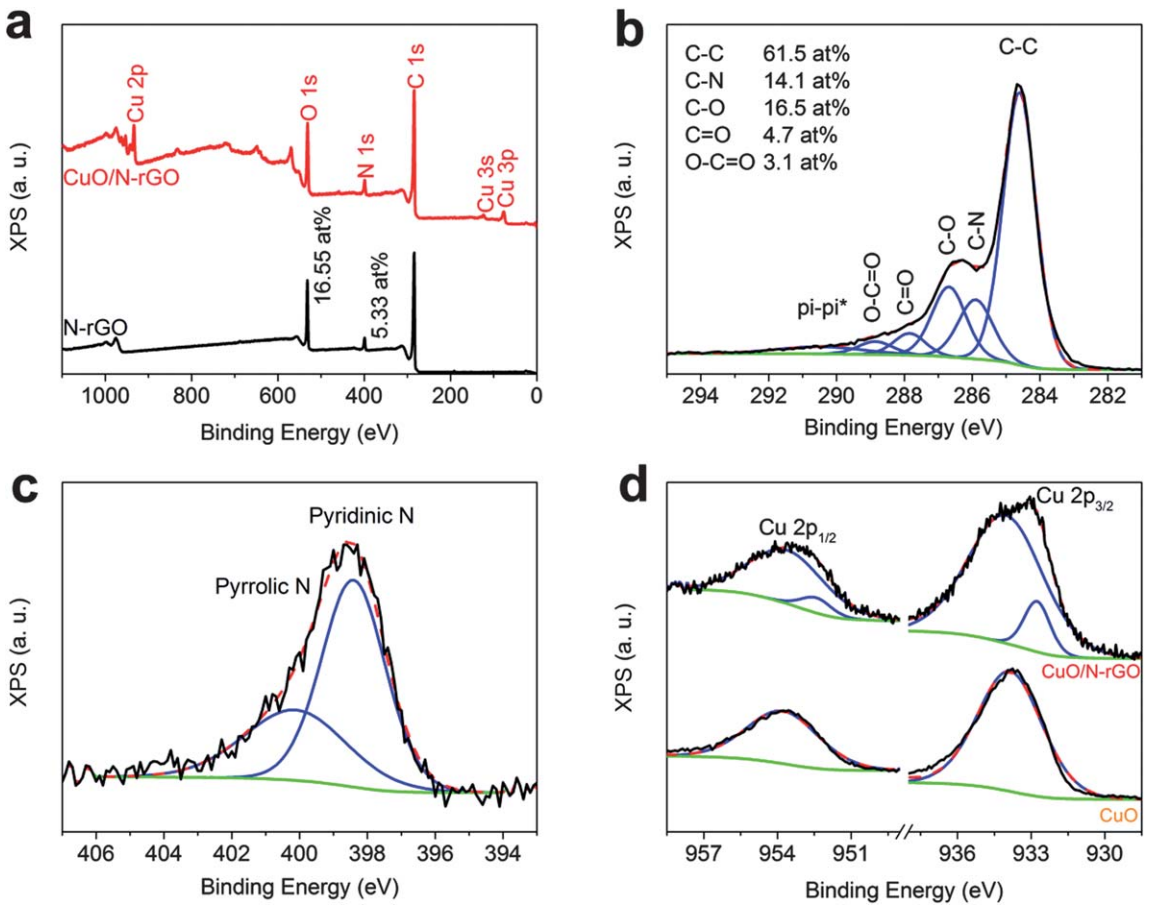

Fig. 3 (a) XPS survey of N-rGO and CuO/N-rGO. High-resolution XPS of C 1s (b) and N 1s (c) of N-rGO. (d) High-resolution XPS of Cu 2p of CuO and CuO/N-rGO.

N-rGO were measured and the results are displayed in Fig. S5.† As expected, the pristine GO shows significant signal from carboxyl and hydroxyl groups while after NH_3 reduction, carboxyl groups nearly vanish but hydroxyl groups still exist. This result is in agreement with the X-ray photoelectron spectroscopy (XPS) results (Fig. 3a, b and S6†) and suggests that the reduction mechanism by NH_3 is the decarboxylation process driven by alkaline and elevated temperature. The elimination of relatively large carboxyl groups is also the reason for decreased interplanar displacement in the XRD pattern. With a considerable amount of hydroxyl groups, N-rGO can be dispersed readily in polar solvents such as water and ethanol, which significantly helps following CuO's growth and its homogeneous distribution. XPS also confirms the presence of N in N-rGO (Fig. 3c). Considering the high oxygen content, the N/C ratio is higher than other reported N doped carbons.[8,11,30] The deconvolution of Cu 2p XPS peaks of pure CuO and CuO/N-rGO is displayed in Fig. 3d. The presence of additional peaks in the CuO/N-rGO can be attributed to Cu bonded to N on N-rGO.

To assess the ORR performance, cyclic voltammetry (CV) of N-rGO, CuO/N-rGO and CuO/GO is measured in 0.1 M KOH (Fig. 4a, b and c). 20 cycles of CV are carried out between −1.2 V and 0.2 V prior to later measurement (Fig. S7†), during which both GO and N-rGO are electrochemically reduced to increase their conductivity. The effect of the conductivity increase is significantly reflected by the change of the CV shape from the 1st to the 20th cycles. The CuO/N-rGO reveals two redox pairs: A_I/C_I (−0.02 V/−0.38 V), which can be attributed to transitions between Cu(II) and Cu(I) in CuO crystals, and A_{II}/C_{II} (−0.34 V/−0.87 V) possibly to transitions between Cu(I) and Cu(0). No significant A_{II}/C_{II} redox pair is observed in N-rGO and CuO/GO. This implies that A_{II}/C_{II} is attributed to a portion of Cu with altered electrochemical property by interacting with N-rGO, in accordance with XPS evidence.

Linear sweep voltammetry (LSV) curves of N-rGO and CuO/N-rGO at different rotating rates on the RDE are shown in Fig. 5a and b. The LSV curves of Pt/C were also recorded and are shown in Fig. S8.† The half-wave potential of the CuO/N-rGO at 1600 rpm is −0.216 V, which is much higher than that of N-rGO (−0.269 V), suggesting the synergistic effect of N and Cu co-existence. Considering that the half-wave potential of Pt/C is −0.152 V, which is 117 mV higher than N-rGO, an increase of 53 mV by CuO incorporation is a considerable kinetic activity enhancement. The electron transfer numbers (n) are calculated from the Koutecky–Levich (KL) plot (Fig. 6a. See formulae in the ESI†). The n (0.37) of the CuO/N-rGO at −0.3 V, which is the actual operating potential of the cathode in alkaline fuel cells,[41] is close to that of Pt/C (4.0) and much higher than that of N-rGO (2.9), suggesting a favoured four-electron process induced by the synergistic effect of the CuO/N-rGO. Furthermore, at −0.3 V, the CuO/N-rGO provides 86% current density of Pt/C, which is much higher than that of N-rGO (59%).

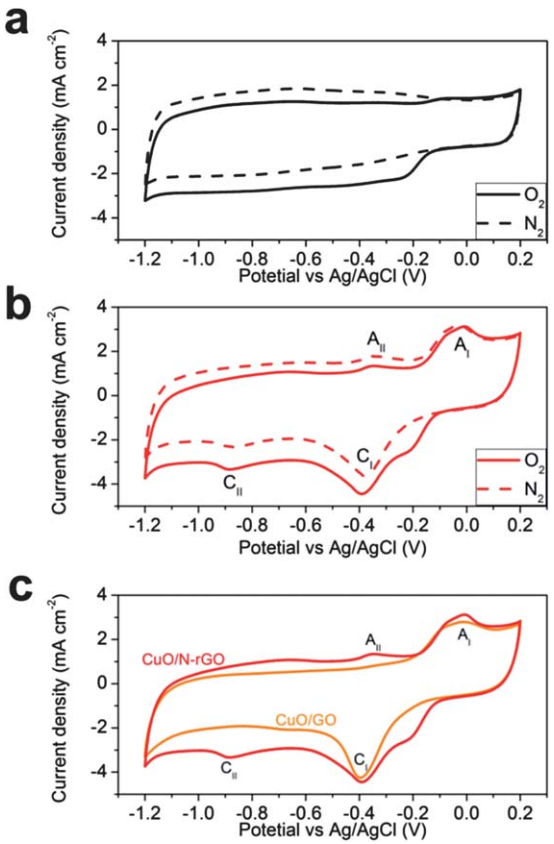

Fig. 4 CV of N-rGO (a) and CuO/N-rGO (b) under O_2 or N_2 saturation (0.1 V s^{-1}). (c) Comparison of CV of CuO/GO and CuO/N-rGO (O_2 saturation, 0.1 V s^{-1}).

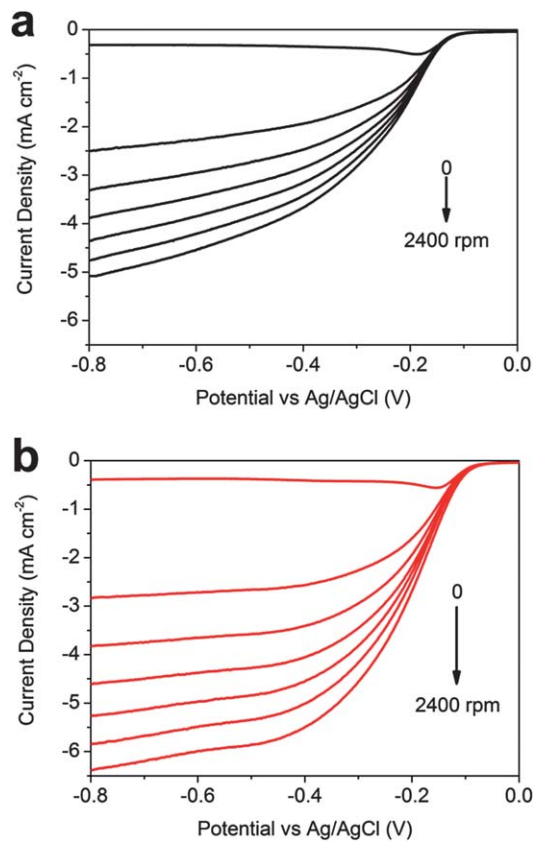

Fig. 5 LSV (5 mV s^{-1}) of N-rGO (a) and CuO/N-rGO (b) at different rotation rates (0, 400, 800, 1200, 1600, 2000 and 2400 rpm).

Fig. 6b shows the kinetic limiting current density (J_K) *vs.* electrode potential of the CuO/N-rGO and N-rGO. The Tafel slopes of both materials are also given. The lower Tafel slope of the CuO/N-rGO confirms higher activity than that of N-rGO. The J_K of the CuO/N-GO is close to that of Pt/C at −0.3 V but much higher than that at −0.6 V. The reason for this higher J_K is the excellent electric conductivity and the effective mass transferring to active catalytic sites within the macropores of the CuO/N-rGO, both of which lead to lower internal resistance of the CuO/N-rGO than Pt/C.

Though the ORR experiences many steps, peroxide is the only stable intermediate that releases from the working electrode. The release of peroxide lowers oxygen utilization thus should be depressed as severely as possible. However, detecting the peroxide production reveals some inside story of ORR. Therefore, LSV of catalysts on the RRDE is also measured, where peroxide is electrochemically oxidized on the Pt ring and the current is recorded. As shown in Fig. 7a, although the CuO/GO gives higher ORR current density than GO, the unchanged onset potential suggests an identical reaction mechanism/pathway, which is confirmed by the ring current where CuO/GO also exceeds the GO with the same curve shape. As a result, CuO/GO shows similar tendency of peroxide percentage (Fig. 7b, formula in the ESI†) and electron transfer number (Fig. S9†) to those of GO. As for the N-rGO, incorporation of CuO not only increases the ORR current but also lifts the onset potential by 35 mV. Furthermore, the ring current of the CuO/N-rGO is much lower than that of N-rGO, resulting in a much lower peroxide percentage and higher n. All these phenomena lead to the conclusion that CuO not only increases the surface area of GO and N-rGO but also adds a significant synergistic effect to N-rGO. Since the N-rGO and CuO/N-rGO have similar curve shapes for both disk and ring currents, we believe that their ORR pathways are identical but with different kinetic parameters.

From the above-mentioned discussion and results, the ORR reaction on our catalysts can be regarded as two successive reactions. Oxygen is firstly reduced into peroxide (in the form of HOO^-) and then water (in the form of OH^-):

$$O_2 + H_2O + 2e^- \rightarrow HOO^- + OH^- \quad (1)$$

$$HOO^- + H_2O + 2e^- \rightarrow 3OH^- \quad (2)$$

Theoretically, peroxide production during ORR on N-graphene is energetically unfavoured since adsorbed oxygen ($O_{(ads)}$) has lower free energy than HOO^-.[42] However it is still possible to produce a lot of peroxide if reaction (2) is relatively slow, because of sluggish removal of $O_{(ads)}$. To understand the ORR dynamics and the function of each component in our catalysts, H_2O_2 is deliberately added into the electrolyte to provide more information. In the strong alkaline electrolyte (0.1 M KOH),

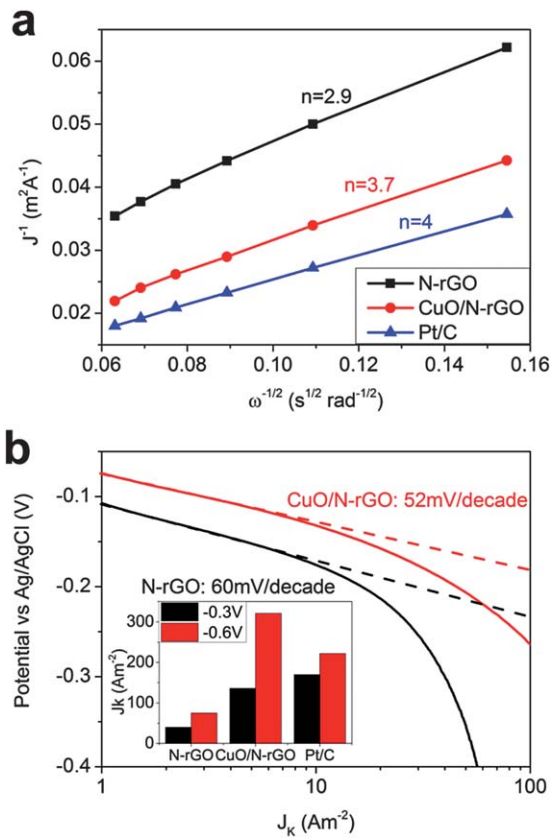

Fig. 6 (a) KL plot of N-rGO, CuO/N-rGO and Pt/C at −0.3 V. (b) Tafel plots and limiting currents (inset) of N-rGO, CuO/N-rGO and Pt/C.

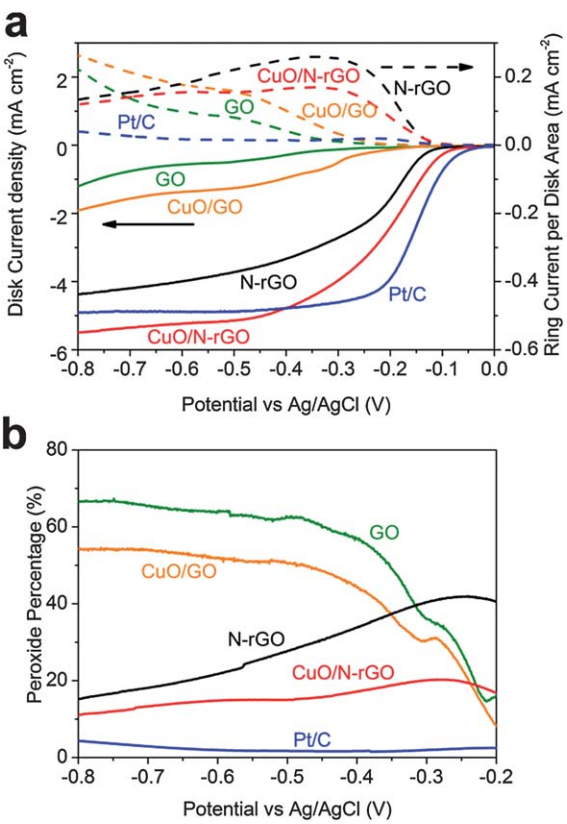

Fig. 7 (a) RRDE disk and ring current density (1600 rpm, 5 mV s^{-1}). (b) Peroxide percentage of the catalysts *vs.* potential.

H_2O_2 ionizes into HOO^- and processes two following reactions on the electrode:

$$HOO^- + OH^- \rightarrow O_2 + H_2O + 2e^- \quad (3)$$

$$HOO^- + H_2O + 2e^- \rightarrow 3OH^- \quad (4)$$

Reaction (3) is the reverse of reaction (1) while reaction (4) is exactly reaction (2). Reaction (3) overcomes the same barrier as reaction (1), but the reversed current direction is helpful to distinguish it from reaction (2). LSV curves (Fig. 8a) of the catalysts show the net current as the sum of the two reactions. GO shows poor activity in both reactions (3) and (4), even if CuO is incorporated. This proves that there is a huge barrier between O_2 and HOO^-, as well as HOO^- and OH^- for GO and CuO/GO. As for N-rGO, it obviously catalyses both reactions with a considerable activity. In reaction (3), the barrier is the adsorption energy of the HOO intermediate,[43] while in reaction (4), the barrier is the adsorption energy of the OH intermediate.[42] Considering that both HOO and OH are radicals with unpaired electron and electron affinity, they have similar tendency to be adsorbed on high spin density and charge density sites induced by N doping.[43] Thus the drop of both barriers is reasonable. As the first reaction in ORR, the lower barrier of reaction (1) leads to higher onset potential. The lower barrier of reaction (2) leads to higher current and lower peroxide percentage in ORR. When CuO is grown on the N-rGO, the slope of LSV is further boosted by 4 times in both reactions (3) and (4), compared with N-rGO. The reason is that the N–Cu interaction further lowers the adsorption energies of HOO and OH, which further accelerate both reactions, thus resulting in the synergistic enhancement of the ORR. Moreover, the 0-current potential of the CuO/N-rGO is positively shifted by 33 mV compared with N-rGO, suggesting a more efficient HOO^- reduction enhancement. Considering that the equilibrium electrode potential of reactions (3) and (4) is −0.179 V and 0.708 V (see ESI†), the overpotential of reaction (3) at 0-current potential is much smaller than reaction (4). This proves that reaction (4) is much more sluggish than reaction (3), and verifies that reaction (2) is the rate controlling step of ORR. Therefore, the enhanced HOO^- reduction activity is essential to the high performance ORR catalyst.

Finally, the CuO/N-rGO is tested in a DMFC to verify its application potential. It is well known that when Pt is used as an ORR catalyst, a DMFC suffers from methanol diffusion across the membrane. An alkaline DMFC also suffers from poor performance of the anion exchange membrane. Therefore, a methanol tolerant ORR catalyst is promising to overcome the problems. Here, the CuO/N-rGO is proved to be totally insensitive to methanol (Fig. S10†). As a result, a circuit can be built up with the CuO/N-rGO cathode (ORR) and Pt/C anode (MeOH oxidation) without the membrane. As shown in Fig. 8b, the open circuit voltages (OCVs) of the whole cells are 0.45 V to 0.5 V. The CuO/N-rGO cathode provides over twice peak power density as that of N-rGO. The OCV of the as-prepared DMFC is lower than the membrane based DMFC because the ORR on Pt/C offsets some methanol oxidation current. Nevertheless, this experiment proves the feasibility of the CuO/N-rGO for application as a cathode in a membrane-free alkaline DMFC, leaving the challenge for developing a more oxygen tolerant anode remaining.

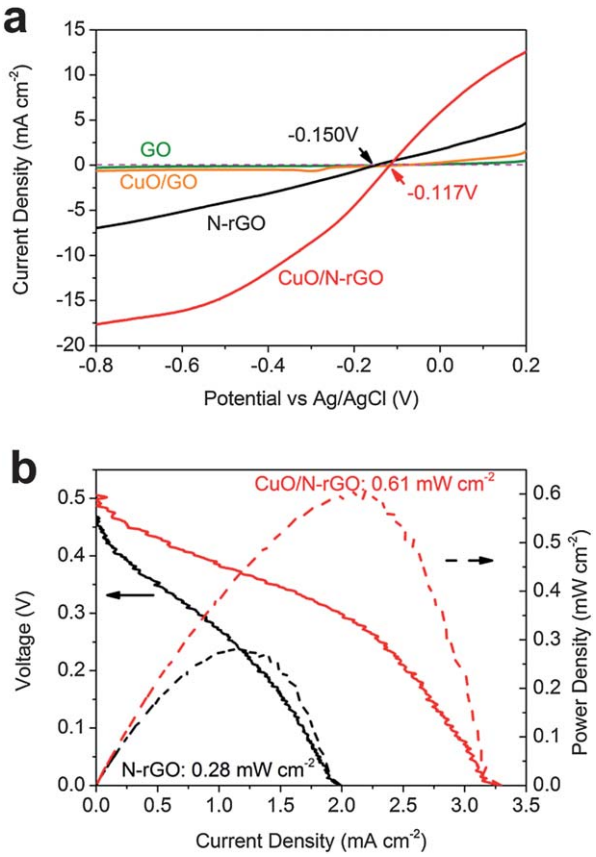

Fig. 8 (a) LSV (1600 rpm, 5 mV s^{-1}) of the catalysts in 0.1 M KOH + 0.01 M H_2O_2. (b) The current density–voltage and current density–power density plot of a DMFC with N-rGO and CuO/N-rGO as cathode catalysts.

4 Conclusions

In conclusion, the CuO/N-rGO nanocomposite shows much higher ORR activity than CuO/GO and N-rGO. The incorporation of CuO onto N-rGO greatly improves both the onset potential and the current density. The mechanism for this improvement is attributed to the synergistic effect of the Cu–N interaction which accelerates oxygen activation and peroxide reduction, and the CuO nanostructure that enlarges the surface area of N-rGO through intercalation. The CuO/N-rGO shows superior HOO^- reduction and oxidization catalytic ability, which not only contributes to ORR enhancement but is also promising in other applications such as H_2O_2 detection/elimination and peroxide based fuel cells. The study also helps to understand the relationship between structure and catalytic activity of such non-precious metal/carbon composite materials and catalyse other applications.

Acknowledgements

This work was financially supported by the Australian Research Council (ARC) through the Discovery Project program (DP130104459, DP1095861 and DP0987969).

Notes and references

1 A. C. Chen and P. Holt-Hindle, *Chem. Rev.*, 2010, **110**, 3767–3804.
2 H. W. Liang, X. A. Cao, F. Zhou, C. H. Cui, W. J. Zhang and S. H. Yu, *Adv. Mater.*, 2011, **23**, 1467–1471.
3 C. H. Cui, L. Gan, H. H. Li, S. H. Yu, M. Heggen and P. Strasser, *Nano Lett.*, 2012, **12**, 5885–5889.
4 C. W. B. Bezerra, L. Zhang, K. C. Lee, H. S. Liu, A. L. B. Marques, E. P. Marques, H. J. Wang and J. J. Zhang, *Electrochim. Acta*, 2008, **53**, 4937–4951.
5 Z. W. Chen, D. Higgins, A. P. Yu, L. Zhang and J. J. Zhang, *Energy Environ. Sci.*, 2011, **4**, 3167–3192.
6 H. B. Wang, T. Maiyalagan and X. Wang, *ACS Catal.*, 2012, **2**, 781–794.
7 I. Y. Jeon, H. J. Choi, S. M. Jung, J. M. Seo, M. J. Kim, L. M. Dai and J. B. Baek, *J. Am. Chem. Soc.*, 2013, **135**, 1386–1393.
8 K. P. Gong, F. Du, Z. H. Xia, M. Durstock and L. M. Dai, *Science*, 2009, **323**, 760–764.
9 S. Kundu, T. C. Nagaiah, W. Xia, Y. M. Wang, S. Van Dommele, J. H. Bitter, M. Santa, G. Grundmeier, M. Bron, W. Schuhmann and M. Muhler, *J. Phys. Chem. C*, 2009, **113**, 14302–14310.
10 T. Sharifi, G. Hu, X. Jia and T. Wagberg, *ACS Nano*, 2012, **6**, 8904–8912.
11 L. T. Qu, Y. Liu, J. B. Baek and L. M. Dai, *ACS Nano*, 2010, **4**, 1321–1326.
12 Q. Q. Li, S. Zhang, L. M. Dai and L. S. Li, *J. Am. Chem. Soc.*, 2012, **134**, 18932–18935.
13 L. F. Lai, J. R. Potts, D. Zhan, L. Wang, C. K. Poh, C. H. Tang, H. Gong, Z. X. Shen, L. Y. Jianyi and R. S. Ruoff, *Energy Environ. Sci.*, 2012, **5**, 7936–7942.
14 W. Yang, T. P. Fellinger and M. Antonietti, *J. Am. Chem. Soc.*, 2011, **133**, 206–209.
15 S. Chen, J. Y. Bi, Y. Zhao, L. J. Yang, C. Zhang, Y. W. Ma, Q. Wu, X. Z. Wang and Z. Hu, *Adv. Mater.*, 2012, **24**, 5593–5597.
16 X. Wang, J. S. Lee, Q. Zhu, J. Liu, Y. Wang and S. Dai, *Chem. Mater.*, 2010, **22**, 2178–2180.
17 H. Jin, H. M. Zhang, H. X. Zhong and J. L. Zhang, *Energy Environ. Sci.*, 2011, **4**, 3389–3394.
18 J. Liang, Y. Zheng, J. Chen, J. Liu, D. Hulicova-Jurcakova, M. Jaroniec and S. Z. Qiao, *Angew. Chem., Int. Ed.*, 2012, **51**, 3892–3896.
19 Y. Zheng, Y. Jiao, J. Chen, J. Liu, J. Liang, A. Du, W. M. Zhang, Z. H. Zhu, S. C. Smith, M. Jaroniec, G. Q. Lu and S. Z. Qiao, *J. Am. Chem. Soc.*, 2011, **133**, 20116–20119.
20 R. A. Sidik, A. B. Anderson, N. P. Subramanian, S. P. Kumaraguru and B. N. Popov, *J. Phys. Chem. B*, 2006, **110**, 1787–1793.
21 T. P. Fellinger, F. Hasche, P. Strasser and M. Antonietti, *J. Am. Chem. Soc.*, 2012, **134**, 4072–4075.
22 J. D. Wiggins-Camacho and K. J. Stevenson, *J. Phys. Chem. C*, 2011, **115**, 20002–20010.
23 F. H. B. Lima, M. L. Calegaro and E. A. Ticianelli, *J. Electroanal. Chem.*, 2006, **590**, 152–160.
24 I. Roche, E. Chainet, M. Chatenet and J. Vondrak, *J. Phys. Chem. C*, 2007, **111**, 1434–1443.
25 J. S. Yang and J. J. Xu, *Electrochem. Commun.*, 2003, **5**, 306–311.
26 F. Jaouen, S. Marcotte, J. P. Dodelet and G. Lindbergh, *J. Phys. Chem. B*, 2003, **107**, 1376–1386.
27 M. Lefevre, E. Proietti, F. Jaouen and J. P. Dodelet, *Science*, 2009, **324**, 71–74.
28 M. Hamdani, R. N. Singh and P. Chartier, *Int. J. Electrochem. Sci.*, 2010, **5**, 556–577.
29 J. B. Xu, P. Gao and T. S. Zhao, *Energy Environ. Sci.*, 2012, **5**, 5333–5339.
30 Y. Y. Liang, Y. G. Li, H. L. Wang, J. G. Zhou, J. Wang, T. Regier and H. J. Dai, *Nat. Mater.*, 2011, **10**, 780–786.
31 Y. Y. Liang, H. L. Wang, J. G. Zhou, Y. G. Li, J. Wang, T. Regier and H. J. Dai, *J. Am. Chem. Soc.*, 2012, **134**, 3517–3523.
32 Y. G. Li, W. Zhou, H. L. Wang, L. M. Xie, Y. Y. Liang, F. Wei, J. C. Idrobo, S. J. Pennycook and H. J. Dai, *Nat. Nanotechnol.*, 2012, **7**, 394–400.
33 Z. S. Wu, S. B. Yang, Y. Sun, K. Parvez, X. L. Feng and K. Mullen, *J. Am. Chem. Soc.*, 2012, **134**, 9082–9085.
34 G. Wu, K. L. More, C. M. Johnston and P. Zelenay, *Science*, 2011, **332**, 443–447.
35 K. Parvez, S. Yang, Y. Hernandez, A. Winter, A. Turchanin, X. Feng and K. Muellen, *ACS Nano*, 2012, **6**, 9541–9550.
36 J. Wang, J. Zhou, Y. Hu and T. Regier, *Energy Environ. Sci.*, 2013, **6**, 926–934.
37 S. Kattel, P. Atanassov and B. Kiefer, *J. Phys. Chem. C*, 2012, **116**, 17378–17383.
38 S. Kattel, P. Atanassov and B. Kiefer, *Phys. Chem. Chem. Phys.*, 2013, **15**, 148–153.
39 X. Y. Yan, X. L. Tong, Y. F. Zhang, X. D. Han, Y. Y. Wang, G. Q. Jin, Y. Qin and X. Y. Guo, *Chem. Commun.*, 2012, **48**, 1892–1894.
40 Y. X. Xu, H. Bai, G. W. Lu, C. Li and G. Q. Shi, *J. Am. Chem. Soc.*, 2008, **130**, 5856–5857.
41 F. Bidault, D. J. L. Brett, P. H. Middleton and N. P. Brandon, *J. Power Sources*, 2009, **187**, 39–48.
42 L. Yu, X. Pan, X. Cao, P. Hu and X. Bao, *J. Catal.*, 2011, **282**, 183–190.
43 L. Zhang and Z. Xia, *J. Phys. Chem. C*, 2011, **115**, 11170–11176.

Electronic Supporting Information

Enhanced Electrochemical Catalytic Activity by Copper Oxide Grown on Nitrogen-doped Reduced Graphene Oxide

Ruifeng Zhou,[a,b] Yao Zheng,[a,b] Denisa Hulicova-Jurcakova[c] and Shi Zhang Qiao[*a]

[a] *School of Chemical Engineering, the University of Adelaide, Adelaide, SA 5005, Australia. Fax: +61 8 8303 4373; Tel: +61 8 8313 6443; E-mail: s.qiao@adelaide.edu.au*

[b] *Australian Institute of Bioengineering and Nanotechnology, the University of Queensland, St Lucia, QLD 4072, Australia*

[c] *School of Chemical Engineering, the University of Queensland, St Lucia, QLD 4072, Australia.*

Chemicals

All chemicals are purchased from Sigma-Aldrich and used without further treatment. Pt/C used is 20% Platinum on Vulcan XC-72, purchased from Fuel Cell Store.

Syntehsis of GO

Graphite flake (3 g) was put into concentrated H_2SO_4 (12 ml), $K_2S_2O_8$ (2.5 g), and P_2O_5 (2.5 g). The mixture was kept at 80 °C for 4.5 h, then cooled to room temperature and diluted with 0.5 L of DI water. The mixture was filtered and washed with DI water. The product was dried in vacuum at 50 °C overnight.

The pretreated graphite was put into cold (0 °C) concentrated H_2SO_4 (120 mL). Then, $KMnO_4$ (15 g) was added gradually under stirring and the temperature of the mixture was kept to be below 20 °C by ice cooling. Successively, the mixture was stirred at 35 °C for 2 h, and then diluted with DI water (250 mL) using ice bath cooling. The mixture was then stirred for 2 h, and then additional 0.7 L of DI water was added. 20 mL of 30% H_2O_2 was added to the mixture. The mixture was washed with 1:10 HCl aqueous solution (1 L) and DI water. The resulting paste-like product was diluted to make a graphite oxide dispersion. Exfoliation was carried out by sonicating graphite oxide dispersion under ambient condition for 30 min, followed with centrifuging at 3000 rpm for 30 min to eliminate unexfoliated graphite.

For measurement of N_2 adsorption-desorption isotherms, the GO is thermally reduced under 200 °C in vacuum to form rGO.

Synthesis of CuO

0.25 ml of 0.1 M $CuCl_2$ was added to 16 ml ethanol and stirred for 5 min at 25°C. Then, 0.75 ml of 0.1 M NaOH was added to the suspension and stirred for another 1 hour. The suspension was then centrifuged, washed and dispersed in ethanol.

Synthesis of CuO/GO.

0.25 ml of 0.1 M $CuCl_2$ was added to 8 ml of GO solution (1 mg ml^{-1} in water) and was stirred for 5 min. Then 0.75 ml of 0.1 M NaOH was added to the suspension and stirred for another 1 hour at 60°C. The suspension was then centrifuged, washed with water and dispersed in ethanol. For measurement of N_2 adsorption-desorption isotherms, the sample is degased under 200 °C in vacuum where GO is

thermally reduced to reduced GO (rGO).

Characterization

SEM images were taken with Philips XL30 FEG SEM. TEM images were collected with Tecnai F20. XRD spectrums were measured with Rigaku Miniflex benchtop XRD with Cu Kα line. N_2 adsorption/desorption measurement was carried out with Micromeritics Tristar II. Surface area is calculated by the multipoint BET method on basis of adsorption curve data. XPS were taken by KRATOS Axis Ultra DLD with Al Kα line. FTIR were collected with Nicolet 6700 FTIR. TGA were measured with SETARAM ABSYSTM Thermogravimetric Analysis.

Formulae

Koutecky-Levich equation:

$$\frac{1}{J} = \frac{1}{J_L} + \frac{1}{J_K}$$

J is the measured current density. J_L is the diffusion-limiting current density. J_K is the kinetic-limiting current density.

$$J_L = 0.62nFC_0(D_0)^{2/3}\nu^{-1/6}\omega^{1/2}$$

Where n is the electron transfer number, F = 96485 C mol^{-1} is Faraday constant, C_0 = 1.2 mol m^{-3} is the concentration of O_2, D_0 = 1.97 × 10-9 m^2 s^{-1} is the diffusion coefficient of O_2 in water, ν = 1.004 × 10^{-6} m2 s^{-1} is the kinematic viscosity of water, and ω is the angular velocity of the electrode.

J_K and n are derived from the slope and intercept of KL plot.

Equation in RRDE Measurement:

$$\%HOO^- = 200 \times \frac{I_r/N}{I_d + I_r/N}$$

$$n = 4 \times \frac{I_d}{I_d + I_r/N}$$

I_r is the ring current and I_d is the disk current. N = 0.37 is the current collection efficiency of the RRDE.

Calculation of equilibrium electrode potential of reaction (3) and (2*)

All the equations and data from Ref. 1.

Estimation of ionic activity coefficient

In electrolyte of 0.1 M KOH and 0.01 M H_2O_2, the concentrations of each kind of ions are:

K^+: 0.1 M, OH^-: 0.09M, HOO^-: 0.01M.

The ionic strength (I) is estimated using equation:

$$I = \frac{1}{2}\sum c_i z_i^2$$

Where c_i and z_i are the concentration and ionic charge of each ions. z_i=1 for all ions so that I=0.1 for our electrolyte.

Ionic activity coefficient of each ion (f_i) is calculated using Debye-Hückel equation:

$$-log f_i = \frac{Az_i^2\sqrt{I}}{1 + B\text{å}_i\sqrt{I}}$$

Where A and B are constants. At 25°C, A=0.5115 and B=0.3291. å_i is the effective radius of each ion in angstrom. For OH^- and HOO^-, å is taken 3.5.

As a result, f=0.761.

Estimation of equilibrium electrode potential

$HOO^- + OH^- \rightleftharpoons O_2 + H_2O + 2e^-$ $\qquad E_3^\Theta = -0.076V\ vs\ SHE$

$HOO^- + H_2O + 2e^- \rightleftharpoons 3OH^-$ $\qquad E_{2*}^\Theta = 0.867V\ vs\ SHE$

The equilibrium electrode potential of reaction is calculated by Nernst equation:

$$E = E^\Theta + \frac{RT}{ZF} lnQ$$

R=8.314 J K^{-1} mol^{-1} is the universal gas constant. T=298K is the absolute temperature. Z is the number of electrons involved in the electrode reaction. Z=2 for both reactions. F=96485 C mol^{-1} is the Faraday constant. Q is the reaction quotient.

For reaction (3), pressure of O_2 is 1 atm. Thus $[O_2]$ is 1.

$$E_3 = E_3^\Theta + \frac{RT}{ZF} ln \frac{[O_2]}{[HO_2^-][OH^-]} = 0.021V\ vs\ SHE$$

For reaction (2*):

$$E_{2*} = E_{2*}^\Theta + \frac{RT}{ZF} ln \frac{[HO_2^-]}{[OH^-]^3} = 0.908V\ vs\ SHE$$

The reference electrode used has potential 0.2 V vs SHE. Thus,

$$E_3 = -0.179V$$

$$E_{2*} = 0.708V$$

Reference

1. *Lange's Handbook of Chemistry*, J. A. Dean, McGraw-Hill, Columbus, 15th edn., 1999, vol. 8, pp. 8.2 - 8.5, 8.132.

Supporting figures

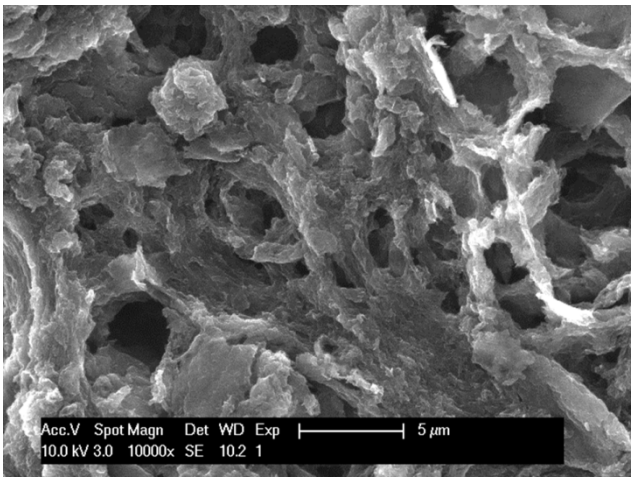

Fig. S1 SEM image of CuO/N-rGO. Micrometer-scale pores are shown.

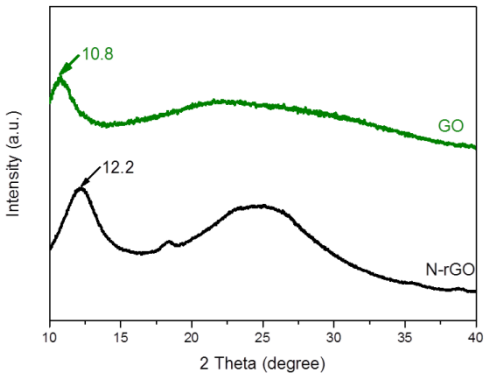

Fig. S2 XRD pattern of GO and N-rGO. High-shifted interplanar diffraction of N-rGO is attributed to decreased interplanar displacement by elimination of functional groups during reduction.

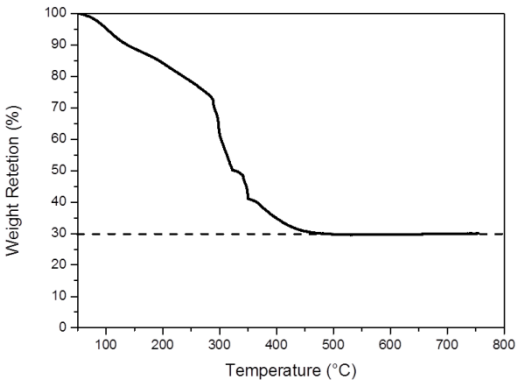

Fig. S3 TGA of CuO/N-rGO in air. N-rGO is burnt out and CuO is remained.

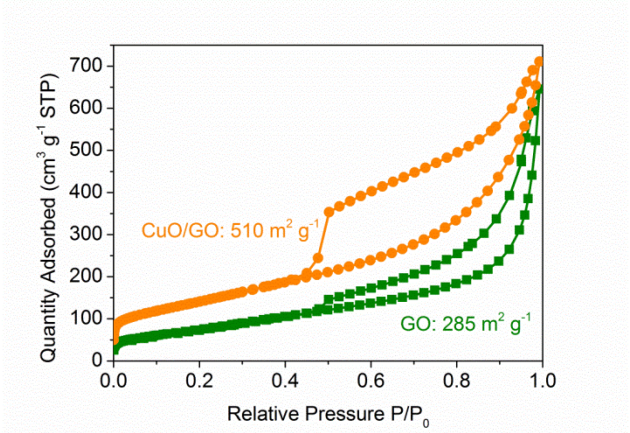

Fig. S4 N_2 adsorption-desorption isotherms of GO and CuO/GO. Specific surface increases by CuO intercorporation.

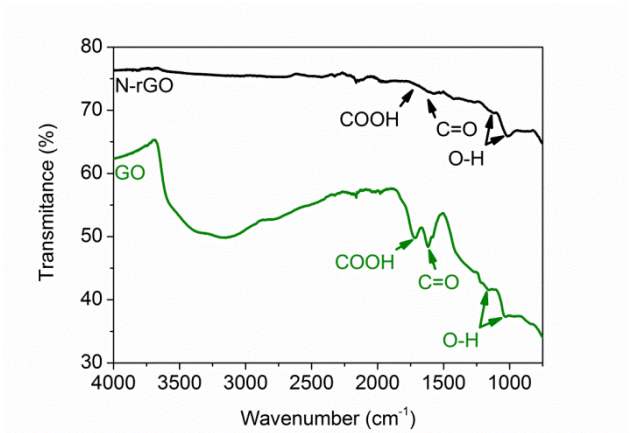

Fig. S5 FTIR of GO and N-rGO. Carboxyl groups are eliminated after reduction while hydroxyl groups remain.

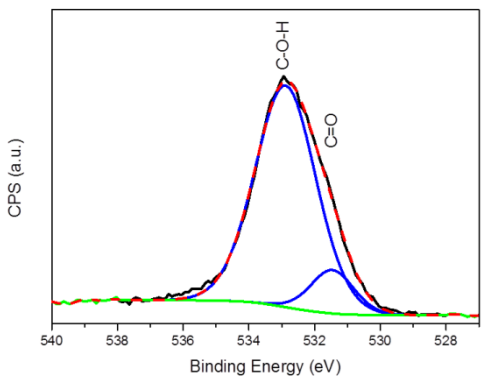

Fig. S6 High resolution XPS of O 1s of N-rGO. Carbonyl groups are of low amount after reduction.

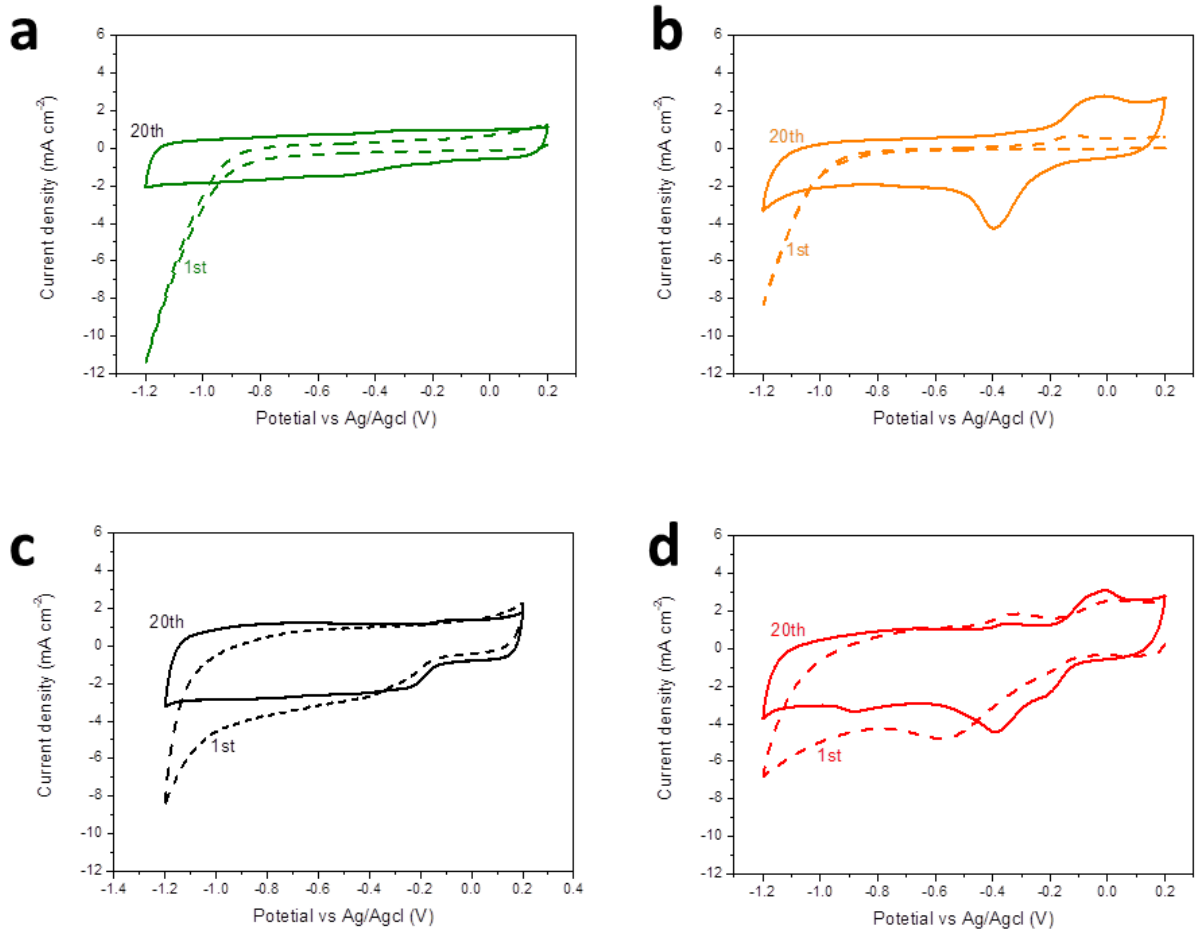

Fig. S7 1st (solid) and 20th (dash) CV of GO (a), CuO/GO (b), N-rGO (c) and CuO/N-rGO (d). GO is a poor in conductivity so that it shows very low capacitance. It is reduced at low potential and achieves high conductivity after 20 cycles of CV. N-rGO already has good conductivity but can still be reduced a bit.

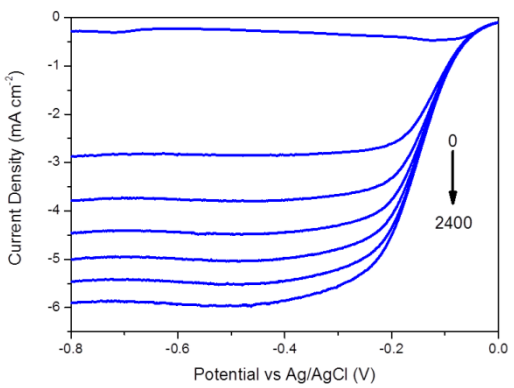

Fig. S8 LSV of Pt/C at different rotation rate (rpm).

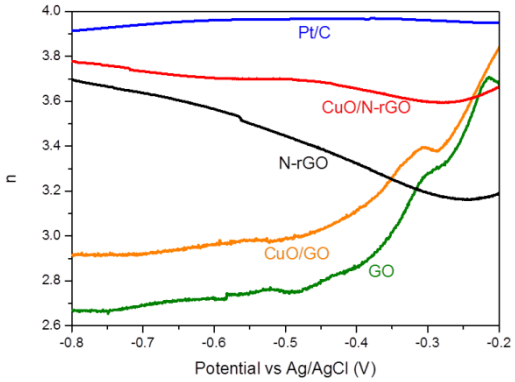

Fig. S9 Electron transfer number of different catalysts calculated from RRDE test. The n is in accordance with that calculated from KL plot.

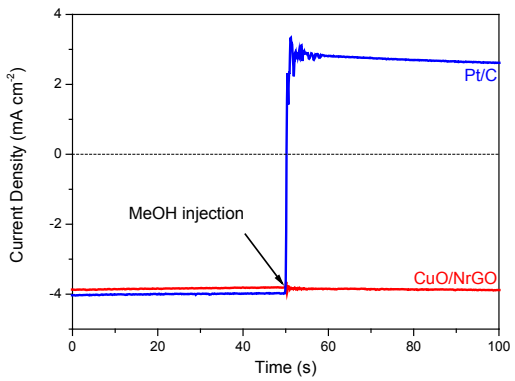

Fig. S10 MeOH tolerance test of CuO/N-rGO and Pt/C under -0.3 V and 1600 rpm.

Chapter 4: Silver/Nitrogen-Doped Graphene Interaction and Its Effect on Electrocatalytic Oxygen Reduction

Introduction

This chapter focuses on the characterization of TM-N interaction. In this chapter, a new nanocomposite Ag/N-rGO is synthesized. I found that the Ag-N interaction can be confirmed by XPS and Raman spectroscopy. The Ag/N-rGO also showed very good ORR performance. The good ORR performance is attributed to Ag-N interaction.

This chapter was published in *Chem. Mater.* **2014**, 26, (20), 5868-5873.

CHEMISTRY OF MATERIALS

Article

pubs.acs.org/cm

Silver/Nitrogen-Doped Graphene Interaction and Its Effect on Electrocatalytic Oxygen Reduction

Ruifeng Zhou[†,‡] and Shi Zhang Qiao*[,†]

[†]School of Chemical Engineering, The University of Adelaide, Adelaide, South Australia 5005, Australia

[‡]Australian Institute for Bioengineering and Nanotechnology, The University of Queensland, St Lucia, Queensland 4072, Australia

Supporting Information

ABSTRACT: Three types of silver/reduced graphene oxide (Ag/rGO) nanocomposites (one doped with nitrogen and another two without) are synthesized to investigate their atomic structures and the oxygen reduction reaction (ORR) performance with them as the electrocatalysts. For the first time, the bonding interaction between Ag and N in N doped rGO (N-rGO) is confirmed by both high resolution X-ray photoelectron spectroscopy (XPS) and surface enhanced Raman spectroscopy (SERS). The Ag/N-rGO shows excellent ORR performance, including very high onset potential and current density, which outperforms those Ag/rGOs without N doping. Detailed electrochemical analysis shows that the ORR mechanism on Ag/N-rGO is different from both Ag and N-rGO, and its excellent performance is caused by the Ag−N bonding which alters the electronic structure of N-rGO.

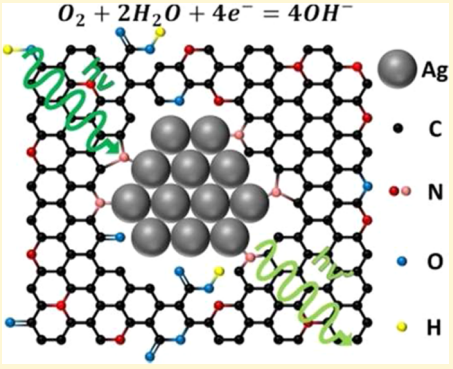

The oxygen reduction reaction (ORR) at the cathode of aqueous electrolyte fuel cells is very sluggish so that the usage of high active catalyst is inevitable.[1,2] Pt is the best catalyst for ORR, but it is too expensive for commercial purpose. Thus, it is critical for fuel cells to reduce the high cost on electrocatalyst. Compared to reducing Pt usage on the electrodes, replacing Pt by some less expensive materials is a more essential and promising way.[3,4] Some nonprecious metal oxides have decent ORR activity, but their low conductivity is a main drawback. Although the overall conductivity of electrocatalyst can be improved by blending conductive agent into the active composite, the electrons still have to pass through the semiconductive particles until they reach the conductive agent, leading to unsatisfactory performance.[5−9] On the other hand, the metal-free catalysts also show very good ORR performance, but they are still not good enough due to some intrinsic problems. For example, carbon based catalysts reduce a large portion of oxygen into hydrogen peroxide (2e reaction) rather than water (4e reaction), making the efficiency of ORR much lower than the theoretical limitation.[10−13] Furthermore, the carbons are usually made rich of pores and defects to maximize their active sites and smooth oxygen diffusion, but the conductivity is heavily destroyed in that case. Therefore, it is still challenging to synthesize an inexpensive catalyst with perfect conductivity and high ORR activity/efficiency simultaneously.

Ag has been considered as an alternative to Pt in alkaline fuel cells due to its unique properties.[14−16] First, the equilibrium potential between Ag and Ag_2O is 1.17 V vs reversible hydrogen electrode (RHE), which is just below the equilibrium potential between oxygen and water (1.23 V) and is well above the practical ORR potential (up to 1 V). Therefore, Ag keeps its metallic state during ORR, ensuring the perfect local conductivity of the active site. Along with other noble metals (e.g., Pt, Au, and Pd), Ag is the cheapest metal to have such property. Another important feature is that Ag is able to reduce O_2 completely into water (4e) within the whole ORR potential window. This is based on the fact that Ag is an excellent catalyst for hydrogen peroxide reduction, oxidation, or disproportionation, so that hydrogen peroxide can hardly escape from its surface.[17−19] These properties indicate that Ag will be an ideal cocatalyst with high-performance metal-free catalysts to improve both the electron conductivity and catalytic efficiency. The main drawback of Ag is the large Tafel slope of ORR, making the ORR rate increase much more slowly than Pt. However, when Ag is coordinated into N doped carbon (NC) frame, new electronic structures may be established which have potential to excite further ORR dynamics.[20,21]

A big challenge on investigating ORR mechanism on metal (M)/NC composites is the characterization and confirmation of M−N interaction. Sophisticated techniques such as X-ray absorption may be necessary.[22−25] Fortunately, nanosized Ag is a perfect material for surface enhanced Raman spectroscopy (SERS).[26,27] Applying SERS to the Ag-NC is possible to answer the questions such as whether and what functional groups on NC interact with Ag. Combing the high-resolution X-ray photoelectron spectroscopy (XPS) technique, the functional groups and their interaction with Ag can be resolved convincingly.

Received: June 23, 2014
Revised: September 25, 2014
Published: September 26, 2014

In this paper, Ag particles are synthesized on three types of rGOs, which are reduced electrochemically (e-rGO), chemically by $NaBH_4$ (c-rGO), and chemically by NH_3 (N-rGO), respectively. The Ag−N interaction in Ag/reduced graphene oxide (Ag/rGO) is carefully studied and confirmed for the first time by XPS and Raman spectroscopy. The functionalities of Ag in Ag/rGO composites are investigated by electrochemical analysis. Ag/N-rGO has higher ORR onset potential and significantly lower Tafel slope than Ag and N-rGO, leading to excellent ORR performance which is close to that of commercial Pt/C but with a much lower price. The Ag/N-rGO also shows a different ORR mechanism from those of Ag and N-rGO, which is proved to be attributed to the Ag−N interaction.

EXPERIMENTAL SECTION

Synthesis of Ag_2O/N-rGO, Ag_2O/c-rGO, and Ag_2O/GO. The synthesis of graphene oxide (GO) is similar to the method reported in ref 28 but with harsher oxidation condition, which is described in the Supporting Information in detail. To synthesize N-rGO, 5 mL of 25% NH_3 aqueous solution was added into 65 mL of 0.1% GO solution. The mixture was stirred at 90 °C for 12 h. To synthesize c-rGO, 1 M NaOH aqueous solution was added into 65 mL of 0.1% GO solution until the pH reached 10. Then, 0.246 g of $NaBH_4$ was added to the solution. The mixture was stirred at 60 °C for 12 h. After reduction, the N-rGO or c-rGO was filtered and washed with water and dispersed in water by supersonication. XPS spectra of GO and rGOs are provided in Supporting Information Figure S1 where the reduction of GO is demonstrated by reduced oxygen content and hydroxide groups.

To prepare Ag_2O/N-rGO or Ag_2O/c-rGO, 10 μL of 0.1 M $AgNO_3$ was added to 10 mL of 0.02% N-rGO or c-rGO suspension under sonication. Then 100 μL of 0.1 M NaOH was added. The products were centrifuged, washed with water, and redispersed in 0.75 mL of water/2-propanol mixture (3:1). To prepare Ag_2O/GO, 10 mL of 0.02% GO aqueous solution was used instead of rGO suspension. X-ray diffraction (XRD) of the Ag_2O/GO is shown in Supporting Information Figure S2.

Preparation of Ag/rGO Electrodes. To prepare Ag/e-rGO on electrodes, 18.5 μL of 0.2% Ag_2O/GO and 18.5 μL of 0.1% Nafion solution were mixed and dipped onto the glassy carbon disk (5.61 mm in diameter) of a rotation ring-disk electrode (RRDE) and dried under ambient condition. The catalyst loading is about 0.15 mg cm^{-2}, containing 0.1 mg cm^{-2} rGO and 0.05 mg cm^{-2} Ag. The electrode was then used as the working electrode in a four-electrode electrochemistry system. In the system, the Pt ring of RRDE, a Ag/AgCl electrode (in 4 M KCl), and a Pt wire were used as the second working electrode, the reference electrode, and the counter electrode, respectively. Oxygen saturated 0.1 M KOH aqueous solution was used as the electrolyte unless otherwise specified. Cyclic voltammetry (CV) was applied to the working electrode between 1.2 V and −0.2 V at 100 mV s^{-1} until a steady CV curve was reached. During the CV, the Ag_2O was reduced into Ag and the GO was reduced to e-rGO (Supporting Information Figure S3). To synthesize Ag/N-rGOs or Ag/c-rGO electrodes, Ag_2O/N-rGO or Ag_2O/c-rGO was used instead of Ag_2O/GO in the above preparation process. The preparation procedure of the samples for characterization after ORR measurement is provided in the Supporting Information.

ORR Measurement. The electrochemical measurement was carried out immediately after the working electrode was prepared. The electrochemistry system was the same as in the synthesis. The linear scanning voltammetry (LSV) was measured with scanning rate of 5 mV s^{-1}. The Pt ring was biased at 1.5 V.

Characterization. Transmission electron microscopy (TEM) images were taken with Tecnai F20. XRD analysis was carried out by Rigaku Miniflex 600 with the Cu Kα line. XPS was taken by KRATOS Axis Ultra DLD with the Al Kα line. Raman spectra were collected with HORIBA LabRAM HR Evolution with 532 nm laser. The power of the laser is set to 1% of the full power unless other specified.

RESULTS AND DISCUSSION

A typical low magnification TEM image of Ag/N-rGO is shown in Figure 1a. Ag particles on the N-rGO are spherical and are

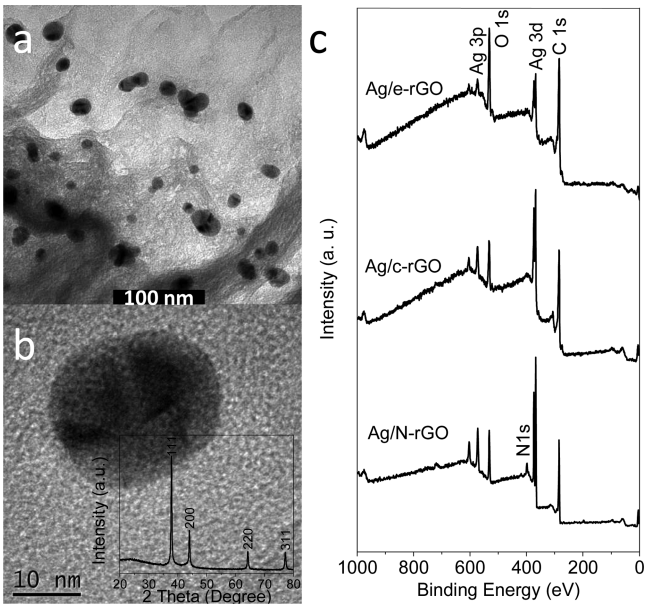

Figure 1. Low (a) and high (b) resolution TEM images of Ag/N-rGO. Inset: XRD pattern of Ag/N-rGO. (c) XPS survey of Ag/rGOs.

uniformly loaded on the N-rGO. The diameters of the particles are between 10 to 30 nm. Figure 1b shows a high resolution TEM image of a Ag particle with clear Ag crystal structure. XRD of the Ag/N-rGO (inset in Figure 1b) shows only the Ag phase in the composite, indicating complete reduction of Ag_2O in the composites. Ag/e-rGO and Ag/c-rGO have similar morphology (Supporting Information Figure S4). The Ag particles in Ag/N-rGO and Ag/c-rGO are larger than those in Ag/e-rGO, which results in narrower peaks of Ag in XRD (Supporting Information Figure S5). The larger Ag particles are attributed to the decreased oxygen containing functional groups after GO reduction which are the nucleation sites of Ag_2O particles.

The elemental analysis of the Ag/rGOs was carried out by XPS. The surveys of the Ag/rGOs are shown in Figure 1c. All the samples contain C, O, and Ag. The O/C atomic ratios are 0.183, 0.144, and 0.258 for e-rGO, c-rGO, and N-rGO respectively, which are higher than those rGOs synthesized at high temperature (usually under 5 atom %). The N content in N-rGO is about 5.9 atom %, which is higher than most N doped graphenes,[23,29] due to highly oxidized GO precursor and low synthesis temperature.

CV measurement is carried out to show the surface condition of the catalysts. The results are shown in Figure 2. Briefly, all rGOs show quite high specific capacitance (50−200 F g^{-1} at 20 mV s^{-1}). The capacitance can be attributed to both high specific surface area (electric double layer capacitance) and redox of carbons (pseudocapacitance). The pseudocapacitance of N-rGO is especially obvious, which is exhibited by the large and nonrectangular CV curve, suggesting that N doping has changed the electrochemical property of graphene. In Ag/rGOs, a Ag redox pair is observed at potential over 1.1 V, which

dx.doi.org/10.1021/cm502260m | Chem. Mater. 2014, 26, 5868−5873

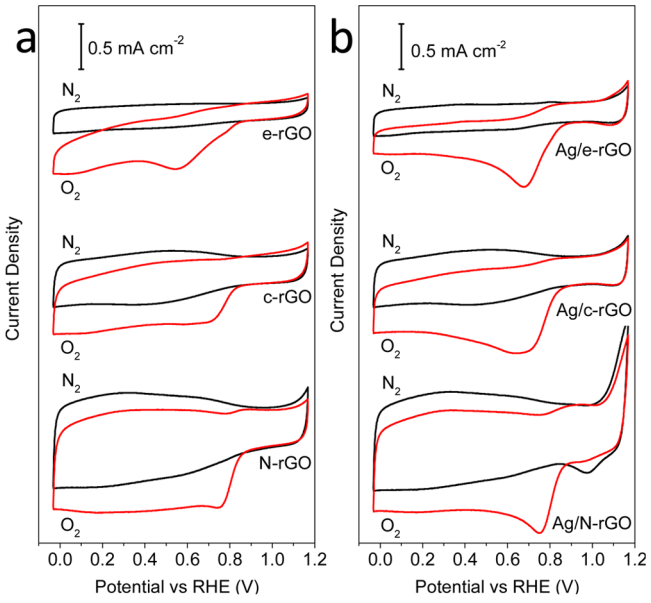

Figure 2. CV curves of e-rGO, c-rGO, and N-rGO (a) and Ag/e-rGO, Ag/c-rGO, and Ag/N-rGO (b) in nitrogen and oxygen saturated electrolytes. The scan rate is 20 mV s^{-1}.

confirms that Ag is electrochemically accessible and that the Ag is in the metallic state during ORR (<0.9 V). When the electrolyte is oxygen saturated, a cathodic peak (starting from 0.9 V) is observed. The peaks from Ag/rGOs are much larger and sharper than those of the corresponding rGO, indicating better ORR performance. rGOs also show a second wide peak (starting from 0.5 V), which is attributed to reduction of peroxide (refer to LSV part for more details). The Ag/rGOs show only one peak, indicating complete ORR from the beginning.

To study the ORR performance and pathway of our catalysts, the LSV measurement on RRDE was carried out. The LSV of Ag, e-rGO, and Ag/e-rGOs are shown in Figure 3a. The Ag shows a typical electrochemical polarization curve on disk

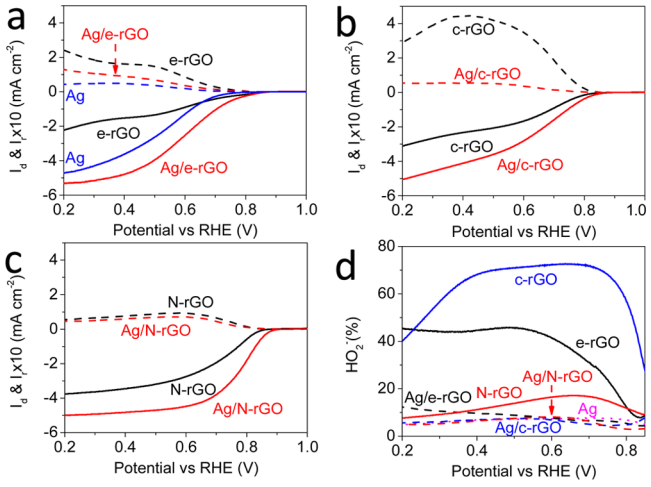

Figure 3. LSV of Ag, e-rGO and Ag/e-rGO (a); c-rGO and Ag/c-rGO (b); and N-rGO and Ag/N-rGO (c) on RRDE at 1600 rpm. The cathodic current (I_d) is the disk current density. The anodic current (I_r) is the ring current normalized by the area of disk and magnified by 10 times for better view. (d) Peroxide production ratio of the catalysts during ORR.

current (I_d), with kinetic limitation at low overpotential and mass transport limitation at high overpotential. The ring current (I_r) of Ag is very low, so very little peroxide is produced (high electron transfer number). Pure e-rGO shows a poor ORR performance, as we reported in a previous paper.[30] The same tendency of I_d and I_r results in a steady and high peroxide percentage below 0.5 V (Figure 3d), indicating the reduction of peroxide on e-rGO is not triggered. As for Ag/e-rGO, the curve shape is the same as that of Ag at high overpotential (Figure 3a), indicating that ORR is mainly contributed by Ag. The higher I_d of Ag/e-rGO than Ag is due to nanosized Ag in Ag/e-rGO. Another important feature is that Ag/e-rGO produces less peroxide than e-rGO, showing that peroxide reduction on Ag was conducted.

The LSV curves of c-rGOs and Ag/c-rGOs are shown in Figure 3b. The c-rGO has slightly better ORR performance than e-rGO. More importantly, I_r of c-rGO decreases at high overpotential due to reduction of peroxide. This may be caused by the trace of B doping in c-rGO, although it is not detected in XPS. As for Ag/c-rGO, the I_d curve shape is similar to that of c-rGO, indicating that the rate controlling process is on the c-rGO rather than Ag. Ag/c-rGO shows better ORR performance than c-rGO due to the reduction of peroxide on Ag.

The N-rGO shows the best ORR performance among rGOs (Figure 3c), which is in accordance with other literature.[29,30] Its peroxide ratio is much lower than e-rGO and c-rGO (Figure 3d). Ag/N-rGO further depresses the peroxide ratio to the same level with Ag, showing that reduction of peroxide on Ag also take places. However, the peroxide production of N-rGO is so low (less than 0.25 mA cm^{-2}) that the reduction of peroxide impossibly provides I_d lift of over 1 mA cm^{-2}. Therefore, Ag/N-rGO definitely cannot be regarded as a physical mixture of Ag and N-rGO, as in Ag/e-rGO and Ag/c-rGO.[20,21] There must be some new ORR mechanism on it.

The LSV at different angular velocities are measured, and the corresponding Kouteky–Levich (KL) plots are also provided (Supporting Information Figure S6 and S7). The electron transfer numbers calculated from the KL equation are generally in accordance with the peroxide ratios from RRDE though the values from RRDE are believed more accurate. The higher linearity of the KL plot of Ag/N-rGO shows that it has higher ratio of homogeneous catalyzing than the other non-Pt catalysts, which is due to enhanced ORR kinetics.

We believe the Ag/N-rGO is an ideal replacement of Pt for ORR in real applications because of the following reasons. First, the price of Ag is about 1/70 of Pt. We compared the Ag/N-rGO and commercial Pt/C at different loadings (Supporting Information Figure S8). Assuming the main cost of catalysts comes from the metals, Ag/N-rGO is comparable to Pt/C at 30 times the price. Although the Ag/N-rGO synthesized in lab scale has 1/6 of the price of commercial 20%Pt/C (Supporting Information Table S1), its price can be largely reduced in industrial manufacturing. Second, Ag/N-rGO is fairly stable, losing only 12% current after 50 000 s ORR (Supporting Information Figure S9). Third, Ag/N-rGO is completely tolerant to methanol (Supporting Information Figure S10), indicating that it is a perfect cathode for direct methanol fuel cells. It also suggests that Ag/N-rGO will hardly be poisoned, e.g., by carbon monoxide.

The Tafel plots of the catalysts are measured to further analyze the ORR behavior and mechanism (Figure 4). The Tafel slope of Ag is 110 mV per decade, which is within the reported range of 80 to 120 mV per decade (Supporting

dx.doi.org/10.1021/cm502260m | Chem. Mater. 2014, 26, 5868–5873

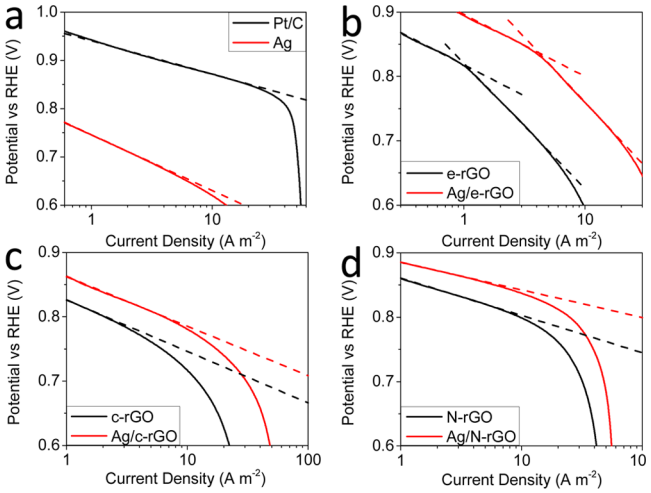

Figure 4. Tafel plot of Pt/C and Ag (a); e-rGO and Ag/e-rGO (b); c-rGO and Ag/c-rGO (c); and N-rGO and Ag/N-rGO (d). Data are collected at 2400 rpm.

Information Table S2) for Ag based catalysts.[14,15,31−34] It is much higher than that of Pt/C (64 mV per decade), showing slower ORR dynamics of Ag catalyst than Pt. The Tafel plot of e-rGO has two distinct linear sections, 96 mV and 190 mV per decade, respectively. Ag/e-rGO has exactly the same Tafel curve shape and slope as e-rGO, strongly suggesting that the reaction on Ag/e-rGO is the same as e-rGO at low potential. The exchange current density of Ag/e-rGO is about 6 times that of e-rGO, which is caused by enlarged surface area due to Ag particles intercalating into e-rGO layers. The Tafel slopes of c-rGO and Ag/c-rGO are very close (77 and 80 mV per decade). The shapes of Tafel plots of N-rGO and Ag/N-rGO still look similar (Figure 4c). However, the Tafel slope of Ag/N-rGO is 43 mV per decade, which is significantly smaller than the N-rGO (55 mV per decade). This change in Tafel slope must be caused by the change of kinetic parameters of ORR, which should be the result of formation of new electron structure by chemical interaction between Ag and N-rGO. On basis of discussions above, Ag/rGO shows Tafel slope close to corresponding rGO rather than Ag, suggesting that the active sites are on rGO rather than on Ag at low over potential. Ag can be regarded as the so-called cocatalyst (to reduce peroxide form rGOs and enhance activity of N-rGO). This is quite different from other Ag/C catalysts where Ag is a catalyst while carbon is merely a support.

To exhibit how Ag interacts with N-rGO, the high resolution XPS of N 1s are measured (Figure 5). Before ORR, four chemical states of N are observed (aminic and pyrrolitic N are too close to be distinguished in XPS), as reported elsewhere. After ORR, oxidized N disappears, while pyrrolitic/aminic N increases. As the total N content does not change significantly, the reduction from oxidized N to pyrrolitic/aminic N is the sole possibility. Moreover, regardless before or after ORR, the average binding energy of N 1s in Ag containing samples is significantly lower than that in the pure N-rGO. Since Ag has very low electronegativity (1.93 vs 2.20 of H, 2.25 of C, and 3.04 of N in the Pauling scale), the decrease of N's binding energy is normal if N bonds to Ag. This is also predicted by DFT calculation, which concludes that pyrrolitic and pyridinic N can bond to Ag and get more negatively charged.[35] Therefore, our XPS result is the direct evidence of Ag−N bonding in Ag/N-rGO. DFT calculation also suggests that Ag−

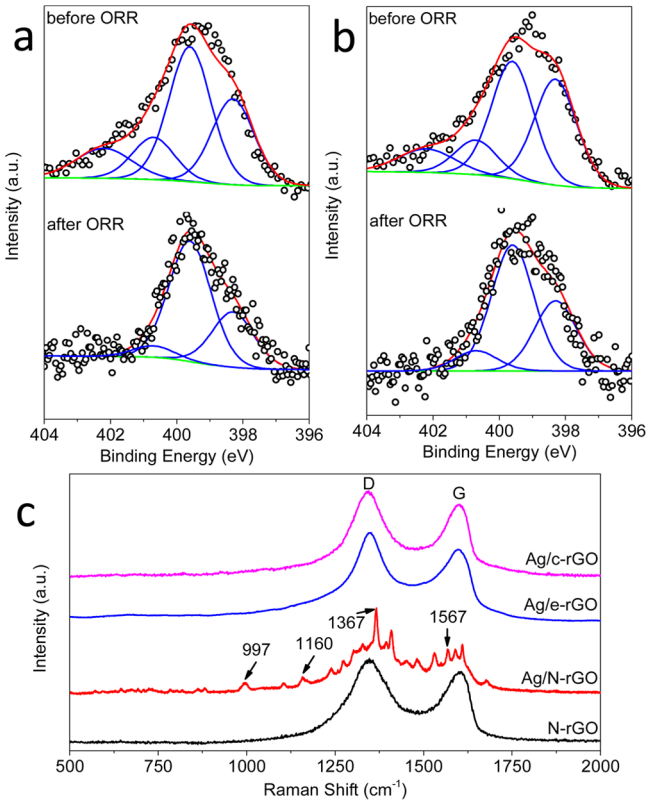

Figure 5. High resolution XPS of N 1s of N-rGO (a) and Ag_2O/N-rGO and Ag/N-rGO (b). The four peaks are pyridinic, pyrrolitic/aminic, graphitic, and oxidized nitrogen, from low to high binding energy, respectively. (c) Raman spectra of N-rGO and Ag/rGOs.

N bonding induces a more positive charge on the adjacent C to N, which is the main reason for improved ORR performance.[36]

The Raman spectroscopy is another powerful method to resolve the atomic structure of carbons. Usually, the Raman signal of the functional groups is too weak, comparing with G and D band from graphitic structure, to be seen. Fortunately, nanosized Ag is an ideal material for SERS in which the Raman signal from the molecules physisorbed or chemisorbed on Ag is significantly enhanced. Moreover, the molecule with a lone pair of electrons (e.g., pyridine and pyrrolic anion) can bond to Ag to yield especially high enhancement (explained by the chemical theory of SERS).[37] In our Raman spectra, all rGOs show typical D and G bands of the graphitic structure (Supporting Information Figure S11). After Ag is incorporated, the Raman signals of Ag/e-rGO and Ag/c-rGO are greatly enhanced, but the patterns remain the same as those of the original rGOs (Supporting Information Figure S12). However, many additional peaks are observed besides G and D bands on Ag/N-rGO (Figure 5c). Although it is impossible to assign each peak to a determinate vibrational mode because of the complexity of the real atomic structure of N-rGO, these peaks do prove some certain structures of N-rGO are bonded with Ag to get extraordinary Raman enhancement. In a typical Raman spectrum of Ag/N-rGO, the most significant peaks (as marked in Figure 5c) coincide with the ring breathing mode of pyridine (around 1000 cm^{-1})[38] or pyrrole (1160 cm^{-1})[39] and some other modes (e.g 1367 cm^{-1} of pyrrole[40] and around 1600 cm^{-1} of pyridine[41,42]), strongly suggesting the existence of pyridinic and pyrrolitic structure in the N-rGO (as also suggested in XPS). Furthermore, the Raman spectrum of Ag/

dx.doi.org/10.1021/cm502260m | Chem. Mater. 2014, 26, 5868−5873

N-rGO varies with the location where Raman signal is collected. In Supporting Information Figure S13, the Raman spectra measured at five different locations of a same Ag/N-rGO sample show additional peaks to G and D bands, but they do not overlap. This suggests that the local structure of N-rGO and Ag−N interaction in Ag/N-rGO is inhomogeneous and complicated. The Raman spectrum of Ag/N-rGO is also sensitive to laser power. Additional peaks can be observed only at carefully selected low laser power (1% of our Raman spectrometer's maximum), but they vanish and the spectrum degenerates to simple G and D modes quickly (within a few seconds), if laser power is increased to 10% or higher. This also proves that the additional peaks come from the functional groups bonded to Ag, which are burned down by the heating effect of strong laser absorption of Ag.

■ CONCLUSIONS

In conclusion, the Ag/N-rGO shows quite different ORR mechanism from Ag and N-rGO and outperforms Ag, N-rGO, and those Ag/rGOs without Ag−N bonding. For the first time, the chemical interaction between Ag and N-rGO is confirmed by high resolution XPS and SERS, which is believed to be the origin of high ORR electrocatalytic activity and altered reaction mechanism. The new material is promising in fuel cell application due to its high activity and efficiency, low price, methanol tolerance, etc. Moreover, our SERS and XPS analysis is instructive for future study on the interaction between metal and doped carbon, as well as the explanation of electrochemical reaction mechanisms. It also implies the future of in situ SERS study as a powerful tool to investigate the mechanism of ORR and other electrochemical reactions.

■ ASSOCIATED CONTENT

Supporting Information

The synthesis of GO, characterization of samples after ORR, estimation of prices of the Ag/N-rGO, comparison of Tafel slopes, and supporting figures. This material is available free of charge via the Internet at http://pubs.acs.org.

■ AUTHOR INFORMATION

Corresponding Author

*E-mail: s.qiao@adelaide.edu.au.

Author Contributions

The manuscript was written and approved by all authors.

Notes

The authors declare no competing financial interest.

■ ACKNOWLEDGMENTS

This work was financially supported by the Australian Research Council (ARC) through the Discovery Project program (DP140104062, DP130104459, and DP1095861).

■ REFERENCES

(1) Katsounaros, I.; Cherevko, S.; Zeradjanin, A. R.; Mayrhofer, K. J. J. *Angew. Chem., Int. Ed.* **2014**, *53*, 102−121.
(2) Wu, J. B.; Yang, H. *Acc. Chem. Res.* **2013**, *46*, 1848−1857.
(3) Chen, Z. W.; Higgins, D.; Yu, A. P.; Zhang, L.; Zhang, J. J. *Energy Environ. Sci.* **2011**, *4*, 3167−3192.
(4) Wang, B. *J. Power Sources* **2005**, *152*, 1−15.
(5) Hamdani, M.; Singh, R. N.; Chartier, P. *Int. J. Electrochem. Sci.* **2010**, *5*, 556−577.
(6) Xu, J. B.; Gao, P.; Zhao, T. S. *Energy Environ. Sci.* **2012**, *5*, 5333−5339.
(7) Wang, Y.-g.; Cheng, L.; Li, F.; Xiong, H.-m.; Xia, Y.-y. *Chem. Mater.* **2007**, *19*, 2095−2101.
(8) Cheng, F.; Su, Y.; Liang, J.; Tao, Z.; Chen, J. *Chem. Mater.* **2010**, *22*, 898−905.
(9) Zhou, W.; Ge, L.; Chen, Z.-G.; Liang, F.; Xu, H.-Y.; Motuzas, J.; Julbe, A.; Zhu, Z. *Chem. Mater.* **2011**, *23*, 4193−4198.
(10) Sidik, R. A.; Anderson, A. B.; Subramanian, N. P.; Kumaraguru, S. P.; Popov, B. N. *J. Phys. Chem. B* **2006**, *110*, 1787−1793.
(11) Fellinger, T. P.; Hasche, F.; Strasser, P.; Antonietti, M. *J. Am. Chem. Soc.* **2012**, *134*, 4072−4075.
(12) Wiggins-Camacho, J. D.; Stevenson, K. J. *J. Phys. Chem. C* **2011**, *115*, 20002−20010.
(13) Wang, X.; Lee, J. S.; Zhu, Q.; Liu, J.; Wang, Y.; Dai, S. *Chem. Mater.* **2010**, *22*, 2178−2180.
(14) Blizanac, B. B.; Ross, P. N.; Markovic, N. M. *J. Phys. Chem. B* **2006**, *110*, 4735−4741.
(15) Chatenet, M.; Genies-Bultel, L.; Aurousseau, M.; Durand, R.; Andolfatto, F. *J. Appl. Electrochem.* **2002**, *32*, 1131−1140.
(16) Guo, J.; Hsu, A.; Chu, D.; Chen, R. *J. Phys. Chem. C* **2010**, *114*, 4324−4330.
(17) Campbell, F. W.; Belding, S. R.; Baron, R.; Xiao, L.; Compton, R. G. *J. Phys. Chem. C* **2009**, *113*, 9053−9062.
(18) Cui, K.; Song, Y.; Yao, Y.; Huang, Z.; Wang, L. *Electrochem. Commun.* **2008**, *10*, 663−667.
(19) Welch, C. M.; Banks, C. E.; Simm, A. O.; Compton, R. G. *Anal. Bioanal. Chem.* **2005**, *382*, 12−21.
(20) Yu, D.; Yao, J.; Qiu, L.; Wu, Y.; Li, L.; Feng, Y.; Liu, Q.; Li, D.; Wang, H. *RSC Adv.* **2013**, *3*, 11552−11555.
(21) Wang, Y.; Wu, H.; Jiang, X. *Electrochim. Acta* **2013**, *108*, 66−73.
(22) Wang, J.; Zhou, J.; Hu, Y.; Regier, T. *Energy Environ. Sci.* **2013**, *6*, 926−934.
(23) Liang, Y.; Li, Y.; Wang, H.; Zhou, J.; Wang, J.; Regier, T.; Dai, H. *Nat. Mater.* **2011**, *10*, 780−786.
(24) Liang, Y. Y.; Wang, H. L.; Zhou, J. G.; Li, Y. G.; Wang, J.; Regier, T.; Dai, H. J. *J. Am. Chem. Soc.* **2012**, *134*, 3517−3523.
(25) Byon, H. R.; Suntivich, J.; Shao-Horn, Y. *Chem. Mater.* **2011**, *23*, 3421−3428.
(26) Moskovits, M. *J. Raman Spectrosc.* **2005**, *36*, 485−496.
(27) Stiles, P. L.; Dieringer, J. A.; Shah, N. C.; Van Duyne, R. R. *Annu. Rev. Anal. Chem.* **2008**, *1*, 601−626.
(28) Xu, Y. X.; Bai, H.; Lu, G. W.; Li, C.; Shi, G. Q. *J. Am. Chem. Soc.* **2008**, *130*, 5856−5857.
(29) Qu, L. T.; Liu, Y.; Baek, J. B.; Dai, L. M. *ACS Nano* **2010**, *4*, 1321−1326.
(30) Zhou, R. F.; Zheng, Y.; Hulicova-Jurcakova, D.; Qiao, S. Z. *J. Mater. Chem. A* **2013**, *1*, 13179−13185.
(31) Xu, X.; Tan, C.; Liu, H.; Wang, F.; Li, Z.; Liu, J.; Ji, J. *J. Electroanal. Chem.* **2013**, *696*, 9−14.
(32) Maheswari, S.; Sridhar, P.; Pitchumani, S. *Electrocatalysis* **2012**, *3*, 13−21.
(33) Tammeveski, L.; Erikson, H.; Sarapuu, A.; Kozlova, J.; Ritslaid, P.; Sammelselg, V.; Tammeveski, K. *Electrochem. Commun.* **2012**, *20*, 15−18.
(34) Lee, C.-L.; Tsai, Y.-L.; Huang, C.-H.; Huang, K.-L. *Electrochem. Commun.* **2013**, *29*, 37−40.
(35) Muniz-Miranda, M.; Cardini, G.; Schettino, V. *Theor. Chem. Acc.* **2004**, *111*, 264−269.
(36) Zhang, L.; Xia, Z. *J. Phys. Chem. C* **2011**, *115*, 11170−11176.
(37) Wu, D. Y.; Li, J. F.; Ren, B.; Tian, Z. Q. *Chem. Soc. Rev.* **2008**, *37*, 1025−1041.
(38) Fleischm, M.; Hendra, P. J.; McQuilla, A. J. *Chem. Phys. Lett.* **1974**, *26*, 163−166.
(39) Singh, D. K.; Srivastava, S. K.; Ojha, A. K.; Asthana, B. P. *Spectrochim. Acta, Part A* **2008**, *71*, 823−829.
(40) Singh, D. K.; Asthana, B. P.; Srivastava, S. K. *J. Mol. Model.* **2012**, *18*, 3541−3552.
(41) Creighton, J. A.; Albrecht, M. G.; Hester, R. E.; Matthew, J. A. D. *Chem. Phys. Lett.* **1978**, *55*, 55−58.

(42) Creighton, J. A.; Blatchford, C. G.; Albrecht, M. G. *J. Chem. Soc., Faraday Trans. II* **1979**, *75*, 790−798.

dx.doi.org/10.1021/cm502260m | *Chem. Mater.* 2014, 26, 5868−5873

Supporting Information

Silver/Nitrogen-Doped Graphene Interaction and its Effect on Electrocatalytic Oxygen Reduction

Ruifeng Zhou[†,‡] and Shi Zhang Qiao[†,*]

†School of Chemical Engineering, the University of Adelaide, Adelaide, SA 5005, Australia.

‡Australian Institute for Bioengineering and Nanotechnology, the University of Queensland, St Lucia, QLD 4072, Australia.

Synthesis of GO:

The synthesis of GO is similar to the cited reference in main text but with harsher oxidation condition.

1. Graphite flake (3 g) was put into concentrated H_2SO_4 (12 ml), $K_2S_2O_8$ (2.5 g), and P_2O_5 (2.5 g).
2. The mixture was kept at 90 °C for 6 h, then cooled to room temperature and diluted with 0.5 L of DI water.
3. The mixture was filtered and washed with DI water. The product was dried in vacuum at 50 °C overnight.
4. The pretreated graphite was put into cold (0 °C) concentrated H_2SO_4 (120 mL). Then, $KMnO_4$ (15 g) was added gradually under stirring and the temperature of the mixture was kept to be below 20 °C by ice cooling.
5. The mixture was stirred at 40 °C for 3 h, and then diluted with DI water (250 mL) using ice bath cooling.
6. The mixture was then stirred for 2 h, and then additional 0.7 L of DI water was added.
7. 20 mL of 30% H_2O_2 was added to the mixture.
8. The mixture was washed with 1:10 HCl aqueous solution (1 L). The resulting graphite oxide was diluted to in DI water.
9. Exfoliation was carried out by sonicating graphite oxide dispersion under ambient condition for 30 min, followed with centrifuging at 3000 rpm for 30 min to eliminate unexfoliated graphite.

Preparing of samples for Characterization after ORR:

All the catalysts characterized after ORR are synthesized without Nafion to avoid its interference.

For Raman spectroscopy of catalyst after ORR, the catalyst was characterized directly on the electrode.

For TEM of catalyst after ORR, the catalyst was scratched off the electrode, dispersed in ethanol by supersonication and dipped on to the TEM grid for characterization.

For XRD and XPS of catalyst after ORR, the synthesis was NOT on the RRDE because much more sample is needed. The preparation starts from 0.2 % suspension of Ag_2O/GO, Ag_2O/c-rGO or Ag_2O/c-rGO. 20 ml of the suspension was dried in a round-bottom flask by a rotary evaporator. The dried flakes of samples were scratched off, collected, sandwiched between two pieces of nickel foam and clipped by a stainless steel tweezers. Then the sandwich was immersed in the electrolyte and the tweezers was connected to the working electrode's lead of the electrochemical workstation. Other electrochemical setups are the same as described in the manuscript. CV was applied to the working electrode between 1.2 V and -0.2 V at 100 mV s^{-1} until steady CV curve was reached. Finally, the catalyst flakes were collected and washed with DI water and dried in vacuum oven at room temperature for further characterization.

Calculation of electron transfer number and peroxide ratio

The peroxide ratio (p) can be calculated from the disk current (I_d) and ring current (I_r) of the RRDE.

$$p = 200\% \times \frac{\frac{I_r}{N}}{I_d + \frac{I_r}{N}}$$

Where N=0.37 is the collection efficiency of our RRDE. At the same time, electron transfer number (n) can be calculated by:

$$n = 4 \times \frac{I_d}{I_d + \frac{I_r}{N}}$$

The n can also be calculated by the Koutecky-Levich equation.

$$\frac{1}{J} = \frac{1}{J_L} + \frac{1}{J_K}$$

Where J is the measured current density (IR compensated). J_K is the kinetic-limiting current density. J_L is the mass-transferring-limiting current density.

$$J_L = 0.62nFC_0(D_0)^{2/3}\nu^{-1/6}\omega^{1/2}$$

Where n is the electron transfer number, F = 96485 C mol^{-1} is the Faraday constant, C_0 = 1.26 mol m^{-3} is the saturated concentration of O_2 under ambient condition, $D_0 = 1.97 \times 10^{-9}$ m^2 s^{-1} is the diffusion coefficient of O_2 in water, $\nu = 1.004 \times 10^{-6}$ m^2 s^{-1} is the kinematic viscosity of water, and ω is the angular velocity (in radian per second) of the electrode.

Prices estimation of the Ag/N-rGO:

The price of each chemical used in synthesis of GO is listed below. The prices are based on Sigma-Aldrich's prices in Australia. The currency unit is Australian dollar (AUD). AUD 1 is about 0.93 USD.*

Table S1. Price estimation of Ag/N-rGO.

Chemical	*Package price*	*Dosage*	*Dosage price(AUD)*
Graphite flakes	AUD 94 / 2.5 kg	3 g	0.11
H_2SO_4	AUD 128 / 2.5 L	132 ml	6.76
$K_2S_2O_8$	AUD 56 / 500 g	2.5 g	0.28
P_2O_5	AUD 73.5 / 500 g	2.5 g	0.37
$KMnO_4$	AUD 92 / 500 g	15 g	2.76
30% H_2O_2	AUD 65 / 500 ml	20 ml	2.6
HCl	AUD 91 / 2.5 L	100 ml	3.64
Total			16.52

The yield of GO from graphite is about 100 %, so the price of GO is about AUD 5.5 g^{-1}.

The price of each chemical used in synthesis of N-rGO is listed below.

Chemical	*Package price*	*Dosage*	*Dosage price(AUD)*
GO	AUD 5.5 / g	0.065 g	0.36
30 % NH_3	AUD 96.5 / 2.5 L	5 ml	0.19
Total			0.55

The yield of N-rGO from graphite is about 50 %, so the price of GO is about AUD 17 g^{-1}.

The price of each chemical used in synthesis of Ag/N-rGO is listed below.

Chemical	*Package price*	*Dosage*	*Dosage price(AUD)*
N-rGO	AUD 17 / g	0.0002 g	0.0034
$AgNO_3$	AUD 388 / 100 g	0.00017 g	0.00066
Total (without Nafion)			0.00406

The mass of final product is 0.000308 g. Therefore, the price per unit mass is about AUD 13.2 g^{-1} (about USD12.3 g^{-1}).

The price of 20% Pt/C in our experiment is USD 79 g^{-1} (6 times of Ag/N-rGO).

The higher price of Ag/N-rGO is caused by:

1. Excessive high price of chemicals purchased from Sigma-Aldrich. Industrial raw materials will be much cheaper.
2. Excessive usage of oxidants, acids, hydrogen peroxide and ammonia in lab synthesis. In industrial manufacturing, the recipe can be optimized and most of the reagents can be recycled to largely reduce the cost.

*Prices and exchange rate are of based on the time when this paper is written.

Kinetics comparison:

Table S2. Tafel slopes of ORR on Ag, C and Ag/C catalysts.

Catalyst	*Condition*	*Tafel slope (mV decade^{-1})**	*Reference*
80 wt.% Ag/C	1 M NaOH 80 °C	66/124	31
30 wt.% Ag/C		62/118	
40 wt.% Ag/C	1 M KOH 25°C	82	32
60 wt.% Ag/C		78	
80 wt.% Ag/C		82	
Ag/ multiwall carbon nanotube	0.1 M KOH	80	33
Ag bulk	1 M NaOH 25 °C	74	15
	1 M NaOH 80 °C	77	
10% Ag/C	1 M NaOH 10 °C	79	
	0.1 M NaOH 25 °C	84	
	0.5 M NaOH 25 °C	70	
	1 M NaOH 25 °C	78	
	1 M NaOH 40 °C	71	
	1 M NaOH 80 °C	65	
Ag (111)	0.1 M KOH 20 °C	93	14
	0.1 M KOH 40 °C	101	
	0.1 M KOH 60 °C	106	
Ag (100)	0.1 M KOH 20 °C	98	
	0.1 M KOH 40 °C	112	
	0.1 M KOH 60 °C	123	
Ag (110)	0.1 M KOH 20 °C	91	
	0.1 M KOH 40 °C	106	
	0.1 M KOH 60 °C	114	
Ag nanocube	0.1 M KOH	60/120	34
Ag polycrystalline	0.1 M KOH 25 °C	110	This
e-rGO		96/190	paper
Ag/e-rGO		96/190	
c-rGO		80	
Ag/c-rGO		77	
N-rGO		55	
Ag/N-rGO		43	

*If two Tafel slopes are provided, the former is at low overpotential, the latter is at high overpotential.

Supporting Figures:

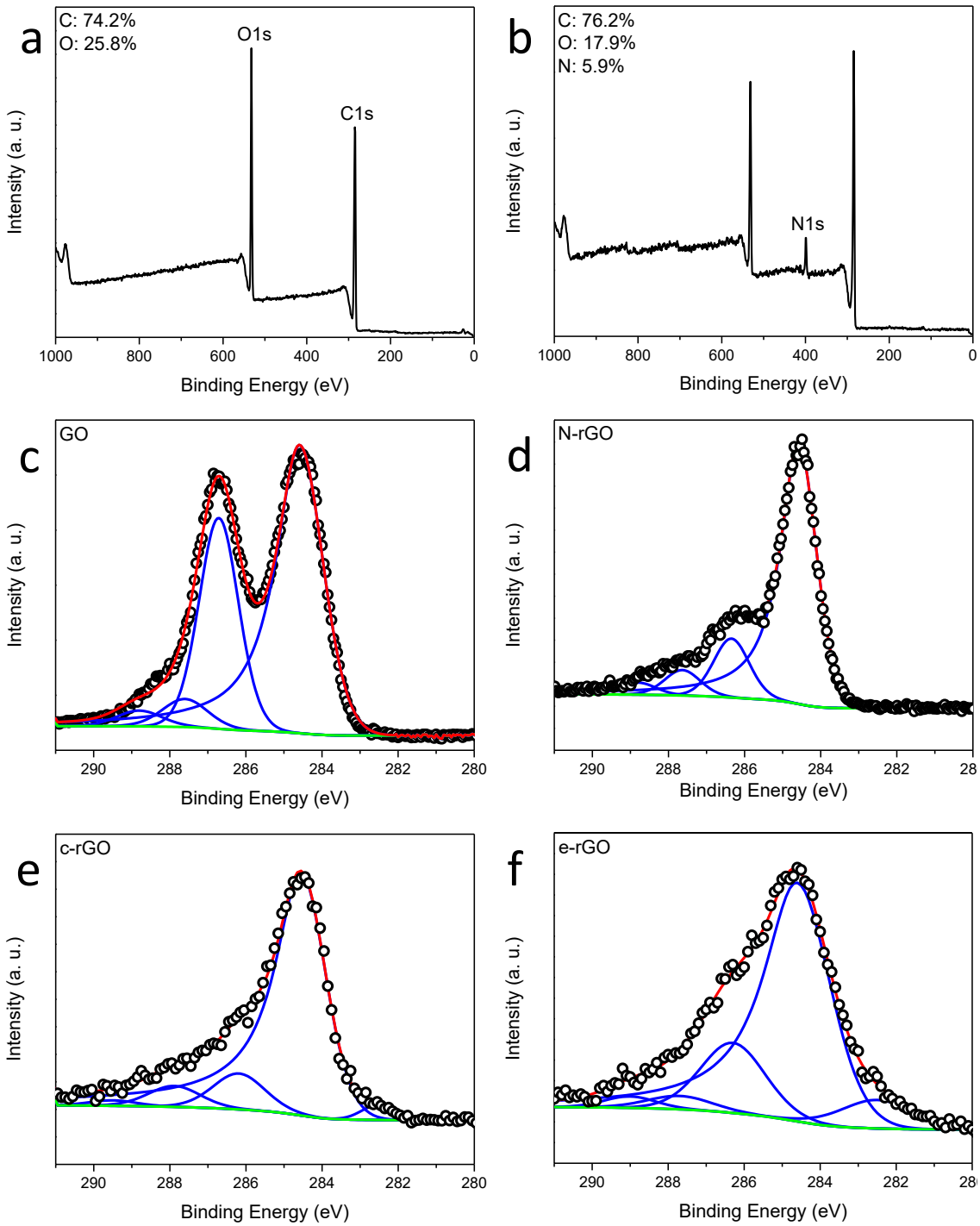

Figure S1 XPS survey of GO (a) and N-rGO (b). High-resolution XPS of C1s of GO (c), N-rGO (d), c-rGO (e) and e-rGO (f). The peaks centred at 284.6 eV, 286.7 eV, 287.6 eV and 288.8 eV are attributed to carbon in C-C, C-OH, C=O and O-C=O structures respectively.

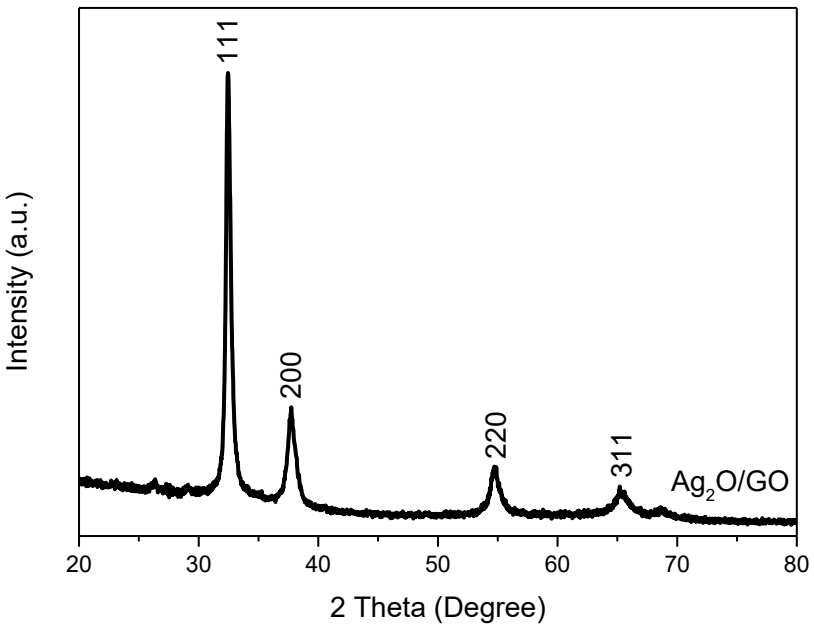

Fig S2. XRD of the Ag_2O/GO. All peaks are attributed to Ag_2O.

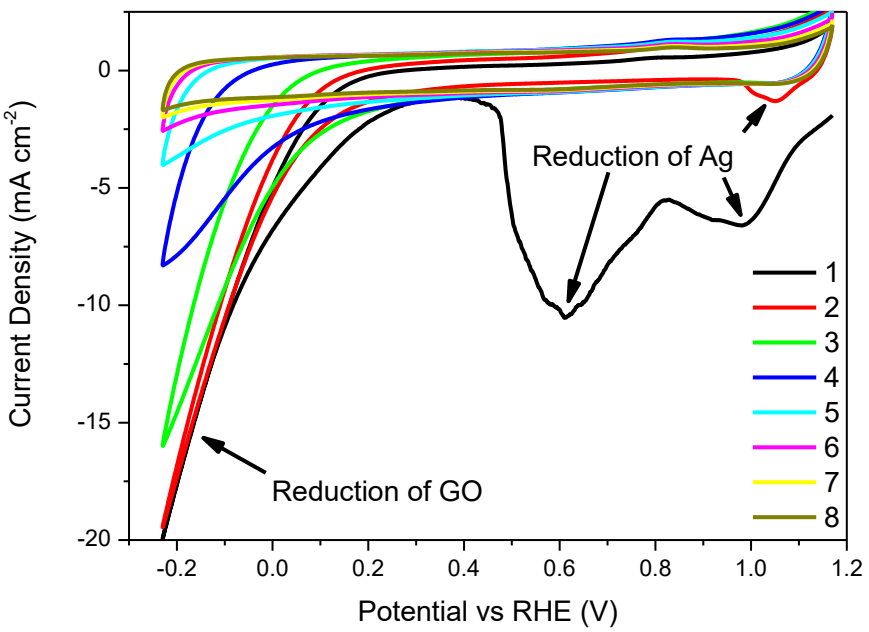

Fig S3. The first 8 cycles of CV of Ag_2O/GO. The scan rate is 100 mv s^{-1}.

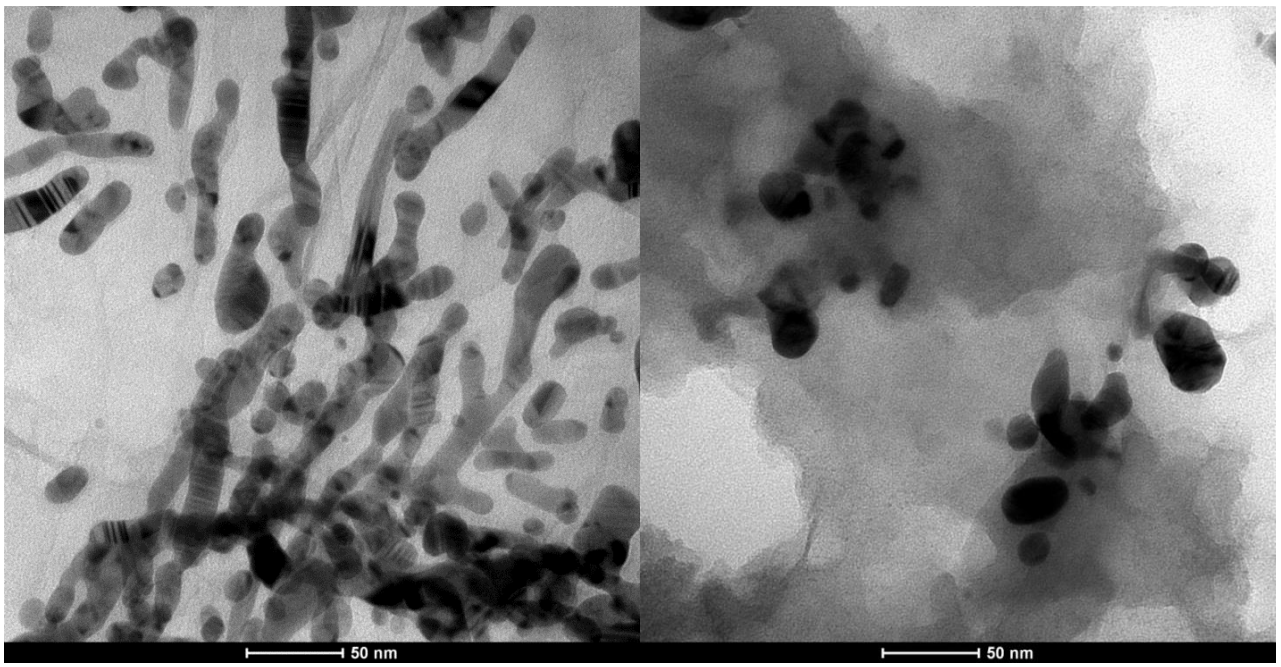

Figure S4 TEM image of Ag/e-rGO (left) and Ag/c-rGO (right).

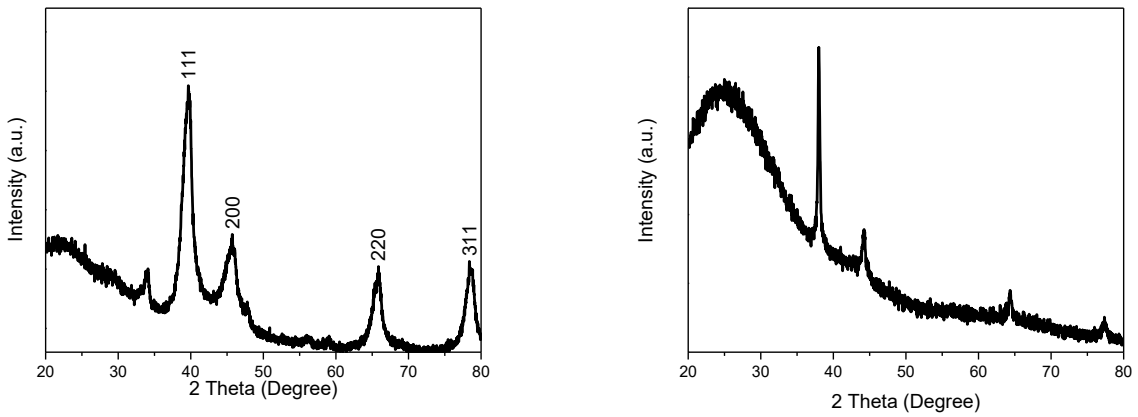

Figure S5 XRD patterns of Ag/e-rGO (left) and Ag/c-rGO (right).

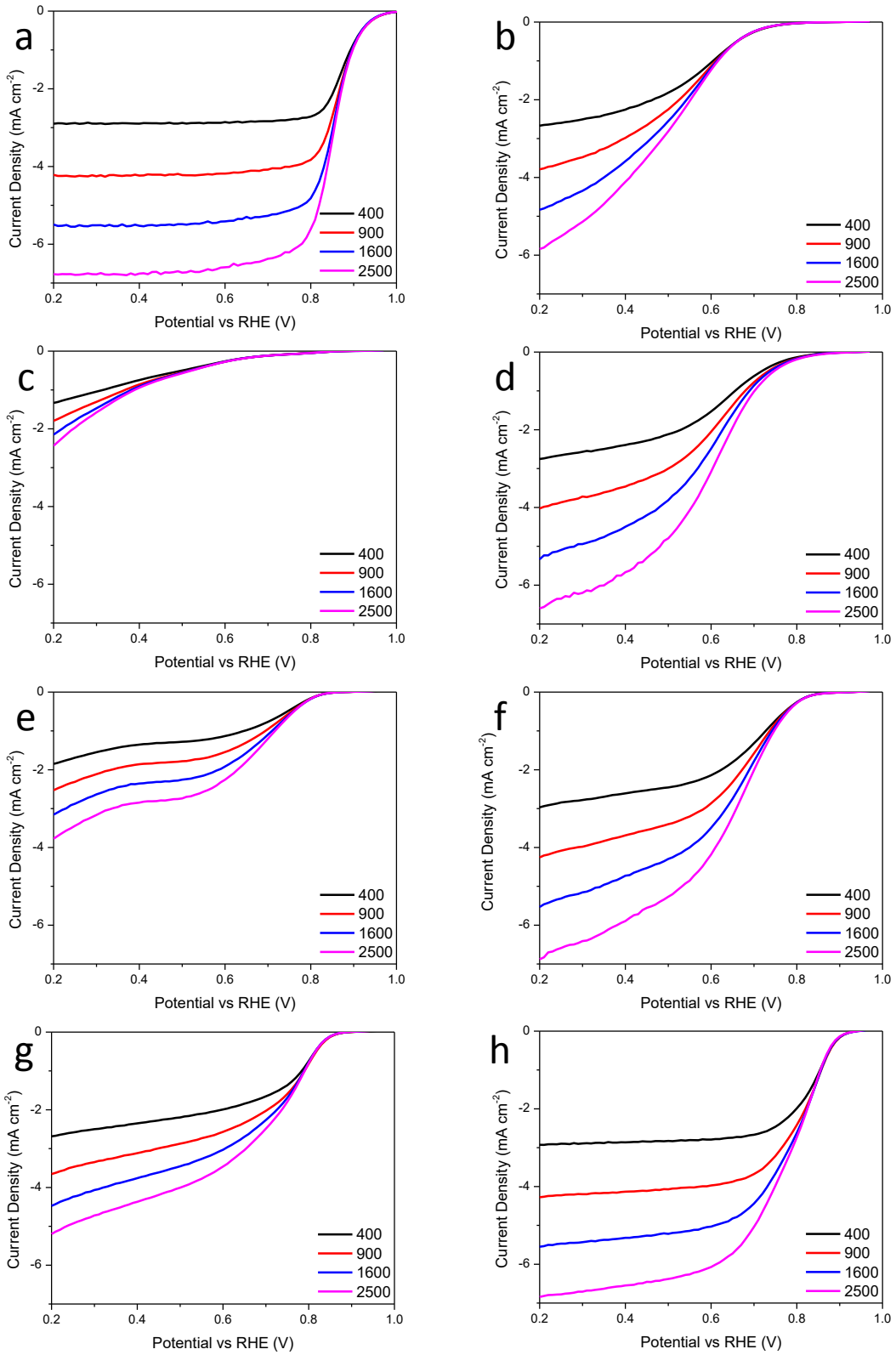

Figure S6. LSV of Pt/C (a), Ag (b), e-rGO (c), Ag/e-rGO (d), c-rGO (e), Ag/c-rGO (f), N-rGO (g) and Ag/N-rGO (h). The scan rate is 5 mV s^{-1} and IR compensated (50 Ω). The legend numbers are angular velocities (rpm).

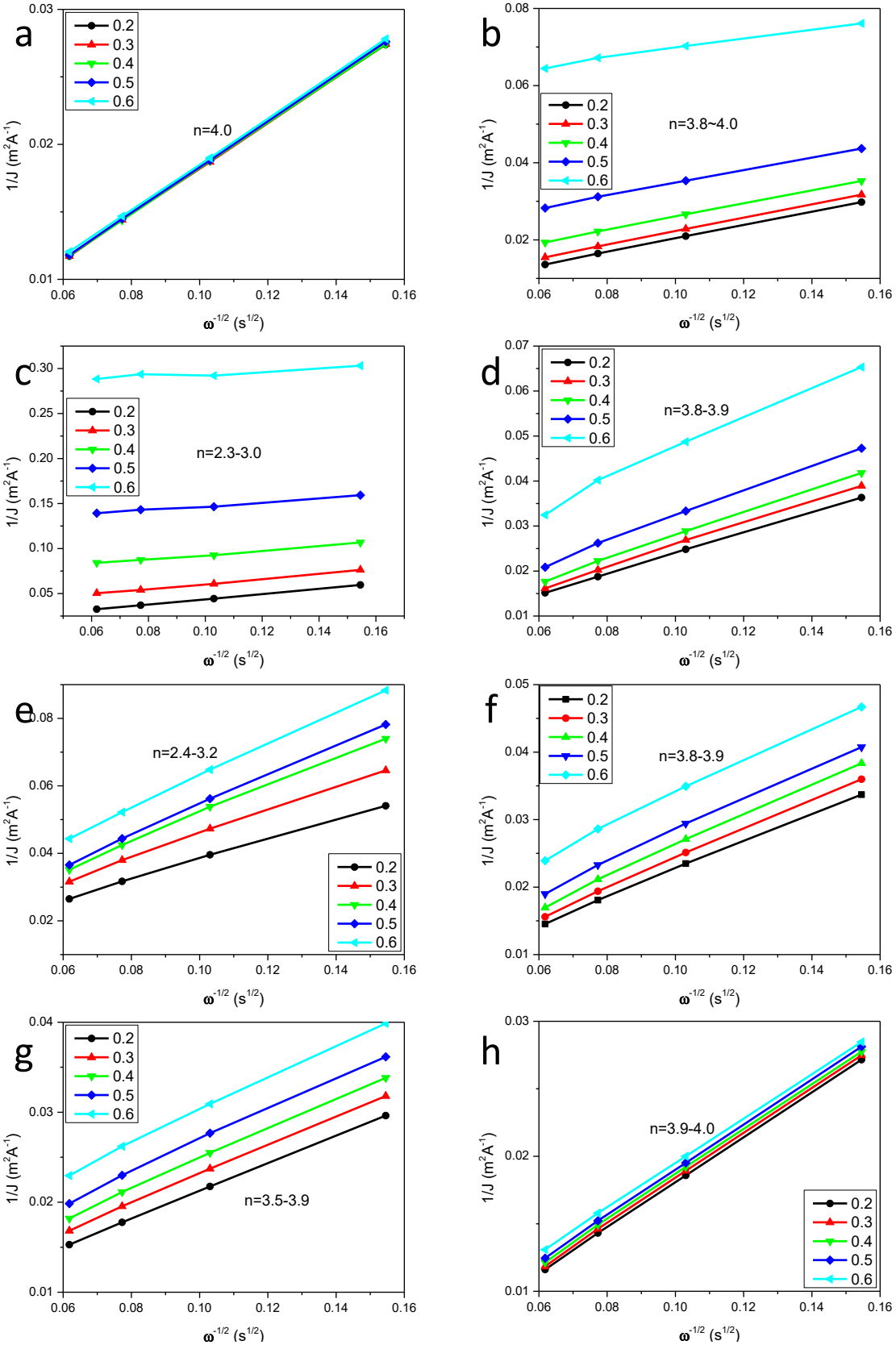

Figure S7. KL plot of Pt/C (a), Ag (b), e-rGO (c), Ag/e-rGO (d), c-rGO (e), Ag/c-rGO (f), N-rGO (g) and Ag/N-rGO (h). The legend numbers are potentials (V).

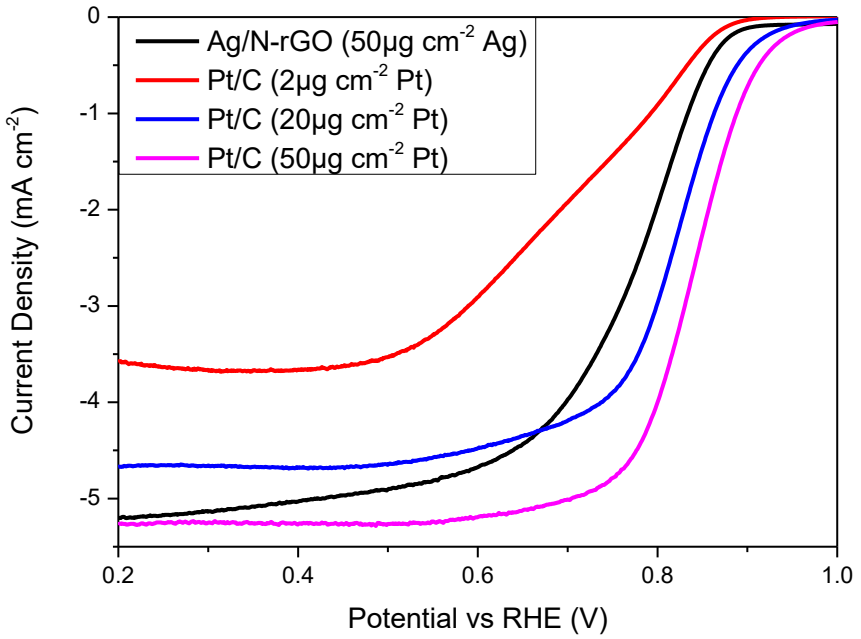

Figure S8 LSV of Ag/N-rGO and Pt/C at 1600 rpm at different catalyst loadings.

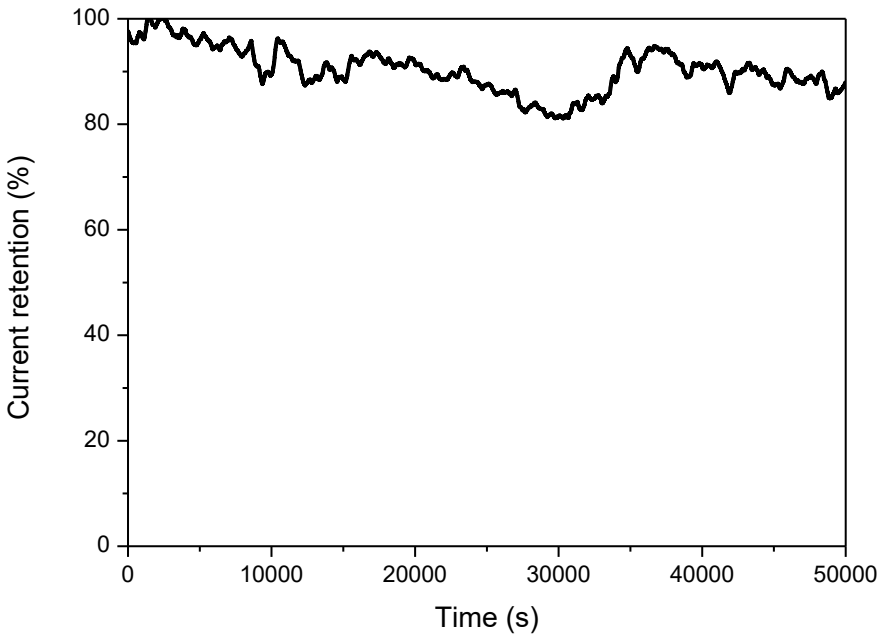

Figure S9. Stability test of Ag/N-rGO. The potential is fixed at 0.8 V.

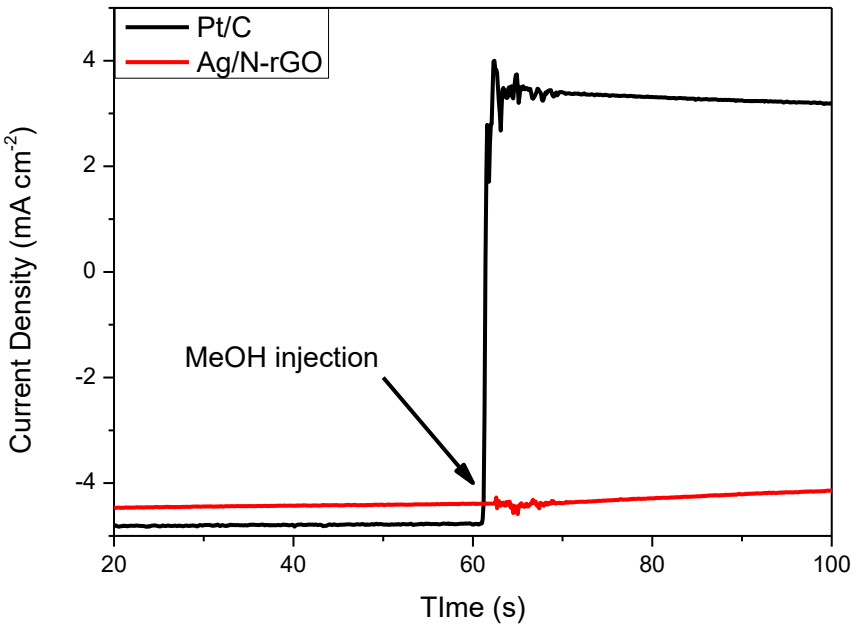

Figure S10 Amperometric curve of Pt/C and Ag/N-rGO at 0.7 V and 1600 rpm in O_2 saturated 0.1 M KOH. Methanol is injected into the electrolyte at the 60th second to reach a concentration of 3 M.

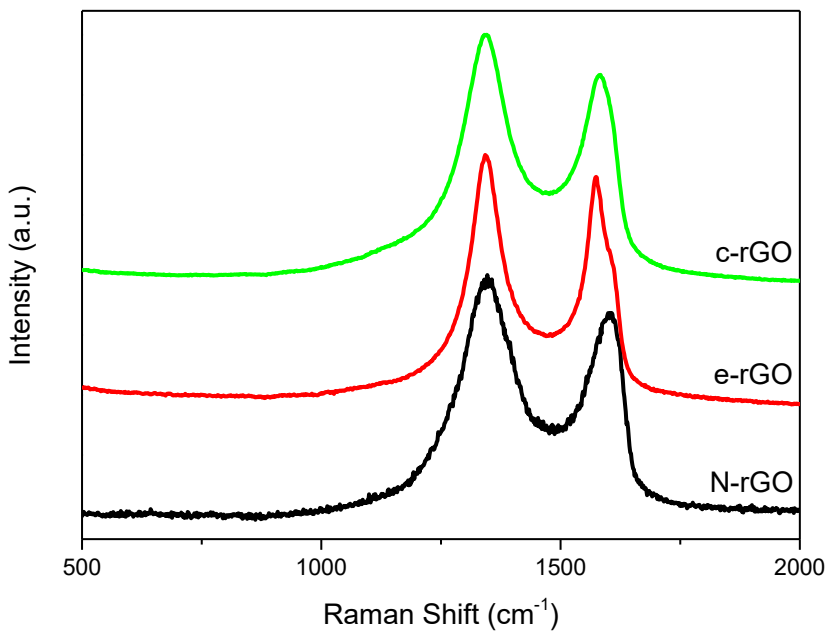

Figure S11 Raman spectra of N-rGO, e-rGO and c-rGO under identical measurement condition. The data are normalized to identical G band intensity.

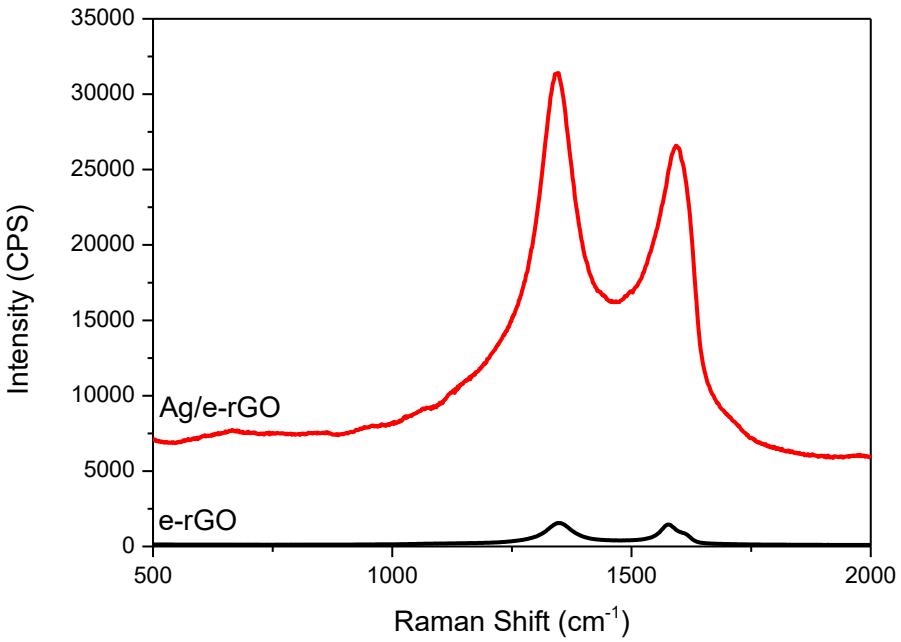

Figure S12 Raman spectra of e-rGO and Ag/e-rGO under identical measurement condition. The data are plotted without any treatment.

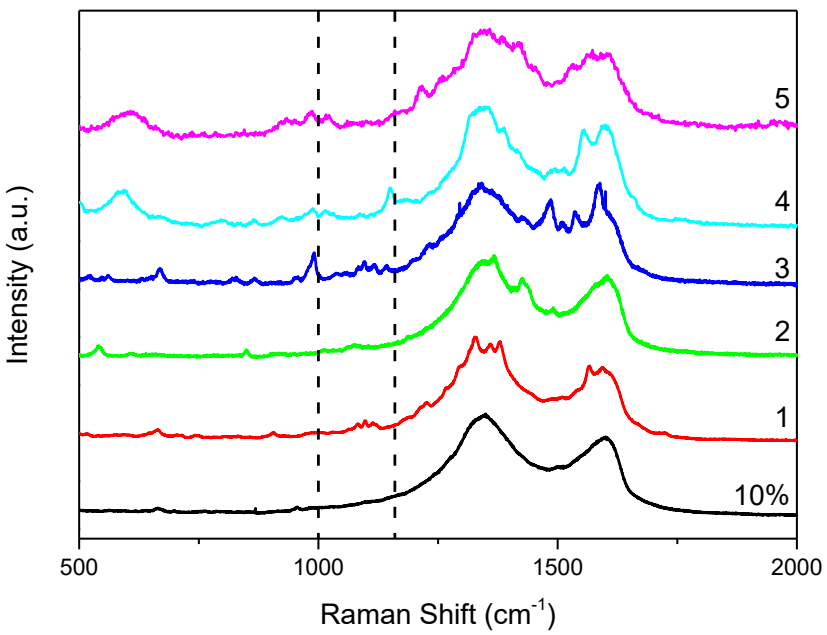

Figure S13 Raman spectra of Ag/N-rGO. Curves 1 to 5 are measured at different locations of the same sample under 1% of full power. The bottom curve is measured under 10% intensity. The dash lines are at 1000 cm^{-1} and 1160 cm^{-1}.

Chapter 5: Fe/N co-doped Graphitic Carbon Bulb for High-Performance Oxygen Reduction Reaction

Introduction

In this chapter, a new route to synthesize TM-NC is tried. It is found that in previous study that Fe-NC interaction cannot be formed at room temperature, so the furnace process was tried and a new precursor, Prussian blue, was used. It is found that the relative low 550 °C pyrolysis temperature is enough to from graphitic and retain high level of N. Higher temperature lead to lower yield and loss of N. The Fe/N-gCB performances as good as Pt/C in alkaline electrolyte and pretty good in acid electrolyte. The Fe/N-gCB is the best among my own catalysts.

This chapter was published in *Chem. Comm.* **2015**, 51, 7561.

ChemComm

COMMUNICATION

View Article Online
View Journal | View Issue

Cite this: *Chem. Commun.*, 2015, **51**, 7516

Received 3rd February 2015,
Accepted 23rd March 2015

DOI: 10.1039/c5cc00995b

www.rsc.org/chemcomm

An Fe/N co-doped graphitic carbon bulb for high-performance oxygen reduction reaction†

Ruifeng Zhou[ab] and Shi Zhang Qiao*[a]

An Fe/N co-doped graphitic carbon bulb is synthesized by Prussian blue with a pyrolysis temperature as low as 550 °C. Fe facilitates the formation of a graphitic structure, while low temperature guarantees high level of nitrogen. The product shows excellent oxygen reduction reaction catalytic activity in both alkaline and acid electrolytes.

To reduce catalyst cost of aqueous fuel cells is the key to their commercialization. Pt based catalysts have the best activity in the most critical reactions such as oxygen reduction reaction (ORR), but their costs are too high. Therefore, a lot of efforts have been exerted to develop the alternative and inexpensive catalysts.[1] Among them, the N doped carbons[2] and their non-precious metal composites[3] are the most popular catalysts owing to their abundant source and decent performance. The metal–nitrogen–carbon systems show better performance than N doped carbons due to the metal–nitrogen synergistic effect. For example, the Fe–N doped carbon systems have shown excellent ORR performance in both alkaline and acid electrolytes.[4]

The N doped carbons are usually synthesized by pyrolyzing the carbon and nitrogen containing precursors together. The selection of appropriate precursors and ideal pyrolysis temperature is still challenging to obtain high nitrogen content, large surface area and highly graphitic carbon with exceptionally high performance. Since N doped carbons naturally have worse activity per electrochemical active area than Pt,[5] they are usually made into a porous structure with very high surface area and defect density.[6] However, the structural defects destroy the conductivity of carbon, which is essential to electrocatalysis. Thus, some studies focus on N doped carbons with graphitic structure, *e.g.* graphene and carbon nanotubes, which have higher conductivity and superior catalytic performance compared with the amorphous N doped carbons.[2] To reach acceptable graphitization, very high temperature is usually inevitable for carbon pyrolysis. Though the pyrolysis of carbon is almost completed at 500 °C, the resultant carbons do not undergo acceptable graphitization and conductivity until 900 °C.[4a,7] Besides graphitization, high temperature is theoretically necessary to form a proper Fe–N structure for the optimized ORR dynamics.[8] Fe–N–C material synthesized at low temperature does not show very good performance.[9] However, the high temperature synthesis also has severe drawbacks. For example, high temperature results in the loss of doped nitrogen, which are essential to ORR. High temperature synthesis is also another origin of high cost of the final product. Thus the preparation of N-doped carbons and their non-precious metal composites (such as Fe/N co-doped carbon) with high nitrogen content, large surface area and excellent graphitization structure (high conductivity) at low temperature is extremely desirable for electrocatalytic studies; however, it has been rarely reported to date. To achieve the above aims, the selection of a precursor may be critical.

In this communication, an Fe/N co-doped graphitic carbon bulb (Fe/N-gCB) is synthesized by using cheap and self-made Prussian blue (PB) as the only precursor. The pyrolysis temperature of PB can be as low as 550 °C. The Fe/N-gCB is produced by etching the iron core of core–shell pyrolyzed PB (PPB). The electron microscopy and spectroscopy techniques show that the Fe/N-gCB is highly graphitized and retains high level of N and Fe. N_2 sorption analysis reveals that the new material has a high specific surface area. The Fe/N-gCB shows excellent ORR performance, comparable to that of Pt/C in an alkaline electrolyte, and fairly good ORR performance in acid electrolyte, which by far outperforms the metal-free catalysts. We proved that the commonly used high temperature is not necessary for the synthesis of good ORR catalysts, if appropriate precursors are used. Higher temperature even reduces the activity of the catalyst because of the loss of nitrogen.

The details of the synthesis of a Fe/N-gCB and all reference materials are provided in the ESI.† The characterization of the reference materials can be found in our previous papers.[10] The transmission electron microscopy (TEM) image of the PB is shown in Fig. S1 (ESI†). X-ray diffraction (XRD) pattern (Fig. S2, ESI†) of the PB shows that it is partially crystallized.

[a] *School of Chemical Engineering, University of Adelaide, Adelaide SA 5005, Australia. E-mail: s.qiao@adelaide.edu.au*
[b] *Australian Institute for Bioengineering and Nanotechnology, University of Queensland, St Lucia QLD 4072, Australia*

† Electronic supplementary information (ESI) available: Synthesis of material, supporting figures. See DOI: 10.1039/c5cc00995b

Pyrolysis of PB is monitored by thermogravimetric analysis (TGA) and the result is shown in Fig. S3 (ESI†). The last rapid pyrolysis step of PB starts at about 500 °C. Above 600 °C, the PPB loses weight continuously and slowly. Some more PPB molecules are synthesized at 600 °C, 700 °C, 800 °C and 900 °C, which are denoted as PPB-600, PPB-700, PPB-800 and PPB-900, respectively. The catalyst yield after acid leach drops dramatically as the synthesis temperature increases. Nothing is left after acid leach of PPB-900. Obviously, the high temperature leads to loss of carbon. The carbon can be oxidized by trace amounts of oxygen in the atmosphere, or react with iron to form Fe_3C (Fig. S4, ESI†). Both reactions are thermodynamically favourable at any temperature, but are accelerated at higher temperature. Thus, 550 °C is an optimized temperature for both complete pyrolysis and high yield.

The TEM images of the PPB are shown in Fig. 1a and b, which exhibit a spherical core–shell shape with an outer diameter from 50 to 100 nm (70 nm on average) and shell thickness from 4 to 12 nm (6 nm on average). The morphology of PPB is very similar to those made from large and crystallized cubic PB.[11] This proves that the formation of core–shell structured PPB is attributed to the migration and rearrangement of atoms during pyrolysis, but not related to the morphology of the PB precursor. The Fourier transformation of the some cores (inset of Fig. 1b) shows a regular hexagonal pattern with a spatial frequency of 5 nm^{-1}, which is in accordance with the (110) index of metallic Fe. After washing with HCl, the Fe core is etched (Fig. 1c). The high resolution TEM image (Fig. 1d) shows that the shell has several layers with each single-layer thickness being 0.34 nm, which is typical to graphitic carbon. The growth of graphitic carbon with Fe as a catalyst has been widely reported for carbon nanotube growth,[12] in which the growth temperature can be as low as 500 to 600 °C.[13] When PB is used as a precursor, the C source is very limited so that growth of graphene layers ceases after shell formation. The TEM analysis also shows that there are some dark dots after HCl etching, which are the Fe particles embedded in a carbon shell and unexposed to HCl. The XRD patterns of the

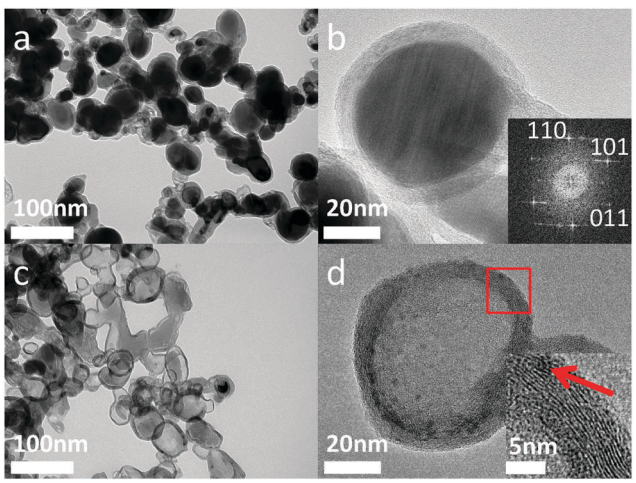

Fig. 1 (a) and (b) TEM images of PPB. Inset: Fourier transformation of the core. (c) and (d) TEM images of a Fe/N-gCB. Inset: the enlarged part in the red frame. The arrow points to an iron dot.

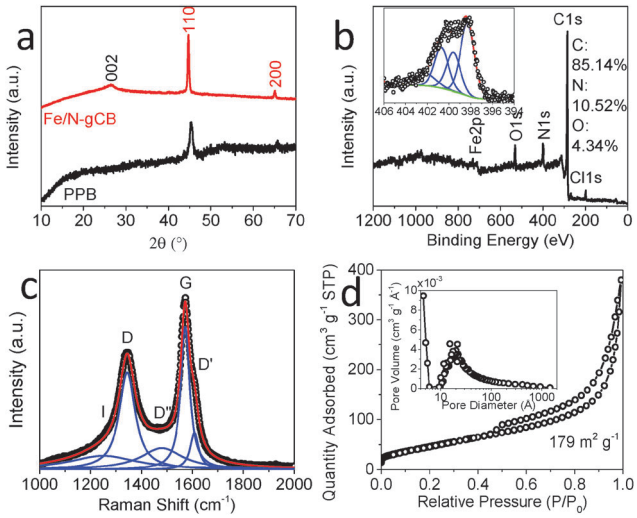

Fig. 2 (a) XRD of PPB and a Fe/N-gCB. The black index is assigned to graphitic carbon and red indexes are assigned to metallic Fe. (b) XPS survey of the Fe/N-gCB. Inset: high resolution XPS of N1s of Fe/N-gCB. (c) Raman spectrum of the Fe/N-gCB. (d) N_2 isothermal sorption of Fe/N-gCB. Inset: corresponding pore distribution.

PPB and Fe/N-gCB are shown in Fig. 2a. Both patterns have significant (110) and (200) peaks from metallic Fe. The XRD pattern of the Fe/N-gCB also shows a peak at 26°, which is attributed to the (002) plane of the graphitic carbon. This peak is not observed in PPB due to very high level of background contributed by amorphous cores (Fig. S5, ESI†).

There are a few key findings from the X-ray photoelectron spectroscopy (XPS) survey of the Fe/N-gCB and high-resolution XPS of N1s (Fig. 2b). First, the nitrogen content in the Fe/N-gCB is surprisingly high (>10%). As far as we know, the nitrogen content in N doped carbon is usually lower than 7%. The high nitrogen content must thank the very high N content in the PB precursor and very low temperature of pyrolysis. The XPS spectra of acid leached PPB-600, PPB-700 and PPB-800 are also recorded (Fig. S6–S8, ESI†). The N content drops from 6.9% of PPB-600 to 1% of PPB-700 and 0% in PPB-800. Second, Fe can be identified from the survey. The calculated atom percentage of Fe from the XPS curve fitting is below 1%, but the actual Fe content is 4% (atom ratio) determined by TGA (Fig. S9, ESI†). The Fe signal is so weak in XPS because it is embedded in carbon layers which screen the XPS signal. Third, the pyridinic N is especially high. A few theoretical and experimental studies have shown that the pyridinic N[14] and Fe in the porphyrin structure[8b,15] have especially high ORR activity.

The Raman spectrum of the Fe/N-gCB is shown in Fig. 2c while the Raman spectra of N-MCN and N-rGO are shown in Fig. S10 and S11 (ESI†) for comparison. For each Raman spectrum, the pattern can be deconvoluted with 5 bands, which are attributed to impurity (I), in-plane defect (D and D′), interstitial defects (D″) and graphitic structure (G).[16] The degree of graphitization can be estimated from the ratio of G and D bands, and the width of peaks. Obviously, the Fe/N-gCB has a higher degree of graphitization than N-rGO, which inherits the graphitic structure from its precursor but suffers from oxidation during its synthesis. As for the N-MCN, although it is

carbonized at 900 °C, it is still amorphous. All these spectroscopic results reveal that Fe is critical to graphitization. In PB, the Fe content is so high and homogeneously distributed that an ideal graphitic structure can form at the low temperature (550 °C).

The N_2 sorption isotherm of the Fe/N-gCB is shown in Fig. 2d. The material shows a specific surface area (SSA) of 179 m^2 g^{-1}, which is higher than the N-rGO (142 m^2 g^{-1}).[3b] Although single-layer graphene has a very high theoretical SSA (2630 m^2 g^{-1}), it may restack easily during the reducing and drying process, causing a decrease of SSA. In contrast, the Fe/N-gCB has a spherical structure which has an exposed surface and interconnected space even after piling up. Considering that Fe contributes to 15% of the weight, whose surface is negligible, the SSA of carbon is about 210 m^2 g^{-1}. The SSA value of the Fe/N-gCB corresponds to 12.5 graphitic layers (4.25 nm), which is lower than our TEM observation. This suggests that not only the inner and outer surfaces of the bulb are accessible but the shell also has pores.

To investigate the ORR performance of the Fe/N-gCB, the linear scanning voltammetry (LSV) measured on a rotating ring-disk electrode (RRDE) is shown in Fig. 3. Commercial Pt/C is also used as a catalyst for comparison. In alkaline electrolyte (Fig. 3a), the ORR onset potential of the Fe/N-gCB is slightly higher than that of Pt/C and their limiting currents are almost the same. The peroxide production of the Fe/N-gCB is extremely low (<6%), which is only slightly higher than that of Pt/C (Fig. 3c). The metal-free N doped carbons usually produce much more peroxide (up to 20%), so the ORR on the Fe/N-gCB is quite different from N doped carbons.[3b,10b] In the acid electrolyte (Fig. 3b), the performance of the Fe/N-gCB is to some extent lower than that of Pt but not too far behind it. The peroxide ratio of the Fe/N-gCB is also very low (<4%, Fig. 3d). Low peroxide production means that the catalyst has high ability in peroxide activation, which can also be used in other applications such as peroxide detection in environmental sensors and peroxide reduction in peroxide based fuel cells. According to Gasteiger's benchmark, the volumic current of a non-Pt catalyst should be at

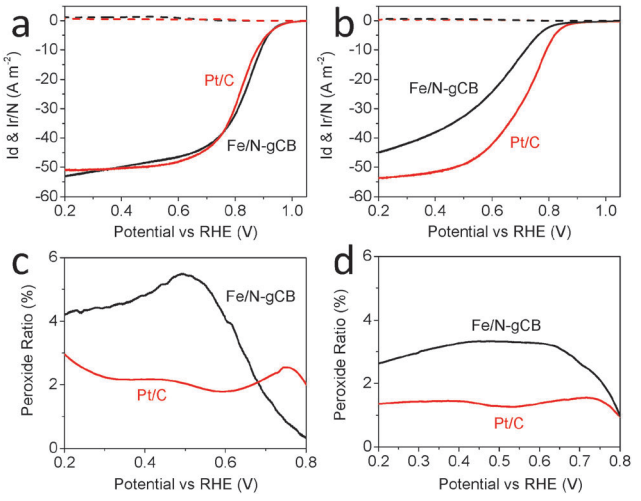

Fig. 3 Normalized disk (I_d) and ring (I_r) current at 1600 rpm in alkaline (a) and acid (b) electrolytes. Both currents are normalized by the area of the disk. Their corresponding peroxide ratios in alkaline (c) and acid (d) electrolytes. The potential *versus* reversible hydrogen electrode (RHE).

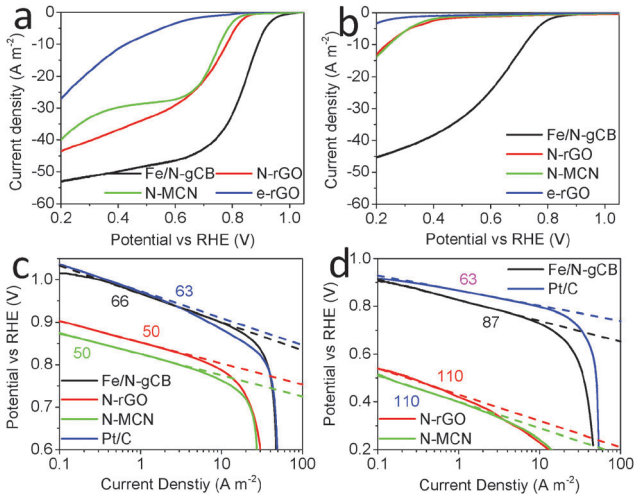

Fig. 4 Normalized disk current at 1600 rpm in alkaline (a) and acid (b) electrolytes. The corresponding Tafel plots in alkaline (c) and acid (d) electrolytes. The numbers are Tafel slopes in mV per decade.

least 1/10 of the Pt/C for economic viability in fuel cell applications.[17] In the acid electrolyte, the current density of the Fe/N-gCB at 0.8 V is about 1/4 of Pt/C. Assuming that the density of the Fe/N-gCB is 1/2 of the Pt/C, the volumic current density of the Fe/N-gCB is 1/8 of Pt/C, which is above the benchmark. As the potential decreases, the volumic current ratio between the Fe/N-gCb and Pt/C increases further.

We compared the ORR performance of the Fe/N-gCB with electrochemically reduced graphene oxide (e-rGO), and two typical N doped carbons, N-MCN and N-rGO (Fig. 4a), whose performance has been reported before.[10] N-MCN and N-rGO have much better performance than e-rGO due to nitrogen doping. However, they are much poorer than the Fe/N-gCB due to lack of Fe. Some studies speculate that the Fe core in the Fe@C structure contributes to ORR catalysis in the alkaline electrolyte.[11] To verify this, the electrochemical properties of the Fe/N-gCB and PPB are compared. In cyclic voltammetry (CV, Fig. S12, ESI†), the PPB exhibits a significant redox pair, which is attributed to the transition between $Fe(OH)_2$ and $Fe(OH)_3$. This proves that the Fe core is oxidized to $Fe(OH)_x$ during the ORR process. CV of the Fe/N-gCB also shows the redox pair but with a much lower area, because most Fe is removed. Their LSVs are shown in Fig. S13 (ESI†). It is obvious that the PPB has a slightly lower performance, with the onset potential being about 35 mV lower. This proves that the $Fe(OH)_x$ core is not active as a ORR catalyst. Since the Fe core is very heavy compared to the carbon shell, the PPB at the same catalyst loading will have much less active sites than the Fe/N-gCB. To verify the function of Fe, another sample named Fe/N-gCB-2 is prepared by etching PPB with more concentrated HCl (1 M), which has a higher chance to remove coordinated Fe. The ORR performance of the Fe/N-gCB-2 is also slightly lower than that of the Fe/N-gCB (Fig. S13, ESI†). This proves that coordinated Fe is very important for the high activity of ORR.[8] In another sample, $Fe(OH)_x$ is combined with N-rGO at room temperature. No performance enhancement is observed. It proves again that the Fe–N bonding

can be formed at an elevated temperature.[8a] In the acidic electrolyte (Fig. 4b), only the Fe/N-gCB shows a noteworthy performance. The undoped e-rGO shows the poorest performance again as expected. The N-rGO and N-MCN have very close performance, whose onset potential is about 400 mV lower than that of the Fe/N-gCB. That means they are almost useless in fuel cells. Obviously, N doping has improved the ORR performance a lot in the acid electrolyte, but the Fe–N interaction is more crucial to make it competitive to Pt/C in practice. The ORR performance of acid leached PBB-600, PBB-700 and PBB-800 is also tested for comparison (Fig. S14 and S15, ESI†). In the alkaline electrolyte, the performance decreases slightly for PPB-600 and PPB-700, but drops dramatically for PPB-800. The trend is in accordance with the trend of the N content. The performance change is more significant in acid electrolyte. A possible reason is that in the acid electrolyte, the ORR performance is more sensitive to the local atomic structure that has changed from 550 °C to 600 °C.

The Tafel plots of these typical catalysts are also provided to give some hints of the ORR mechanism. In the alkaline electrolyte, the N-MCN and N-rGO show exactly the same Tafel slope (Fig. 4c). This implies that they share the same ORR mechanism at low overpotential. The Fe/N-gCN and Pt/C also have very close Tafel slopes so they undergo the same ORR mechanism, although they are completely different materials. The coordinated Fe atoms are supposed to create new active sites (Fe atom itself in addition to C bonded to N) with a very high catalytic activity whose mechanism is similar to Pt. This is in accordance with theoretical calculations.[8b,15] The Fe/N-gCB-2, which has a lower Fe content, shows exactly the same Tafel slope as the Fe/N-gCB but lower exchange current density (Fig. S16, ESI†). The Tafel plot of PPB is also the same. Both the PPB and Fe/N-gCB-2 have the same Fe–N–C structure as the Fe/N-gCB but less active site density. This proves again that the Fe atoms are the main active centres in the Fe–N–C structure. In acid electrolyte, Pt/C keeps the same Tafel slope as in alkaline electrolyte (Fig. 4c and d). The Tafel slope of the Fe/N-gCB in acid electrolyte is a little higher than that in alkaline electrolyte (Fig. 4c and d). A possible reason is that the acid changes part of the local atomic structure to the Fe–N active centres.

Finally we checked the ORR stability of the Fe/N-gCB. The current retention *vs.* time lapse plot is shown in Fig. S17 (ESI†). In alkaline electrolyte, the Fe/N-gCB shows very good stability in a 50 000 s test, retaining 90% of the initial current. In the acidic electrolyte, the stability is to some extent lower (70%). It is reasonable because Fe can be etched by a strong acid like H_2SO_4 used in this experiment, especially with saturated O_2. This, on the other hand, proves the importance of Fe in the Fe/N-gCB for ORR. The LSVs of the Fe/N-gCB before and after the 50 000 s test are shown in Fig. S18 and S19 (ESI†). Current densities are slightly lower in both acid and alkaline electrolytes after the 50 000 s test than the original ones.

In conclusion, we have synthesized a novel Fe/N-gCB as a high-performance ORR catalyst. The key findings include: (1) highly graphitic and lowly defective carbon with extraordinarily high N content can be synthesized at low temperature of 550 °C. (2) High Fe content facilitates the formation of high specific surface area and graphitic structure at low temperature. (3) The low temperature process retains high level of N. Both yield and N content decrease as synthesis temperature increases. (4) Fe/N-gCB shows comparable performance with Pt/C in alkaline electrolyte and adequate performance in acidic electrolyte. (5) Only the Fe coordinated to N in the shell can contribute ORR activity. (6) High temperature synthesis reduces the activity of final product. We believe the Fe/N-gCB is a very promising catalyst for ORR and our findings are informative for future study on ORR catalysts.

This work is financially supported by the Australian Research Council (ARC) through the Discovery Project programs (DP130104459 and DP140104062).

Notes and references

1 (*a*) Y. Zheng, Y. Jiao, M. Jaroniec, Y. Jin and S. Z. Qiao, *Small*, 2012, **8**, 3550; (*b*) Y. Zheng, J. Liu, J. Liang, M. Jaroniec and S. Z. Qiao, *Energy Environ. Sci.*, 2012, **5**, 6717.
2 (*a*) L. T. Qu, Y. Liu, J. B. Baek and L. M. Dai, *ACS Nano*, 2010, **4**, 1321; (*b*) K. P. Gong, F. Du, Z. H. Xia, M. Durstock and L. M. Dai, *Science*, 2009, **323**, 760.
3 (*a*) Y. Liang, Y. Li, H. Wang, J. Zhou, J. Wang, T. Regier and H. Dai, *Nat. Mater.*, 2011, **10**, 780; (*b*) R. F. Zhou, Y. Zheng, D. Hulicova-Jurcakova and S. Z. Qiao, *J. Mater. Chem. A*, 2013, **1**, 13179; (*c*) J. Duan, Y. Zheng, S. Chen, Y. Tang, M. Jaroniec and S. Qiao, *Chem. Commun.*, 2013, **49**, 7705.
4 (*a*) J. Liang, R. F. Zhou, X. M. Chen, Y. H. Tang and S. Z. Qiao, *Adv. Mater.*, 2014, **26**, 6074; (*b*) Y. G. Li, W. Zhou, H. L. Wang, L. M. Xie, Y. Y. Liang, F. Wei, J. C. Idrobo, S. J. Pennycook and H. J. Dai, *Nat. Nanotechnol.*, 2012, **7**, 394; (*c*) M. Lefevre, E. Proietti, F. Jaouen and J. P. Dodelet, *Science*, 2009, **324**, 71.
5 Y. Jiao, Y. Zheng, M. Jaroniec and S. Z. Qiao, *J. Am. Chem. Soc.*, 2014, **136**, 4394.
6 (*a*) Y. J. Zhang, M. Chu, L. Yang, W. F. Deng, Y. M. Tan, M. Ma and Q. J. Xie, *Chem. Commun.*, 2014, **50**, 6382; (*b*) W. Wei, H. Liang, K. Parvez, X. Zhuang, X. Feng and K. Muellen, *Angew. Chem., Int. Ed.*, 2014, **53**, 1570.
7 (*a*) D. Geng, Y. Chen, Y. Chen, Y. Li, R. Li, X. Sun, S. Ye and S. Knights, *Energy Environ. Sci.*, 2011, **4**, 760; (*b*) R. L. Liu, D. Q. Wu, X. L. Feng and K. Mullen, *Angew. Chem., Int. Ed.*, 2010, **49**, 2565.
8 (*a*) N. Ramaswamy, U. Tylus, Q. Y. Jia and S. Mukerjee, *J. Am. Chem. Soc.*, 2013, **135**, 15443; (*b*) S. Kattel and G. F. Wang, *J. Mater. Chem. A*, 2013, **1**, 10790.
9 Z. S. Wu, S. B. Yang, Y. Sun, K. Parvez, X. L. Feng and K. Mullen, *J. Am. Chem. Soc.*, 2012, **134**, 9082.
10 (*a*) T. Yang, J. Liu, R. Zhou, Z. Chen, H. Xu, S. Z. Qiao and M. J. Monteiro, *J. Mater. Chem. A*, 2014, **2**, 18139; (*b*) R. F. Zhou and S. Z. Qiao, *Chem. Mater.*, 2014, **26**, 5868.
11 Y. Hou, T. Huang, Z. Wen, S. Mao, S. Cui and J. Chen, *Adv. Energy Mater.*, 2014, **4**, 1400337.
12 X. Feng, K. Liu, X. Xie, R. Zhou, L. Zhang, Q. Li, S. Fan and K. Jiang, *J. Phys. Chem. C*, 2009, **113**, 9623.
13 (*a*) Y. M. Shyu and F. C. N. Hong, *Mater. Chem. Phys.*, 2001, **72**, 223; (*b*) Y. J. Li, Z. Sun, S. P. Lau, G. Y. Chen and B. K. Tay, *Appl. Phys. Lett.*, 2001, **79**, 1670.
14 (*a*) L. Zhang and Z. Xia, *J. Phys. Chem. C*, 2011, **115**, 11170; (*b*) J. Chen, X. Wang, X. Cui, G. Yang and W. Zheng, *Chem. Commun.*, 2014, **50**, 557.
15 C. E. Szakacs, M. Lefevre, U. I. Kramm, J. P. Dodelet and F. Vidal, *Phys. Chem. Chem. Phys.*, 2014, **16**, 13654.
16 A. Cuesta, P. Dhamelincourt, J. Laureyns, A. Martinezalonso and J. M. D. Tascon, *Carbon*, 1994, **32**, 1523.
17 H. A. Gasteiger, S. S. Kocha, B. Sompalli and F. T. Wagner, *Appl. Catal., B*, 2005, **56**, 9.

Electronic Supporting information

Fe/N co-doped graphitic carbon bulb for high-performance oxygen reduction reaction

Ruifeng Zhou[a,b] and Shi Zhang Qiao[a]*

[a] School of Chemical Engineering, University of Adelaide, Adelaide SA 5005 Australia.

[b] Australian Institute for Bioengineering and Nanotechnology, University of Queensland, St Lucia QLD 4072 Australia.

Email: s.qiao@adelaide.edu.au

I. Experimental Section

Synthesis of Fe/N-gCB

In a typical synthesis of Fe/N-gCB, 1 ml of 1 M $FeCl_3$ solution was added drop by drop to a 10 ml of 0.05 M $K_4Fe(CN)_6$ solution at room temperature with stirring. The sediment (PB) was filtered, washed and dried at 50 °C overnight in vacuum. The PB was then heated in a tube furnace from room temperature to 550 °C with temperature ramping of 3 °C per minute, kept for 3 hours and cooled to room, under N_2 protection. The PPB was washed with 20 ml of 0.1 M HCl, filtered and washed with water and dried, resulting the Fe/N-gCB.

Synthesis of e-rGO, N-rGO and $Fe(OH)_x$/N-rGO

Graphite flake (3 g) was mixed with concentrated H_2SO_4 (12 ml), $K_2S_2O_8$ (2.5 g), and P_2O_5 (2.5 g). The mixture was kept at 90 °C for 6 h, then cooled to room temperature and diluted with 0.5 L of DI water. The suspension was filtered and washed with DI water. The solid was dried in vacuum at 50 °C overnight. The pretreated graphite was put into cold (0 °C) concentrated H_2SO_4 (120 mL). Then, $KMnO_4$ (15 g) was added gradually under stirring and the temperature of the mixture was kept to be below 20 °C by ice cooling. The mixture was stirred at 40 °C for 3 h, and then diluted with DI water (250 mL) using ice bath cooling.

It was then stirred for 2 h, and then additional 0.7 L of DI water was added. 20 mL of 30% H_2O_2 was added to the mixture. It was washed with 1:10 HCl aqueous solution (1 L). The resulting graphite oxide was diluted to in DI water. Exfoliation was carried out by sonicating graphite oxide dispersion under ambient condition for 30 min, followed with centrifuging at 3000 rpm for 30 min to eliminate unexfoliated graphite.

To prepare e-rGO on electrodes, 50 µl 0.1 % GO solution was dipped on the disk of RRDE and dried under ambient conditon. The electrode was then used as the working electrode in the electrochemical setup described below. Cyclic voltammetry (CV) was applied to the working electrode between 1.2 V and -0.2 V at 100 mV s^{-1} until steady CV curve was reached. During the CV, the GO was reduced to e-rGO.

To synthesize N-rGO, 5 ml of 25% NH_3 aqueous solution was added into 65 ml 0.1% GO solution. The solution was stirred at 90 °C for 12 h. After reduction, the N-rGO was filtered and washed with water and dispersed in water by supersonication.

To prepare Fe(OH)x/N-rGO, 10 µl of 0.1 M $FeCl_3$ was added to 10 ml of 0.02 % N-rGO suspension under sonication. Then 100 µl of 0.1 M NaOH was added. The products were centrifuged and washed with water and re-dispersed

Synthesis of N-MCN

In a typical synthesis N-MCN, a solution was prepared by mixing 80 mL ethanol and 200 mL of distilled water. Subsequently, 1 g F127, 1.3 g CTAB, and 2 g cysteine were added in the mixed solution under continuous stirring. Then, 2 g 3-aminophenol was added and stirred until a complete dissolution. Next, 2.8 mL of 37 wt% formaldehyde was dropped in and kept stirring for another 24 h at 25 °C. Finally, the mixture was transferred to autoclave and kept at 100 °C for another 24 h. The resulting resin was obtained by washing with water and ethanol for 3 times. In order to obtain N-MCN, The resin were carbonized under N_2 flow in the tube furnace. It were heated at rate of 1°C/min up to 350 °C, kept for 2 h, heated at 1 °C /min up to 700 °C and kept for 4 h.

Characterization

The thermogravimetric analysis (TGA) was measured with SETARAM ABSYSTM TGA. Transmission electron microscopy (TEM) images were taken with Tecnai F20. X-ray diffraction was taken by Rigaku Miniflex 600 with Cu Kα line. X-ray photoelectron spectroscopy (XPS) was taken by KRATOS Axis Ultra DLD with Al Kα line. Raman spectroscopy was taken with HORIBA LabRAM HR Evolution with 532 nm laser.

Electrochemical measurement

2 mg Fe/N-gCB was dispersed in 2 ml of 0.2 % nafion aqueous solution by supersonication. 50 µl of the catalyst ink was dipped onto the glassy carbon working electrode (5.61 mm in diameter) of a rotating ring-disk electrode (RRDE) and dried under ambient condition. The final catalyst loading on RRDE are about 0.2 mg cm^{-2}. When testing Pt/C, the loading is 0.2 mg cm^{-2}. The electrode was then used as the working electrode in a 3-electrode electrochemistry system where a Ag/AgCl (4 M KCl) electrode and a Pt wire were used as the reference electrode and counter electrode respectively. O_2 saturated 0.1 M KOH aqueous solution and 0.05 M H_2SO_4 aqueous solution were used as alkaline and acid electrolytes respectively. CV was applied to the working electrode between 0 V and 1.2 V (vs RHE, hereinafter the same) at 100 mV s^{-1} until steady CV curve was reached. When testing stability, the potential is set to 0.7 V for basic electrolyte and 0.3 V for acidic electrolyte, with O_2 inlet of 5 SCCM (standard cubic centimetres per minute).

II. Supporting Figures

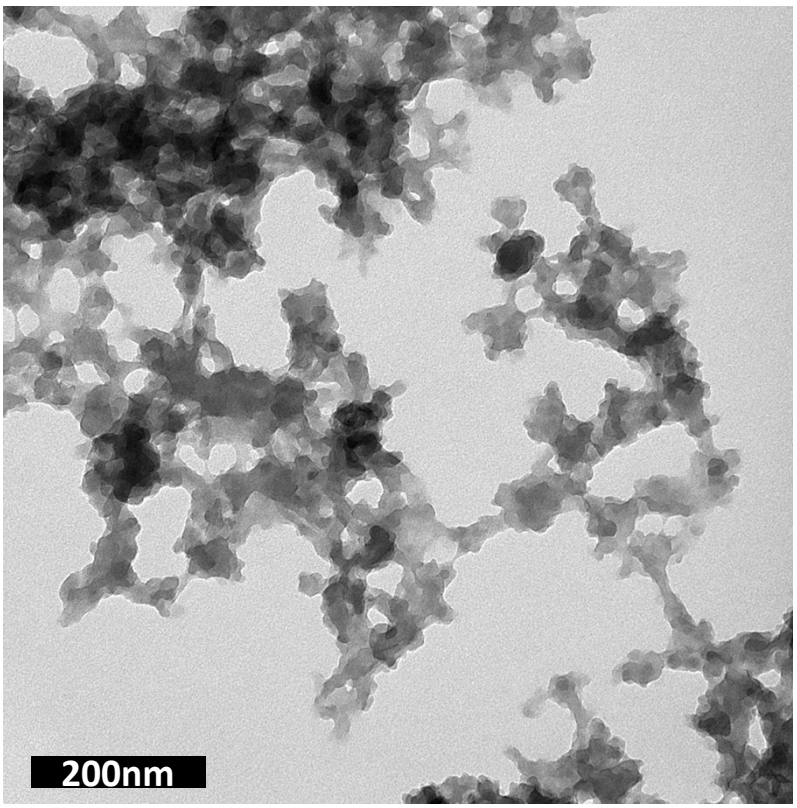

Figure S1. TEM image of PB.

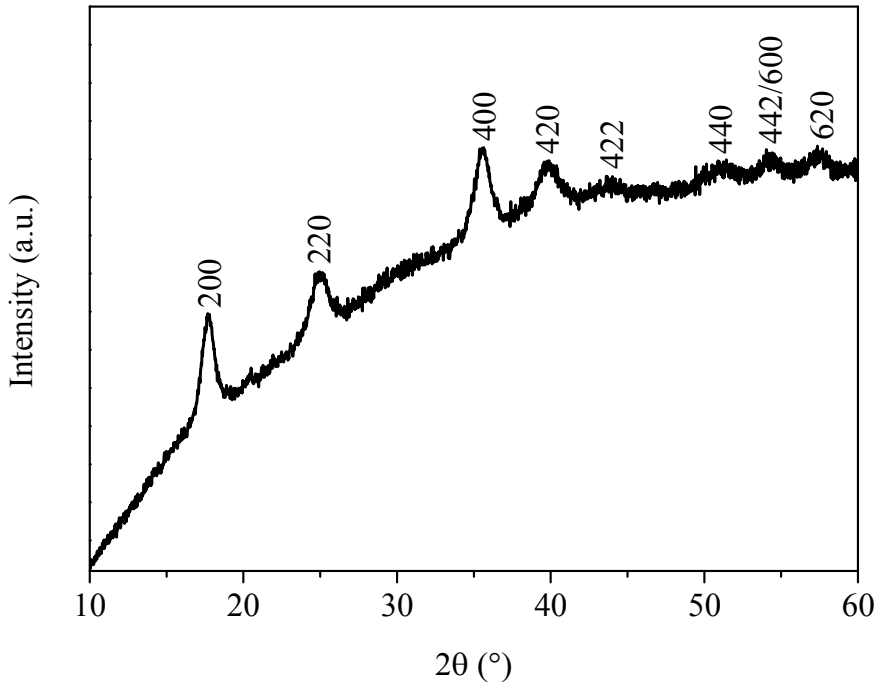

Figure S2. XRD pattern of PB.

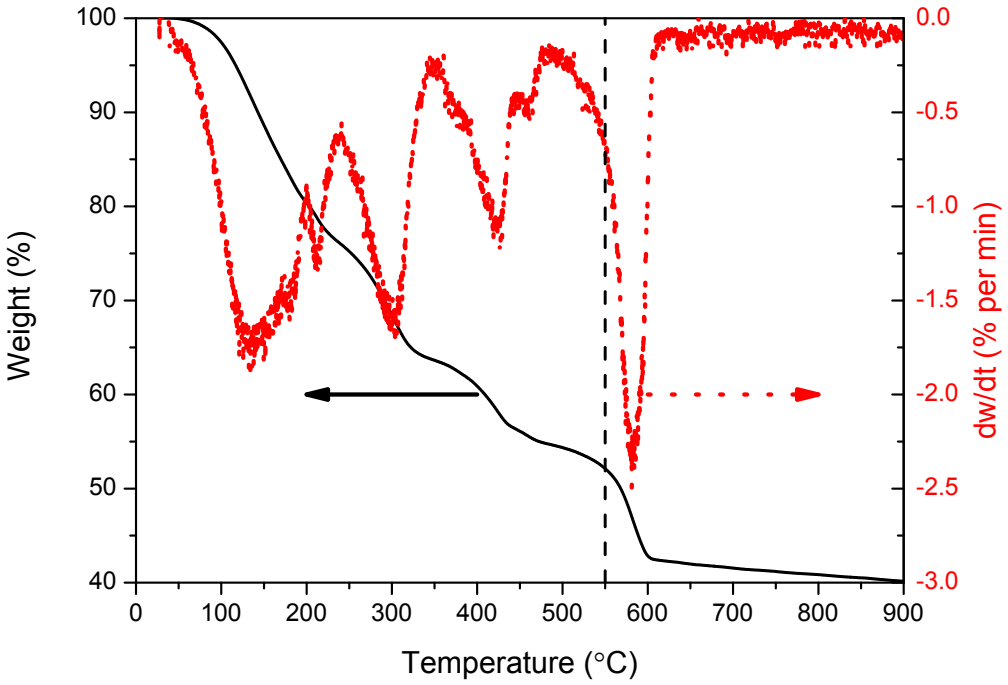

Figure S3. TGA of Pyrolysis of PB in N_2.

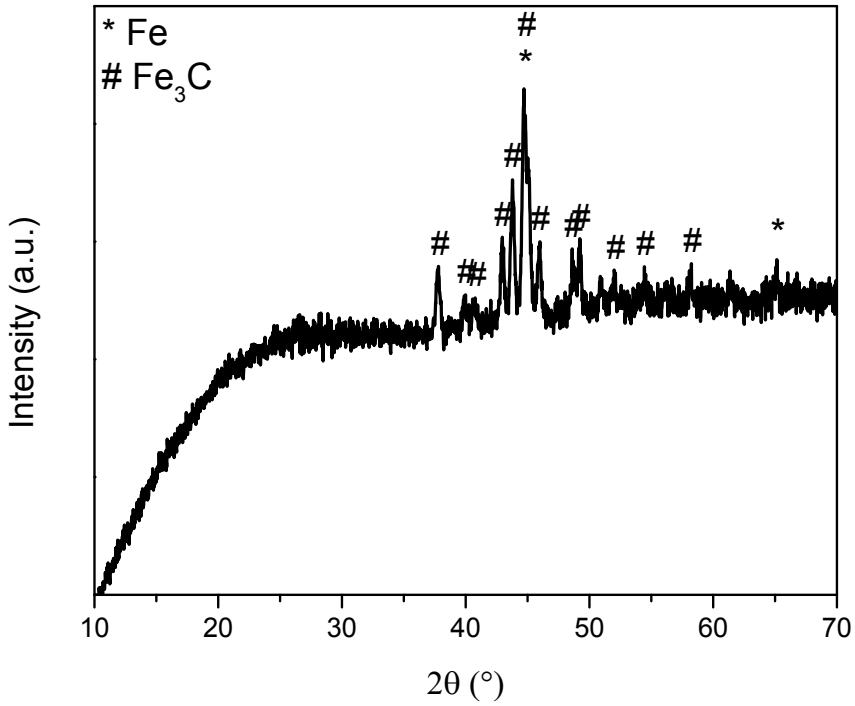

Figure S4. XRD of PPB at 900 °C.

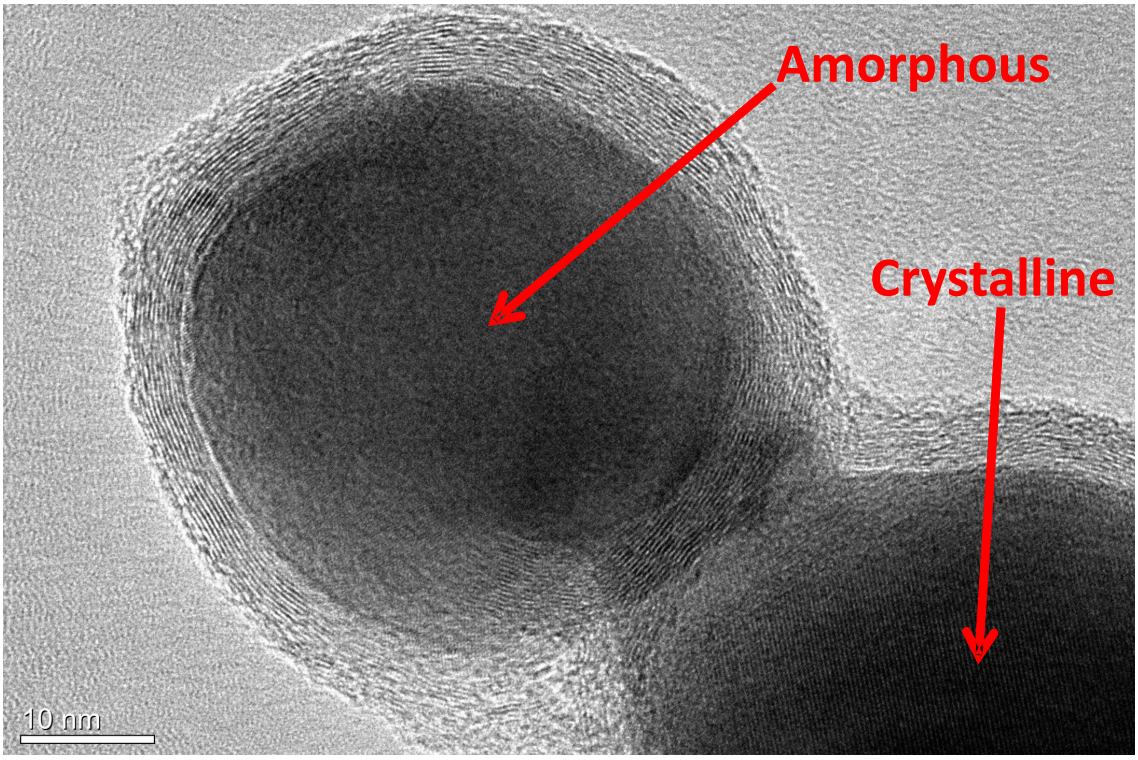

Figure S5. TEM image of PPB.

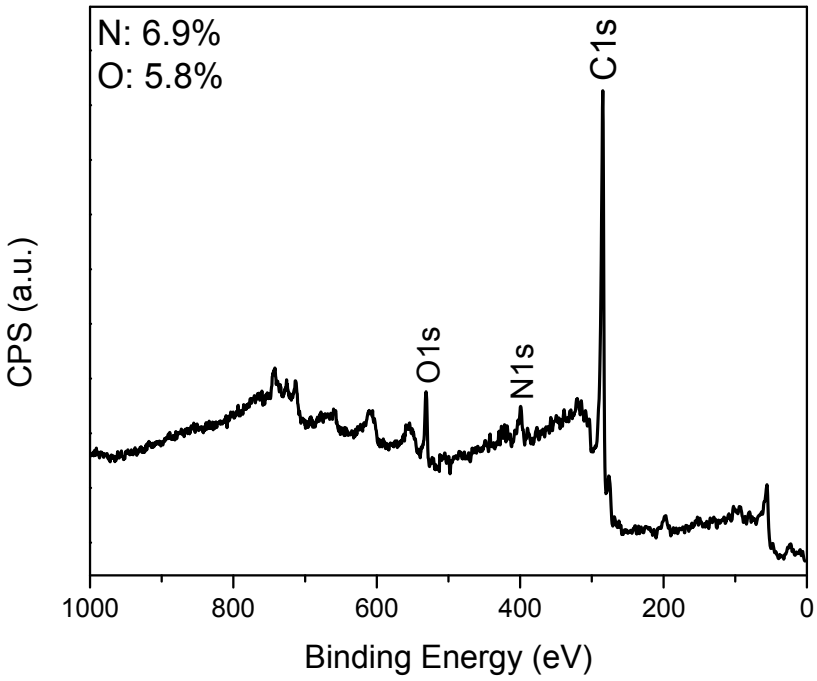

Figure S6. XPS of acid leached PPB from 600 °C.

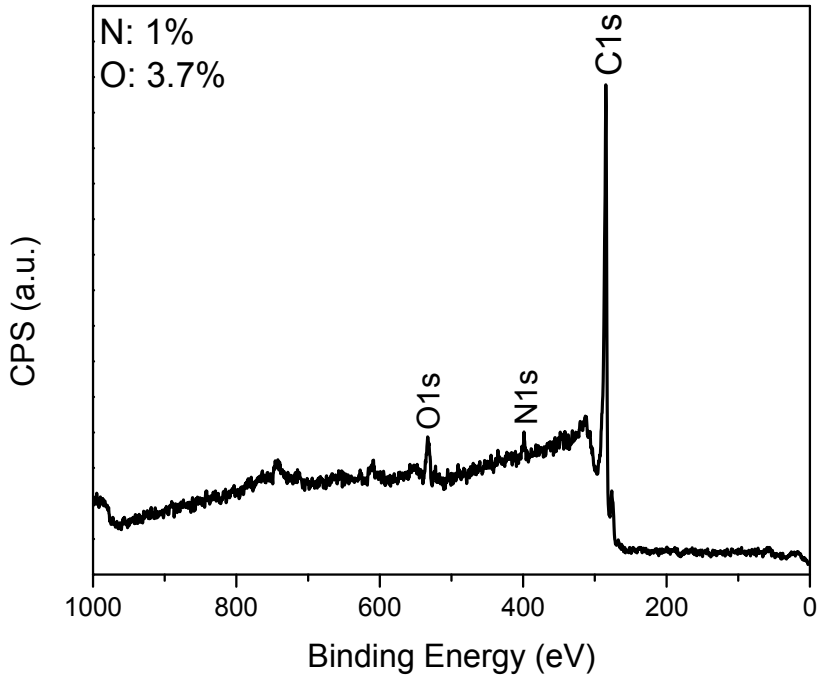

Figure S7. XPS of acid leached PPB from 700 °C.

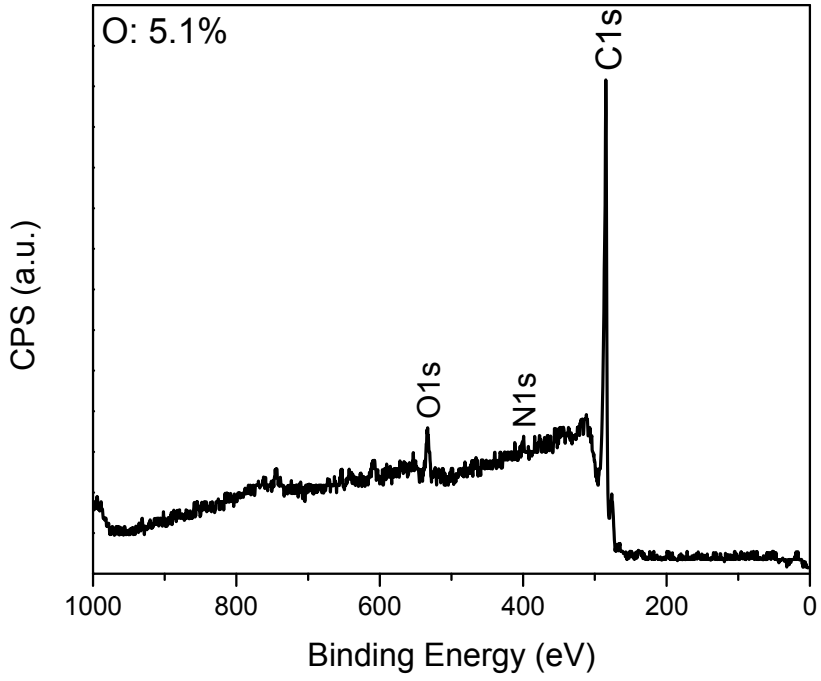

Figure S8. XPS of acid leached PPB from 800 °C.

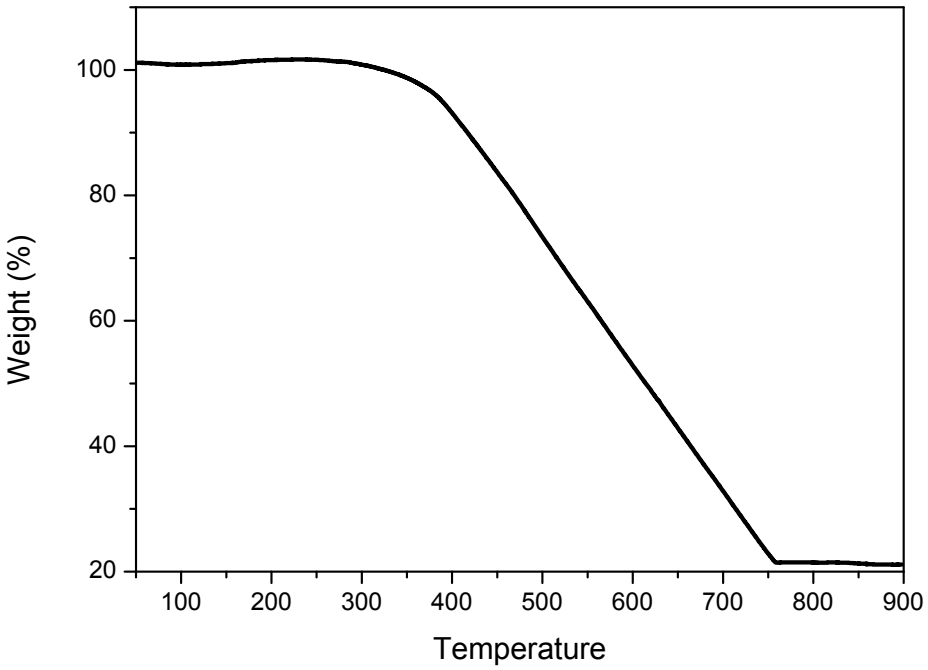

Figure S9. TGA of Fe/N-gCB in air.

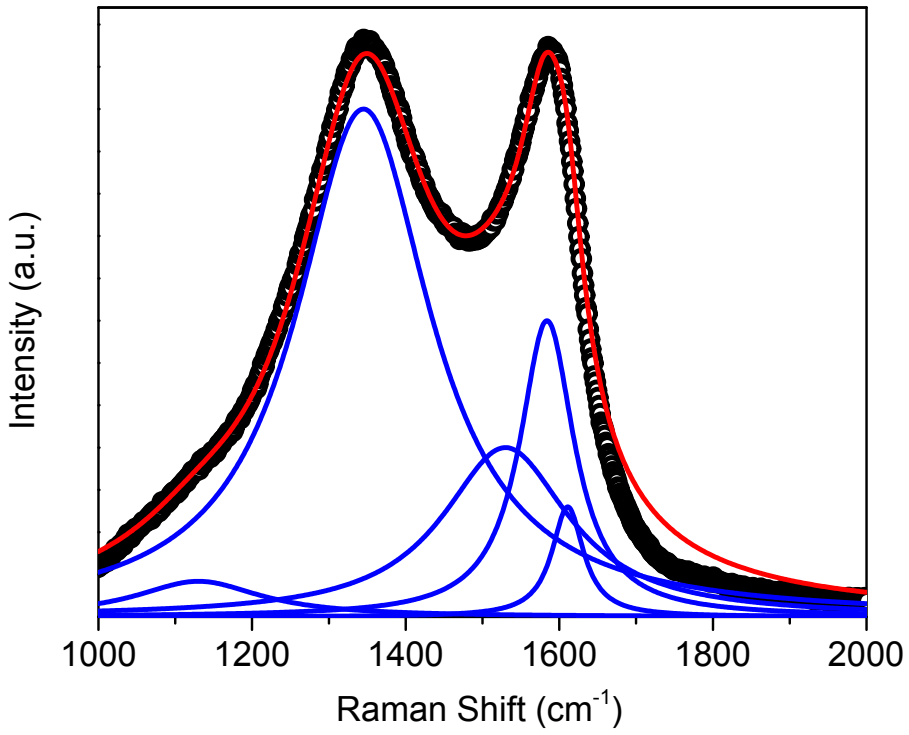

Figure S10. Raman spectrum of N-MCN.

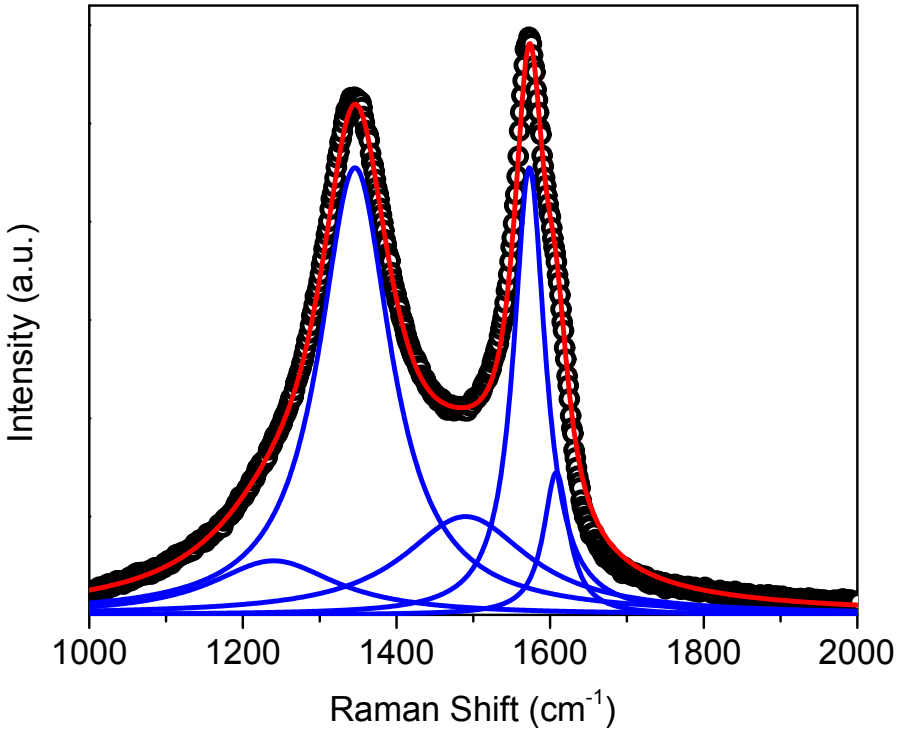

Figure S11. Raman spectrum of N-rGO.

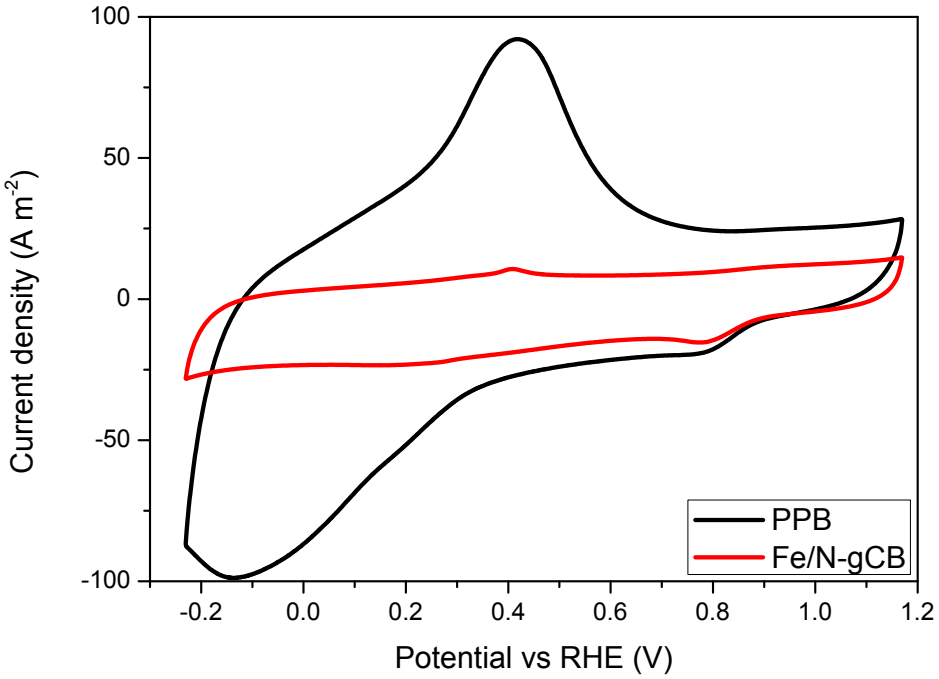

Figure S12. CVs of Fe/N-gCB and PPB in O_2 saturated 0.1 M KOH.

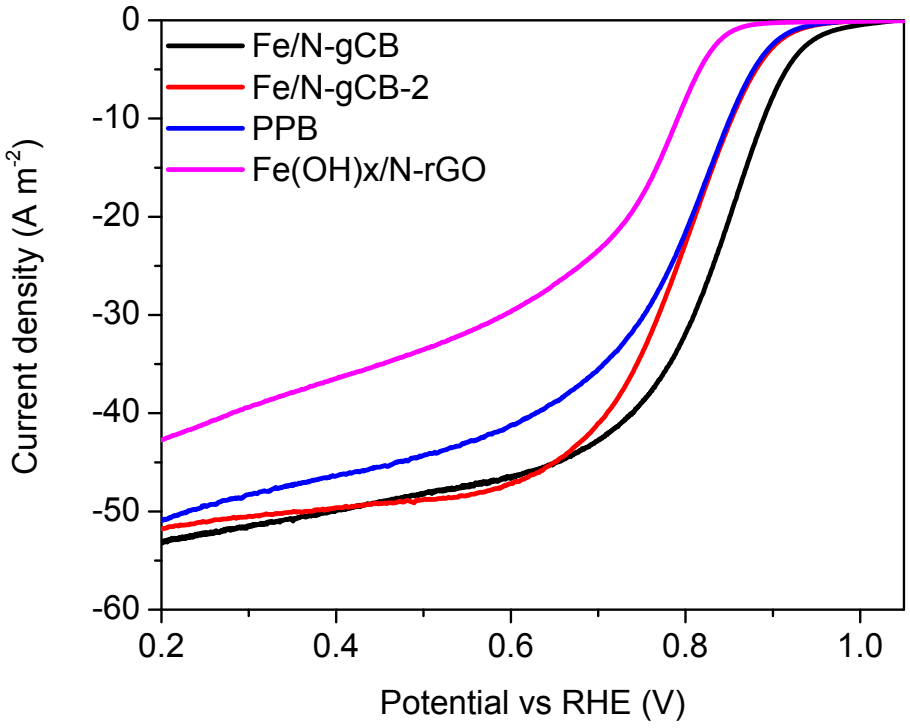

Figure S13. Normalized disk current at 1600 rpm in alkaline electrolyte.

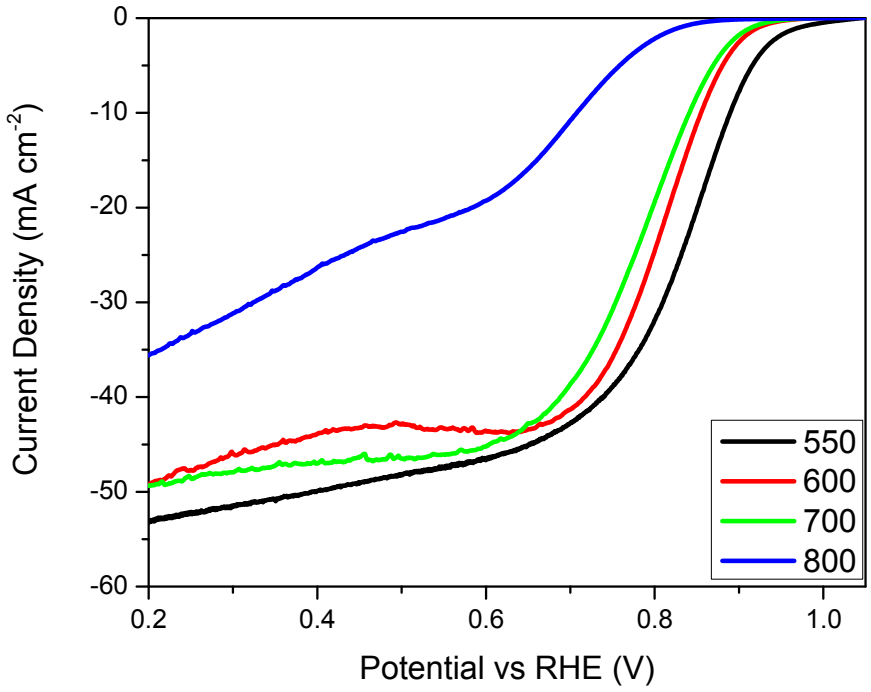

Figure S14. LSV of acid leached PPBs in alkaline electrolyte.

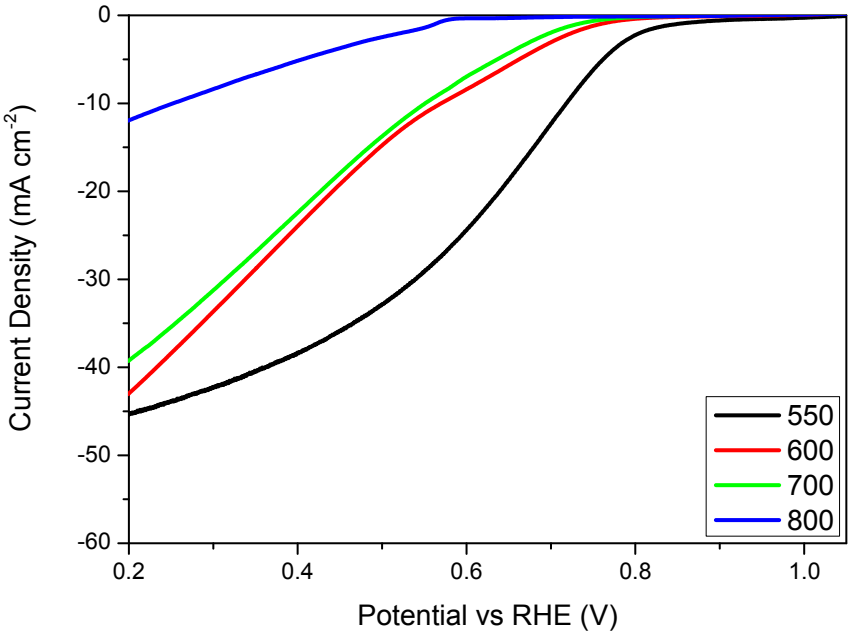

Figure S15. LSV of acid leached PPBs in acide electrolyte.

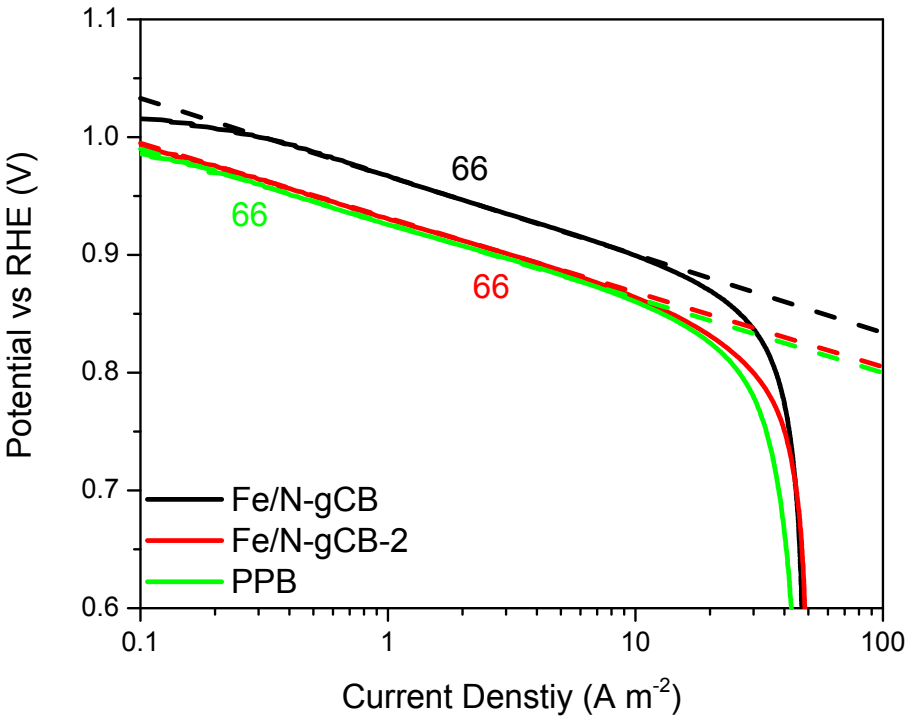

Figure S16. Tafel plots in alkaline electrolyte.

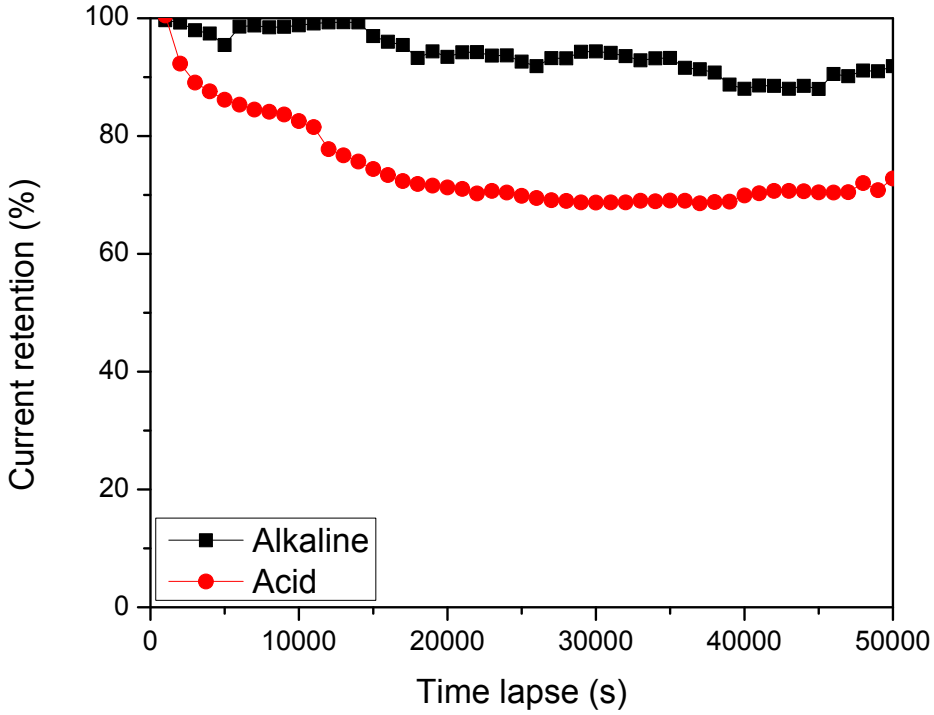

Figure S17. Stability of ORR of Fe/N-gCB in alkaline and acid electrolytes.

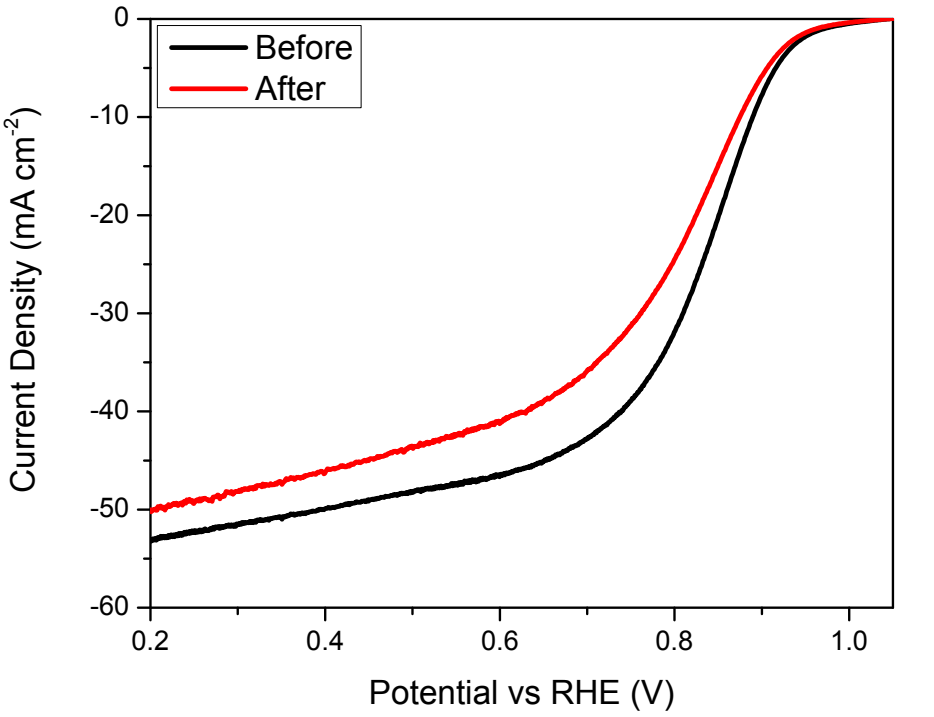

Figure S18. LSV of Fe/N-gCB before and after 50,000 s test in alkaline electrolyte.

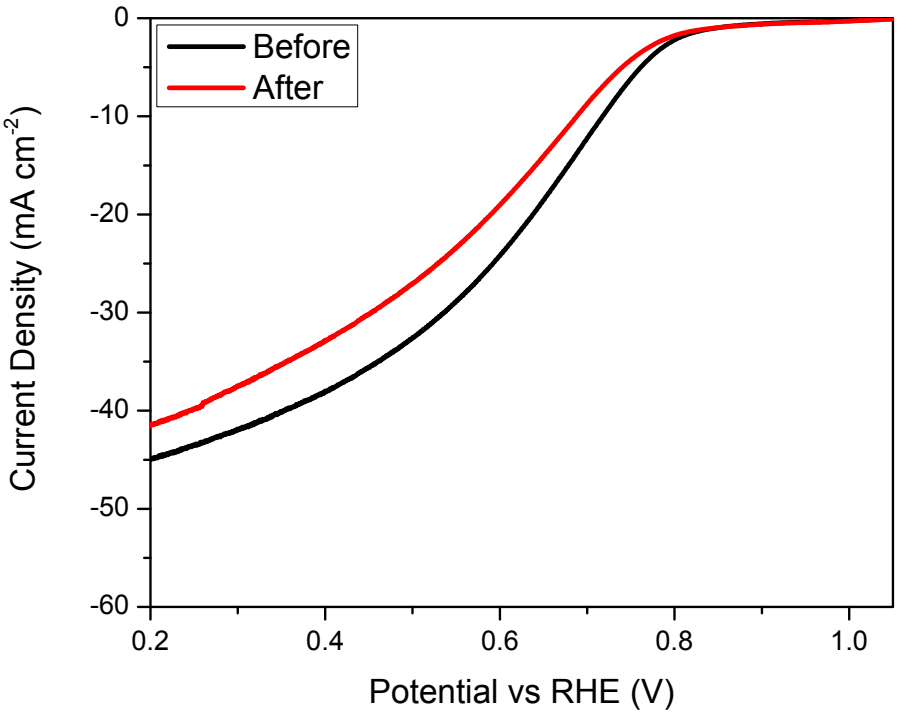

Figure S19. LSV of Fe/N-gCB before and after 50,000 s test in acid electrolyte.

Chapter 6: Measurement of Electron Transfer Number of Oxygen Reduction Reaction: from Theory to Experiment

Introduction

Based on extensive study on ORR, it is found that in the conventional calculation of electron transfer number, the electron transfer number calculated from RRDE and KL methods always don't coincide. Therefore, a lot of experiments were conducted to find the relationship between measuring condition and result. It is found that the only way to get correct electron transfer number is the RRDE method with calibrated collection coefficient. The KL method is not suitable because ORR is not a one-step, irreversible and first order reaction.

This chapter is submitted to J. Am. Chem. Soc.

Measurement of Electron Transfer Number of Oxygen Reduction Reaction: from Theory to Experiment

Ruifeng Zhou[1, 2], Yao Zheng[1], Piotr Zelenay[3] and Shi Zhang Qiao[1, *]

1 School of Chemical Engineering, the University of Adelaide, Adelaide, SA 5005, Australia.

2 Australian Institute for Bioengineering and Nanotechnology, the University of Queensland, St Lucia, QLD 4072, Australia.

3 Materials Physics and Applications Division, Los Alamos National Laboratory, Los Alamos, NM 87545, USA.

ABSTRACT: The forced convection methods on rotation electrode are carefully investigated to study the calculation of electron transfer number (n) of oxygen reduction reaction (ORR) on various catalysts in alkaline electrolyte. It is found that the widely used Koutechy-Levich (KL) method is not suitable to determine n for ORR neither theoretically nor experimentally. Theoretically, the ORR is neither a single-step nor irreversible reaction, therefore does not meeting the precondition of KL method. Experimentally, the n of oxygen reduction is significantly dependent on the angular velocity of the rotating electrode, contradicting the assumption of constant n in KL theory. By constructing an improved mathematical model, the relationship between n and angular velocity is built. The experimental results agree with the model perfectly on most tested catalysts, meanwhile it is proved that the ORR is not first-order on the other catalysts. The recommended way to determine n in alkaline electrolyte is using the rotation ring-disk electrode with a properly biased Au ring, assisted by calibrated collection efficiency.

INTRODUCITON

The electron transfer number (n) is at the center of the research on electrocatalytic oxygen reduction reaction (ORR) in aqueous electrolytes, which not only exhibits the efficiency of oxygen conversion, but also provides the information of ORR mechanism. In practice, a low n leads to an inexpensive and safe way of H_2O_2 production,[1-4] but high H_2O_2 concentration degenerates the proton exchange membrane in fuel cells.[5-7]. As the rise of research in ORR and fuel cells, increasing reports have adopted n value as a key parameter to evaluate the performance of a certain electrocatalyst.[8-13] Conventionally, two experimental methods are widely used to determine n, i.e. the rotation ring-disk electrode (RRDE) method and the Koutecky-Levich (KL) method. However, these methods were developed tens of years ago based on some simple elementary reactions.[14-16] The applicability of the methods for ORR has not been re-examined for a long time, especially on recently developed nano –structured and 3D catalysts and in alkaline electrolyte. According to our and the others' previous studies on a wide variety of electrocatalysts, the n calculated by RRDE (n_{RRDE}) and KL (n_{KL}) methods usually didn't coincide.[17-23] The KL plots were not perfectly linear and the calculated n values by KL method sometimes exceed the theoretical limitation. Thus, it is highly desirable to carefully re-examine these methods from both theoretical and experimental perspectives to figure out the problem and provide a general, correct, and accurate way to determine n.

Basic concept and traditional calculation methods of n.

During ORR, an O_2 molecule can receive either 2 or 4 electrons to form H_2O_2 or H_2O (in the form of HO_2^- and OH^- in alkaline electrolyte), as shown in reaction (4e) and (2e).

$$O_2 + 2H_2O + 4e^- \rightarrow 4OH^- \quad (4e)$$

$$O_2 + H_2O + 2e^- \rightarrow HO_2^- + OH^- \quad (2e)$$

H_2O_2 can be further reduced to H_2O as:

$$HO_2^- + H_2O + 2e \rightarrow 3OH^- \quad (2'e)$$

The combination of (2e) and (2'e) results in the same result as (4e). The difference between the direct and indirect pathways is whether H_2O_2 is released to the electrolyte. The n is defined as the arithmetic mean of the number of electrons finally received by an O_2 molecule in ORR. Experimentally, there are two dominantly used methods to calculate n of ORR based on the forced convection on a rotation electrode, i.e. the RRDE and KL method. In the RRDE method, the ORR is conducted on the disk electrode and the produced H_2O_2 can be directly measured by oxidizing it on the ring with a high potential as:

$$HO_2^- + OH^- \rightarrow O_2 + H_2O + 2e^- \quad (-2e)$$

The n_{RRDE} can be calculated from the disk current (I_d) and ring current (I_r) by:

$$n = 4 \times \frac{I_d}{I_d + \frac{I_r}{N_C}} \quad (1)$$

where N_C is the collection efficiency of the RRDE, defined as the fraction of product from the disk to the ring. Analogously, the H_2O_2 ratio (p) is defined as the fraction of O_2 reduced into H_2O_2, calculated as:

$$p = 2 \times \frac{\frac{I_r}{N_C}}{I_d + \frac{I_r}{N_C}} \quad (2)$$

Obviously, n and p have the relationship as:

$$n = 4 - 2p \quad (3)$$

Another method is based on the KL theory as equation (4), which describes the current density behavior on a rotation disk electrode (RDE).[24]

$$\frac{1}{j} = \frac{1}{j_K} + \frac{1}{j_L} = \frac{1}{B}\omega^{-\frac{1}{2}} + \frac{1}{j_K} \quad (4)$$

where j, j_K and j_L are the aspect, kinetic-limited and mass transfer-limited current densities, respectively. The j_K is assumed to be a constant at a certain potential. The j_L is proportional to the square root of angular velocity (ω) of the RDE. The reciprocal of proportionality coefficient (B) is:

$$B = 0.62D^{\frac{2}{3}}\nu^{-\frac{1}{6}}nFC^{*} \quad (5)$$

where D is the diffusion coefficient of the reactant; ν is the kinematic viscosity of the electrolyte; F is the faraday constant; C^{*} is the concentration of the reactant in the bulk electrolyte. Therefore n could be deduced from the slope of 1/j versus $\omega^{-1/2}$ plot (KL plot).

Brief review of the history of calculation of n. Early ORR studies are all based on Pt catalyst in acid electrolyte. Frumkin et al. firstly used RRDE to qualitatively detect the H_2O_2 produced in ORR,[14] but they didn't raise the concept of n or p at that time. The concept of p was raised by Muller et al.[15] who measured I_d and I_r under different ω and got different I_r/I_d at a certain potential, which means that the p is not constants at certain potential in ORR. From 1960s to 1980s, a few works studied the ORR mechanism were based on I_r/I_d vs ω and mathematical modeling,[25-28] without considering n or p. In these papers, it is a consensus that I_r/I_d depends on ω, therefore n or p is not an intrinsic property of a catalyst but changes with measurement conditions. Moreover, Damjanovic et al.[29] theoretically proved that the ratio between the rates of a electrochemical reaction's direct and indirect pathways has linear relationship with $\omega^{-1/2}$ under the assumption that all the sub-reactions are first-order. Obviously, ORR has such parallel pathways, i.e. the (4e) and the (2e) + (2'e) reactions, so I_r/I_d should depend on ω but this key fact has been ignored by most researchers since 1990s. For example, Gasteriger et al. reported different I_r/I_d at different ω but they didn't discuss its origin.[30-31] From the start of 21st century, most researchers focused on the development of new catalysts but mistook n as an intrinsic property of the catalyst. Additionally, the recent papers also didn't check the proper condition used in RRDE method in alkaline electrolytes.

The KL theory was originally developed to determine some physical quantities, such as the diffusion coefficient of a solute by a certain electrochemical reaction (i.e. with a pre-known n). It is difficult to trace the very first paper using KL method to calculate the n of ORR; but some usage started to appear as early as 1990s.[32] Thereafter, more papers just used the equation (4) to calculate n according to the text books[24, 33], while the others just cited existing papers without considering the specific limitation and pre-condition. However, it is obvious that the basis of KL method contradicts the result of RRDE method. In KL theory, n must be independent with ω while as aforementioned, it has been proved to be not true for ORR by the RRDE method, at least on Pt based catalysts. Theoretically, the KL method is only valid on one-step reactions, but ORR is obviously multistep involving at least one releasable intermediate. An important review paper by Johnson et al.[34] examined the validity of KL method to estimate n for various multistep reactions. They concluded that the KL plot must not be linear for multistep reactions and the KL plot slope can be a function of ω and potential, even if n is fixed. Compton et al. also proved that the KL plot will be affected by the coverage of catalysts on working electrode.[35] Therefore, all above evidences indicate that KL method should not be applicable for ORR.

Some problems have been reviewed recently by Lee et al. who summarized the inconsistencies in literature.[36] Some other papers also experimentally observed and reported the contradiction between n_{RRDE} and n_{KL}, but they didn't interpret their origin.[21-23] In our previous papers we also continuously found nonlinear KL plot and inconsistencies between n_{RRDE} and n_{KL}.[17-20] In some high quality papers only RRDE method was used, probably because the authors had perceived the problems.[13, 37-39] However, a lot of papers still used KL method to calculate n. Thus, systematic experimental and theoretical studies are extremely desirable to figure out the problems and develop a correct and accurate method to measure n.

Based on aforementioned concerns, in this paper, both KL and RRDE methods are tested carefully on some presentative catalysts including metals (Au, Ag and Ru) and carbon-based catalysts (O, N and Co/N doped graphenes), with planar or 3D structure. A mathematical model has also been derived to explain the measured results. The new findings include:

1. In RRDE method, different with previous studies which adopted the N_C from its manufacturer, we found that N_C decreases significantly with catalyst loading. Furthermore, when the electrode surface is rough, N_C also decreases dramatically with ω.

2. The widely applied RRDE method with a Pt ring is not suitable for H_2O_2 collection in alkaline electrolyte because the oxidation of H_2O_2 on Pt is not mass transfer limited. As an alternative, a Au ring biased at 1.2 V is suitable for H_2O_2 collection and can derive accurate n values.

3. The n value significantly depends on ω for all tested catalysts at any potential, which means the KL method, which requires n to be a constant at certain potential, is not applicable for ORR. As a result, the calculated n_{KL} is significantly different from n_{RRDE} on all tested catalysts at almost any potential.

4. Last but most important, by introducing a simple mathematical model, it is proved that if the all sub-reactions in ORR are first-order, the value of n must depend on ω and the 1/p vs $\omega^{-1/2}$ plot must be linear, providing a fundamental explanation of observed phenomenon. Our results also show that the order of ORR is not 1 on some specific electrocatalysts.

These findings prove that only the RRDE method with properly biased Au ring and calibrated N_C is correct both theoretically and experimentally. The conclusions are critical and essential to correctly understand the n of ORR, at the same time also pave the way of its accurate measurement.

METHODS

The preparations of catalysts are described in detail in the Supporting Information. The disk diameter, ring inner diameter and ring outer diameter of the RRDE (AFE7R9GCPT or AFE7R9GCAU, Pine Research Instrument) are 5.61 mm, 6.25 mm, and 7.92 mm, respectively. The N_C provided by the manufacturer is 0.37. A Ag/AgCl (in 4 M KCl) reference electrode and a Pt wire counter electrode were used. The calibaration of N_C, and H2O2 collection tests are described in results and discussion.

0.1 M KOH is used as the electrolyte for ORR. The ORR polarization curves were collected using linear scanning voltammetry (LSV) from 1 V to 0 V (vs reversible hydrogen electrode, RHE) with scanning rate of 10 mV s^{-1} in O_2-saturated electrolyte. The potential was IR compensated with electrolyte

resistance (30 Ω). The currents were subtracted with the background measured in O_2-free electrolyte.

The n_{RRDE} was calculated by equation (1). The n_{KL} was calculated by linear fitting (least squares) of the KL plot. The parameters used in KL equation are provided in the Supporting Information.

RESULTS AND DISCUSSION

N_C of RRDE loaded with catalysts. There are two things to be confirmed before RRDE method is used. First, the N_C should be known. Second, the collection reaction on the ring must be limited by mass transfer.[24] The N_C of an ideal RRDE is determined only by its geometry parameters i.e. independent on reaction or ω. However, when a thick catalyst layer is loaded on the disk, the geometry of the overall electrode changes. Thus, it is necessary to calibrate N_C of any RRDE loaded with catalyst. The calibration of N_C is carried out with the simple one-electron transfer redox pair (See Supporting Information for detail).

$$Fe(CN)_6^{3-} + e^- \underset{ring}{\overset{disk}{\rightleftarrows}} Fe(CN)_6^{4-}$$

Firstly, the LSV of the glassy carbon (GC) disk and Pt ring was checked. The results are shown in Figure S1 and S2. Obviously, when the ring is biased at 1.5 V, the I_r is limited by the mass transfer. So the ratio between I_r and I_d is N_C. The N_C values of RRDE loaded with catalysts are shown in Figure 1a.

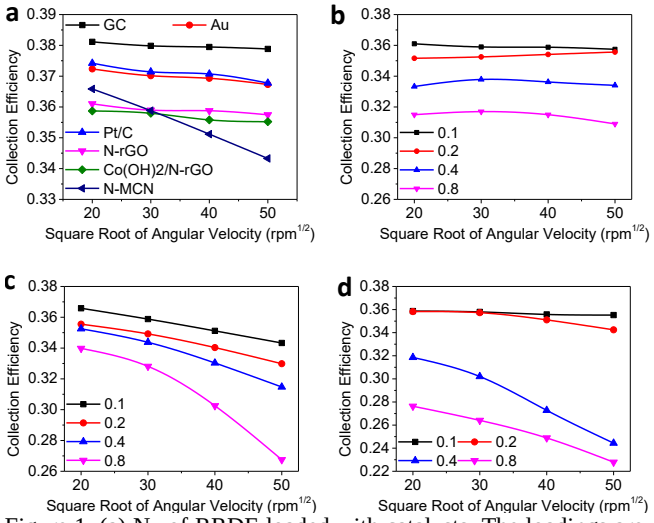

Figure 1. (a) N_C of RRDE loaded with catalysts. The loadings are the 0.1 mg cm^{-2} except Au. (b-d) N_C of RRDE loaded with N-rGO (b), N-MCN (c) and $Co(OH)_2$/N-rGO (d). The numbers are the loading amount of catalysts in mg cm^{-2}.

Surprisingly, the N_C of bare RRDE is not 0.37 as provided by the manufacturer, but close to 0.38, probably due to the slight change in geometry after heavy usage. All the RRDE loaded with catalyst show lower N_C than the bare RRDE. The reason is that when catalyst is loaded on the disk, the electrode-electrolyte interface is a little off the plane of the ring, which decreases the fraction of the product from the catalyst to the ring. Nitrogen doped reduced graphene oxide (N-rGO) and nitrogen doped mesoporous carbon nanosphere (N-MCN) are typical metal-fee ORR catalysts, so that they are used as benchmarks. As shown in Figure 1b, N_C of RRDE loaded with N-rGO decreases significantly as loading (i.e. thickness) increases. The N_C of RRDE loaded with N-MCN not only decreases with the increase of catalyst loading, but also decreases significantly with increase of ω (Figure 1c). The decrease of N_C with increase of ω is attributed to the turbulence. As shown in Figure S3 and S4, the surface of N-rGO electrode is fairly smooth, while surface of N-MCN electrode is quite rough. Turbulence takes places when the fluid flows over a rough surface, which breaks the linearity of the hydrodynamic model of RRDE and leads to unexpected N_C. The turbulence degree increases with the roughness of the surface and the speed of the fluid, in accordance with the trend of N_C. The N_C of RRDE loaded with $Co(OH)_2$/N-rGO decreases dramatically only when the loading of catalysts is high (Figure 1d) because the roughness of its electrode surface is between N-rGO and N-MCN (Figure S5). Note that this type of 3D metal oxide/graphene composites are well known for their porous structure and high surface area, which are regarded as the reason of their high ORR performance.[9] However, the 3D surface actually changes the geometry of the RRDE and introduces turbulence so the measured results may not reflex the real catalytic behavior.

H_2O_2 collection by Pt and Au ring. It is critical that, during the collection experiment, all the products from the disk anticipate the collection reaction on the ring. In other words, the collection reaction on the ring must be limited by mass transfer (like in Figure S1). As long as we know, no report has examined H_2O_2 oxidation in alkaline electrolyte on Pt ring. Traditionally, the ring potential is set to 1.2 V to 1.5 V, which is just below the onset potential of oxygen evolution, so it is considered high enough to oxidize all the H_2O_2. Here, measurements are carried out to verify it. Figure 2a shows the cyclic voltammetry (CV) of Pt ring. The equivalent ring current density ($j_{r,E}$) is used in the plot because in the forced convection hydrodynamic theory,[24] the mass transfer limited current of a rotation ring electrode is:

$$i_{r,L} = B\omega^{\frac{1}{2}}\pi(r_3^3 - r_2^3)^{\frac{2}{3}} \quad (6)$$

where r_2 and r_3 are the inner and outer diameters of the ring. The term $\pi(r_3^3 - r_2^3)^{\frac{2}{3}}$ has exactly the same function as the area. So the $j_{r,E}$ is defined as:

$$j_{r,E} = \frac{i_r}{\pi(r_3^3 - r_2^3)^{\frac{2}{3}}} \quad (7)$$

where i_r is the measured ring current.

It is clear that the CV of Pt ring in 0.1 M KOH with 1 mM H_2O_2 does not show a typical mass transfer limitation at any potential. As the upper limit of CV increases from 1.1 V to 1.7 V, the height of the loops increases significantly. It suggests that a reversible redox processes on surface Pt atoms exists in this potential range. The CV loop of Pt ring in absence of H_2O_2 is much smaller, so this redox process must be induced by H_2O_2. As a result, the Pt ring current is not only contributed by H_2O_2 oxidation but also the redox of surface Pt atoms. Furthermore, once the Pt is oxidized by higher potential, the current is lowered and cannot be recovered even if it is reduced by scanning back to 0.8 V. Figure 2b shows the CV of a Au ring under the same condition. Similar to Pt, the Au has significant redox induced by H_2O_2. However, the oxidation of Au does not take place until 1.2 V, where a mass transfer limitation of H_2O_2 oxidation seems to be already achieved. The current on Au is also higher than that on Pt at any potential. Figure 2c and 2d show the CV on Pt and Au rings, with fixed range but different ω. Again, Pt does not show polarization curves in the form of mass transfer limitation but Au does. The current on Au is always higher than that on Pt, especially

at high ω, because at higher ω, the H_2O_2 concentration on the ring is higher, so the oxidation degree of surface Pt is higher, and the H_2O_2 oxidation activity on Pt is lower.

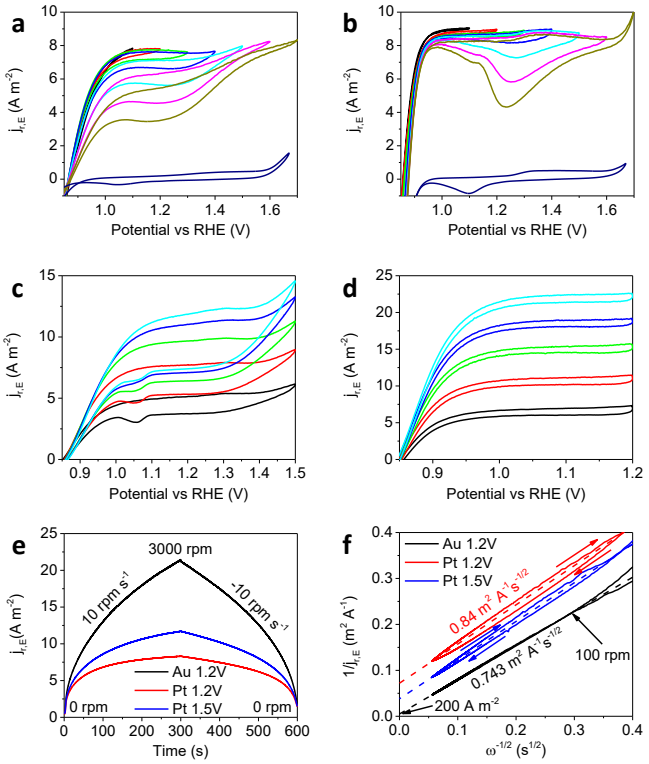

Figure 2. CV of Pt ring (a) and Au ring (b) at 400 rpm. CV of Pt ring (c) and Au ring (d) at ω of 225 rpm, 625 rpm, 1225 rpm, 2025 rpm and 3025 rpm from bottom to top. The scann rate is 10 mV s^{-1}. (e) The amperometric i-t plots. (f) KL plot derived from (e). The electrolyte is 0.1 M KOH containing 1 mM H_2O_2 for all experiments except the lowest curves in (a) and (b).

To prove the H_2O_2 oxidation on Au ring at 1.2 V is mass transfer limited, the amperometric i-t measurements were taken. This time, the potential was fixed while the ω scans from 0 rpm to 3000 rpm and back to 0 rpm in 10 rpm s^{-1}. As shown in Figure 2e, the current on Au ring at 1.2 V is much higher than on the Pt ring at 1.2 V and 1.5 V. The corresponding KL plots are shown in Figure 2f. On Au ring, the positive and negative scans overlap very well in the range of 100 rpm to 3000 rpm, which means the H_2O_2 oxidation on Au is highly reproducible. The extrapolation of KL plot results in an intercept of 200 A m^{-2}, which is at least 5 times higher than the ring currents in ORR (shown later). So the H_2O_2 oxidation must be very close to mass transfer limitation on Au ring. In contrast, the KL plots of positive and negative scans of Pt ring do not overlap. The current of positive scan is larger than that of the negative scan, because the H_2O_2 concentration on the Pt surface increases with increasing the ω, so the Pt ring is getting more oxidized, so an additional anodic current is added to the H_2O_2 oxidation during positive scan, vice versa. This phenomenon is in accordance with the CV result. Moreover, the KL plots of Pt ring are not linear, the intercepts are far from origin, and the slopes are larger than that on the Au ring. All these results prove that the Pt ring current is not mass transfer limited. Therefore, using Pt ring to collect H_2O_2 can lead to underestimated p or overestimated n. In contrast, Au ring biased at 1.2 V is suitable for H_2O_2 collection in alkaline electrolyte. The ORR results shown below are all based on RRDE with Au ring.

Measurement Errors in KL method. Beside the N_C and ring reaction, many other factors can cause errors in electrochemical measurement, which impact the result of n. The resistance and capacitance can influence the measured potential and current density but they can be corrected easily by IR compensation and background subtraction. However, the instability of system and the change of geometry are inevitable.

First, the ORR current is not extremely stable on any catalyst. Even if the change of activity is too small to be observed by naked eye, it may have significant impact to the regression analysis in KL method when current is very small, near onset potential. The environmental parameters, e.g. the viscosity of electrolyte, the diffusion coefficient of O_2 and the saturation concentration of O_2, are also unstable. All of them depend on temperature while the saturation concentration of O_2 also depends on atmospheric pressure, which is even more difficult to control. Moreover, when a RDE is used, it is impossible to seal the electrochemical cell perfectly. Therefore, the rotation of electrode may introduce the air into the cell which causes inhomogeneous distribution of O_2 concentration (lower than saturation) in the electrolyte. All these uncertainties can cause errors in KL method which cannot be eliminated.

Second, the N_C has been proved to be affected by the catalyst layer due to the change in geometry. The KL method uses the same hydrodynamic model so it must be affected too. To evaluate this impact, the reduction of $Fe(CN)_6^{3-}$ is used again, in which n is always 1. Therefore, the KL plot must be linear, and all the data points must coincide at same ω, if the reaction is mass transfer limited. Any inconsistent data can be attributed to the change of hydrodynamics.

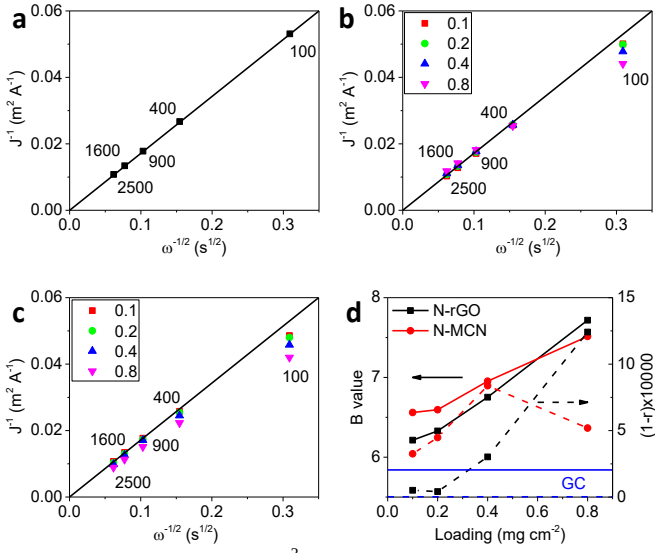

Figure 3. KL plot of $Fe(CN)_6^{3-}$ on bare (a), N-rGO (b) or N-MCN (c) loaded RDE. The potential is 0.1 V .The numbers beside the line are ω in rpm and the numbers in legend are the loading amount of catalysts in mg cm^{-2}. (d) B and r values of the corresponding KL plot.

KL plot of $Fe(CN)_6^{3-}$ reduction on bare RDE at 0.1 V is shown in Figure 3a. As expected, the KL plot shows extremely good linearity with correlation coefficient (r) as high as 0.999998. The fitted line passes the origin, showing very large the J_K so the apparent current is completely limited by mass transfer. This proves that the KL theory is suitable and accurate for $Fe(CN)_6^{3-}$ reduction on an ideal RDE. Afterwards, the KL plots are measured on N-rGO and N-MCN loaded RDE

under same condition. As shown in figure 3b and 3c, the data points obviously don't lie on the fitted line of bare RDE. The deviation increases as the loading of catalysts increases, which is caused by the change of geometry of electrode as aforementioned. In this case, if the KL plots are still mandatorily linear fitted, the B value of equation (4) is quite different from what resulted from bare RDE (Figure 3d). On bare RDE, B is 5.84, while on RDE loaded with N-rGO or N-MCN, it increases from about 6.05 to 7.7 as the loading increases. As a result, if n is calculated from the KL plot, an error from 3 % to 30 % can be induced. The r of KL plot on N-rGO and N-MCN loaded RDE range from 0.99995 to 0.9988. For naked eye, they are already very linear, but actually far poorer than that on bare RDE. This proves that n_{KL} may not be accurate even if the KL plot "looks linear". In our measurement of n_{KL} for ORR in the next session, the lowest catalyst loading is applied so the most accurate possible results are shown. The linearity of KL plot for ORR is expected to be close to that of $Fe(CN)_6^{3-}$ reduction, i.e. r is 0.99995 on N-GO, if the KL theory itself is correct. Another thing to be worthwhile to note is that, on a rough catalyst (e.g. N-MCN), the mass transfer limited current density is always higher than on a bare RDE. This difference has nothing to do with catalytic activity but entirely caused by the geometry of electrode. So the reported ultrahigh ORR current density of such catalysts cannot be attributed to activity.

Result of n. Three metals (Au, Ag and Ru) and three typical carbon-based materials were tested as broadly representative catalysts. Among which, the electrochemically reduced graphene oxide (e-rGO) is a typical oxygen doped carbon. N-rGO is a typical nitrogen doped carbon. $Co(OH)_2$/N-rGO is typical non-precious metal catalysts with metal-nitrogen-carbon structure. All the catalysts are thin and smooth enough to keep the change of geometry of RRDE negligible. The RRDE polarization curves are provided in Figure S6 – S17. The ring current densities are normalized by disk area and divided by N_C. The n_{KL} are calculated based on j_d at different all ω. The KL plots at selected potentials are provided in Figure S18 to S23. The n_{RRDE} and n_{KL} of the catalysts are shown in Figure 4.

As the calculated n_{KL} also depends on the parameters in equation (5), Ru is used as a benchmark to calibrate them. The n_{RRDE} of Ru is very close to 4 at 0.2 V (Figure 4a). At this potential, the ORR on Ru is also mass transfer limited (Figure S6). Therefore j is equal to j_L and n is 4 in equation (5). By using proper parameters (see Supporting Information), the n_{KL} at 0.2 V is set to 4. These parameters are used for all later n_{KL} calculation. Below 0.2 V, the underpotential hydrogen deposition occurs so that the n_{KL} is affected. Above 0.2 V, n_{RRDE} decreases with potential at any ω. A significant splitting of n_{RRDE} is also observed. In contrast, n_{KL} increases as potential increases from 0.2 V, which exceeds the theoretical limitation of 4, and even goes to infinity at higher potential. The trend of n on Au, Ag, N-rGO and $Co(OH)_2$/N-rGO are similar to Ru. On them, the n_{RRDE} decreases as ω increases, the n_{KL} are higher than the n_{RRDE} and the n_{KL} go to infinity at high potential. The only exception is e-rGO, on which n_{RRDE} increase as ω increases, the n_{KL} are mostly lower than the n_{RRDE} and go below 2 (another theoretical limitation) at high potential. As we have proved in previous sessions, the n_{RRDE} is considered to be the real n, so the n_{KL} must not be real n because it not only contradicts n_{RRDE} but also exceeds the theoretical limitation. Therefore, adopting KL method to these materials can induce a huge error in calculated n value.

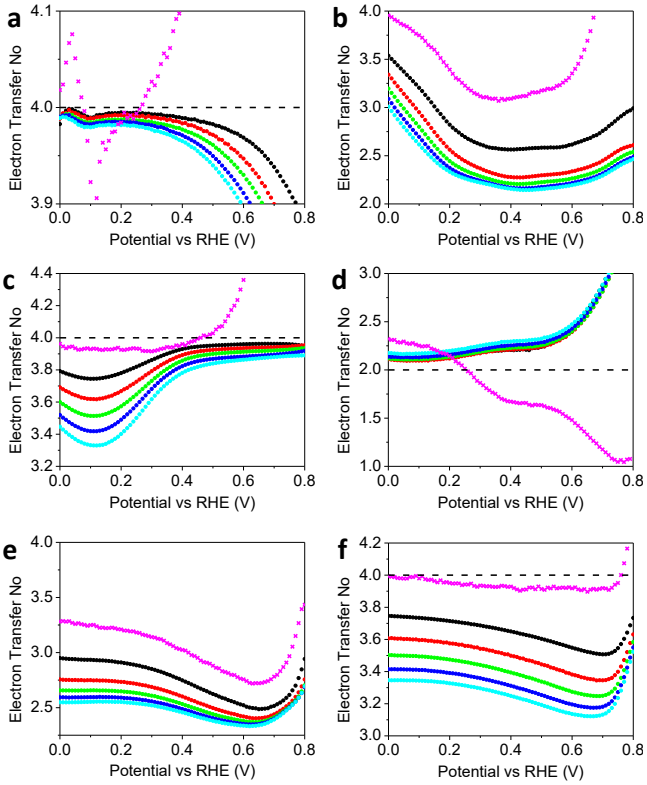

Figure 4. The n of Ru (a), Au (b), Ag (c), e-rGO (d), N-rGO (e) and $Co(OH)_2$/N-rGO (f). n_{RRDE} (circles) are measured at ω of 225 rpm (Black), 625 rpm (red), 1225 rpm (green) 2025 rpm (blue) and 3025 rpm (cyan). Magenta cross: n_{KL}.

A catalyst is defined as a "normal" catalyst by us, if n decreases as ω increases. The relationship between n_{KL} and n_{RRDE} can be explained by the calculation process of n_{KL} as follows. When KL equation is used, the j_L is assumed proportional to $\omega^{1/2}$, but on a "normal" catalyst, j_L increases slower than assumed because of decrease of n, so the KL slope is also lower than expected. The lower KL slope leads to higher calculated n_{KL}. The trend is just reversed on a "abnormal" catalyst whose n increases as ω increases.

Another way to examine the KL method is to investigate the r of KL plot. Figure 5 shows that r of all the catalysts except $Co(OH)_2$/N-rGO are lower than 0.99995. For example, the r of KL plot of N-rGO is about 0.9997 at most potential, which is significantly lower than the measured value of the $Fe(CN)_6^{3-}$ reduction (0.99995). Theoretically, the non-linearity can be attributed to random error or systematic error. The random error should make r fluctuate heavily but it actually changes relatively smoothly with potential so the non-linearity should be caused by the error of KL method itself. Note that even on the $Co(OH)_2$/N-rGO whose KL plot is very linear by any standard, the n_{KL} is still very different from the n_{RRDE}. This suggests that though the linearity of KL plot is the necessary condition of the validity of KL method, it is not the sufficient condition. In other words, the n_{KL} can still very inaccurate even if the KL plot is very linear.

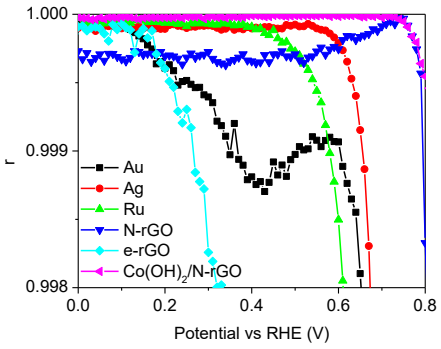

Figure 5. Correlation coefficients of KL plots of ORR.

Mathematical modeling. To figure out the problems in KL method and explain our results, the derivation of KL equation is carefully examined. A simple solution of the convective-diffusion equation on a one-step and irreversible reaction is provided in the Supporting Information, which is exactly the same as described in Bard's text book.[24] The result is represented by:

$$\frac{j}{nF} = m(C^* - C^0) \quad (8)$$

where j is the current density; C^0 is concentrations of reactant on electrode surface; m is the mass transfer coefficient of the reactant, which is given by:

$$m = 0.62D^{\frac{2}{3}}\nu^{-\frac{1}{6}}\omega^{\frac{1}{2}} \quad (9)$$

The physical meaning of equation (8) is that the current density is proportional to the flux of reactant. If the reaction is first-order, the current density is proportional C^0:

$$j = nkFC^0 \quad (10)$$

where k is the reaction rate constant. Combining equation (8) and (10) yields:

$$\frac{1}{j} = \frac{1}{nFmC^*} + \frac{1}{nkFC^*} \quad (11)$$

where $nFmC^*$ is the current density limited by mass transfer, which is denoted by j_L (Levich theory). $nkFC^*$ is the current density limited by reaction kinetics (in absence of mass transfer effect), which is denoted by j_K (Koutecky theory). Then equation (10) can be rewritten as equation (4). Note that this result is based on the assumption of *one-step*, *irreversible* and *first-order* reaction. As for ORR, the reaction is obviously not one-step as discussed in the introduction. Furthermore, the equilibrium potential of reaction (2e) is about 0.7 V, which is within the ORR potential window (0 to 1 V), so reaction (2e) is reversible. Therefore, the conditions of KL theory are not satisfied by ORR. A revised form of KL equations for ORR can be derived, which takes into account the multistep and reversible natures of ORR but retains the first-order assumption, as shown below.

In ORR, there are two reactants: the O_2 and the H_2O_2. Their corresponding parameters (C, m and D) are subscripted by O and P respectively. The current densities and rate constants of reaction (4e), (2e) and (2'e) are subscripted by 4, 2 (forward reaction), -2 (backward reaction) and 2' respectively. According to the solution of the convective-diffusion equation, the following equations are derived, which are similar to equation (8):

$$\frac{j_4}{4F} + \frac{j_2}{2F} = m_O(C_O^* - C_O^0) \quad (13)$$

$$\frac{j_{2'}}{2F} - \frac{j_2}{2F} = m_P(C_P^* - C_P^0) \quad (14)$$

The physical meaning of equation (13) and (14) is that the current densities of O_2 and H_2O_2 related reactions are proportional to their fluxes. C_P^* is 0 because no H_2O_2 exists in the bulk electrolyte. Assuming the all the reactions are first-order, similar to equation (10), the current densities of the sub-reactions can be presented as:

$$j_4 = 4Fk_4C_O^0 \quad (15)$$

$$j_{2'} = 2Fk_{2'}C_P^0 \quad (16)$$

$$j_2 = 2Fk_2C_O^0 - 2Fk_{-2}C_P^0 \quad (17)$$

Here, we have 5 unknowns: j_2, j_4, $j_{2'}$, C_O^0 and C_P^0; and 5 linear equations: (13) - (17). Therefore all the unknowns can be solved. The complete set of solution is listed below:

$$C_P^0 = \frac{k_2m_OC_O^*}{(k_4+k_2+m_O)(k_{-2}+k_{2'}+m_P)-k_2k_{-2}} \quad (18)$$

$$C_O^0 = \frac{m_OC_O^*(k_{-2}+k_{2'}+m_P)}{(k_4+k_2+m_O)(k_{-2}+k_{2'}+m_P)-k_2k_{-2}} \quad (19)$$

$$j_4 = \frac{4Fk_4m_OC_O^*(k_{-2}+k_{2'}+m_P)}{(k_4+k_2+m_O)(k_{-2}+k_{2'}+m_P)-k_2k_{-2}} \quad (20)$$

$$j_{2'} = \frac{2Fk_2k_{2'}m_OC_O^*}{(k_4+k_2+m_O)(k_{-2}+k_{2'}+m_P)-k_2k_{-2}} \quad (21)$$

$$j_2 = \frac{2Fk_2m_OC_O^*(k_{2'}+m_P)}{(k_4+k_2+m_O)(k_{-2}+k_{2'}+m_P)-k_2k_{-2}} \quad (22)$$

The disk current is the sum of j_4, j_2 and $j_{2'}$, which is:

$$j_d = 2Fm_OC_O^*\frac{2k_4(k_{-2}+k_{2'}+m_P)+2k_{2'}k_2+k_2m_P}{(k_4+k_2+m_O)(k_{-2}+k_{2'}+m_P)-k_2k_{-2}} \quad (23)$$

Obviously, j_d is no longer in the form of KL equation (4). Therefore, no linear relationship between $1/j_d$ and $\omega^{-1/2}$ is expected. Furthermore, at very high potential, $k_4 \to 0$, $k_2 \to 0$, $k_{2'} \to 0$ and $k_{-2} \to \infty$. Equation (23) is simplified to:

$$j_d = 4Fk_4C_O^* \quad (24)$$

If j_d is independent on ω, the KL slope is 0, so the calculated n_{KL} is infinity. That is why all n_{KL} values go to infinity in figure 4, except e-rGO. The ring current is the rate of net H_2O_2 production:

$$\frac{j_r}{N_C} = j_2 - j_{2'} = \frac{2Fm_Pm_OC_O^*k_2}{(k_4+k_2+m_O)(k_{-2}+k_{2'}+m_P)-k_{-2}k_2} \quad (25)$$

Note that the ratio between j_r and j_d is not a constant at certain rate constants (functions of potential). It is a function of m_O and m_P, i.e. the ω. These results theoretically prove that the n is a function of ω and KL method is not correct for ORR. Inserting equation (24) and (25) into equation (2) yields:

$$p = \frac{m_Pk_2}{(k_4+k_2)(k_{-2}+k_{2'}+m_P)-k_{-2}k_2} \quad (26)$$

Or:

$$\frac{1}{p} = \left[\frac{k_4}{k_2}k_{-2} + k_{2'}\left(\frac{k_4}{k_2}+1\right)\right]\frac{1}{m_P} + \left(\frac{k_4}{k_2}+1\right) \quad (27)$$

This result shows that 1/p has linear relationship with $1/m_p$. 1/p is independent on ω if and only if both $k_{2'}$ and k_{-2} are 0 because k_4/k_2 is positive. This suggests that the dependency of p on ω is originated from reaction (2'e) and (2e), in which H_2O_2 is the reactant. To understand this dependency, divide equation (18) by (19):

$$\frac{C_P^0}{C_O^0} = \frac{k_2}{k_{-2}+k_{2'}+m_P} \quad (28)$$

Equation (28) shows that C_P^0 increases slower than C_O^0 with ω. It is because higher ω not only accelerates O_2 transfer to the electrode but also the H_2O_2 transfer from electrode. Therefore the increase of rate of H_2O_2 production reaction with ω is faster than that of H_2O_2 consumption reaction, therefore p increases with ω.

The 1/p vs $1/m_p$ plot can be used as the criteria of applicability of our model. If the model is correct, the plot must be linear, the slope must be positive and the intercept must be larger than 1. The 1/p vs $1/m_P$ plots on the tested catalysts are shown in Figure 6. Obviously, the linearity of 1/p vs $1/m_P$ plots is not perfectly good on all catalyst, but quite good on Ag, N-rGO and $Co(OH)_2$/N-rGO. On Ru, the peroxide ratio is too small so that the effect of underpotential hydrogen deposition is significant, but the trend is in consistent with our model. On Au, the linearity of the plots is not good though they increase monotonically. On e-rGO, the plots violate our model significantly. The plots are non-linear and decrease monotonically. Combining the discussion in n results, we can conclude that our model is correct on "normal" catalysts but incorrect on the "abnormal" catalysts. Au seems to be "normal" but actually "abnormal".

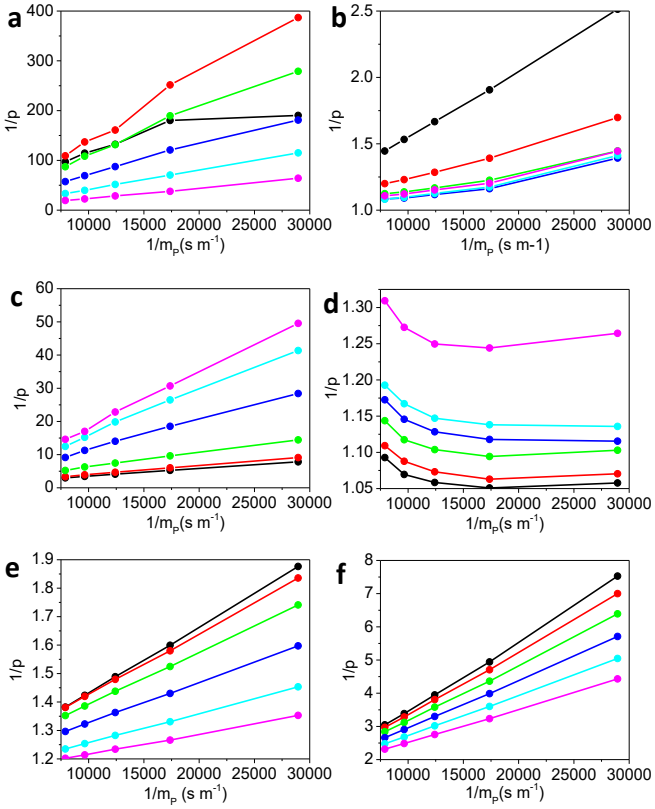

Figure 6. 1/p vs $1/m_P$ plot of ORR on Ru (a), Au (b), Ag (c), e-rGO (d), N-rGO (e) and $Co(OH)_2$/N-rGO (f). The potential is 0.1 V (black), 0.2 V (red), 0.3 V (green), 0.4 V (blue), 0.5 V (cyan) and 0.6 V (magenta), respectively.

Now the only remaining question is that why our model could be incorrect on "abnormal" catalysts. By reconsidering our derivation, it is found that equation (13) and (14) are the results of convective-diffusive equation which has solid theoretical background and has been verified in practice for a long time. Equations (15) to (17) are based on the assumption that all the sub-reactions are first order. In fact, an electrochemical reaction doesn't need to be first-order. For example, the order of the simplest hydrogen evolution reaction depends on both catalyst and coverage (potential).[40] ORR is more complicated due to more intermediates and steps. In fact, there has already been a long-term controversy on the order of ORR on Pt.[41-43] According to our result, the order of the sub-reactions of ORR on the "normal" catalysts can be close to 1 but far from 1 on the "abnormal" catalysts.

CONCLUSIONS

We examine the measurement of electron transfer number of ORR by both experiment and theory. In the RRDE measurement method, we find that the collection coefficient depends on the loading amount and surface roughness of catalysts significantly. To get accurate result, the loading amount of catalysts should be the lowest and the collection coefficient must be calibrated for each measurement. The Pt ring is proved not suitable for H_2O_2 collection experiment in alkaline electrolyte. Alternatively, the Au ring biased at 1.2 V guarantees the collection coefficient is valid. We also find that the electron transfer number is dependent on angular velocity and the KL method provides greatly different results from the RRDE method. By establishing a new mathematical model, we found that the KL method is not suitable for determining electron transfer number of ORR since ORR is neither one-step nor reversible. We further proved that the ORR is not first-order on some catalysts. Only RRDE method with calibrated N_C and properly biased Au ring is reliable both theoretically and experimentally. These contributions will help the researchers to measure ORR performance accurately and understand the ORR mechanism correctly.

ASSOCIATED CONTENT

Supporting Information. The synthesis of materials, SEM of samples, and LSV and KL plot of ORR can be found in the supporting information. This material is available free of charge via the Internet at http://pubs.acs.org.

AUTHOR INFORMATION

Corresponding Author

***E-mail: s.qiao@adelaide.edu.au**

Author Contributions

S.Z. Qiao designed the research. R.F. Zhou synthesized materials, conducted characterizations, electrochemical measurements and built the mathematical model. All authors discussed and analyzed the data. The manuscript was written through contributions of all authors. All authors have given approval to the final version of the manuscript.

ACKNOWLEDGMENTS

This work is financially supported by the Australian Research Council (ARC) through the Discovery Project programs (DP130104459 and DP140104062).

REFERENCES

1. Jirkovsky, J. S.; Panas, I.; Ahlberg, E.; Halasa, M.; Romani, S.; Schiffrin, D. J., *J. Am. Chem. Soc.* **2011,** *133* (48), 19432-19441.
2. Assumpcao, M.; De Souza, R. F. B.; Rascio, D. C.; Silva, J. C. M.; Calegaro, M. L.; Gaubeur, I.; Paixao, T.; Hammer, P.; Lanza, M. R. V.; Santos, M. C., *Carbon* **2011,** *49* (8), 2842-2851.
3. Fu, L.; You, S. J.; Yang, F. L.; Gao, M. M.; Fang, X. H.; Zhang, G. Q., *J. Chem. Technol. Biotechnol.* **2010,** *85* (5), 715-719.
4. Siahrostami, S.; Verdaguer-Casadevall, A.; Karamad, M.; Deiana, D.; Malacrida, P.; Wickman, B.; Escudero-Escribano, M.; Paoli, E. A.; Frydendal, R.; Hansen, T. W.; Chorkendorff, I.; Stephens, I. E. L.; Rossmeisl, J., *Nat. Mater.* **2013,** *12* (12), 1137-1143.
5. Li, H.; Tsay, K.; Wang, H. J.; Shen, J.; Wu, S. H.; Zhang, J. J.; Jia, N. Y.; Wessel, S.; Abouatallah, R.; Joos, N.; Schrooten, J., *J. Power Sources* **2010,** *195* (24), 8089-8093.
6. Qiao, J. L.; Saito, M.; Hayamizu, K.; Okada, T., *J. Electrochem. Soc.* **2006,** *153* (6), A967-A974.
7. Yu, J. R.; Yi, B. L.; Xing, D. M.; Liu, F. Q.; Shao, Z. G.; Fu, Y. Z., *Phys. Chem. Chem. Phys.* **2003,** *5* (3), 611-615.

8. Liang, Y. Y.; Wang, H. L.; Zhou, J. G.; Li, Y. G.; Wang, J.; Regier, T.; Dai, H. J., *J. Am. Chem. Soc.* **2012,** *134* (7), 3517-3523.
9. Wu, Z. S.; Yang, S. B.; Sun, Y.; Parvez, K.; Feng, X. L.; Mullen, K., *J. Am. Chem. Soc.* **2012,** *134* (22), 9082-9085.
10. Liang, Y. Y.; Li, Y. G.; Wang, H. L.; Zhou, J. G.; Wang, J.; Regier, T.; Dai, H. J., *Nat. Mater.* **2011,** *10* (10), 780-786.
11. Li, Y. G.; Zhou, W.; Wang, H. L.; Xie, L. M.; Liang, Y. Y.; Wei, F.; Idrobo, J. C.; Pennycook, S. J.; Dai, H. J., *Nat. Nanotech.* **2012,** *7* (6), 394-400.
12. Gong, K. P.; Du, F.; Xia, Z. H.; Durstock, M.; Dai, L. M., *Science* **2009,** *323* (5915), 760-764.
13. Wu, G.; More, K. L.; Johnston, C. M.; Zelenay, P., *Science* **2011,** *332* (6028), 443-447.
14. Frumkin, A.; Nekrasov, L.; Levich, B.; Ivanov, J., *J. Electroanal. Chem.* **1959,** *1* (1), 84-90.
15. Müller, L.; Nekrassow, L., *Electrochim. Acta* **1964,** *9* (7), 1015-1023.
16. Koutecky, J.; Levich, B. G., *Zh. Fiz. Khim.* **1958,** *32* (7), 1565-1575.
17. Zhou, R. F.; Zheng, Y.; Hulicova-Jurcakova, D.; Qiao, S. Z., *J. Mater. Chem. A* **2013,** *1* (42), 13179-13185.
18. Zhou, R. F.; Qiao, S. Z., *Chem. Mater.* **2014,** *26* (20), 5868-5873.
19. Duan, J. J.; Zheng, Y.; Chen, S.; Tang, Y. H.; Jaroniec, M.; Qiao, S. Z., *Chem. Commun.* **2013,** *49* (70), 7705-7707.
20. Zheng, Y.; Jiao, Y.; Ge, L.; Jaroniec, M.; Qiao, S. Z., *Angew. Chem. Int. Ed.* **2013,** *52* (11), 3110-3116.
21. Kim, J.-D.; Pyun, S.-I.; Yang, T.-H.; Ju, J.-B., *J. Electroanal. Chem.* **1995,** *383* (1–2), 161-166.
22. Mamlouk, M.; Kumar, S. M. S.; Gouerec, P.; Scott, K., *J. Power Sources* **2011,** *196* (18), 7594-7600.
23. Zhang, H.-J.; Li, H.; Li, X.; Qiu, H.; Yuan, X.; Zhao, B.; Ma, Z.-F.; Yang, J., *Int. J. Hydrogen Energy* **2014,** *39* (1), 267-276.
24. Bard, A. J.; Faulkner, L. R., *Electrochemical Methods: Fundamentals and Applications*. Wiley: 2000.
25. Wroblowa, H. S.; Yen Chi, P.; Razumney, G., *J. Electroanal. Chem. Interfacial Electrochem.* **1976,** *69* (2), 195-201.
26. Hsueh, K. L.; Chin, D. T.; Srinivasan, S., *J. Electroanal. Chem. Interfacial Electrochem.* **1983,** *153* (1–2), 79-95.
27. Anastasijevic, N. A.; Vesovic, V.; Adzic, R. R., *J. Electroanal. Chem.* **1987,** *229* (1-2), 305-316.
28. Anastasijevic, N. A.; Vesovic, V.; Adzic, R. R., *J. Electroanal. Chem.* **1987,** *229* (1-2), 317-325.
29. Damjanovic, A.; Genshaw, M. A.; Bockris, J. O.; apos; M., *J. Chem. Phys.* **1966,** *45* (11), 4057-4059.
30. Markovic, N. M.; Gasteiger, H. A.; Philip, N., *J. Phys. Chem.* **1996,** *100* (16), 6715-6721.
31. Markovic, N. M.; Gasteiger, H. A.; Ross, P. N., *J. Phys. Chem.* **1995,** *99* (11), 3411-3415.
32. El Mouahid, O.; Coutanceau, C.; Belgsir, E. M.; Crouigneau, P.; Léger, J. M.; Lamy, C., *J. Electroanal. Chem.* **1997,** *426* (1–2), 117-123.
33. Pleskov, I. U. V.; Filinovskiĭ, V. I. U., *The rotating disc electrode*. Consultants Bureau: 1976.
34. Treimer, S.; Tang, A.; Johnson, D. C., *Electroanalysis* **2002,** *14* (3), 165-171.
35. Masa, J.; Batchelor-McAuley, C.; Schuhmann, W.; Compton, R., *Nano Research* **2014,** *7* (1), 71-78.
36. Shin, D.; Jeong, B.; Choun, M.; Ocon, J. D.; Lee, J., *RSC Adv.* **2015,** *5* (2), 1571-1580.
37. Zhou, R.; Qiao, S. Z., *Chem. Commun.* **2015,** *51* (35), 7516-7519.
38. Wu, G.; More, K. L.; Xu, P.; Wang, H. L.; Ferrandon, M.; Kropf, A. J.; Myers, D. J.; Ma, S. G.; Johnston, C. M.; Zelenay, P., *Chem. Commun.* **2013,** *49* (32), 3291-3293.
39. Chung, H. T.; Won, J. H.; Zelenay, P., *Nat. Commun.* **2013,** *4*.
40. Conway, B. E.; Salomon, M., *Electrochim. Acta* **1964,** *9* (12), 1599-1615.
41. Ross, P. N.; Andricacos, P. C., *J. Electroanal. Chem. Interfacial Electrochem.* **1983,** *154* (1–2), 205-215.
42. Ross, P. N.; Cairns, E. J.; Striebel, K.; McLarnon, F.; Andricacos, P. C., *Electrochim. Acta* **1987,** *32* (2), 355-355.
43. Hsueh, K. L.; Chang, H. H.; Chin, D. T.; Srinivasan, S., *Electrochim. Acta* **1985,** *30* (9), 1137-1142.

Supporting information

Electron Transfer Number of Oxygen Reduction Reaction: from Theory to Measurement

Ruifeng Zhou[1, 2], Yao Zheng[1], Piotr Zelenay[3] and Shi Zhang Qiao[1, *]

1 School of Chemical Engineering, the University of Adelaide, Adelaide, SA 5005, Australia.

2 Australian Institute for Bioengineering and Nanotechnology, the University of Queensland, St Lucia, QLD 4072, Australia.

3 Materials Physics and Applications Division, Los Alamos National Laboratory, Los Alamos, NM 87545, USA.

1. Experimental and Calculation Details

1.1 Preparation of catalysts

N-MCN: In a typical synthesis of N-MCN, a solution was prepared by mixing 80 mL ethanol and 200 mL of distilled water. Subsequently, 1 g of F127, 1.3 g of CTAB, and 2 g of cysteine were added into the mixed solution under continuous stirring. Then, 2 g of 3-aminophenol was added and stirred until it was completely dissolved. Next, 2.8 mL of 37 wt% formaldehyde was dropped in and the stirring was kept for another 24 h at 25 °C. Finally, the mixture was transferred to autoclave and kept at 100 °C for another 24 h. The resulting resin was obtained by washing with water and ethanol for 3 times. In order to obtain N-MCN, the resin were carbonized under N_2 flow in the tube furnace by heating up to 350 °C with a rate of 1 °C/min, dwelling of 2 h, then heating up to 700 °C with a rate of 1 °C/min and dwelling for 4 h.

N-rGO: Graphite flake (3 g) was mixed with concentrated H_2SO_4 (12 ml), $K_2S_2O_8$ (2.5 g), and P_2O_5 (2.5 g). The mixture was kept at 90 °C for 6 h, then cooled to room temperature and diluted with 0.5 L of DI water. The suspension was filtered and washed with DI water. The solid was dried in vacuum at 50 °C overnight. The pre-treated graphite was put into cold (0 °C) concentrated H_2SO_4 (120 mL). Then, $KMnO_4$ (15 g) was added gradually under stirring and the temperature of the mixture was kept to be below 20 °C by ice cooling. The mixture was stirred at 40 °C for 3 h, and then diluted with DI water (250 mL) using ice bath cooling. It was then stirred for 2 h, and additional 0.7 L of DI water was added. 20 mL of 30% H_2O_2 was added to the mixture. Then it was washed with 1:10 HCl aqueous solution (1 L).

The resulting graphite oxide was diluted in DI water. Exfoliation was carried out by sonicating graphite oxide dispersion under ambient condition for 30 min, followed with centrifuging at 3000 rpm for 30 min to eliminate unexfoliated graphite.

To synthesize N-rGO, 5 ml of 25% NH_3 aqueous solution was added into 65 ml 0.1% GO solution. The solution was stirred at 90 °C for 12 h. After reduction, the N-rGO was filtered and washed with water and dispersed in water by supersonication.

1.2 Preparation of electrode

N-MCN: 2 mg of N-MCN was dispersed in 0.2 % Nafion aqueous solution by supersonication. The 25 μL of the catalyst ink was dipped on the disk electrode and dried under ambient environment.

e-rGO: 25 μL of 0.1 % GO aqueous suspension and 25 μL of 0.1 % Nafion aqueous solution were dipped on the disk electrode and dried under ambient environment. CV from -0.2 V to 1 V was applied to the electrode until the GO was fully reduced (no significant cathodic current is observed).

N-rGO: 25 μL of 0.1 % N-rGO aqueous suspension and 25 μL of 0.1 % Nafion aqueous solution were dipped on the disk electrode and dried under ambient environment.

$Co(OH)_2$/N-rGO: 25 μL of 0.1 M $CoCl_2$ was dipped on the N-rGO electrode. The electrode was kept in water saturated atmosphere for 1 hour. The $Co(Ac)_2$ drop was then flushed with DI water and the electrode was dried under ambient environment.

Au: the disk as the working electrode is immersed in 0.025 M $HAuCl_4$ solution. A Pt wire was used as a counter electrode. A constant current of -2.5 mA cm^{-2} was applied to the electrode for 100 s. The electrode was then washed with DI water.

Ag: the disk as the working electrode is immersed in 0.1 M $AgNO_3$ solution. A Pt wire was used as a counter electrode. A constant current of -2.5 mA cm^{-2} was applied to the electrode for 100 s. The electrode was then washed with DI water.

Ru: the disk as the working electrode was immersed in 0.05 M $RuCl_3$ solution. A Pt wire was used as a counter electrode. A constant current of -2.5 mA cm^{-2} was applied to the electrode for 100 s. The electrode was then washed with DI water.

1.3 Calibration of N_C

When calibrating N_C, N_2 saturated 0.1 M KOH and 0.004 M $K_3Fe(CN)_6$ were used as the electrolyte. The electrodes were the same as ORR measurement. The electrode was rotated at the certain angular velocity and the amperometric i-t measurement was applied. The disk was set to 0.1 V and the ring was set to 1.5 V. The reaction on disk and ring are:

Disk: $Fe(\mathrm{CN})_6{}^{3-} + e^- \rightarrow Fe(\mathrm{CN})_6{}^{4-}$

Ring: $Fe(\mathrm{CN})_6{}^{4-} \rightarrow Fe(\mathrm{CN})_6{}^{3-} + e^-$

The measurement lasted 60 s and the disk and ring currents (I_d and I_r) of the last 10 s were averaged. The measurement was repeated once with the disk disconnected. The ring currents (I_{r0}) of the last 10 s were averaged. I_{r0} includes all the anodic currents that are not from $Fe(CN)_6^{4-}$ reduced on the disk. They may be oxidation of water, free $Fe(CN)_6^{4-}$ or any impurities. The N is calculated by the equation:

$$N_C = \frac{I_r - I_{r0}}{I_d}$$

1.4 Parameters used in KL method

F = 96485 C

$C_O^* = 1.22\ m^{-3}$

$D_O = 1.98 * 10^{-9}\ m^2\ s^{-1}$

$\nu = 1.004 * 10^{-6}\ m^2\ s^{-1}$

$D_P = 1.27 * 10^{-9}\ m^2\ s^{-1}$

1.5 Derivation of KL equation

On a rotation disk, the approximate solution of the velocity ($\vec{v}$) of liquid near disk surface is represented in cylindrical coordinates by:

$$\vec{v} = v_r\hat{r} + v_\varphi\hat{y} + v_y\hat{\varphi}$$

$$v_r = r\omega\left(a\gamma - \frac{\gamma^2}{2} - \frac{b\gamma^3}{3} + o(\gamma^3)\right) \approx -0.51\omega^{\frac{3}{2}}\nu^{-\frac{1}{2}}ry$$

$$v_\varphi = r\omega\left(1 - b\gamma^2 - \frac{a\gamma^3}{3} + o(\gamma^3)\right) \approx r\omega$$

$$v_y = r\omega\left(-a\gamma^2 - \frac{\gamma^3}{3} - \frac{b\gamma^4}{6} + o(\gamma^3)\right) \approx -0.51\omega^{\frac{3}{2}}\nu^{-\frac{1}{2}}y^2$$

$$\gamma = \left(\frac{\omega}{\nu}\right)^{\frac{1}{2}} y$$

$\hat{r}$, $\hat{\varphi}$ and $\hat{y}$ are unit vectors in in radial, azimuthal and axial directions respectively, from centre of the disk. r, φ and y are the radial, azimuthal and axial displacement. υ_r, υ_φ and υ_y are the velocities in radial, azimuthal and axial directions. ω is the angular velocity of the disk. ν is the kinematic viscosity of the liquid. α and β are constants. o(x) is high level infinitesimal of x.

The general convective-diffusion equation is:

$$\vec{J} = -D\nabla C - \frac{zF}{RT}DC\nabla\Phi + C\vec{v}$$

J is the flux of a certain species. The three items represent diffusion, migration and convection successively. For solution containing an excess of supporting electrolyte, the ionic migration term can be neglected. D is the diffusion coefficient. C is the concentration. The variation of concentration with time is given by:

$$\frac{\partial C}{\partial t} = -\nabla \cdot \vec{J} = D\nabla^2 C - \nabla C \cdot \vec{v}$$

In steady case,

$$\frac{\partial C}{\partial t} = 0$$

In cylindrical coordinates,

$$\vec{\nabla} = \frac{\partial}{\partial r}\hat{r} + \frac{\partial}{\partial y}\hat{y} + \frac{\partial}{\partial \varphi}\frac{1}{r}\hat{\varphi}$$

$$\nabla^2 = \frac{1}{r}\left[\frac{\partial}{\partial r}\left(r\frac{\partial}{\partial r}\right) + \frac{\partial}{\partial y}\left(r\frac{\partial}{\partial y}\right) + \frac{\partial}{\partial \varphi}\left(\frac{1}{r}\frac{\partial}{\partial \varphi}\right)\right]$$

So that,

$$v_r\frac{\partial C}{\partial r} + \frac{v_\varphi}{r}\frac{\partial C}{\partial \varphi} + v_y\frac{\partial C}{\partial y} = D\left[\frac{1}{r}\frac{\partial}{\partial r}\left(r\frac{\partial C}{\partial r}\right) + \frac{1}{r^2}\frac{\partial^2 C}{\partial \varphi^2} + \frac{\partial^2 C}{\partial y^2}\right]$$

For the reason of symmetry,

$$\frac{\partial C}{\partial \varphi} = 0$$

For the limiting current condition C=0 at y=0. And, since υ_y does not depends on r,

$$\frac{\partial C}{\partial r} = 0$$

As a result,

$$\upsilon_y \frac{\partial C}{\partial y} = D \frac{\partial^2 C}{\partial y^2}$$

Or,

$$\frac{\partial^2 C}{\partial y^2} = -\frac{y^2}{B}\frac{\partial C}{\partial y}$$

$$B = 1.96 D \omega^{-\frac{3}{2}} \nu^{\frac{1}{2}}$$

Let

$$X = \frac{\partial C}{\partial y}$$

Then,

$$\frac{\partial X}{\partial y} = -\frac{y^2}{B} X$$

$$\int \frac{1}{X} dX = -\frac{1}{B} \int y^2 dy$$

$$\ln \frac{X}{X_0} = -\frac{1}{3B} y^3$$

Return to C,

$$\frac{\partial C}{\partial y} = \frac{\partial C}{\partial y}\Big|_{y=0} e^{-\frac{1}{3B} y^3}$$

$$C|_{y=\infty} - C|_{y=0} = \frac{\partial C}{\partial y}\Big|_{y=0} \int_0^{\infty} e^{-\frac{1}{3B} y^3} dy$$

Let, $C|_{y=\infty} = C^*$ and $C|_{y=0} = C^0$, and do the integral,

$$C^* - C^0 = \left.\frac{\partial C}{\partial y}\right|_{y=0} 0.893(3B)^{\frac{1}{3}} = 1.61 D^{\frac{1}{3}} \omega^{-\frac{1}{2}} \nu^{\frac{1}{6}} \left.\frac{\partial C}{\partial y}\right|_{y=0}$$

$$\left.\frac{\partial C}{\partial y}\right|_{y=0} = 0.62 D^{-\frac{1}{3}} \nu^{-\frac{1}{6}} \omega^{\frac{1}{2}} (C^* - C^0) = \frac{m}{D}(C^* - C^0)$$

$$m = 0.62 D^{\frac{2}{3}} \nu^{-\frac{1}{6}} \omega^{\frac{1}{2}}$$

m is defined the mass transfer coefficient.

The current is the flux at the electrode surface,

$$j = nFD \left.\frac{\partial C}{\partial y}\right|_{y=0} = nFm(C^* - C^0)$$

2. Supporting Figures

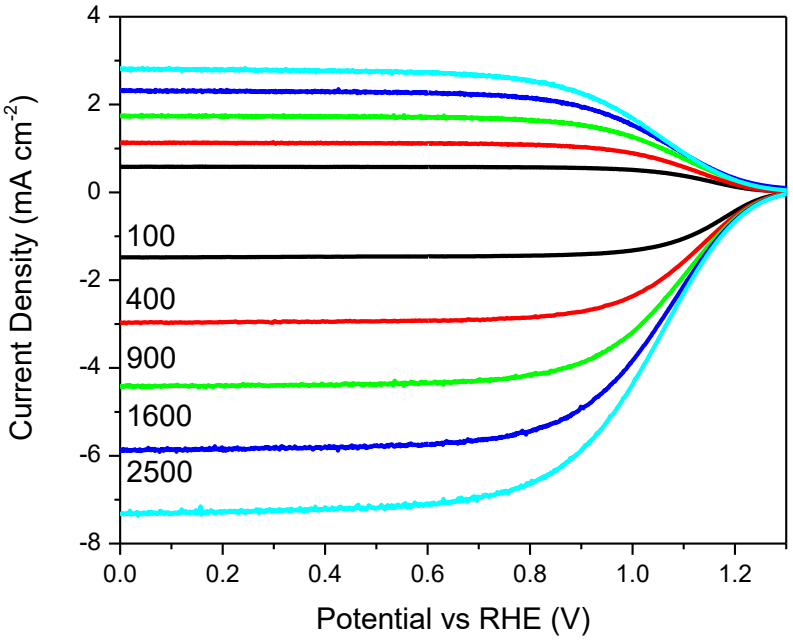

Figure S1. LSV of bare GC disk in 0.1 M KOH and 0.004 M $K_3Fe(CN)_6$. The ring is biased at 1.5V. The cathodic current is disk current and the anodic current is ring current. The current is normalized with disk area. The legends are angular velocity in rpm.

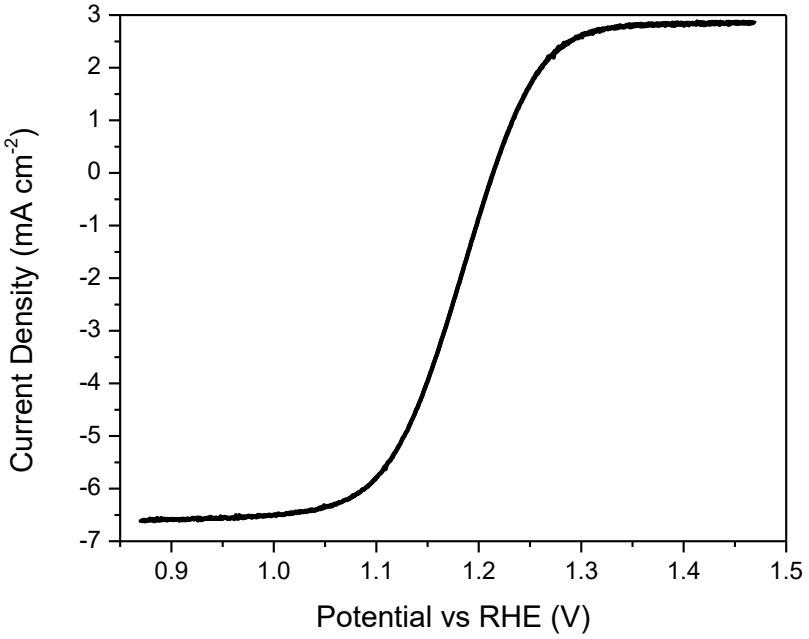

Figure S2. LSV of Pt ring in 0.1 M KOH and 0.004 M $K_3Fe(CN)_6$. The disk is bare GC and biased at 0.1 V. The current is normalized with disk area.

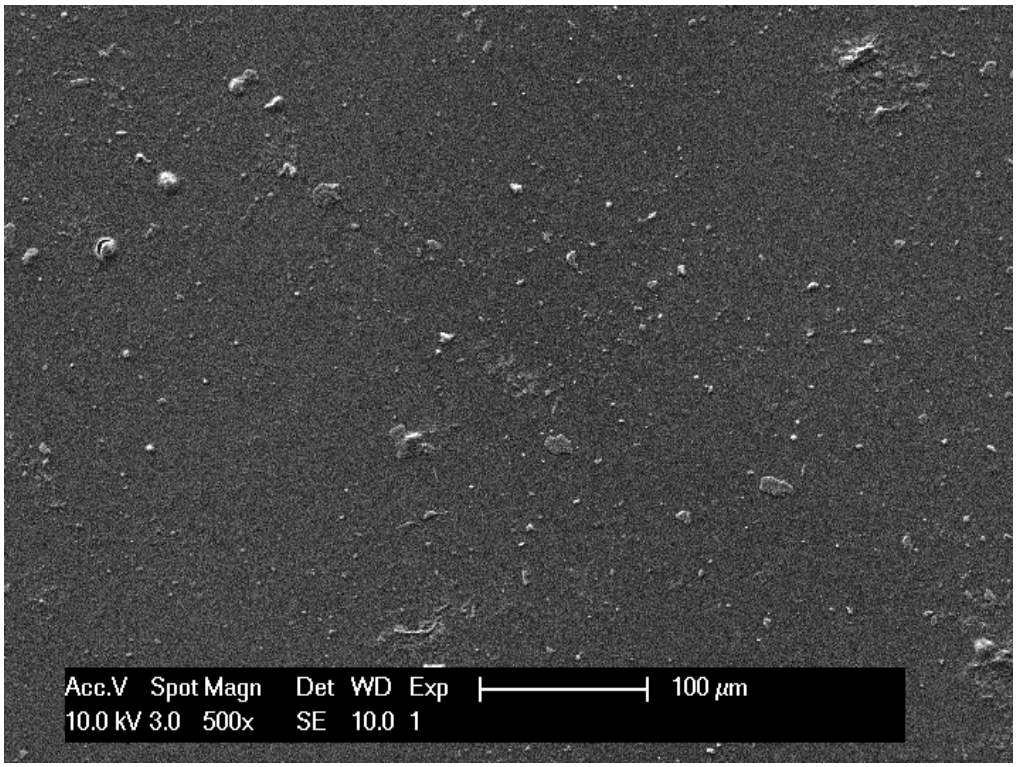

Figure S3. SEM image of the surface of N-rGO electrode.

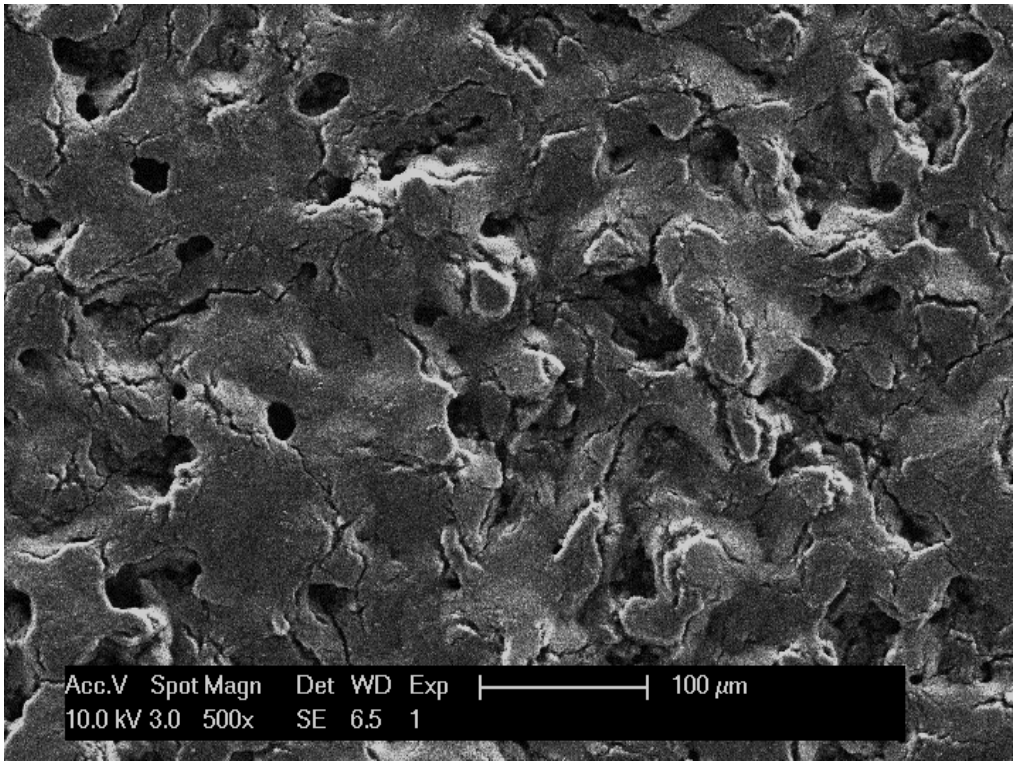

Figure S4. SEM image of the surface of N-MCN electrode.

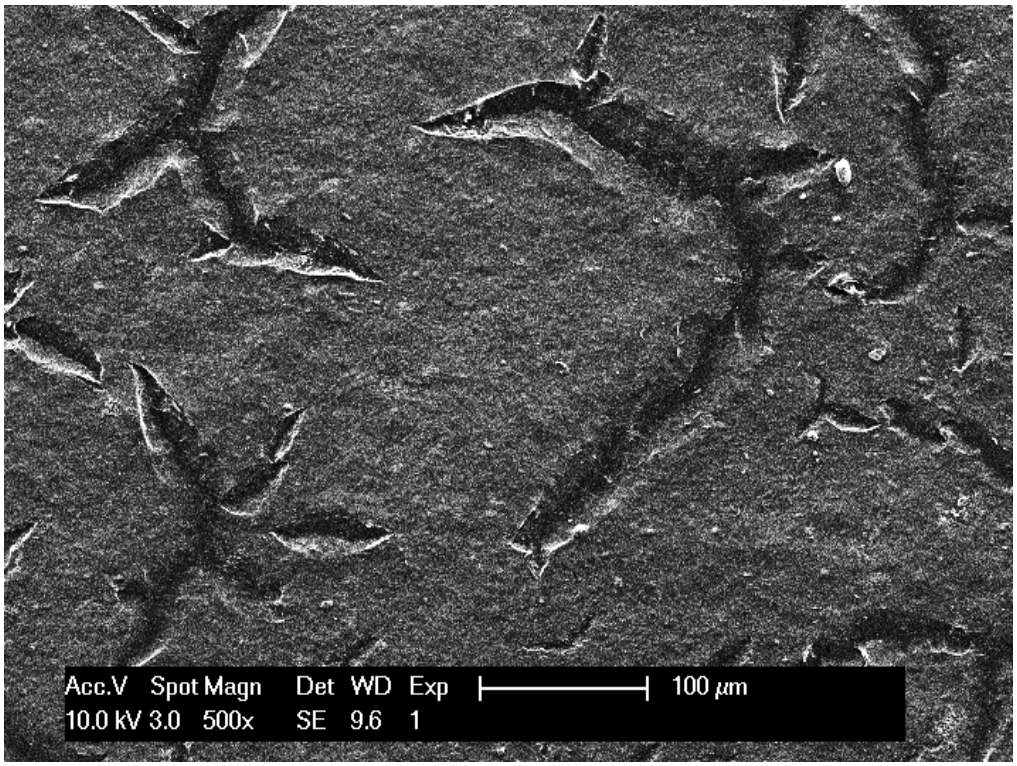

Figure S5. SEM image of the surface $Co(OH)_2$/N-rGO electrode.

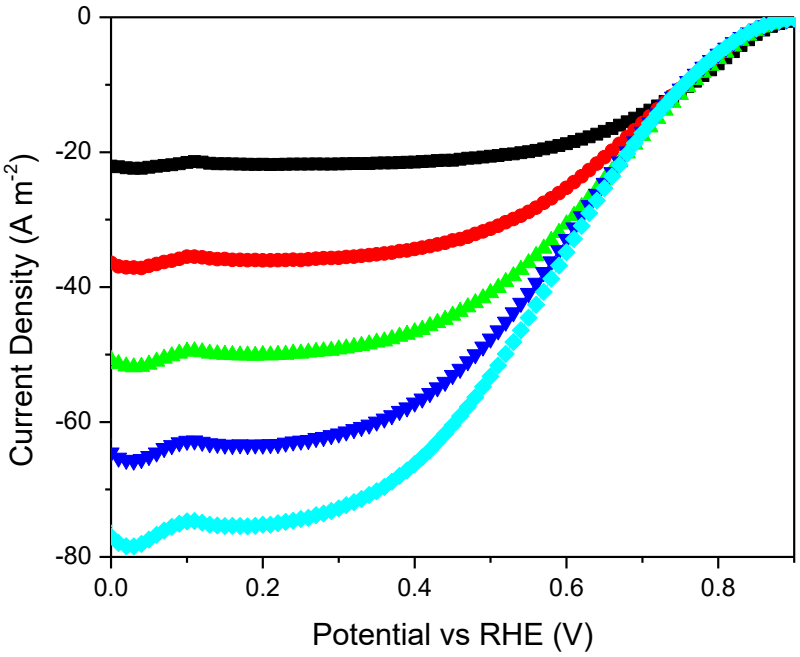

Figure S6. LSV of the Ru disk. The angular velocities are 225 rpm (Black), 625 rpm (red), 1225 rpm (green) 2025 rpm (blue) and 3025 rpm (cyan).

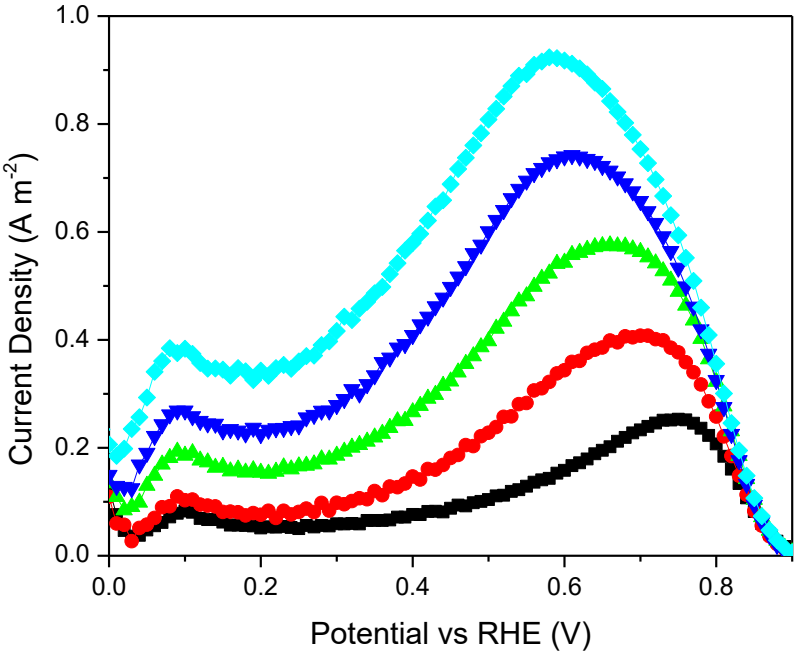

Figure S7. Ring current densities of Ru.

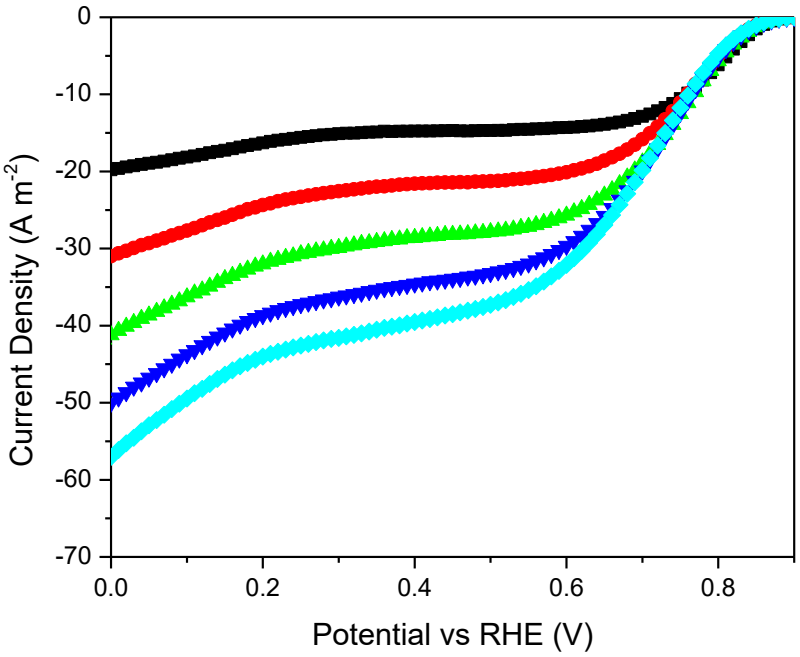

Figure S8. LSV of the Au disk.

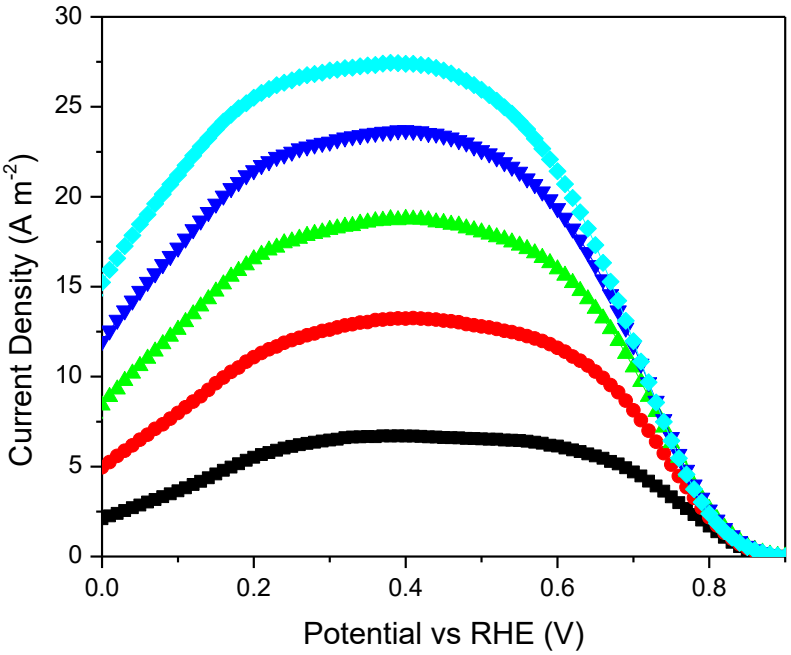

Figure S9. Ring current densities of Au.

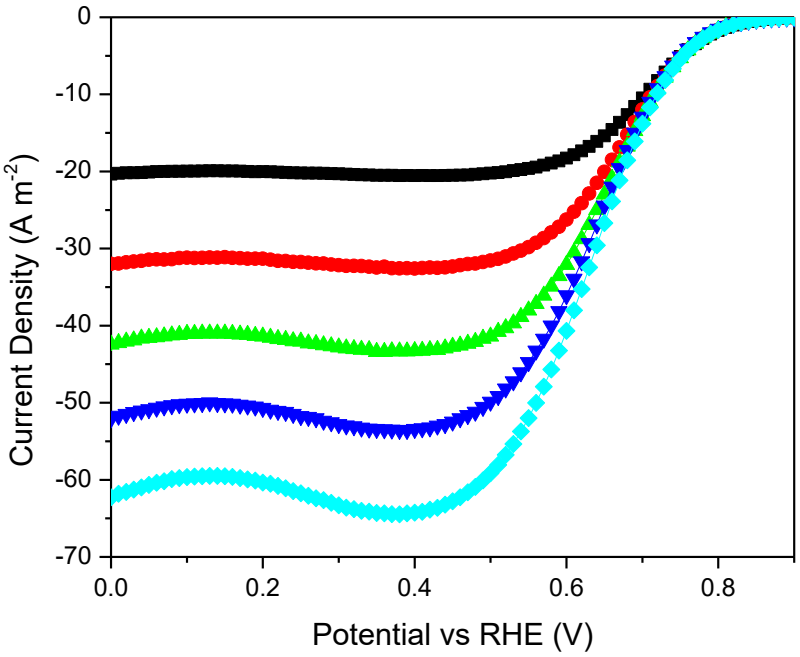

Figure S10. LSV of the Ag disk.

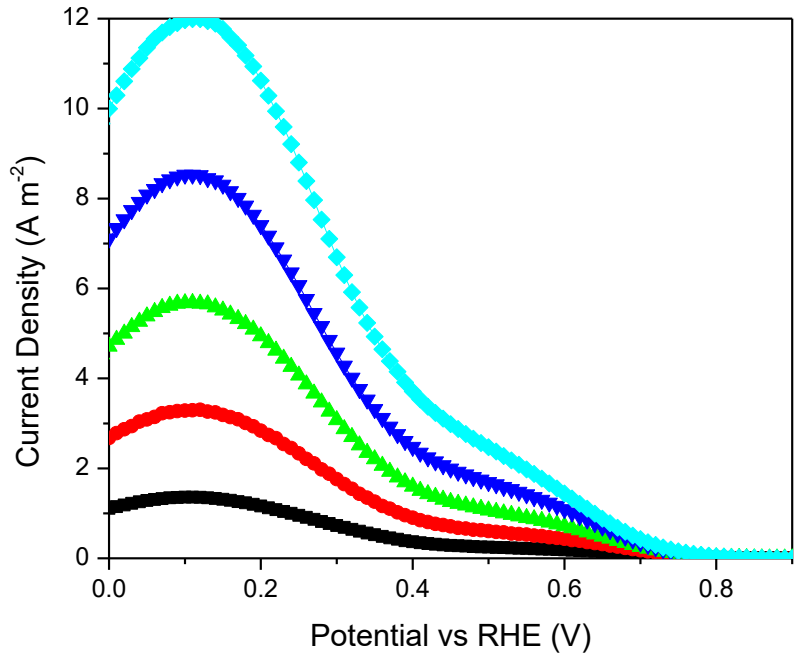

Figure S11. Ring current densities of Ag.

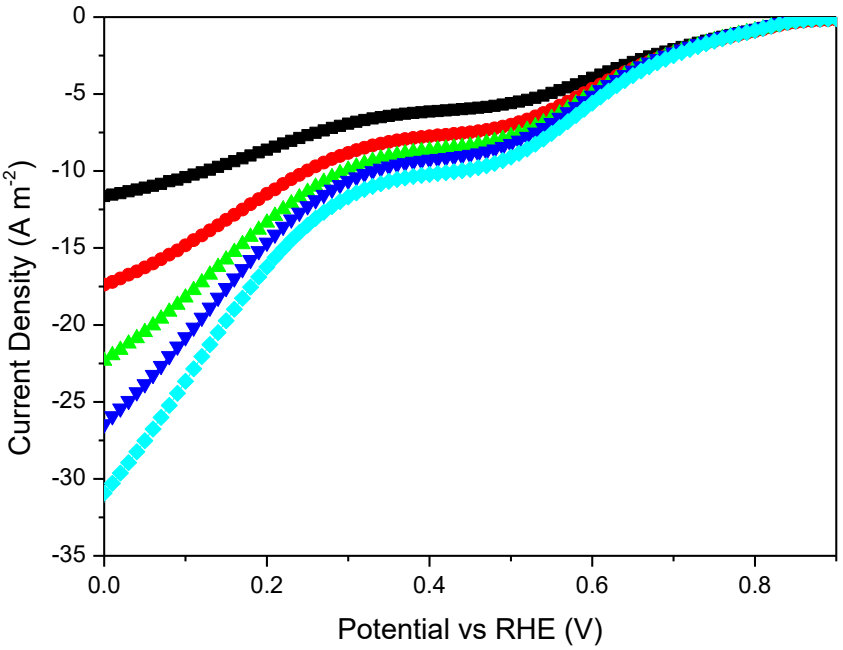

Figure S12. LSV of the e-rGO disk.

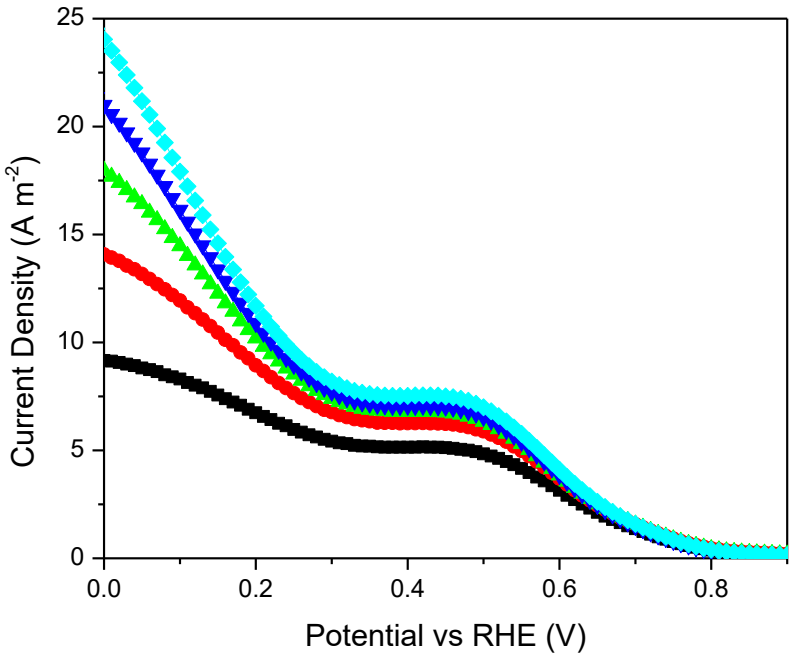

Figure S13. Ring current densities of e-rGO.

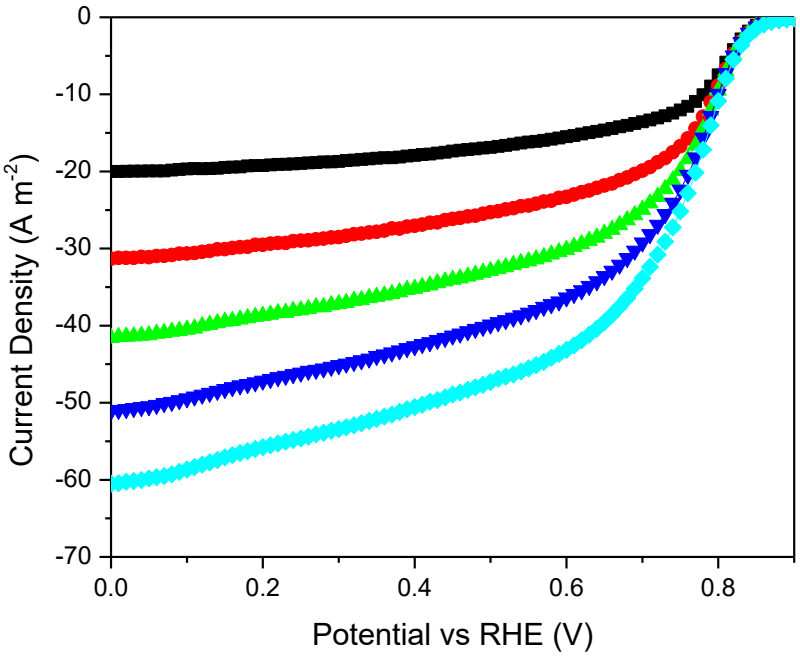

Figure S14. LSV of N-rGO disk.

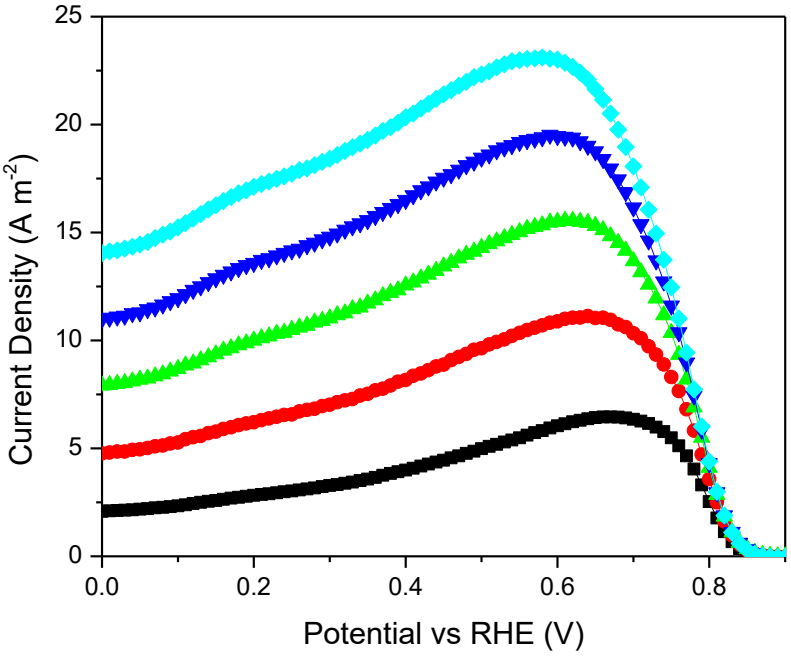

Figure S15. Ring current densities of N-rGO.

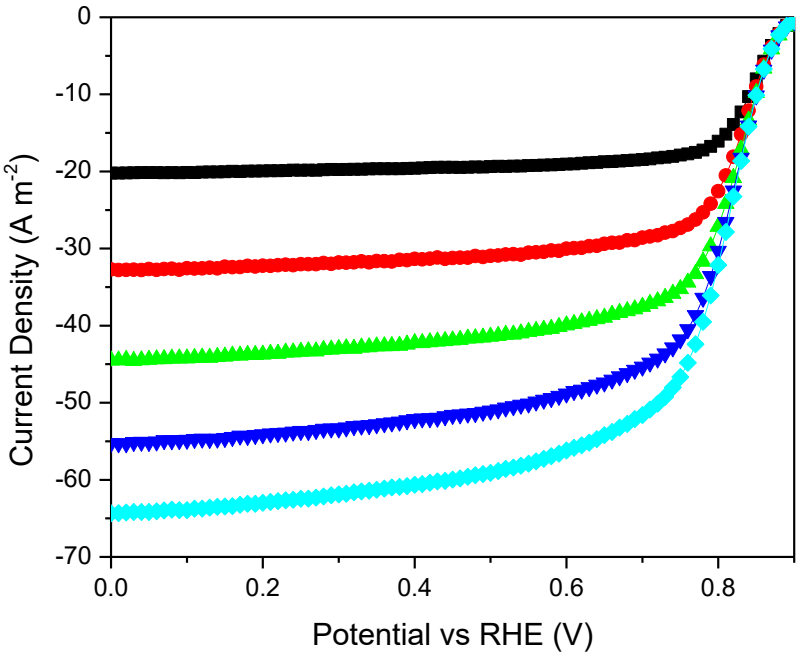

Figure S16. LSV of the $Co(OH)_2$/N-rGO disk.

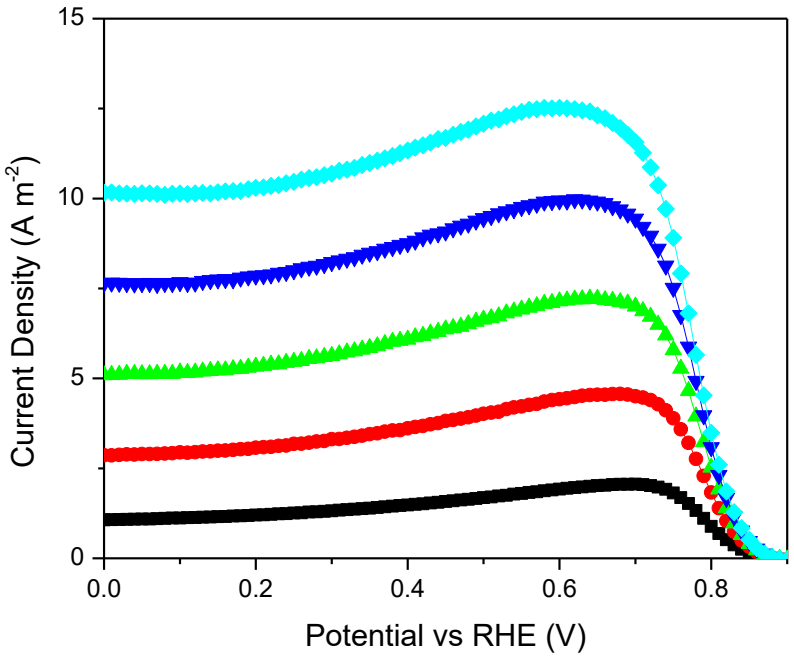

Figure S17. Ring current densities of $Co(OH)_2$/N-rGO.

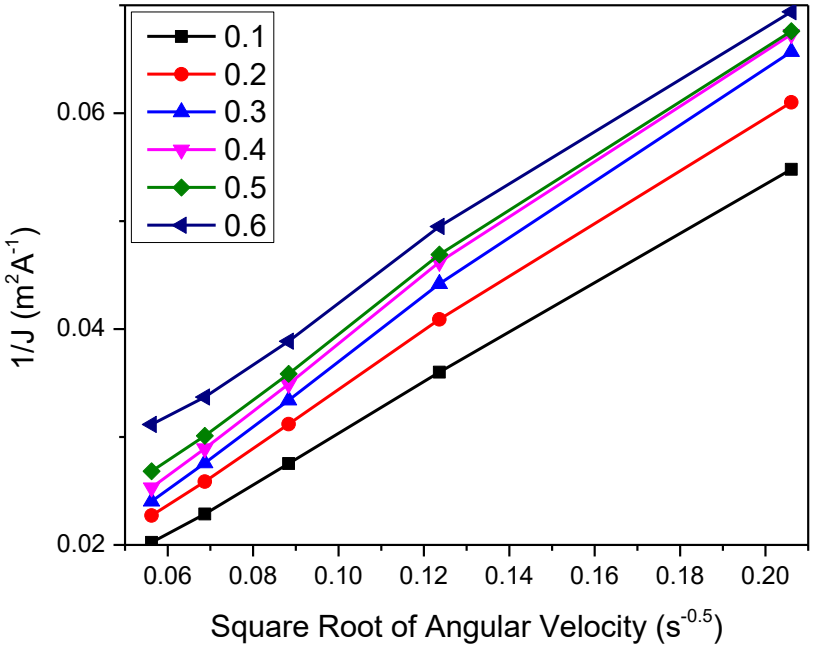

Figure S18. KL plots of Au.

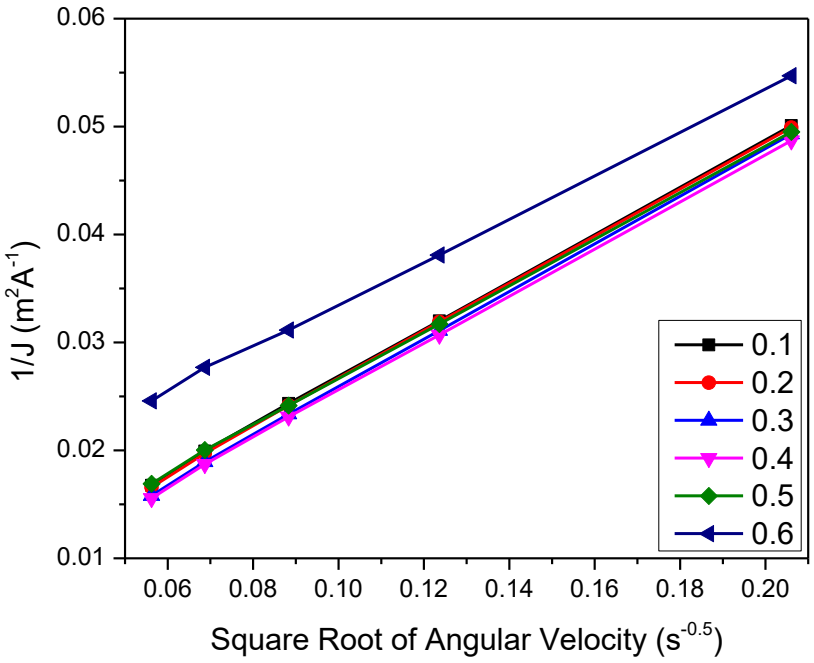

Figure S19. KL plots of Ag.

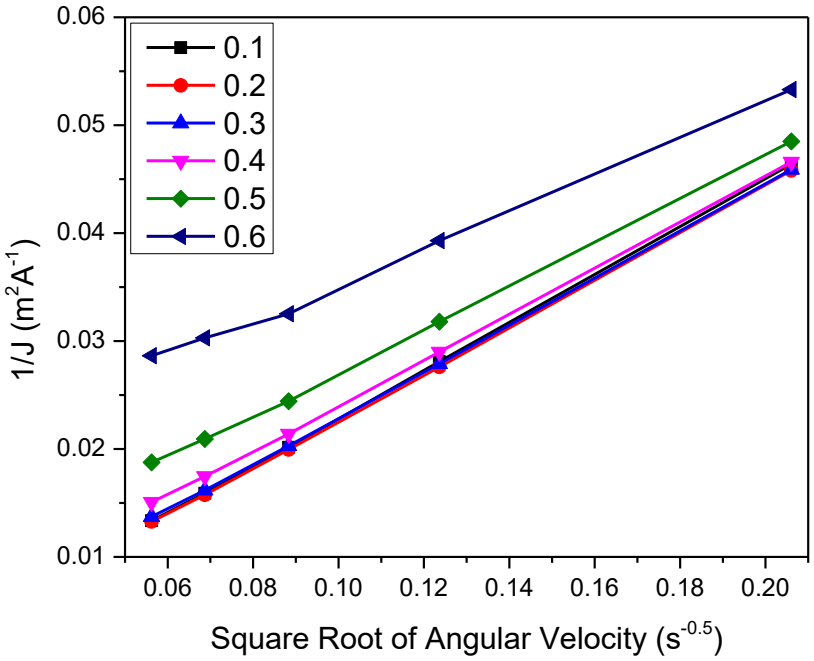

Figure S20. KL plots of Ru.

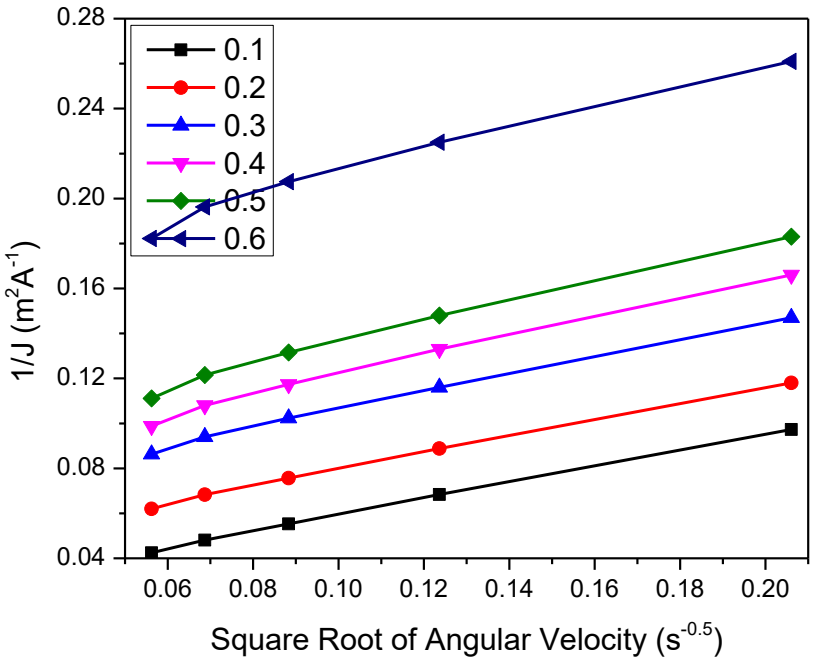

Figure S21. KL plots of e-rGO.

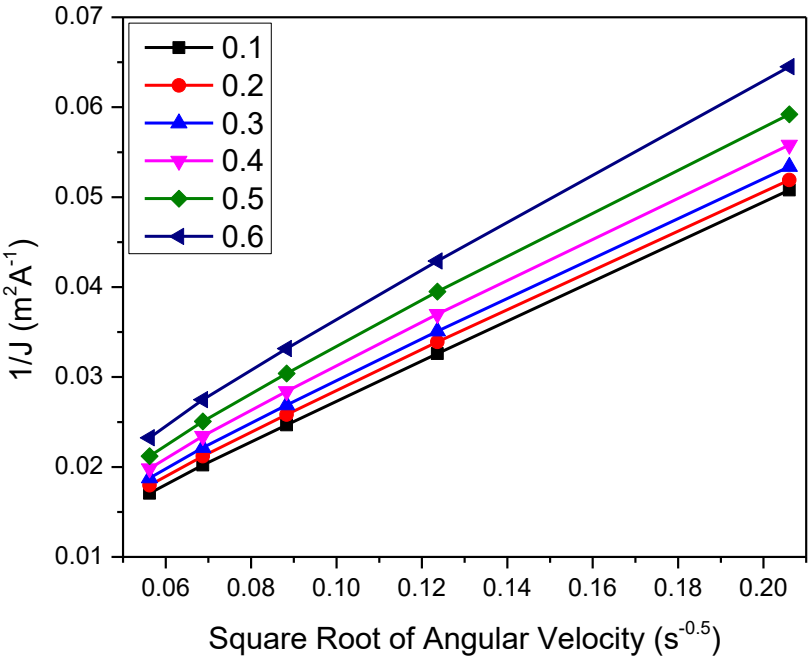

Figure S22. KL plots of N-rGO.

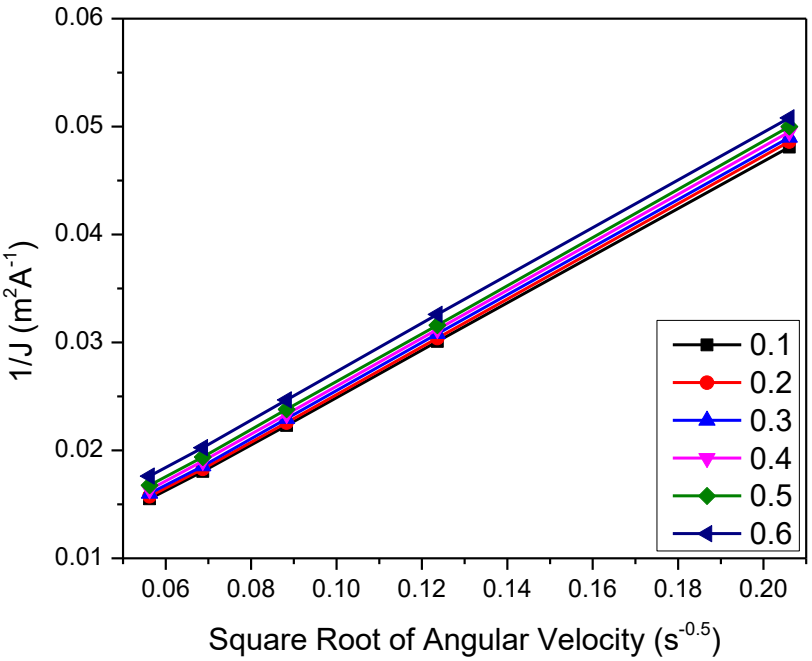

Figure S23. KL plots of $Co(OH)_2$/N-rGO.

Chapter 7: The kinetic parameters and mechanism of the oxygen reduction reaction on non-Platinum catalysts

Introduction

This chapter is the extension of the last chapter. In the last chapter, it is proved that the orders of reaction of ORR's sub-reactions are not 1. Therefore, KL method is not suitable in determining the electron transfer number. In this chapter, a method is developed to calculate the oxygen and peroxide concentration on the electrode surface, as well as the current density of each sub-reaction. Using this method, the rate constants and order of the sub-reactions of ORR can be determined. It is find that the order of peroxide reduction reaction can be either higher or lower than1. The reasons of this difference are attributed to the occupation of active site and the indirect interaction between reaction intermediates (named the Langmuir effect and Temkin effect).

The kinetic parameters and mechanism of the oxygen reduction reaction on non-Platinum catalysts

Ruifeng Zhou and Shizhang Qiao

Introduction

The oxygen reduction reaction (ORR) is at the centre of some key energy conversion and storage devices such as fuel cells and metal-air batteries etc. A lot of efforts have been devoted to develop new inexpensive ORR catalyst based on carbon and/or non-precious metals.[1-9] Theoretical studies, for example the density functional theory (DFT) studies, have also been devoted to the reveal their mechanism.[10-13] There is still a gap between the theoretical and experimental studies. Though theoretical studies can explain and predict the ORR performance in experiments, the experiments can hardly verify the ORR mechanism proposed in theoretical studies. The problem is that in experimental studies, researchers always focus on performance, e.g. current density, but ignore some very important kinetic parameters such as the rate constant and order of the reaction.

The kinetic parameters of reaction describe the relationship between reaction rate and reactant concentration. This quantity can be measured by experiment and used to explain the mechanism of the reaction. In electrochemsitry, the current density can be written in the following equation:

$$j = nFk(C^0)^{\alpha} \quad (1)$$

Where n is the electron transfer number, F is the Faradic constant, k is the rate constant, α is the order and C^0 is the concertation of the reactant on the surface of the electrode. In ORR, the reaction can be divided into several steps and 3 main sub-reactions:

$$O_2 + 2H_2O + 4e^- \rightarrow 4OH^- \quad (4e)$$

$$O_2 + H_2O + 2e^- \rightarrow HO_2^- + OH^- \quad (2e)$$

$$HO_2^- + H_2O + 2e \rightarrow 3OH^- \quad (2'e)$$

The kinetic parameters of these reactions are never measured. For historical reasons, the order of the overall and sub-reactions are assumed 1 in text books.[14] This value is probably true Pt catalyst.[15-16] The first-order assumption is also the precondition of using Koutechy-Levich equation to calculate electron transfer number, so it is widely defaulted in

recent study. If the reaction is first order and has a certain electron transfer number, the plot of j^{-1} vs $\omega^{-1/2}$ is linear. In sequence, some early researchers use the linearity of KL to judge whether ORR is first order.[17-20] However, this judgment has very severe flaws:

1. The ORR is not an elementary reaction. On Pt, the direct reaction (4e) is much quicker than the others, so ORR is close to one-step. But on other catalysts where reaction (2e) is significant, the order of the overall current density is meaningless.
2. The linearity of KL plot is the necessary but not sufficient condition of first order of reaction. In fact, if the current density is close to mass transfer limitation, the current density will follow Levich equation whatever the order of reaction is. So the linear KL plot is always linear in that case.
3. The criterion of linearity is vague. The relationship between how linear the KL plot is and how close the order is to 1 is never built.

In our last paper, we proved that the orders of the sub-reactions of ORR are not necessarily 1. Therefore the determination of real order of reaction of the all sub-reactions in ORR is still demanding.

The rate constant is also crucial to study the reaction. In ORR, the mass transfer has a significant impact on the current density, so it is difficult to retrieve the kinetic limited current density. Traditionally, the kinetic limited current density is calculated from the Koutecky- Levich (KL) equation. However, we proved in the last paper that the KL is not suitable for ORR because is neither one-step nor irreversible. Thus, a new and reliable method is also desired to get the kinetic limited current density.

The essence of determination of kinetic parameters of an electrochemical reaction is to measure the current density as a function of reactant concentration. In ORR, it is much more difficult than it sounds. First, the concentration of O_2 on electrode surface is far from that in the bulk electrolyte, so a specific method is necessary to determine it. Second, the current density of reaction (2e), (4e) and (2'e) are not directly measurable. They are embedded in the overall current density so another specific method is also necessary.

In this paper, a method is developed for the first time to determine the O_2 concentration on the electrode surface. The method is based on forced convection theory on rotation ring disk electrode (RRDE). The value of j_4, j_2 and $j_{2'}$ are, for the first time, determined by separating them from the overall current density with the assistant of an independently measured current density of peroxide reduction reaction (PRR). With these methods, the rate constants and orders of all ORR sub-reactions are determined on a metal (Au) and

three carbon based catalysts (e-rGO, N-rGO and $Co(OH)_2$/N-rGO). We have shown the potential to study the ORR mechanism by experiment with the new methods.

Method

1. Modelling

To calculate the kinetic parameters of reaction (2e), (4e) and (2'e), the concentration of O_2 on the electrode surface is measured and calculated. The solution of forced diffusive-convection equation of ORR on RDE is given in our last paper.

$$\frac{j_4}{4F} + \frac{j_2}{2F} = m_O(C_O^* - C_O^0) \quad (2)$$

$$\frac{j_{2\prime}}{2F} - \frac{j_2}{2F} = -C_P^0\, m_P \quad (3)$$

In ORR, when a RRDE is used, the measured current densities are expressed by:

$$j_d = -j_4 - j_2 - j_{2\prime} \quad (4)$$

$$\frac{j_r}{N} = j_2 - j_{2\prime} \quad (5)$$

Combing equation (4), (5) and (2) yield:

$$-j_d + \frac{j_r}{N} = j_4 + 2j_2 = 4Fm_O(C_O^* - C_O^0) = j_O \quad (6)$$

j_O is a virtual current density which is positive and proportional to O_2 flux. Thus the concentration of O_2 on the electrode surface is expressed by the measured values by:

$$C_O^0 = C_O^* - \frac{j_O}{4Fm_O} \quad (7)$$

At the same time, the concentration of H_2O_2 on the electrode surface is expressed by the measured values by:

$$C_P^0 = \frac{1}{2Fm_P}\frac{j_r}{N} \quad (8)$$

To calculate the order of reaction, the current densities of the sub-reactions must be determined i.e. j_4, j_2 and j_2'. However, there are only two measured values i.e. j_d and j_r. Therefore a more value must be measured. To measure an extra value, the H_2O_2 is introduced into an O_2-free electrolyte. When H_2O_2 is reduced, the solution of diffusive-convection equation is:

$$\frac{j_P}{2F} = m_P(C_P^* - C_P^0) \quad (9)$$

The expression of H_2O_2 concentration on electrode surface is:

$$C_P^0 = C_P^* - \frac{j_P}{2Fm_P} \quad (10)$$

By changing the C_P^*, a relationship between C_P^0 and j_P can be built. The order (α_P) and rate constant (k_P) are calculated from equation (1). j_P and $j_{2'}$ share same order and rate constant so the j_4 and j_2 in ORR are expressed:

$$j_4 = -j_d - \frac{j_r}{N} - 2j_{2'} \quad (11)$$

$$j_2 = \frac{j_r}{N} + j_{2'} \quad (12)$$

Here $j_{2'}$ is calculated from equation (1) and C_P^0, which is determined by equation (8). So far, all concentrations and current densities are expressed by measured values. At different C_O^*, a series of the C_O^0, j_4, j_2 and $j_{2'}$ can be calculated. Thus the kinetic parameters can be determined.

2. Experiment

The control of C_O^* is achieved by purging a mixture of O_2 and N_2 into the electrochemical cell. Two flow controller/meters were used to control O_2 and N_2 flows separately. The relative flow of O_2 (in %) is defined as the ratio between O_2 and the total flows. The selected relative O_2 flows are 6 %, 12 %, 25 %, 50% and 100 %. The cell was purged with the gas for 10 min with electrode rotated at 3000 rpm before the start of the experiment, when the C_O^* was stabilized. The C_O^* was determined by a separate experiment with a Ru RDE using the Levich equation.

$$j = nFmC^* \quad (13)$$

The Ru RDE was biased at 0.2 V where the ORR is dominated by 4 electron transfer and mass transfer limitation, so the levich equation is valid. The angular velocity ramped continuously from 0 rpm to 3000 rpm. The reverse of the slopes of the 1/j vs 1/nFm plots are the C_O^*.

The catalysts preparing and electrochemical setup are exactly the same as in ORR described our last paper. When testing the ORR, the angular velocity was fixed at 3000 rpm. Cyclic voltammetry (CV) was applied to the disk from 1.1 V to 0 V at 10 mV s^{-1}. The

ring (Au) was biased at 1.2 V. A blank CV (O_2 free) is measured for background subtraction. The data shown are from the negative scan of CV.

When testing the PRR, the electrolyte is purged by N_2 (i.e. O_2 free). The electrode was rotated at 3000 rpm. The volume of electrolyte is 100 ml. 0.01, 0.02, 0.05, 0.1 or 0.2 ml of 1 M H_2O_2 was injected into the electrolyte so the C_P^* were 0.1, 0.2, 0.5, 1 and 2 mole m^{-3} respectively. CV was applied to the disk from 1.1 V to 0 V at 10 mV s^{-1}. A blank CV (H_2O_2 free) is measured for background subtraction.

Results and Discussion

Firstly, The C_O^* at selected relative O_2 flows are determined. The 1/j vs 1/nFm plots on Ru at 0.2 V are shown in figure S1. Good linearity and reproducibility are achieved at angular velocity from 200 to 3000 rpm. The intercept of the extrapolation is very close to the origin, confirming that the reaction is mass transfer limited. The calculated C_O^* are used for later calculation.

The polarization curve of ORR on Au and N-rGO, $Co(OH)_2$/N-rGO, e-rGO are shown in figure 1. From the disk and ring current, the electron transfer number (n) can be calculated. The results are shown in figure 2. According to the conclusion of last paper, n is independent on C_O^* if all the orders of the sub-reactions are 1. More generally speaking, if the orders of all sub-reactions are identical, the ratio between their rates is independent on C_O^*. In consequence, the n is independent on C_O^*. Figure 2 shows that on all catalysts, n depends on C_O^* slightly. It proves that the orders of the sub-reactions are close to each other but not exactly identical. This conclusion is in consistence with the one from the last paper, though different methods are adopted, so we believe them to be reliable.

The current densities of PRR are shown in figure 3. Comparing figure 3 with figure 1, it is not difficult to find that the PRR current density has significant relationship with the ORR current density and peroxide ratio. On a catalyst with high PRR current density, the ORR current density is always high, vice versa. This is reasonable because ORR and PRR are essentially similar. They share same intermediate HO* (* stands for adsorption point). Even if ORR has other intermediates such as O_2*, HOO* and O*, their adsorption energies have the same trend as HO*, suggested by DFT calculation.[10] Furthermore, the higher the PRR current density is, the lower the peroxide ratio of ORR is. This is also easy to understand because if H_2O_2 is reduced quickly, less H_2O_2 will be released to electrolyte, as shown in equation (4).

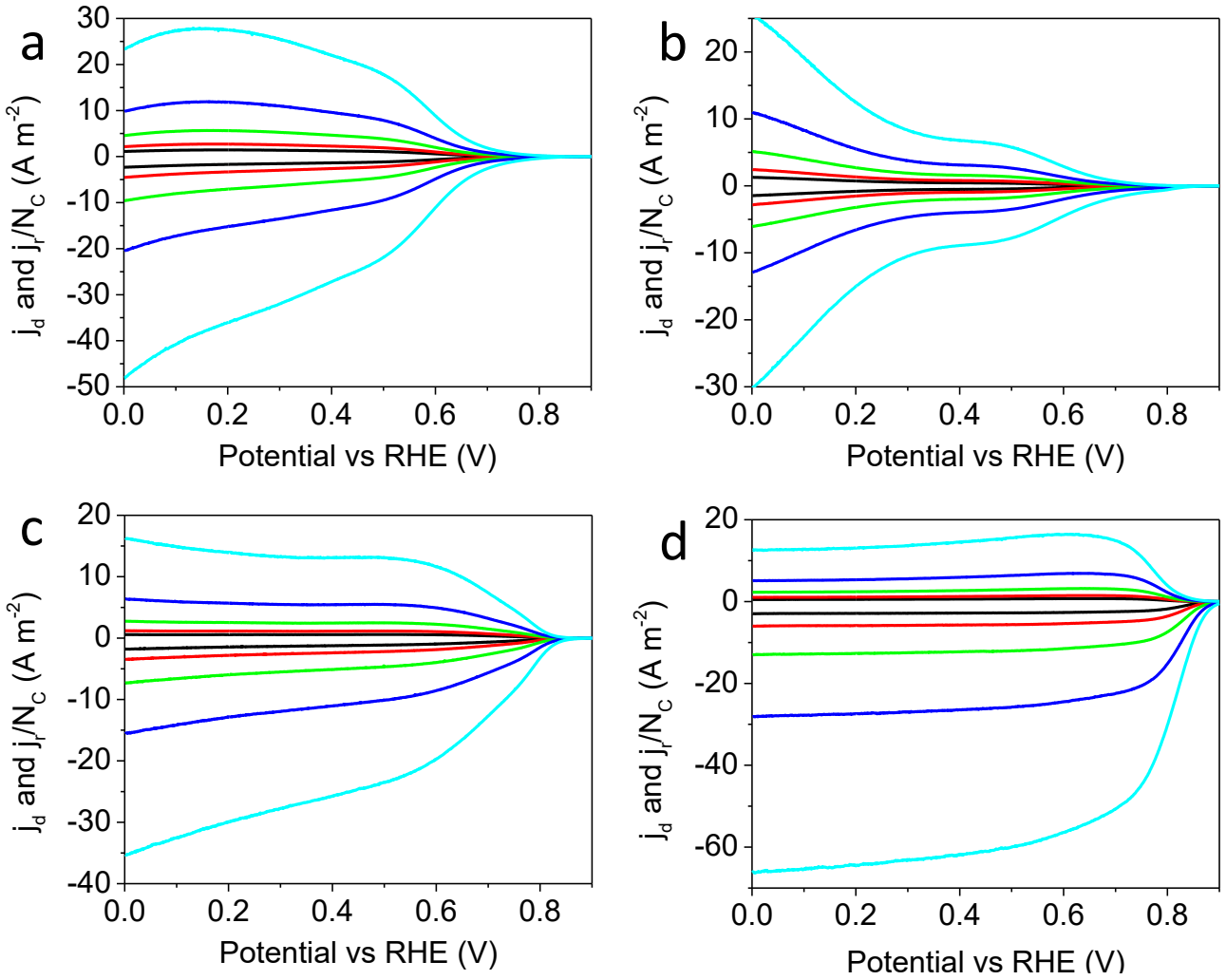

Figure 1. The disk current density and normalized ring current density during ORR on Au (a), e-rGO (b), N-rGO (c) and $Co(OH)_2$/N-rGO (d). The relative O_2 flows are 6 (Black), 12 (red), 25 (green), 50 (blue) and 100 (cyan).

With data from figure 3 and equation (9), the H_2O_2 concentration on electrode surface is calculated. The results are provided in figure S2. Assuming the PRR is a reaction of a certain order, the relationship between j_P and C_p^0 can be expressed by:

$$\log(j_P) = \alpha_P \log(C_P^0) + \log(2Fk_P) \qquad (14)$$

Based on the data in figure 3, the $\log(j_P)$ vs $\log(C_p^0)$ plots can be drawn. Then the α_P and k_P can be calculated. The selected plots at 0.1 V, 0.2 V, 0.3 V, 0.4 V, 0.5 V and 0.6 V are provided in figure S3. It is shown that the linearity of the plots is acceptably good, so that the calculated α_P and k_P should be accurate enough.

Similarly, the C_O^0 and C_p^0 of ORR can be calculated based on data of figure 1 and equation (7) and (8). The results are shown in figure S4. The j_O is calculated with j_d and j_r and equation (7). The $j_{2'}$ is calculated with C_P^0 and equation (14) with corresponding k_P

and α_P. The results are shown in figure S5. The j_2 and j_4 are calculated with equation (11) and (12). The plot of j_2 and j_4 are shown in figure S6. With all these data, the $\log(j_O)$ vs $\log(C_O^0)$, $\log(j_4)$ vs $\log(C_O^0)$ and $\log(j_2)$ vs $\log(C_O^0)$ plots are shown in figure S7, S8 and S9. The slopes and intercepts of the plots are the orders and rate constants of the corresponding reactions. The rate constants and orders are shown in figure 4 and figure 5.

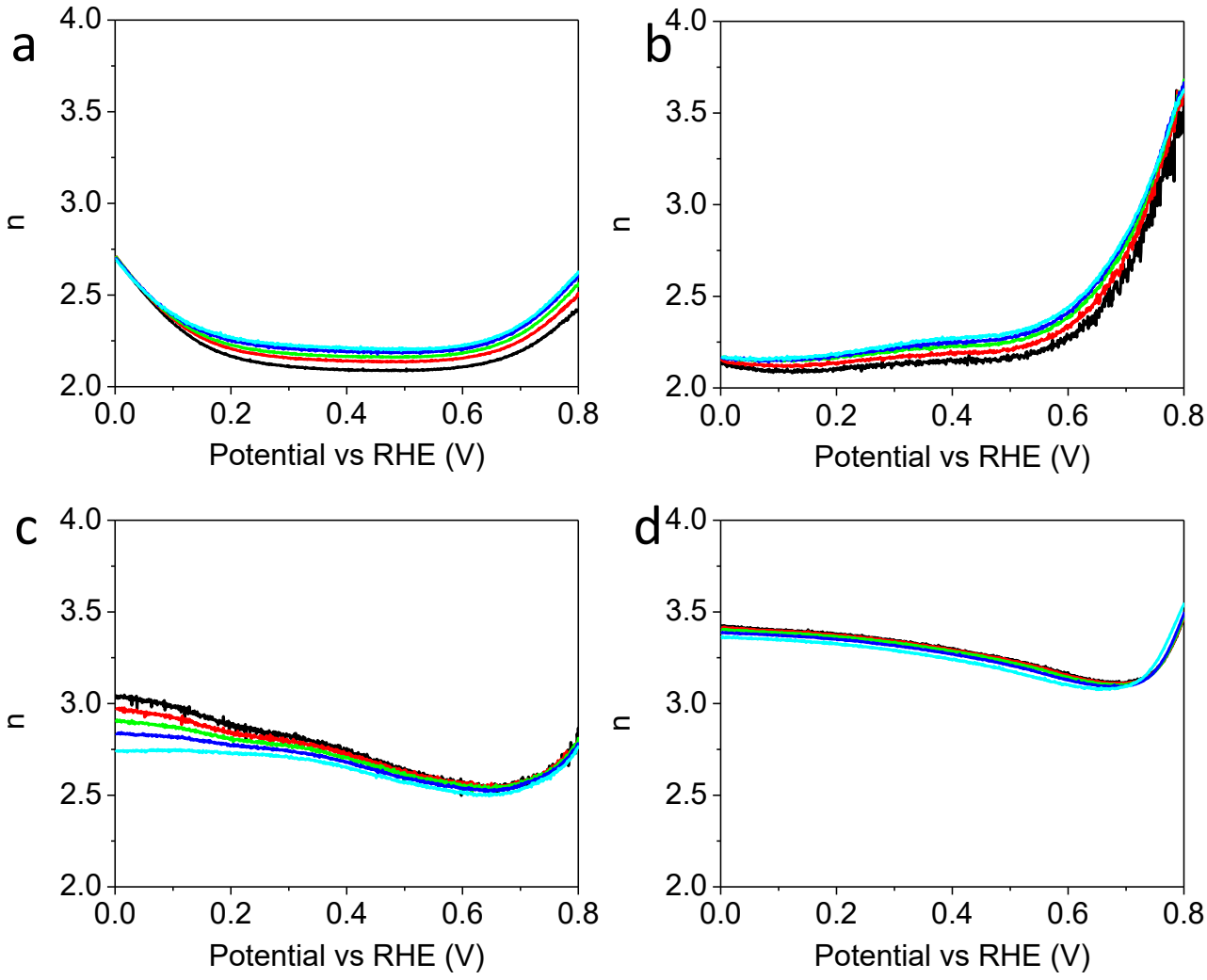

Figure 2. The electron transfer number of ORR on Au (a), e-rGO (b), N-rGO (c) and $Co(OH)_2$/N-rGO (d). The relative O_2 flows are 6 (Black), 12 (red), 25 (green), 50 (blue) and 100 (cyan).

The rate constant is actually the rate of reaction at $\log(C_O^0) = 0$, where the C_O^0 is 1 mole m^{-3}. This concentration is close to the saturation concentration of 1 atm O_2 in water (1.22 mole m^{-3}). So the as calculated rate constants directly reflect the rate of the reactions near saturation, and is a direct indicator of the catalyst performance in real fuel cells.

Figure 4 shows the rate constants. Consider Au first. Though j_r decreases as potential decreases at low potential, the k_2 continues to increase. This is reasonable because when

potential decreases, the overpotenital of reaction (2e) increases. So it is demonstrated that the j_2, as well as j_4, is separated from the measured j_d and j_r successfully.

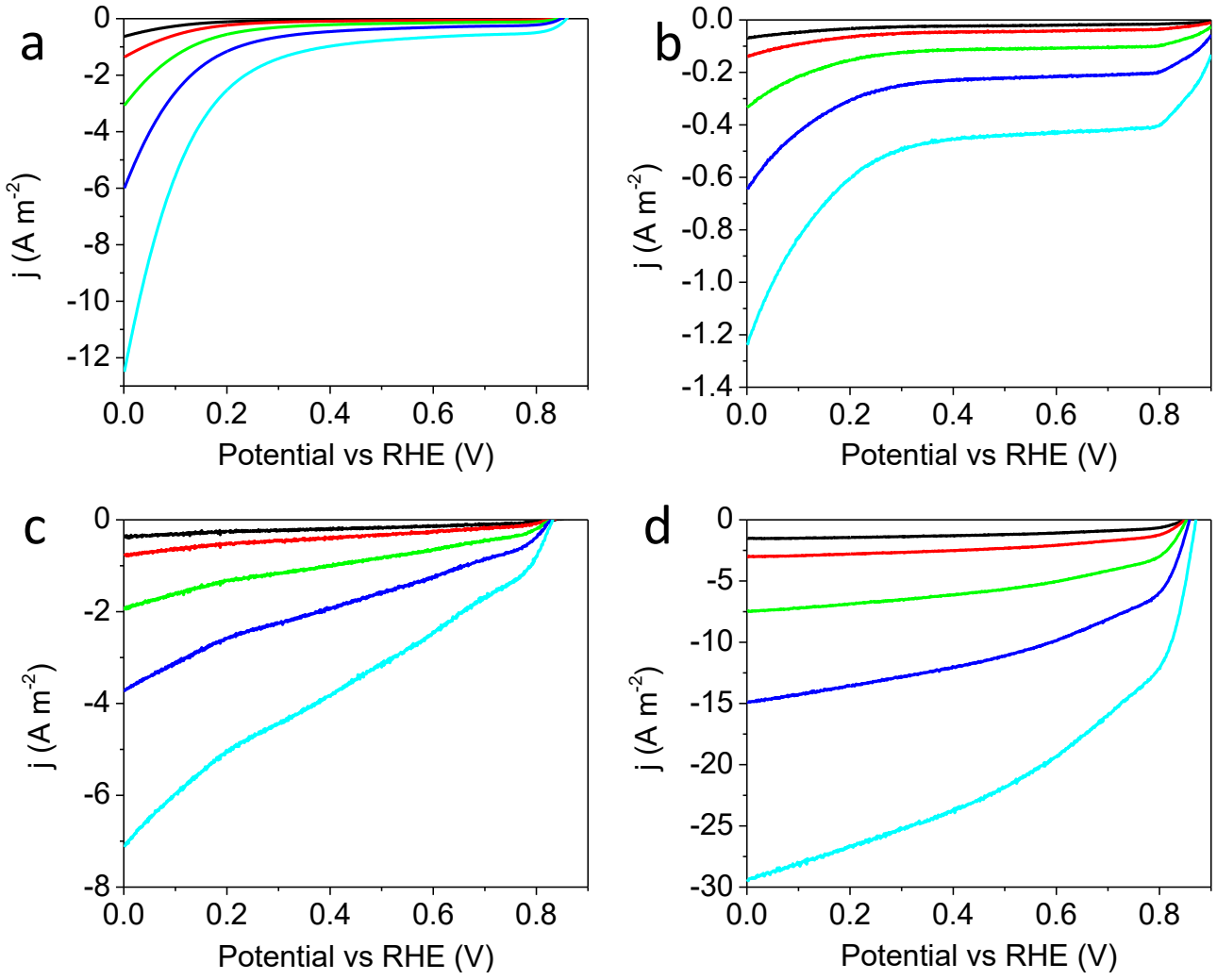

Figure 3. The PRR current densities of Au (a), e-rGO (b), N-rGO (c) and $Co(OH)_2$/N-rGO (d). The peroxide concentrations are 0.1 mM (Black), 0.2 mM (red), 0.5 mM (green), 1 mM (blue) and 2 mM (cyan).

Another significance of rate constant compared to the current density is that the Tafel slope can be calculated with high precision. In Tafel theory, the mass transfer is absent. However, the saturation concentration of oxygen is so low that mass transfer affects current density just below the onset potential. Traditionally, the kinetic current density is calculated from KL equation but we have proved that the KL equation is not suitable for multistep reaction such as ORR. So the only correct way is to calculate the rate constant. Though it is still difficult to explain the Tafel slope quantitatively, the real Tafel slope does provide some information about reaction mechanism.

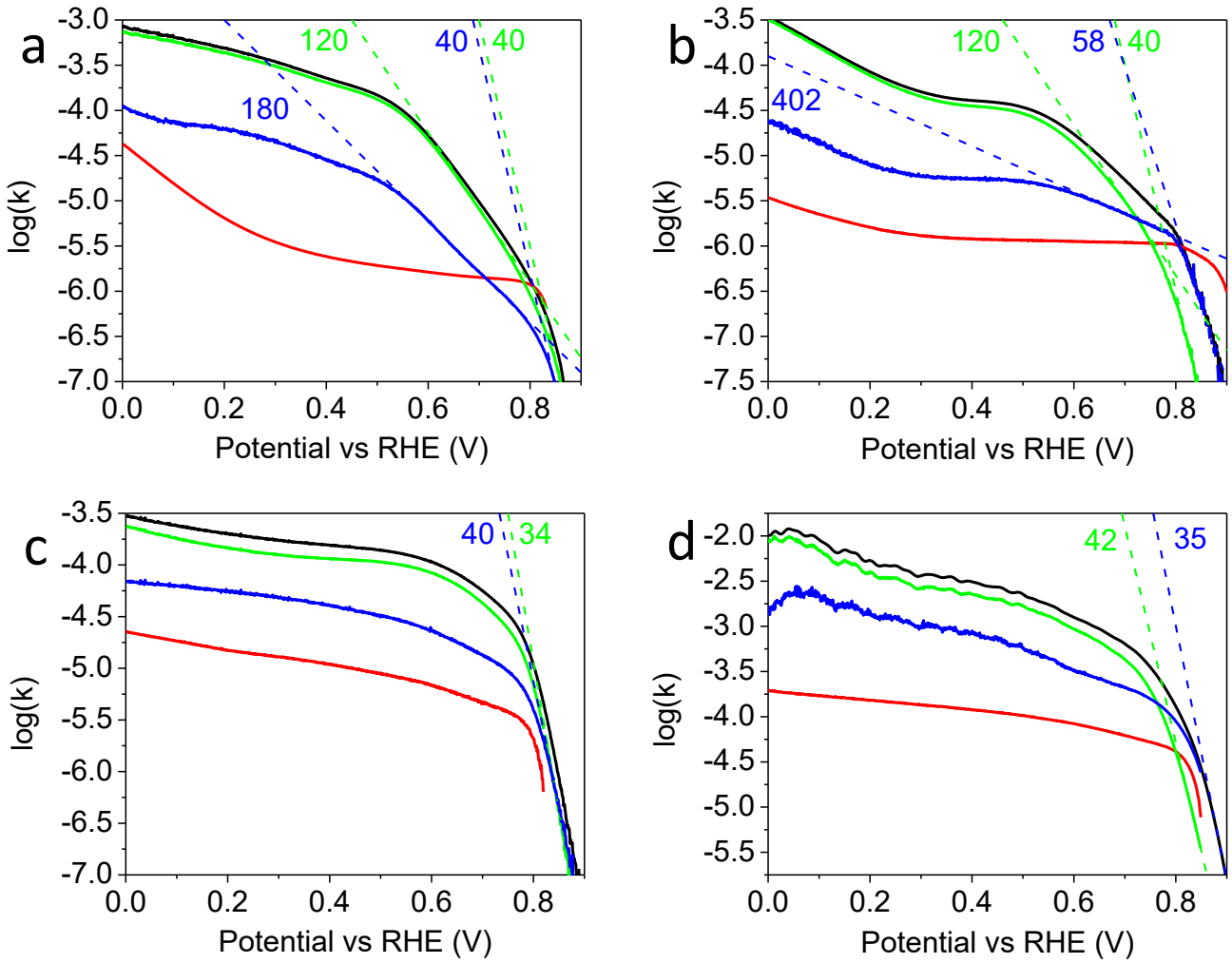

Figure 4. The rate constants of reactions of j_O (black), $j_{2'}$ (red), j_2 (green) and j_4 (blue) on Au (a), e-rGO (b), N-rGO (c) and $Co(OH)_2$/N-rGO (d). The rate constants are in m s^{-1}. The Tafel slopes are in mV $decade^{-1}$.

Up to now, it is difficult to give a complete explanation of the data, but some clue of the ORR mechanism can be found. First, the rate constants reach some limitation at low potential. This phenomenon is very similar to that of the mass transfer limitation. However, the mass transfer has been considered in rate constant. Therefore, there is another limitation on rate constant before electron transfer. It is attributed to the adsorption of O_2 on the catalyst, which is the start of ORR. At very low potential, all electron transfer steps are fast enough so the rate of ORR, is entirely limited by O_2 adsorption. Second, there must be some interaction between adsrobates. The interaction is not only the competition on active sites (Langmuir adsorption) because it lets the order lower than 1. In fact, the order is sometimes obviously higher than 1. Therefore, there must be some interaction which promotes the reaction. A possible interaction is the Temkin adsorption in which the adsorption energy changes with coverage. In most case, adsorption energy decreases as coverage increases. So the increases of coverage accelerates the steps in which the

adsorption energy limited the reaction rate. I is proved on Au that the adsorption energy of O is lower a coverage of 0.5 than 0, so the ordrer of reaction (4e) on Au is higher than 1.[21]

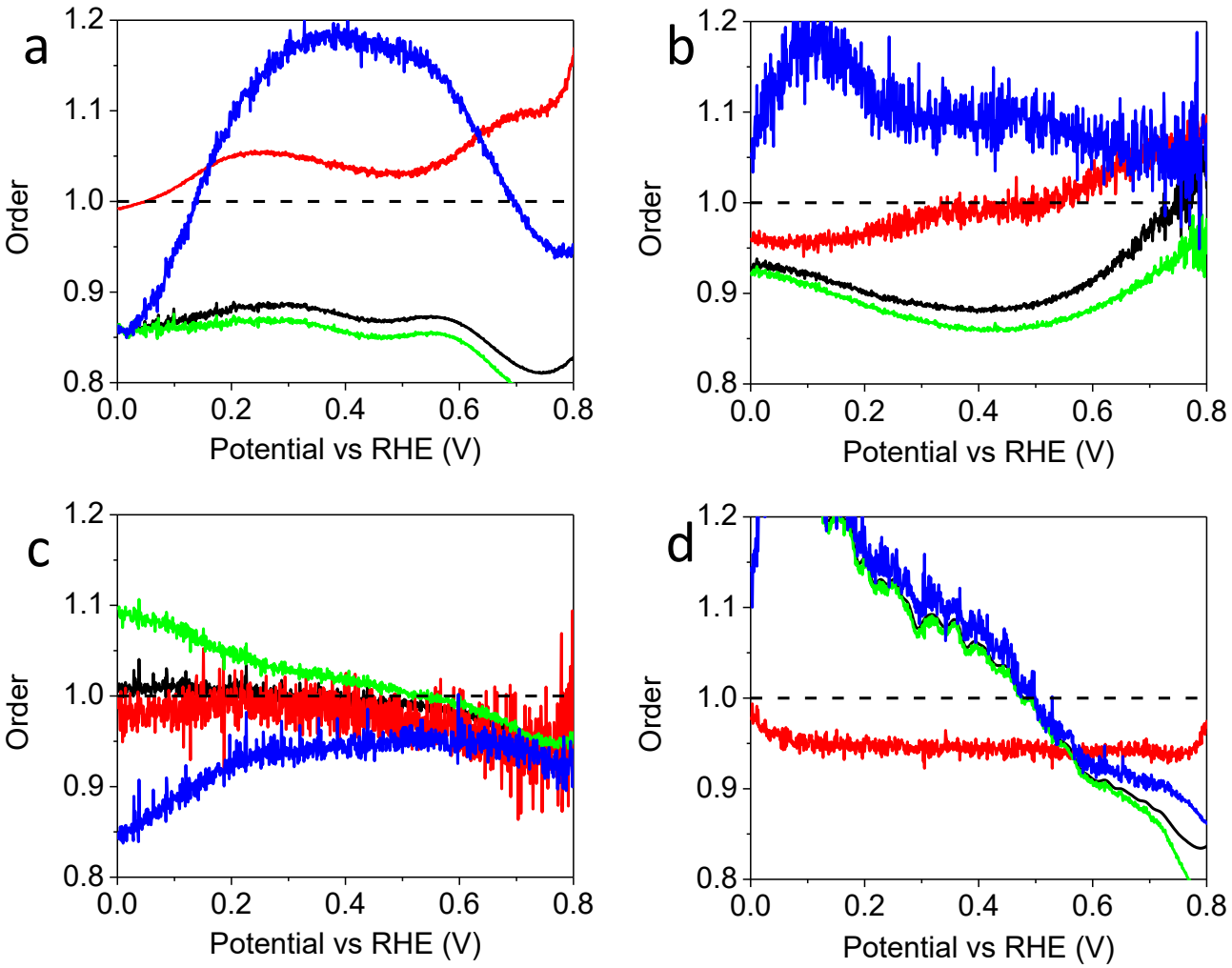

Figure 5. The order of reactions of j_O (black), $j_{2'}$ (red), j_2 (green) and j_4 (blue) on Au (a), e-rGO (b), N-rGO (c) and $Co(OH)_2$/N-rGO (d).

Conclusion

In conclusion, a method to control and determine the O_2 and H_2O_2 concentrations on the electrode surface during ORR and PRR is developed. The current densities of sub-reactions in ORR are derived. With this method, the rate constants and orders of sub-reactions of ORR can be calculated. The reaction mechanism is discussed based on the results. It is found that the orders of the sub-reactions are not identical on a same catalyst. The orders are explained by the Langmuir effect Temkin effect.

1. Liang, J.; Du, X.; Gibson, C.; Du, X. W.; Qiao, S. Z., *Adv. Mater.* **2013,** *25* (43), 6226-6231.

2. Liang, J.; Jiao, Y.; Jaroniec, M.; Qiao, S. Z., *Angew. Chem. Int. Ed.* **2012,** *51* (46), 11496-11500.

3. Liang, J.; Zheng, Y.; Chen, J.; Liu, J.; Hulicova-Jurcakova, D.; Jaroniec, M.; Qiao, S. Z., *Angew. Chem. Int. Ed.* **2012,** *51* (16), 3892-3896.
4. Liang, J.; Zhou, R. F.; Chen, X. M.; Tang, Y. H.; Qiao, S. Z., *Adv. Mater.* **2014,** *26* (35), 6074-9.
5. Zheng, Y.; Jiao, Y.; Chen, J.; Liu, J.; Liang, J.; Du, A.; Zhang, W. M.; Zhu, Z. H.; Smith, S. C.; Jaroniec, M.; Lu, G. Q.; Qiao, S. Z., *J. Am. Chem. Soc.* **2011,** *133* (50), 20116-20119.
6. Zheng, Y.; Jiao, Y.; Ge, L.; Jaroniec, M.; Qiao, S. Z., *Angew. Chem. Int. Ed.* **2013,** *52* (11), 3110-3116.
7. Zhou, R.; Qiao, S. Z., *Chem. Commun.* **2015,** *51* (35), 7516-7519.
8. Zhou, R. F.; Qiao, S. Z., *Chem. Mater.* **2014,** *26* (20), 5868-5873.
9. Zhou, R. F.; Zheng, Y.; Hulicova-Jurcakova, D.; Qiao, S. Z., *J. Mater. Chem. A* **2013,** *1* (42), 13179-13185.
10. Norskov, J. K.; Rossmeisl, J.; Logadottir, A.; Lindqvist, L.; Kitchin, J. R.; Bligaard, T.; Jonsson, H., *J. Phys. Chem. B* **2004,** *108* (46), 17886-17892.
11. Calle-Vallejo, F.; Martinez, J. I.; Rossmeisl, J., *Phys. Chem. Chem. Phys.* **2011,** *13* (34), 15639-15643.
12. Zhang, L.; Xia, Z., *J. Phys. Chem. C* **2011,** *115* (22), 11170-11176.
13. Jiao, Y.; Zheng, Y.; Jaroniec, M.; Qiao, S. Z., *J. Am. Chem. Soc.* **2014,** *136* (11), 4394-4403.
14. Bard, A. J.; Faulkner, L. R., *Electrochemical Methods: Fundamentals and Applications*. Wiley: 2000.
15. Paulus, U. A.; Schmidt, T. J.; Gasteiger, H. A.; Behm, R. J., *J. Electroanal. Chem.* **2001,** *495* (2), 134-145.
16. Mukerjee, S.; Srinivasan, S., *J. Electroanal. Chem.* **1993,** *357* (1–2), 201-224.
17. Ross, P. N.; Andricacos, P. C., *J. Electroanal. Chem. Interfacial Electrochem.* **1983,** *154* (1–2), 205-215.
18. Hsueh, K. L.; Chang, H. H.; Chin, D. T.; Srinivasan, S., *Electrochim. Acta* **1985,** *30* (9), 1137-1142.
19. Ross, P. N.; Cairns, E. J.; Striebel, K.; McLarnon, F.; Andricacos, P. C., *Electrochim. Acta* **1987,** *32* (2), 355-355.
20. Kim, J.-D.; Pyun, S.-I.; Yang, T.-H.; Ju, J.-B., *J. Electroanal. Chem.* **1995,** *383* (1–2), 161-166.
21. Shi, H.; Stampfl, C., *Physi. Rev. B* **2007,** *76* (7), 075327.

Supporting information

The kinetic parameters and mechanism of the oxygen reduction reaction on non-Platinum catalysts

Ruifeng Zhou and Shizhang Qiao

Supporting figures

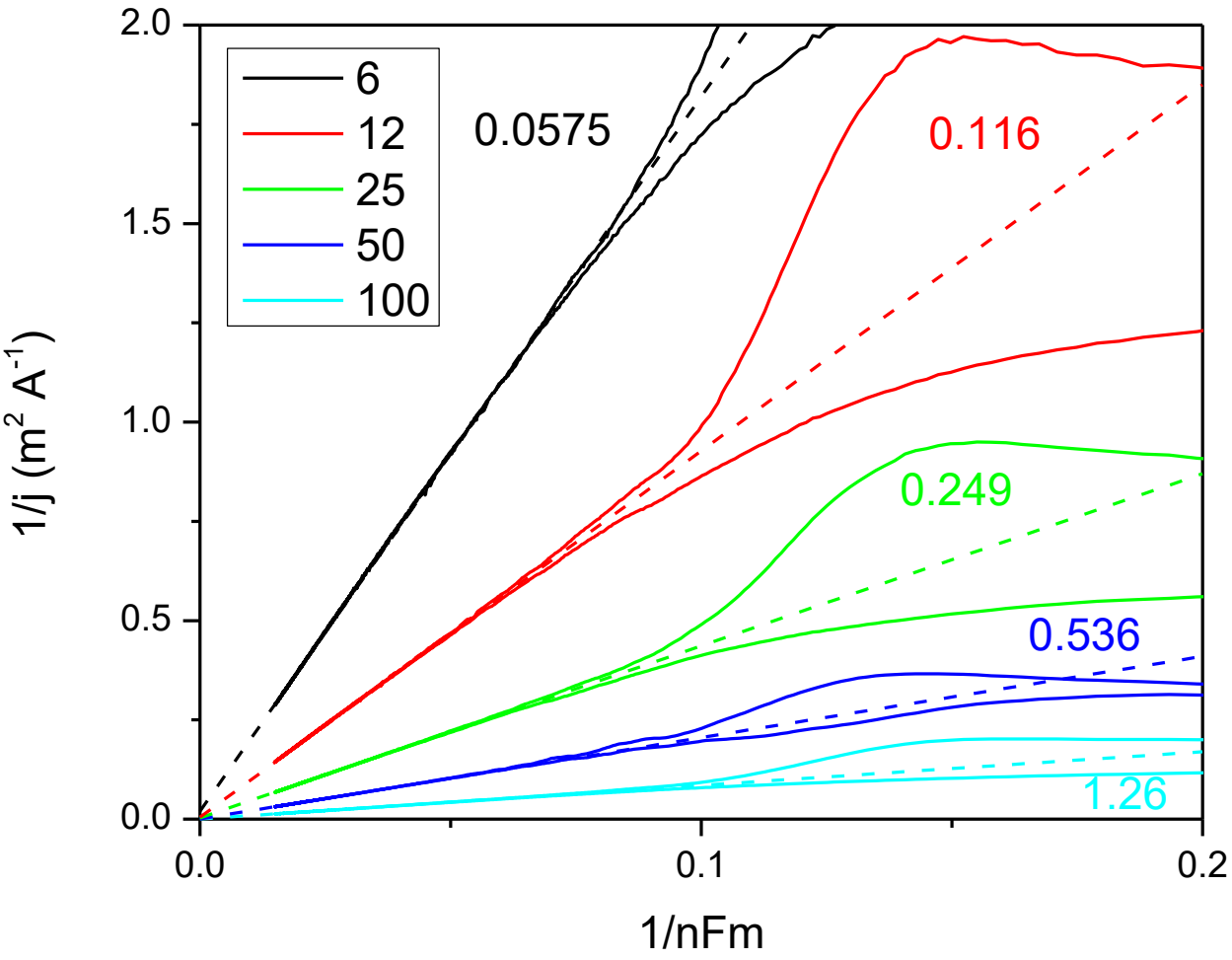

Figure S1. 1/j vs 1/nFm plot at selected relative O_2 flows (in %). The number beside dash lines are the C_O^* in mole m^{-3}.

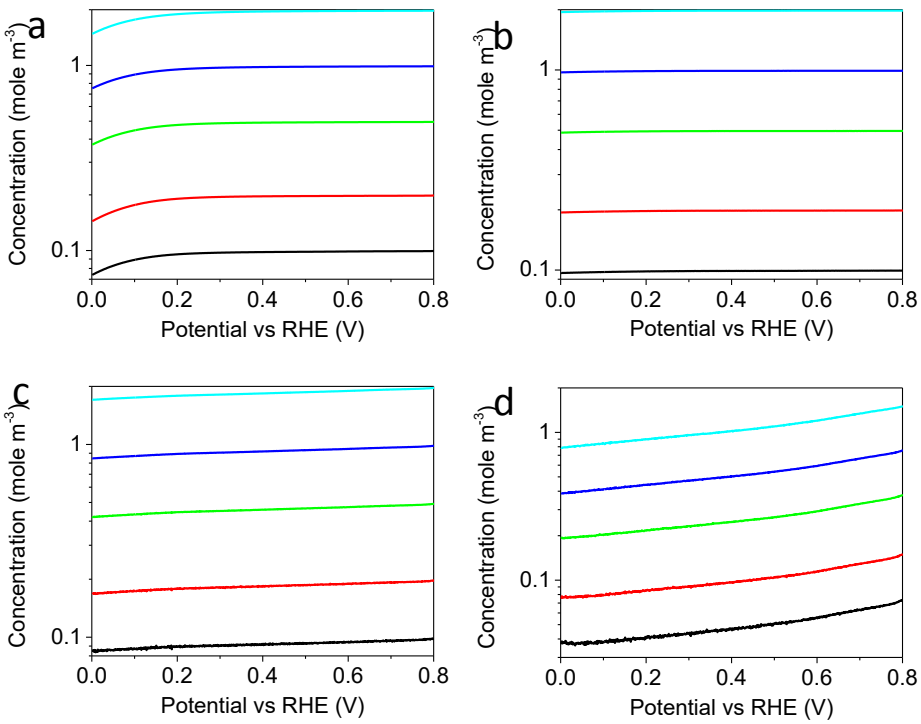

Figure S2. The C_P^0 during PRR on Au (a), e-rGO (b), N-rGO (c) and $Co(OH)_2$/N-rGO (d). The peroxide concentrations are 0.1 mM (Black), 0.2 mM (red), 0.5 mM (green), 1 mM (blue) and 2 mM (cyan).

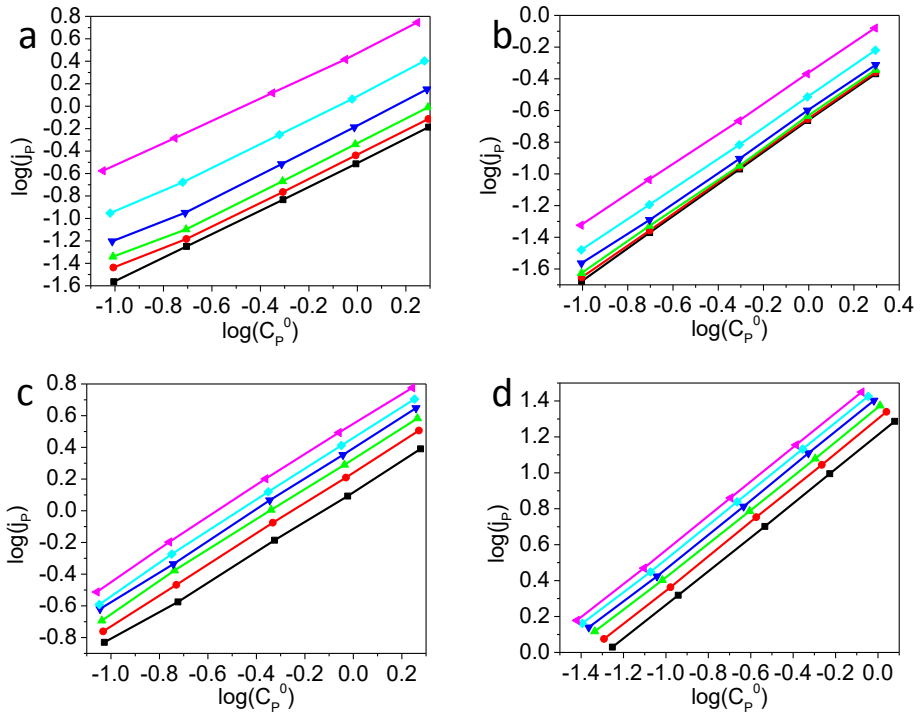

Figure S3. The $\log(C_P^0)$ vs $\log(j_P)$ plot of Au (a), e-rGO (b), N-rGO (c) and $Co(OH)_2$/N-rGO (d). The C_P^0 is in mole m^{-3}. The j_P is in A m^{-2}. The potentials are 0.6 V (Black), 0.5 V (red), 0.4 V (green), 0.5 V (blue), 0.2 V (cyan) and 0.1 V (magenta).

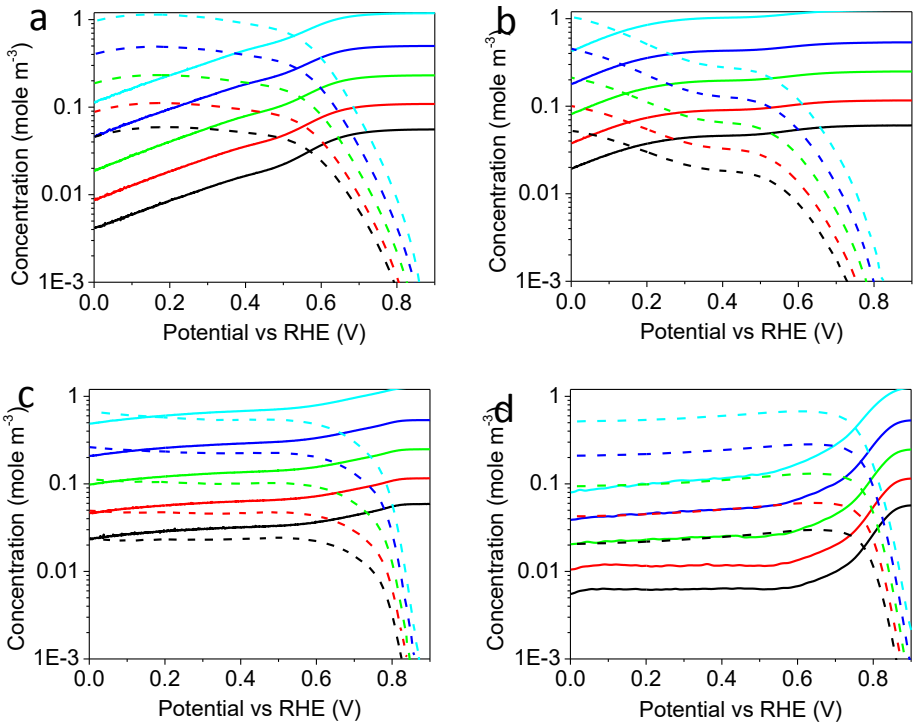

Figure S4. The C_O^0 (solid) and C_P^0 (dash) during ORR on Au (a), e-rGO (b), N-rGO (c) and $Co(OH)_2$/N-rGO (d). The relative O_2 flows are 6 (Black), 12 (red), 25 (green), 50 (blue) and 100 (cyan).

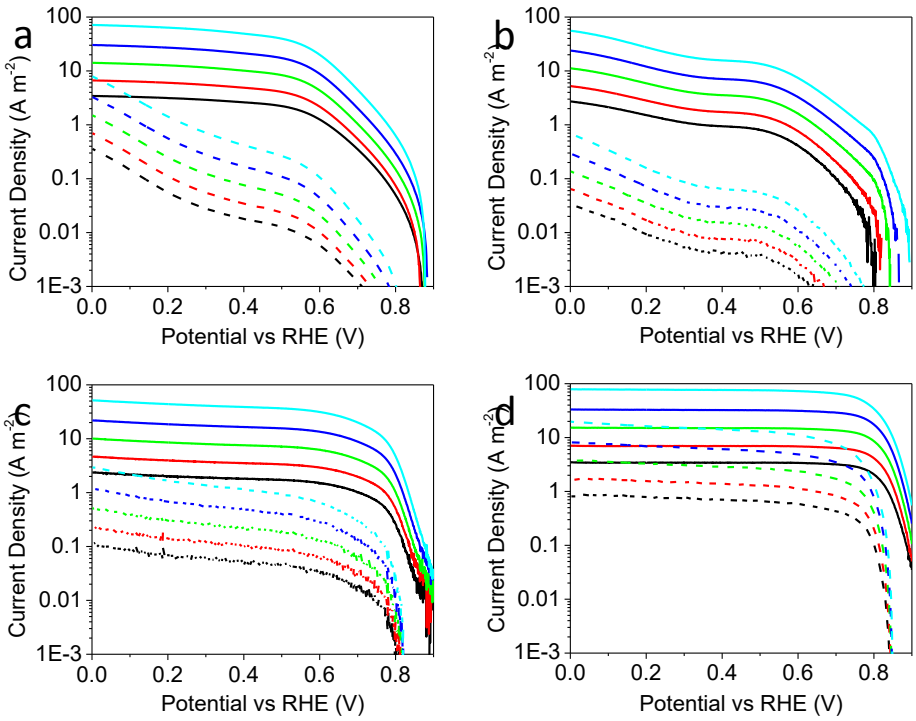

Figure S5. The j_O (solid) and $j_{2'}$ (dash) during ORR on Au (a), e-rGO (b), N-rGO (c) and $Co(OH)_2$/N-rGO (d). The relative O_2 flows are 6 (Black), 12 (red), 25 (green), 50 (blue) and 100 (cyan).

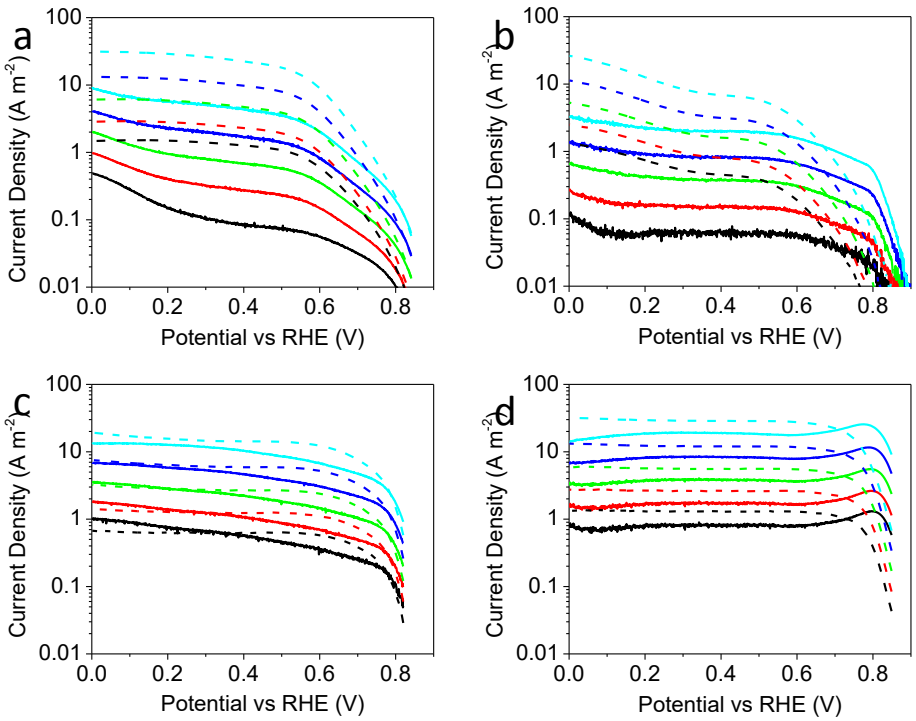

Figure S6. The j_4 (solid) and j_2 (dash) during ORR on Au (a), e-rGO (b), N-rGO (c) and $Co(OH)_2$/N-rGO (d). The relative O_2 flows are 6 (Black), 12 (red), 25 (green), 50 (blue) and 100 (cyan).

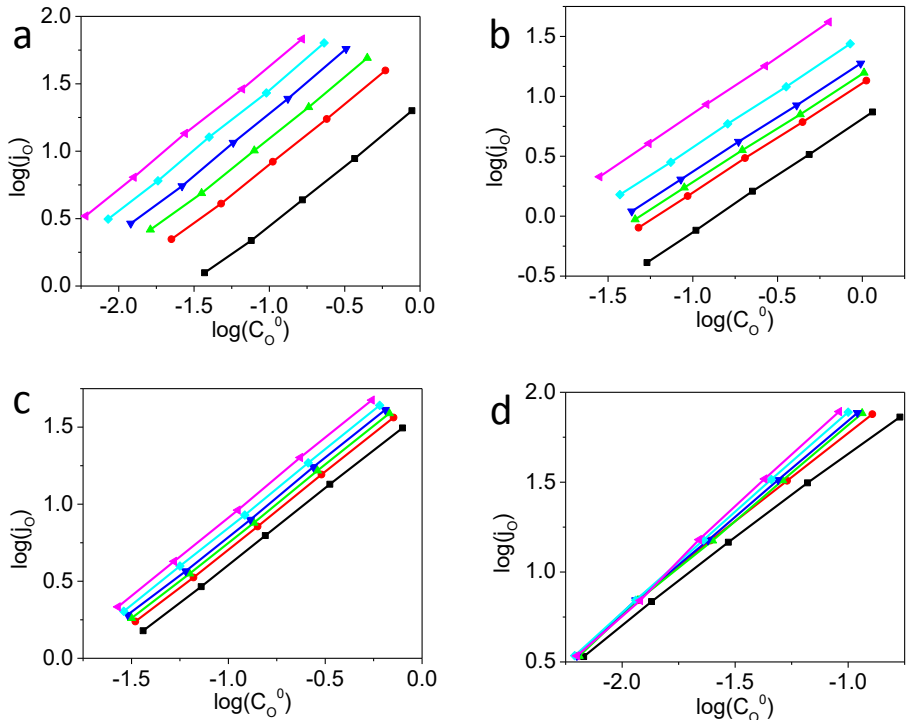

Figure S7. The $\log(C_O^0)$ vs $\log(j_O)$ plot of Au (a), e-rGO (b), N-rGO (c) and $Co(OH)_2$/N-rGO (d). The C_O^0 is in mole m^{-3}. The j_O is in A m^{-2}. The potentials are 0.6 V (Black), 0.5 V (red), 0.4 V (green), 0.5 V (blue), 0.2 V (cyan) and 0.1 V (magenta).

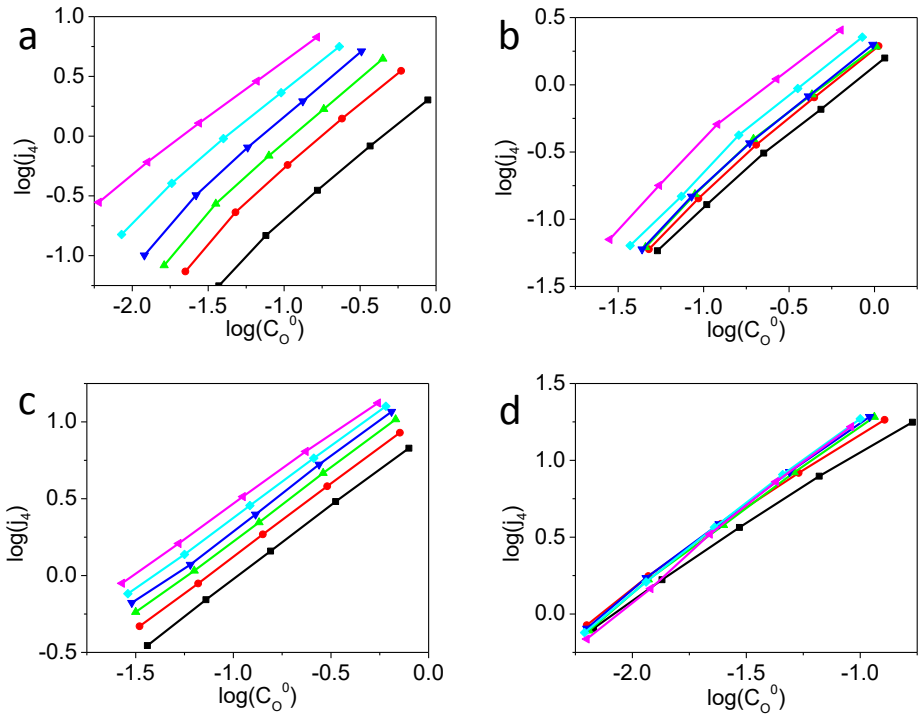

Figure S8. The $\log(C_O^0)$ vs $\log(j_4)$ plot of Au (a), e-rGO (b), N-rGO (c) and $Co(OH)_2$/N-rGO (d). The C_O^0 is in mole m^{-3}. The j_4 is in A m^{-2}. The potentials are 0.6 V (Black), 0.5 V (red), 0.4 V (green), 0.5 V (blue), 0.2 V (cyan) and 0.1 V (magenta).

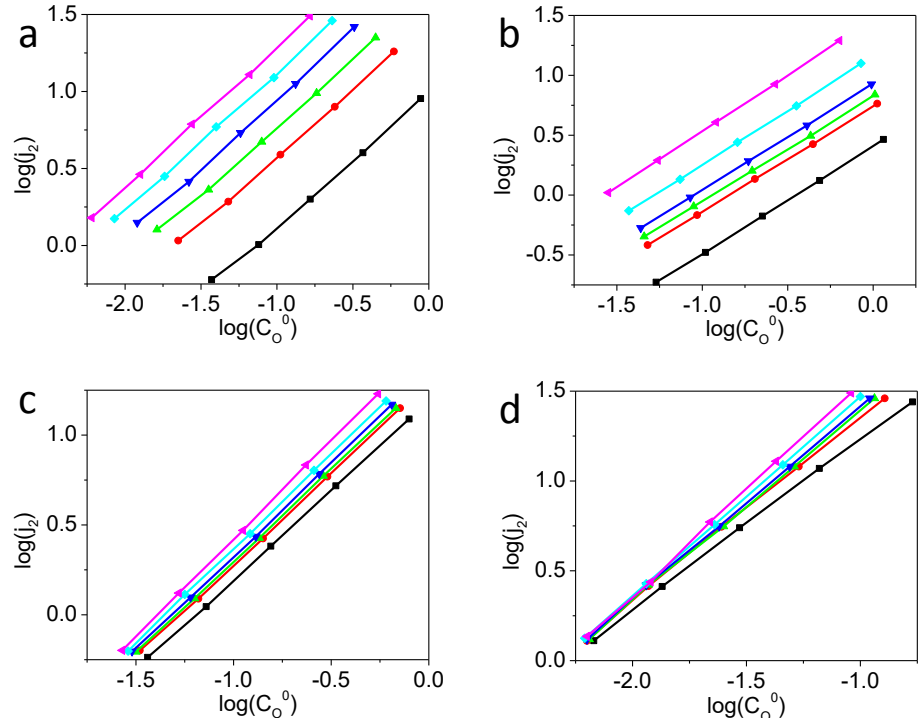

Figure S9. The $\log(C_O^0)$ vs $\log(j_2)$ plot of Au (a), e-rGO (b), N-rGO (c) and $Co(OH)_2$/N-rGO (d). The C_O^0 is in mole m^{-3}. The j_2 is in A m^{-2}. The potentials are 0.6 V (Black), 0.5 V (red), 0.4 V (green), 0.5 V (blue), 0.2 V (cyan) and 0.1 V (magenta).

Chapter 8: Conclusion and Recommendation

8.1 Conclusion

In this thesis, the ORR catalysed by non-precious metal catalysts have been studied, i.e. TM-NCs, from the aspect of material synthesis, physical characterization, performance test and mechanism discussion. The main contributions of this thesis are summarized below.

1. Synthesis. A mature method to synthesize N-rGO by a simple hydrothermal reduction of GO by NH_3 have been developed. The as prepared N-rGO is water soluble, which can be easily made into composite of non-precious metals such as Cu and Ag etc. A method to synthesize Fe/N-rGO from PB with a very low pyrolysis temperature was also developed. Fe facilitates formation of graphitic structure at relatively low temperature. The low temperature retains high level of N.
2. Characterization. All the synthesized materials are characterized by multiple techniques to reveal their composition, morphology and SSA etc. Especially emphasize was paid on the characterization of the TM-N interaction because it is considered as the origin of ORR activity. It is found that XPS and SERS are capable to confirm the interaction.
3. Performance. The ORR performance of CuO/N-rGO and Ag/N-rGO are all very good. The performance is close to commercial Pt/C in alkaline electrolyte. The Fe/N-gCB even shows as good performance as Pt/C in alkaline electrolyte and pretty good performance in acid electrolyte. The high performance makes these catalysts promising in commercial application.
4. Mechanism. The ORR mechanism of each catalyst was discuss. The mechanism is reflected by the peroxide ratio and Tafel slope etc. The incorporation of TM definitely change the ORR mechanism of NC, which is responsible for the enhance performance.

Based on huge amount of electrochemical measurement, it is found that the conventional method in determining the electron transfer number is questionable. The electron transfer numbers measured by RRDE and KL methods don't coincide. Furthermore, it is found the electron transfer number is a function of angular velocity of the electrode, which is beyond the understanding of the researchers in this area. Therefore, a series of experiment were conducted. The forced convection theory was used to prove that even if the sub-reactions in ORR are first order, the electron transfer number will be a function of angular velocity.

And, on some catalysts, the ORR must not first order. Therefore the KL method is not suitable for determining electron transfer number.

Finally, I developed a method to calculate the concentration of oxygen on surface of RDE. Using that method, the order of reaction of each sub-reaction in ORR can be determined. It is found that the order of sub-reaction in ORR can be either higher or lower than 1. The lower order is attributed to occupation of active site while the higher order is attributed to indirect interaction between adsorbed intermediates. These findings are very important to understand the microscopic mechanism of ORR

8.2 Recommendation

In this thesis, all the questions in the aims listed in chapter 1 was tried to be answered. Of course, the results are just a small progress in this area. Based on my experience during the study, some specific question can be raised, which could be answered in the future.

1. What is the exact structure of TM-NC? How to determine it? This question is very tough because in practice, there are numerous possible NC structures in one sample. Each structure will have a series of response to characterization. All these responses from different structures overlap, so that the analysis will be extremely difficult. A possible resolution may be synthesis of standard sample, such as Fe phthalocyanine, which has only one and known structure. Using these standard samples as base, the actual structure of TM-NC may be resoluted.
2. What is the most active TM-NC structure for ORR? This question has been partly answered by theoretical calculation. However, as the lack of ideal sample, the activity of different TM-NC structures have not been tested by experiment. The ideal sample may not synthesized by conventional method. Some more precise techniques, down to atom level, may be necessary.
3. How to synthesize to best TM-NC for ORR? It is the most common question, but still worthy studying for its potential application
4. What is the mechanism of ORR on TM-NC? Again, some advanced techniques that have atomic precision should be used. The intermediates of ORR have never been directly seen, but its existence is the essential to the validity of proposed mechanism. Furthermore, the adsorption energy is considered the limitation of reaction rate, but it is never measured by experiment. All these measurements need breakthrough ideas and methods.